

## ABSTRACT

KIM, JUNGSIK(JUSTIN). Area-Selective Deposition of Organic/Inorganic Materials by Atomic Layer Deposition, Molecular Layer Deposition and Chemical Vapor Deposition. (Under the direction of Gregory N. Parsons).

Thin film deposition is a key technique for semiconductor fabrication such as 3D non-volatile flash memory (NAND), fin field-effect transistor (FinFET), and dynamic random-access memory (DRAM). To continue scaling beyond the 5 nm node size, chemical vapor deposition (CVD), atomic layer deposition (ALD) and molecular layer deposition (MLD) are vigorously investigated in the semiconductor industry due to their conformal growth on 3D complex structure with nanoscale thickness control.

CVD, ALD and MLD play a pivotal role in achieving bottom-up fabrication, so-called “area-selective deposition (ASD)”. While standard top-down lithography has fundamental problems in 5 nm node scale including edge placement error and line edge roughness led by physical misalignment, chemically self-aligned ASD can address these challenges owing to its capability of precise dimension control even less than 5 nm feature size. Furthermore, ASD integration can simplify the fabrication sequence, reducing the process cost and chemical mechanical polishing (CMP) overburden.

This dissertation presents a comprehensive understanding of various thin film depositions by CVD, ALD and MLD, providing a new outlook for developing different ASD capabilities. A range of inorganic and organic materials are explored, and different surface characterization and theoretical studies are used to understand film nucleation and selectivity mechanism. The first part (Chapter 3 and 4) of this dissertation focuses on developing ASD of organic materials, whereas the second part (Chapter 5, 6, and 7) include ASD of inorganic materials, particularly process integration (orthogonal ASD) and metals (tungsten and cobalt).

In the first part of this dissertation, ASD of conjugated polymers including poly(3,4-ethylenedioxythiophene) (PEDOT), polyaniline (PANI), polypyrrole (PPY), and polythiophene (PTH) is studied with MLD and CVD processes. A direct quantitative comparison of ASD between MLD and CVD is discussed with experimental and analytical characterization. Inherent ASD of PEDOT is observed on SiO<sub>2</sub> vs. Si-H, attributed to the localized reduction of the SbCl<sub>5</sub> oxidant on Si-H surfaces. The selectivity results indicate that PEDOT ASD by MLD processes (~8 nm) can be further enhanced by CVD process (~36 nm) due to the fast growth rate of the CVD process. This finding is extended to explore different conjugate polymers such as PPY, PTH, and PANI using reactive monomers and the same SbCl<sub>5</sub> oxidant. The effects of process parameters on film characteristics are investigated to study basic growth behavior. Based on this understanding, ASD of different conjugated polymers is comparatively evaluated.

In the second part of this dissertation, the orthogonal ASD of titanium dioxide (TiO<sub>2</sub>)/tungsten (W) ASDs and metal ASDs of cobalt and tungsten are discussed. For the orthogonal ASD, the integration of two ASD processes on a single patterned substrate where self-aligned growth is obtained, *i.e.* TiO<sub>2</sub> ASD on SiO<sub>2</sub> followed by W ASD on Si-H. Sequential effect on obtaining orthogonal ASD is studied and nanoscale patterning of TiO<sub>2</sub>/W on SiO<sub>2</sub>/Si-H patterned wafers is demonstrated. The successful orthogonal demonstration is attributed to simultaneous etching and deposition during W ALD processes. Cobalt metal ASD processes are studied using bis(1,4-di-tert-butyl-1,3-diazadienyl)cobalt (CoDAD) and formic acid, showing CVD growth rather than ALD growth due to the instability of CoDAD precursor. W metal ASD is explored by using repeated ALD and atomic layer etching (ALE) supercycle to understand the etching effect on the subsequent W growth.

© Copyright 2022 by JungSik Kim

All Rights Reserved

Area-Selective Deposition of Organic/Inorganic Materials by Atomic Layer Deposition,  
Molecular Layer Deposition and Chemical Vapor Deposition

by  
JungSik Kim

A dissertation submitted to the Graduate Faculty of  
North Carolina State University  
in partial fulfillment of the  
requirements for the degree of  
Doctor of Philosophy

Chemical Engineering

Raleigh, North Carolina  
2022

APPROVED BY:

---

Dr. Gregory N. Parsons  
Committee Chair

---

Dr. Jan Genzer

---

Dr. H. Henry Lamb

---

Dr. Divine Kumah

## **DEDICATION**

To my family, our research group and friends for their support during this long journey.

## **BIOGRAPHY**

JungSik(Justin) Kim was born and raised in Seoul/Daejeon, South Korea. After graduating from Bomoon High School in Daejeon, South Korea, Justin went to Tohoku University in Sendai, Japan to study materials science engineering. During his undergraduate and master at Tohoku University, Justin studied Cu metallization for c-Si solar cells with wet-based barrier layers under the direction of Koike Junichi. Justin was also involved in various social activities including Sendai International Relationship Association (SIRA), Tohoku University Korean Student Association, and Tohoku University International Soccer Team. After finishing his master degree at 2014, Justin went back to Korea to serve his military service at Daegu Gyeongbuk Institute of Science and Technology (DGIST) in Daegu, South Korea. The main role during this period was developing thin film solar cells using earth-abundant elements such as Cu, Zn, Sn, S and Se. While working as a researcher at DGIST, Justin enjoyed fundamental and systematic research, leading him to pursue the doctorate degree at North Carolina State University (NCSU). He was fortunate to receive a position in Gregory Parsons' research group in 2017. The spring of his first year at NCSU, Justin met his fiancé, Dorothy Eunji You. From August 2022, Justin will start a position at LAM Research in Fremont, CA.

## ACKNOWLEDGMENTS

There are several people to whom I am truly indebted for the completion of this work. First, I must thank my mentor, Dr. Gregory Parsons, for guiding and supporting me throughout the entire graduate studies. Second, I must thank my fiancé, Dorothy Eunji You, for making me stay confident on my work and providing endless love and joy. Without her encouragement and support, this dissertation would not have been possible. I also must thank my family for giving me a full of energy to pursue this degree and praying for me throughout my studies.

I am also extremely thankful to the Parsons' research group member and friends in my department, both past and present members. Working with them enables me to learn invaluable experience not only academic knowledge but also a sense of humor. Without them, my journey would never have been achieved. It was my fortune and honor to meet and work with my colleagues.

## TABLE OF CONTENTS

<b>LIST OF TABLES .....</b>	<b>ix</b>
<b>LIST OF FIGURES .....</b>	<b>xi</b>
<b>Chapter 1 Introduction and Background .....</b>	<b>1</b>
1.1 Thin Film Deposition .....	1
1.1.1 Chemical Vapor Deposition (CVD).....	2
1.1.2 Atomic Layer Deposition (ALD).....	3
1.1.3 Molecular Layer Deposition (MLD).....	5
1.2 Area-Selective Deposition (ASD).....	5
1.3 Objective and Overview of Work .....	8
1.4 References .....	10
<b>Chapter 2 Experimental Tools.....</b>	<b>18</b>
2.1 Atomic Layer Deposition Reactor.....	18
2.2 Quartz Crystal Microbalance (QCM) Analysis.....	22
2.3 Spectroscopic Ellipsometry (SE) .....	26
2.4 Profilometry .....	28
2.5 X-Ray Photoelectron Spectroscopy (XPS) .....	29
2.6 X-Ray Reflectivity (XRR) .....	30
2.7 Scanning Electron Microscopy (SEM) .....	33
2.8 Transmission Electron Microscopy (TEM) .....	33
2.9 Four Point Probe.....	34
2.10 Fourier Transform Infrared Spectroscopy (FTIR) .....	35
2.11 References .....	36
<b>Chapter 3 Nanopatterned Area-Selective Vapor Deposition of PEDOT on SiO<sub>2</sub> vs. Si-H: Improved Selectivity using Chemical Vapor Deposition vs. Molecular Layer Deposition ..</b>	<b>37</b>
3.1 Abstract .....	37
3.2 Introduction.....	38
3.3 Experimental Section .....	41
3.3.1 Deposition Reactants .....	41
3.3.2 Deposition Substrates.....	41
3.3.3 Reactor Design and Reaction Sequence .....	42
3.3.4 Sample Characterization .....	43
3.4 Results and Discussion.....	45
3.4.1 Area-Selective MLD of PEDOT on Blanket Substrates.....	47

3.4.2	Area-Selective MLD on Patterned Substrates .....	51
3.4.3	Area-Selective CVD of PEDOT on Blanket Substrates .....	52
3.4.4	Area-Selective CVD on Patterned Substrates.....	54
3.4.5	Vertical vs. Lateral Growth.....	55
3.4.6	Mechanism for PEDOT Selectivity on SiO <sub>2</sub> vs. Si-H.....	57
3.4.7	Quantified Selectivity and Comparison of MLD vs. CVD.....	58
3.5	Summary .....	60
3.6	Supporting Information .....	62
3.6.1	Definition of Selectivity( $S(t_{growth})$ ), and Area-Selective Deposition Figures of Merit 62	
3.6.2	Nucleation Model Description.....	63
3.6.3	Model Fitting and Results.....	64
3.7	References .....	74
<b>Chapter 4</b>	<b>Area-Selective Deposition of Conjugated Polymers .....</b>	<b>80</b>
4.1	Abstract .....	80
4.2	Introduction .....	80
4.3	Experimental Section .....	81
4.3.1	Substrate preparation .....	81
4.3.2	Reactor and Process Sequence.....	82
4.3.3	Characterization Methods .....	84
4.4	Results and Discussion.....	85
4.4.1	Polypyrrole deposition .....	85
4.4.2	Polythiophene Deposition.....	97
4.4.3	Polyaniline Deposition.....	99
4.4.5	Area-selective Deposition of Conjugated Polymers.....	106
4.5	Summary .....	112
4.7	References .....	114
<b>Chapter 5</b>	<b>Multimaterial Self-Aligned Nanopatterning by Simultaneous Adjacent Thin Film Deposition and Etching.....</b>	<b>119</b>
5.1	Abstract .....	119
5.2	Introduction .....	120
5.3	Experimental Section .....	122
5.3.1	Substrate Preparation. ....	122
5.3.3	TiO <sub>2</sub> ALD/ALE Supercycles Condition. ....	124

5.3.4	W ALD Cycles Condition.....	124
5.3.5	Integrated Sequence of “TiO <sub>2</sub> ALD/ALE → HF Dipping → W ALD”.....	125
5.3.6	HF/TMA Exposures on ZnO and Al <sub>2</sub> O <sub>3</sub> .....	125
5.3.7	Characterization.....	126
5.4	Results and Discussion.....	127
5.4.1	Extension to Other Material Systems.....	140
5.5	Summary.....	144
5.6	Supporting Information.....	145
5.6.1	Effect of intermediate surface treatments (H <sub>2</sub> +Ar plasma and HF dip) on W growth	145
5.7	References.....	153
<b>Chapter 6 Cobalt metal deposition using bis(1,4-di-tert-butyl-1,3-diazadienyl)cobalt and formic acid with atomic layer deposition and chemical vapor deposition.....</b>		<b>159</b>
6.1	Abstract.....	159
6.2	Introduction.....	159
6.3	Experimental Section.....	161
6.3.1	Substrate preparation.....	161
6.3.2	Reactor and Process Sequence.....	162
6.3.3	Characterization Methods.....	165
6.4	Results and Discussion.....	165
6.4.1	Basic Growth Behavior.....	165
6.4.2	Cobalt ASD and film quality.....	172
6.6	Summary.....	181
6.8	References.....	182
<b>Chapter 7 Tungsten metal deposition with atomic layer deposition/atomic layer etching to achieve area-selective deposition.....</b>		<b>186</b>
7.1	Abstract.....	186
7.2	Introduction.....	186
7.3	Experimental Section.....	190
7.3.1	Substrate Surface Preparation and Deposition Reactants.....	190
7.3.2	Reactor Design and Reactor Sequence.....	191
7.3.3	Sample Characterization.....	192
7.5	Results and Discussion.....	193
7.7	Summary.....	201
7.9	References.....	202

<b>APPENDICES</b> .....	<b>207</b>
Appendix A. Co-Authored Publications .....	208
A.1 Effect of reactant dosing on selectivity during area-selective deposition of TiO <sub>2</sub> <i>via</i> integrated atomic layer deposition and atomic layer etching.....	208
A.2 Oxidative molecular layer deposition of PEDOT using volatile antimony(V) chloride oxidant.....	210

## LIST OF TABLES

Table 2.1	Reactor diagnostic.....	22
Table 2.2	Mass gain comparison on unpolished and polished QCM crystals .....	26
Table 2.3	Summary of the parameters resulting from the fitting of the XRR data.....	33
Table 3.1	Quantitative Comparison of PEDOT ASD <i>via</i> MLD <i>vs.</i> CVD. ....	60
Table 3.2	PEDOT thickness on SiO <sub>2</sub> measured by SE, XRR and SEM. Films were deposited on SiO <sub>2</sub> at 100 °C using SbCl <sub>5</sub> /N <sub>2</sub> /EDOT/N <sub>2</sub> = 0.1/60/2/60 s.....	67
Table 3.3	Elemental composition from XPS analysis. Values are given in atomic % . ....	69
Table 3.4	PEDOT surface roughness on SiO <sub>2</sub> and Si-H by AFM. Each RMS is the average of three measurements scanned over 2 x 2 μm. ....	71
Table 4.1	Basic chemical properties of different monomers. ....	83
Table 4.2	The conductivity and thickness of PPY films by CVD at 50 and 150 °C. For the thickness measurement, SE and profilometer were compared. ....	94
Table 4.3	Elemental composition from XPS analysis and RMS values from AFM results for PPY on Si-OH with various MLD and CVD temperatures. XPS values are given in atomic % . ....	96
Table 4.4	Elemental composition from XPS analysis and RMS values from AFM results for PTH on Si-OH at 25 °C by CVD. XPS values are given in atomic %.....	99
Table 4.5	Elemental composition from XPS analysis and RMS values from AFM results for PANI on Si-OH with various CVD temperatures. XPS values are given in atomic % . ....	105
Table 5.1	XPS atomic fraction (at.%) measured on Si-H and TiO <sub>2</sub> before and after exposure to 15 or 20 cycles of SiH <sub>4</sub> /WF <sub>6</sub> at 220 °C. <sup>a</sup> .....	133
Table 5.2	A partial list of example material systems showing thermodynamic feasibility for self-aligned patterning <i>via</i> simultaneous deposition and etching. <sup>a</sup> .....	142
Table 5.3	XPS atomic concentration (%) data collected from Si-H substrates after TiO <sub>2</sub> (= 12 supercycles of TiO <sub>2</sub> ALD/ALE at 150 °C) and W (= 10 cycles of SiH <sub>4</sub> /WF <sub>6</sub> at 220 °C). The effect of two treatments, “H <sub>2</sub> *” and “HF”, between the TiO <sub>2</sub> and W steps was tested. “H <sub>2</sub> *” = 4% H <sub>2</sub> /Ar plasma for 300 s at 10 watts; and “HF” = 5 s dip in dilute 5% HF. The HF dip allowed the most substantial growth of W...149	149
Table 5.4	Thickness of TiO <sub>2</sub> or W measured by ellipsometry on blanket Si-H and Si-OH substrates after TiO <sub>2</sub> deposition at 150 °C followed by SiH <sub>4</sub> /WF <sub>6</sub> at 220 °C. Between TiO <sub>2</sub> and W steps, the samples received a 5 s dip in dilute HF. The Si-H and Si-OH substrates were treated simultaneously to each reaction. The TiO <sub>2</sub> was done using 20 ALD/ALE supercycles at 150 °C, leading to ASD of TiO <sub>2</sub> predominantly on Si-OH. The SiH <sub>4</sub> /WF <sub>6</sub> was performed for 15 cycles. A second pair of substrates was also prepared with ASD TiO <sub>2</sub> , and those samples were	

	treated with 20 SiH <sub>4</sub> /WF <sub>6</sub> cycles. The W thickness is determined with ellipsometry using a correlation between delta value and thickness. <sup>6</sup> .....	150
Table 5.5	Surface composition determined by XPS for Si-H and TiO <sub>2</sub> after exposure to SiH <sub>4</sub> /WF <sub>6</sub> at 220 °C and after exposing the same samples to 5 doses of BCl <sub>3</sub> gas. Each BCl <sub>3</sub> dose included 1 s BCl <sub>3</sub> exposure and 45 s N <sub>2</sub> purge. The TiO <sub>2</sub> was deposited on Si-OH using 20 ALD/ALE supercycles at 150 °C. Before the SiH <sub>4</sub> /WF <sub>6</sub> treatment, the Si-H surface was also exposed to the same TiO <sub>2</sub> treatment of 20 ALD/ALE supercycles at 150 °C. Results show a large W signal on Si-H due to W deposition, with some residual W on TiO <sub>2</sub> due to residual WO <sub>3</sub> vapor etching intermediate. After BCl <sub>3</sub> treatment, the WO <sub>3</sub> signal is smaller, consistent with WO <sub>3</sub> etching by BCl <sub>3</sub> . The W surface on Si-H showed no B after the BCl <sub>3</sub> treatment.....	151
Table 6.1	Basic chemical properties of precursors for Cobalt deposition. <sup>28</sup> .....	163
Table 6.2	Process condition comparison using CoDAD precursors for Co deposition. ....	172
Table 6.3	Photographic images of surface color change and sheet resistance before/after Co deposition on various substrates.....	175
Table 6.4	Elemental composition from XPS analysis in Figure 6.7. Values are given in atomic %.....	178
Table 6.5	Elemental composition from XPS analysis in Figure 6.9. Values are given in atomic %.....	180
Table 7.1	W thickness on Si-H measured by SE and TEM at 220 °C.....	194
Table 7.2	W ALD and ALE supercycle conditions.....	197
Table 7.3	Elemental composition from XPS analysis. Values are given in atomic %.....	199

## LIST OF FIGURES

Figure 1.1	Reaction sequence of atomic layer deposition (ALD) and molecular layer deposition (MLD).....	4
Figure 2.1	Reactor Scheme.....	18
Figure 2.2	Reactor pumping speed comparison. ....	21
Figure 2.3	QCM crystal roughness effect on mass gain during Al <sub>2</sub> O <sub>3</sub> ALD process.....	25
Figure 2.4	High resolution XPS scan of Sb 3d/O 1s for polypyrrole film on Si substrate by CVD at 50 °C.....	30
Figure 2.5	X-ray reflectivity pattern of 200 and 400 cycles of PEDOT MLD on thermal SiO <sub>2</sub> (100 nm)/Si at 100 °C.....	32
Figure 3.1	(a) Quartz crystal microbalance mass uptake during PEDOT MLD cycles using EDOT and SbCl <sub>5</sub> at 100 °C, (b) enlarged view of (a) showing a large mass uptake during the SbCl <sub>5</sub> and a slight mass decrease during the EDOT dose, and (c) proposed reaction scheme for the PEDOT oMLD process. ....	47
Figure 3.2	PEDOT film thickness vs. MLD cycles at 100 °C on SiO <sub>2</sub> and Si-H using (a) SbCl <sub>5</sub> /N <sub>2</sub> /EDOT/N <sub>2</sub> = 0.5/60/2/60 s and (b) SbCl <sub>5</sub> /N <sub>2</sub> /EDOT/N <sub>2</sub> = 0.1/60/2/60 s. The dashed lines are fits to an analytical model described in the text. ....	49
Figure 3.3	Cross-sectional SEM images of films deposited on SiO <sub>2</sub> using (a) 200 and (b) 400 cycles of MLD. XPS spectra collected in the S 2p region on (c) SiO <sub>2</sub> and (d) Si-H after 50, 100, 200, and 400 cycles of MLD. ....	50
Figure 3.4	Plan-view SEM images for (a) 200 and (b) 400 MLD cycles at 100 °C on Si-H/SiO <sub>2</sub> substrates. Cross-sectional STEM images for (c) 200 MLD cycles at 100 °C on Si-H/SiO <sub>2</sub> substrates, (d) enlarged view of (c), and (e) EDX elemental mapping of the corresponding region. All samples were deposited on 3 μm Si-H/SiO <sub>2</sub> line/space-patterned wafers. ....	52
Figure 3.5	PEDOT film thickness vs. CVD process time at 150 °C on SiO <sub>2</sub> and Si-H under 0.37 Torr. The dashed lines are fits to an analytical model described in the text. ..	53
Figure 3.6	Angled-view SEM images of PEDOT CVD on Si-H/SiO <sub>2</sub> -patterned wafers at 150 °C for (a–c) = 10 s, (d–f) 15 s, and (g–i) 30 s. ....	55
Figure 3.7	Angled-view SEM images of PEDOT CVD at 150 °C for (a) 15 s on a coplanar 130 nm SiO <sub>2</sub> /130 nm Si-H line-patterned wafer and (b) 30 s on a coplanar 130 nm SiO <sub>2</sub> /430 nm Si-H line-patterned wafer. The PEDOT growth on SiO <sub>2</sub> extends laterally over the top of the adjacent Si-H, and the distance of the lateral growth is approximately equal to the vertical growth thickness. ....	56
Figure 3.8	PEDOT ASD experimental results along with model output fits using (a) MLD with SbCl <sub>5</sub> = 0.5 s/cycle at 100 °C, (b) MLD with SbCl <sub>5</sub> = 0.1 s/cycle at 100 °C, and (c) CVD conditions at 150 °C. The model parameters corresponding to the resulting line fits are also given for each data set. ....	66

Figure 3.9	The effect of reactant dose times of (a) $\text{SbCl}_5$ and (b) EDOT on PEDOT growth on $\text{SiO}_2$ at $100\text{ }^\circ\text{C}$ . EDOT dose was held constant at 2.0 s for (a) and $\text{SbCl}_5$ dose time was held constant 0.5 s for (b). Dashed lines in (a) and (b) are drawn as guides to the eye. Panel (c) shows the thickness/cycle at different temperatures using the dose conditions indicated. All data were measured by spectroscopic ellipsometry and the error bar was from the standard deviation of three separate measurements. ....	67
Figure 3.10	High resolution XPS scans of (a) Cl 2p, (b) C 1s (c) Sb 3d/O 1s, (d) Si 2p on $\text{SiO}_2$ substrates and (e) Cl 2p, (f) C 1s, (g) Sb 3d/O 1s, (h) Si 2p on Si-H substrates for various MLD cycles at $100\text{ }^\circ\text{C}$ . To clearly see the peak change, each spectrum was offset on the y-axis. Peak positions were calibrated by referencing the adventitious C 1s peak to 285.0 eV. Note that for the Sb 3d peak deconvolution, Sb 3d <sub>5/2</sub> and 3d <sub>3/2</sub> peaks were separated by 9.32 eV with a relative intensity of 3 to 2. ....	68
Figure 3.11	Plan-view SEM images of PEDOT films formed using (a) 100, (b) 200, and (c) 400 MLD cycles on $\text{SiO}_2$ and Si-H at $100\text{ }^\circ\text{C}$ . After 100 cycles on $\text{SiO}_2$ , panel (a) shows non-uniform surface structure, consistent with PEDOT nuclei. As MLD cycles increase to 200 and 400 cycles, the surface texture on the $\text{SiO}_2$ becomes more uniform, consistent with nuclei coalescence and uniform growth. On the Si-H substrates, no PEDOT nuclei are observed after 100 or 200 MLD cycles. After 400 cycles, white particles appear on the surface, consistent with PEDOT nucleation. ....	70
Figure 3.12	Thermodynamic analysis (HSC Chemistry 7.1) showing the expected equilibrium species concentrations at 1 Torr at temperatures between 25 and $400\text{ }^\circ\text{C}$ for: (a) 1 kmol of $\text{Si}_{(s)}$ + 1 kmol of $\text{SbCl}_{5(g)}$ ; and (b) 1 kmol of $\text{SiO}_{2(s)}$ + 1 kmol of $\text{SbCl}_{5(g)}$ . The plots show that $\text{SbCl}_5$ is expected to react with silicon, but no reaction is expected on $\text{SiO}_2$ . ....	72
Figure 3.13	Cross-sectional SEM images of bare Si-H/ $\text{SiO}_2$ patterned substrates and cross-sectional STEM image of the Si-H/ $\text{SiO}_2$ patterned substrates after multiple doses of $\text{SbCl}_5$ (without EDOT exposure) at $100\text{ }^\circ\text{C}$ . Sample-to-sample variation in the starting pattern production process causes differences in the $\text{SiO}_2$ edge profile shape. The $\text{SbCl}_5$ doses led to loss of silicon, with more etching at the Si-H/ $\text{SiO}_2$ boundary region. The extent of $\text{SbCl}_5$ exposure was larger than that used for ASD of PEDOT shown in Figure 3.4. For this test, the $\text{SbCl}_5$ doses were performed with PEDOT coated on the inner reactor walls, rather than the typical $\text{Al}_2\text{O}_3$ prepared during chamber conditioning. We find that the PEDOT on the reactor wall absorbs $\text{SbCl}_5$ during the dose period and releases it during the purge, leading to a larger $\text{SbCl}_5$ dose than expected. ....	73
Figure 4.1	Quartz crystal microbalance mass uptake during PPY CVD process using pyrrole and $\text{SbCl}_5$ at $175\text{ }^\circ\text{C}$ . As a control experiment, the mass uptake was measured during only dose of pyrrole or $\text{SbCl}_5$ , indicating no noticeable mass change during separate dose of the reactant. ....	87

Figure 4.2	The effect of reactant dose times of (a) SbCl <sub>5</sub> and (b) Pyrrole on the growth rate of PPY deposited on Si-OH at 125 °C. Pyrrole dose was held constant 2 s for (a) and SbCl <sub>5</sub> dose time was held constant at 1 s for (b). The effect of purge time on the growth rate of PPY. PPY thickness at 125 °C as a function of MLD cycles on Si-OH. SbCl <sub>5</sub> and pyrrole doses were held constant at 0.5 and 0.5 for (c), and 1 and 2 s for (d), respectively. All thicknesses were measured by spectroscopic ellipsometry and the error bar was from multiple sets average. Lines were drawn as guides to the eye.....	88
Figure 4.3	(a) PPY film thickness as a function of MLD deposition temperature on Si-OH using SbCl <sub>5</sub> /N <sub>2</sub> /Pyrrole/N <sub>2</sub> = 1.0/10/2.0/10 s. (b) PPY film thickness as a function of CVD deposition temperature on Si-OH. The CVD deposition time and the working pressure were held at 15 s and 1 Torr, respectively. For both MLD and CVD processes, the SbCl <sub>5</sub> and pyrrole source temperatures were held at 50 and 25 °C, respectively. (c) Three samples were loaded with distance of 9 cm to test the thickness gradient of the reactor. All thicknesses were measured by spectroscopic ellipsometry and the error bar was from multiple sets average. Lines were drawn as guides to the eye.....	90
Figure 4.4	FTIR spectra of PPY on double-side polished Si-OH at different (a) MLD temperatures and (b) CVD temperatures. All the spectra were normalized by the Si-Si peak (~610 cm <sup>-1</sup> ) and subtracted to the bare Si-OH spectra. MLD samples were deposited following SbCl <sub>5</sub> /N <sub>2</sub> /Py/N <sub>2</sub> = 1.0/10/2.0/10s. Same samples were measured for Figure 4.4, 6 and 7.....	93
Figure 4.5	(a) Snapshot of profilometer scan region, and step height measured by profilometer of (a) PPY CVD at 50 °C and (b) PPY CVD at 150 °C. Step height was made by scratching the surface with the tweezer. Panel (b) shows a clear step height whereas panel (c) shows no step height due to the strong adhesion of deposited film on the substrate.....	94
Figure 4.6	High resolution XPS scans of C 1s, N 1s, Cl 2p, and Sb 3d/O 1s after PPY deposition on Si-OH at different CVD temperatures. For a peak deconvolution of Sb 3d and O 1s, a peak distance of 9.34 eV and a relative intensity of 1.5 between Sb 3d <sub>5/2</sub> and Sb3d <sub>3/2</sub> were used. ....	95
Figure 4.7	AFM images of (a) bare Si-OH, PPY deposited on Si-OH by CVD processes at (b) 50 °C and (c) 200 °C. Each RMS value is the average of three different measurements. ....	96
Figure 4.8	(a) Polythiophene (PTH) thickness as a function of MLD cycles on Si-OH at 25 and 50 °C. The MLD sequence followed: SbCl <sub>5</sub> (50 °C)/N <sub>2</sub> /thiophene(25 °C)/N <sub>2</sub> = 0.5/1.0/0.1/1.0 s. (b) PTH thickness as a function of CVD time on Si-OH at 25 °C. (c) The effect of CVD temperatures on PTH thickness after 30 s of CVD process time. All thicknesses were measured by spectroscopic ellipsometry and the error bar was from multiple sets average. Lines were drawn as guides to the eye. ....	98

Figure 4.9	High resolution XPS scans of C 1s, Cl 2p, S 2p and Sb 3d/O 1s after PTH deposition on Si-OH at 25 °C. For a peak deconvolution of Sb 3d and O 1s, a peak distance of 9.34 eV and a relative intensity of 1.5 between Sb 3d <sub>5/2</sub> and Sb3d <sub>3/2</sub> were used. ....	98
Figure 4.10	(a) The effect of purge time on the growth rate of polyaniline (PANI) on Si-OH at 25 °C. SbCl <sub>5</sub> and aniline dose times were held constant 0.1 s. (b) PANI thickness as a function of MLD cycles on Si-OH at 75 °C. The effect of (c) MLD and (d) CVD temperatures on PANI thickness on Si-OH. For (b) and (c), the MLD sequence followed: SbCl <sub>5</sub> (50 °C)/N <sub>2</sub> /aniline(60 °C)/N <sub>2</sub> = 0.1/10/0.1/10 s. For (d), CVD process time was held at 30 s. All thicknesses were measured by spectroscopic ellipsometry and the error bar was from multiple sets average. Lines were drawn as guides to the eye. ....	102
Figure 4.11	FTIR spectra of PANI on double-side polished Si-OH at different CVD. All the spectra were normalized by the Si-Si peak (~610 cm <sup>-1</sup> ) and subtracted to the bare Si-OH spectra. Same samples were used for Figure 4.11, 12 and 13. ....	103
Figure 4.12	AFM images of PPY deposited on Si-OH by CVD processes at (a) 25 °C, (b) 75 °C and (c) 125 °C. Each RMS value is the average of three different measurements. For (b), red line on 2D mapping indicates the linescan on the bottom of 3D mapping. ....	104
Figure 4.13	High resolution XPS scans of C 1s, N 1s, Cl 2p, and Sb 3d/O 1s after PANI deposition on Si-OH at different CVD temperatures. For a peak deconvolution of Sb 3d and O 1s, a peak distance of 9.34 eV and a relative intensity of 1.5 between Sb 3d <sub>5/2</sub> and Sb3d <sub>3/2</sub> were used. ....	105
Figure 4.14	Area-selective deposition (ASD) of polypyrrole (PPY) on SiO <sub>2</sub> vs. Si-H as a function of MLD cycle at (a) 75, (b) 100, (c) 125, and (d) 150 °C. (e) Substrate selectivity of PPY as a function of MLD cycles at 125 °C. All MLD processes followed: SbCl <sub>5</sub> /N <sub>2</sub> /Pyrrole/N <sub>2</sub> = 1.0/10/2.0/10 s. (f) ASD of PPY by CVD at different temperatures (50 – 300 °C) on SiO <sub>2</sub> vs. Si-H. CVD deposition time was held at 15 s. All thicknesses were measured by spectroscopic ellipsometry and the error bar was from multiple sets average. ....	108
Figure 4.15	Polypyrrole (PPY) selectivity as a function of the thickness of PPY on SiO <sub>2</sub> at (a) various MLD temperatures and (b) CVD temperatures. Selectivity was calculated based on the thickness data measured by spectroscopic ellipsometry and Eq. (1.1). ....	110
Figure 4.16	Cross-sectional SEM images of (a) bare Cu and (b) after 50 cycles of (SbCl <sub>5</sub> (40 °C)/N <sub>2</sub> = 0.1/60 s) doses on Cu substrates. All scales are the same. Top right of each image shows the photographic image of each sample, describing the surface color change. ....	110
Figure 4.17	Area-selective deposition of (a) PEDOT, (b) PPY, (c) PTH, and (d) PANI with various CVD temperatures. Blue heightened region indicates selective window on SiO <sub>2</sub> vs. Si-H. For PTH, pulse CVD was used to improve the film uniformity.	

All thicknesses were measured by spectroscopic ellipsometry and the error bar was from multiple sets average. Lines were drawn as guides to the eye. .... 111

- Figure 5.1 Schematic for self-aligned patterning using simultaneous deposition and etching: (a) starting Si-H/TiO<sub>2</sub> pattern exposed to a set of reactants (in this example, SiH<sub>4</sub>/WF<sub>6</sub> in an ALD-type reaction sequence for 20 cycles), yielding W growth on silicon, with no growth in the TiO<sub>2</sub> region due to simultaneous TiO<sub>2</sub> etching. (b) Mass change (ng/cm<sup>2</sup>) measured by QCM during SiH<sub>4</sub>/WF<sub>6</sub> exposures (SiH<sub>4</sub>/Ar/WF<sub>6</sub>/Ar = 45/45/1/60 s) at 220 °C, along with the expected reactions during SiH<sub>4</sub> and WF<sub>6</sub> exposure steps on W and on TiO<sub>2</sub> surfaces. The indicated product species are from thermodynamic analysis. A QCM precoated with Al<sub>2</sub>O<sub>3</sub> shows net mass gain indicating favorable ALD of W (blue line). On the basis of the density of W, the growth rate is ~0.5 nm/cycle. Under identical conditions, a QCM crystal precoated with TiO<sub>2</sub> shows net mass loss corresponding to etching (black line), with an etch rate of ~0.1 nm/cycle. (c) Overall Gibbs free energy change for SiH<sub>4</sub>/WF<sub>6</sub> reactions on TiO<sub>2</sub> (red) and Si (black) surfaces, consistent with the QCM results in panel b. (d) Thermodynamic equilibrium product compositions for WF<sub>6</sub> reacting with an equimolar composition of TiO<sub>2</sub>, further supporting simultaneous deposition and etching.... 131
- Figure 5.2 Self-aligned orthogonal micro-scale patterning of TiO<sub>2</sub> and W films: (a) schematic sequence used for preparation of patterned sacrificial TiO<sub>2</sub> layer, followed by simultaneous deposition and etching to form the self-aligned W and TiO<sub>2</sub>; (b) cross-sectional STEM and STEM-EDX after 15 SiH<sub>4</sub>/WF<sub>6</sub> cycles; and (c) data collected from an identical sample after 20 SiH<sub>4</sub>/WF<sub>6</sub> cycles. The images show the SiH<sub>4</sub>/WF<sub>6</sub> cycles produce net W deposition in exposed Si-H regions, with simultaneous etching of the sacrificial TiO<sub>2</sub> layer. .... 135
- Figure 5.3 Angled view SEM for: (a) Si-H/SiO<sub>2</sub> patterns with no TiO<sub>2</sub> present after 20 cycles of SiH<sub>4</sub>/WF<sub>6</sub>, indicating W deposition on both of Si-H and SiO<sub>2</sub>; (b) the sample from Figure 5.2b, showing surface texture consistent with W deposition on Si-H and simultaneous etching of the TiO<sub>2</sub>; and (c) the sample from Figure 5.2c showing a small number of W nuclei on SiO<sub>2</sub>, consistent with consumption of the TiO<sub>2</sub> sacrificial layer. .... 137
- Figure 5.4 (a) Broad-view schematic of the orthogonal selective deposition of W and TiO<sub>2</sub> on Si-H/SiO<sub>2</sub> patterned surfaces (200 nm width and ~100 nm height) after TiO<sub>2</sub> 20 supercycles and W 15 cycles; (b) cross-sectional STEM of the multiple patterns; (c) zoom-in view of one pattern from (b); (d) STEM-EDX corresponding to image (c). .... 139
- Figure 5.5 (a) Collected QCM mass gain data from Al<sub>2</sub>O<sub>3</sub> or ZnO precoated crystals during 15 cycles of (HF/TMA) exposures. (b) AlF<sub>3</sub> deposition mechanism on Al<sub>2</sub>O<sub>3</sub> surface and (c) ZnO atomic layer etching mechanism on ZnO during 15 HF/TMA cycles. Reaction schemes indicate the expected dominant products from thermodynamic analysis. .... 143
- Figure 5.6 XPS spectra collected from blanket Si-OH wafers after TiO<sub>2</sub> deposition at 150°C followed by SiH<sub>4</sub>/WF<sub>6</sub> at 220°C. The TiO<sub>2</sub> was done using 20 ALD/ALE

supercycles, leading to favorable TiO<sub>2</sub> growth on the Si-OH. The SiH<sub>4</sub>/WF<sub>6</sub> was performed for 15 cycles. (a) Ti 2p region showing TiO<sub>2</sub> with no signal for TiSi<sub>2</sub>, consistent with no reaction during the SiH<sub>4</sub> dose step. (b) W 4f spectra showing some WO<sub>3</sub> present after SiH<sub>4</sub>/WF<sub>6</sub> at 220°C. The thin residual WO<sub>3</sub> layer does not accumulate during SiH<sub>4</sub>/WF<sub>6</sub> treatment, and can be removed by exposure to BCl<sub>3</sub> (Table 4.6).<sup>1,2</sup> ..... 147

- Figure 5.7 (a) Ellipsometry delta parameter ( $\Delta$ ) at  $\lambda = 700$  nm on Si-H substrates after various treatments: “Si-H” = starting Si-H surface prepared by treating Si-OH with 30 s dip in dilute (5%) HF; “Si-H + W” = HF dip + W (*i.e.* no TiO<sub>2</sub> ALD/ALE); “Si-H + TiO<sub>2</sub> + W” = no intermediate treatment between TiO<sub>2</sub> and W; “Si-H + TiO<sub>2</sub> + H\* + W” = intermediate treatment with 4% H<sub>2</sub>/Ar plasma for 300 s at 10 watts. “Si-H + TiO<sub>2</sub> + HF + W” = intermediate treatment with 5 s dip in dilute 5% HF. A smaller value for  $\Delta$  corresponds to a thicker W film. The TiO<sub>2</sub> treatment was 12 ALD/ALE supercycles at 150°C, and the W step was 10 cycles of SiH<sub>4</sub>/WF<sub>6</sub> at 220°C. The 12 TiO<sub>2</sub> ALD/ALE supercycles leads to minimal TiO<sub>2</sub> on Si-H, but surface damage can influence subsequent W nucleation and growth.<sup>13</sup> After TiO<sub>2</sub> deposition, the HF dip allowed the largest amount of W growth on Si-H during the SiH<sub>4</sub>/WF<sub>6</sub>. (b) XPS W 4d spectra collected from the last 3 samples in (a). The largest W signal is observed for the sample treated with the intermediate HF dip. (c) TiO<sub>2</sub> and W thickness on Si-OH and Si-H substrates, respectively, after each step during the TiO<sub>2</sub> ALD/ALE + HF + W ALD sequence. The HF dip etched a small amount of TiO<sub>2</sub>, but the TiO<sub>2</sub> thickness was sufficient to enable sacrificial etching during W deposition. 148
- Figure 5.8 TEM/STEM images of self-aligned nano-patterned W and TiO<sub>2</sub> formed by simultaneous deposition and etching, prepared using the same conditions as used for the images in Figure 5.4: (a) bright field TEM; and (b) STEM images of W/TiO<sub>2</sub> on Si-H/SiO<sub>2</sub> nano-patterned substrates; (c) and (d) high magnification view of two different regions from image (b). ..... 152
- Figure 6.1 (a) A reactor scheme and (b) photographic images of the reactor. .... 164
- Figure 6.2 Pressure profile during 10 cycles of CoDAD/N<sub>2</sub>/Formic acid/N<sub>2</sub> = 30/60/0.1/60 s. .... 167
- Figure 6.3 QCM analysis during CoDAD(heated at 100 °C)/N<sub>2</sub>/F.A/N<sub>2</sub> = 10/60/0.1/60 s for 50 cycles at 180 °C and (b) an enlarged view of (a) showing large mass uptake during Co-DAD and slight mass decrease during formic acid dose, and (c) the net mass change per each cycle. A blue square shows the net mass change during CoDAD dose, a green triangle show the net mass change during F.A dose, and a red plus indicates the sum of CoDAD and F.A during single cycle..... 169
- Figure 6.4 Purge effects on the QCM mass change..... 170
- Figure 6.5 Formic acid purge effects on the QCM mass change..... 170
- Figure 6.6 (a) Co film growth rate as a function of Co-DAD dose time at 180 °C. While the previous study exhibits saturation curve with a growth rate of 0.2 Å/s, the obtained results from QCM analysis shows CVD growth behavior with lower

	growth rate (0.05 Å/s). (b) Co film growth rate as a function of chamber temperature comparing CoDAD/Formic acid, CoDAD only and, previous study ( <i>Kerrigan et al.</i> ) <sup>25-27</sup> . Film growth rate was based on QCM results and Co density. ....	172
Figure 6.7	High resolution XPS scans on different substrates (Cu, Au, Si-H, and TiO <sub>2</sub> ) after 600 cycles of CoDAD/N <sub>2</sub> /Formic acid/N <sub>2</sub> = 20/60/0.1/60 s at 180 °C. ....	176
Figure 6.8	Cross-sectional SEM images of (a) bare Cu, Co on Cu substrates after (b) 600 cycles of CoDAD/N <sub>2</sub> /Formic acid/N <sub>2</sub> = 20/60/0.1/60 s and (c) 600 cycles of CoDAD/N <sub>2</sub> = 20/60 s (Only DAD) at 180 °C. (d) AFM images of bare Cu with 2D, 3D and linescan results showing 20-60 nm columnar features on bare Cu substrates. ....	177
Figure 6.9	High resolution XPS depth profile scans on different substrates on Cu after (a) 600 cycles of CoDAD/N <sub>2</sub> /Formic acid/N <sub>2</sub> = 20/60/0.1/60 s and (b) 600 cycles of CoDAD/N <sub>2</sub> = 20/60 s (Only DAD) at 180 °C. Note that the result of etch 0 s on panel a is the same result on Cu in Figure 6.7. Etch was performed by Ar sputtering. ....	179
Figure 7.1	(a) Scheme of the integrated ALD/ALE supercycle (3 cycles) sequence, (b) TiO <sub>2</sub> thickness as a function of ALD cycle at 170 °C on Si-H and Si-OH. (c) TiO <sub>2</sub> thickness as a function of ALD/ALE supercycle at 170 °C on Si-H and Si-OH. Thickness measured by spectroscopy ellipsometry. Figure reproduced from ref. <sup>24</sup> .....	189
Figure 7.2	(a) Quartz crystal microbalance of W ALD (WF <sub>6</sub> /SiH <sub>4</sub> ) followed by W ALE using O <sub>2</sub> and WF <sub>6</sub> at various temperatures (220~300 °C). (b) An expansion of panel (a) showing mass change vs. process time using (2 x O <sub>2</sub> )/(3 x WF <sub>6</sub> ). Figure reproduced from ref. <sup>7</sup> .....	190
Figure 7.3	W film thickness on Si-H surfaces as a function of ALD cycle with various temperature. Thickness was measured by spectroscopic ellipsometry. Data at 220 and 275 °C were averaged from at least three different runs. The results are compared with the previously reported result. <sup>6</sup> .....	194
Figure 7.4	Top-down SEM images of various W ALD/ALE processes on Si-OH at 275 °C. All scales are the same. Unwanted W nuclei is observed after 15 W ALD and the W nuclei can be clearly removed with W ALE processes. ....	195
Figure 7.5	Top-down SEM images of various W ALD/ALE processes on Si-H at 275 °C. All scales are the same. RMS values are the average of three different measurements measured by AFM. With increasing the supercycle, the surface morphology on Si-H gradually changes, whereas no significant change is observed on the surface roughness. ....	196
Figure 7.6	High resolution XPS scans of (a) O 1s and (b) W 4f on Si-H at 275 °C after 10 W ALD, 1 supercycle (N = 1, 10 W ALD → 10 W ALE), N = 2, and N = 3. ....	198

Figure 7.7 QCM mass change of 3 supercycles of W ALD/ALE (red) and 4 supercycles of W ALD/ALE (blue) where 5 cycles of H<sub>2</sub>O were sequentially dosed before O<sub>2</sub> dose..... 200

## Chapter 1 Introduction and Background

### 1.1 Thin Film Deposition

Thin film deposition is a process of depositing thin layers onto a substrate material to improve/modify the properties of substrates. Thin film is an essential technique for modern electronic applications. Among a myriad of applications, thin film deposition in this dissertation is mainly for semiconductor fabrication where sub-nanoscale control is vital to continue a scaling beyond the 5 nm technology node. To fabricate 3D complex nanoscale devices such as 3D non-volatile flash memory (NAND), fin field-effect transistor (FinFET), dynamic random-access memory (DRAM), a wide range of traditional and advanced vapor phase thin film technology has been employed and developed.

Vapor phase thin film technique can be broadly divided into two categories: the process is based on physical or chemical deposition.<sup>1</sup> Physical vapor deposition (PVD) includes cathodic sputtering, ion implantation, molecular beam epitaxy (MBE), pulsed layer deposition and electron beam/thermal evaporation.<sup>2</sup> PVD can be proceeded by vaporizing a solid target material through physical means such as high power, laser, and plasma. The gasified material will condense on substrates, yielding robust and pure thin films. PVD process requires high vacuum ( $5 \times 10^{-4} - 5 \times 10^{-7}$  Torr) and cooling platform. Although PVD was developed in 1966,<sup>2</sup> it is still being implemented for seed/barrier layers including tantalum (Ta),<sup>3</sup> tantalum nitride (TaN),<sup>4</sup> and titanium nitride (TiN)<sup>5</sup> layers for middle-of-line (MOL) and back-end-of-line (BEOL) metallization.

Chemical vapor deposition (CVD) is a process where deposition is driven by a chemical reaction between precursors. In specific, these processes include CVD, atomic layer deposition (ALD), and molecular layer deposition (MLD), depending on the deposited materials and the

sequence of precursor delivery. While the orientation of deposition by PVD is one-direction (anisotropic, so-called “line-of-sight”), CVD offers conformal coverage on 3D complex features. In order to precisely control the critical dimension of nanopatterning, these techniques have been extensively applied to the advanced patterning processes. This chapter provides a basic background regarding CVD, ALD, and MLD which will be main methodology for this dissertation.

### 1.1.1 Chemical Vapor Deposition (CVD)

Chemical vapor deposition (CVD) is processed with flowing precursors into a chamber and a film is deposited by chemical reactions. CVD has advantages over PVD in terms of conformal coverage, selective deposition and high throughput.<sup>6,7</sup> There are a wide range of CVD variants depending on the wall temperature (hot and cold wall), working pressure (atmospheric, low-pressure, and ultra-vacuum), and enhanced radicals (plasma, ions, photons, lasers, and hot filaments).<sup>8</sup> Given that CVD process is based on chemical reactions, the choice of precursors is substantially important to control the purity and deposition rate of the films. When it comes to designing the CVD precursors, a number of requirements should be considered as followed: high vapor pressure to deliver the reactants; high reactivity to obtain high quality films; benign chemicals; and thermal stability to prevent chemical decomposition.

In general, CVD precursors can be classified into three types: inorganic precursors which contain no carbon bond; metal-organic precursors which contain organic ligands without metal-carbon bond; and organometallic precursors which contain organic ligands with metal-carbon bond.<sup>1</sup> Inorganic precursors such as metal halides typically are chemically stable, thereby requiring high deposition temperature and strong reducing agents. As many metal halides are solid at room

temperature, delivering these reactants is more challenging than liquid and vapor reactants. On the contrary, metal-organic and organometallic precursors are easily delivered and reacted at lower temperatures. However, these processes readily have impurity incorporation (C, O, F, Cl). To enhance the purity of the film, the chemical reaction pathway should be carefully designed.

### 1.1.2 Atomic Layer Deposition (ALD)

While CVD can improve the film coverage on complex features, it still shows poor coverage on extremely high aspect ratio. Atomic layer deposition (ALD) can address these challenges.<sup>9,10</sup> Similar to CVD, ALD is a vapor-based thin film deposition based on chemical reactions. ALD offers continuous and conformal thin films with thickness control at the atomic level scale and tunable film composition. The precise thickness control can be obtained by sequential precursor doses where each precursor is alternatively delivered into a reactor followed by an inert gas purge shown in **Figure 1.1**. When precursor A is flowed into the reactor, precursor A adsorbs on the surface by forming chemisorption or physisorption. During N<sub>2</sub> purge step, unreacted reactant is removed such that the substrate surface is self-terminated by adsorbed reactant A. During the subsequent reactant B dose, chemical reaction only occurs on the surface, leading to sub monolayer growth (~0.1 nm/cycle) and then, the surface is terminated by reactant B. By repeating this sequence, layer-by-layer growth can be obtained *via* ALD. While CVD growth is relying on both surface and bulk reactions, ALD growth only promoted by the surface reaction enables more isotropic growth. It is worth to note that although the growth rate of an ideal ALD growth should be close a monolayer per cycle, the observed growth rate is often less than the thickness of the monolayer due to steric hinderance effects,<sup>11,12</sup> incomplete ligand removal,<sup>13</sup> and desorption of the reactant.<sup>14</sup>

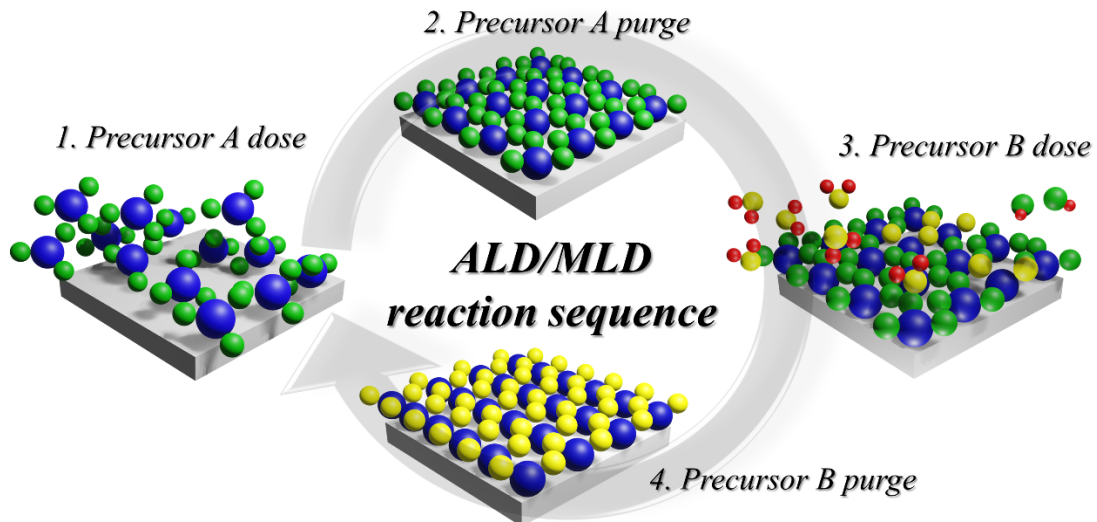


**Figure 1.1** Reaction sequence of atomic layer deposition (ALD) and molecular layer deposition (MLD).

In general, the operating temperature of ALD is much lower than CVD. This implies that ALD process is more suitable for a process requiring lower temperature such as BEOL processes ( $< 400\text{ }^{\circ}\text{C}$ ).<sup>15,16</sup> On the contrary, lower reaction temperature by ALD processes can lead to unwanted element incorporation of the film due to insufficient ligand exchange. ALD processes exhibit ALD temperature window where the growth rate is independent of temperatures.<sup>17,18</sup> Out of the ALD temperature regime, the reaction behavior dramatically changes depending on the kinetic reactivity and temperatures: condensation, no reaction, CVD growth by decomposition, and surface desorption. In this regard, operating the ALD process within the ALD temperature window is important to keep the advantage of ALD processes.

### 1.1.3 Molecular Layer Deposition (MLD)

Molecular layer deposition (MLD) is a thin film deposition technique to deposit organic and hybrid organic/inorganic thin films.<sup>19</sup> MLD can be applied to airgap,<sup>20</sup> low-k deposition,<sup>21</sup> nucleation inhibitors<sup>22</sup> and photoresists<sup>23</sup> for semiconductor processing. Analogous to ALD, MLD can control the film thickness in subatomic range and the composition ratio using a binary sequence of self-limiting half-reactions. In general, most of organic precursors composed of long chains are bulky, leading to higher growth than ALD.

MLD reaction stems from the organic chemistry. One of the greatest advantages of MLD over ALD is flexibility of organic precursors from a range of organic chemistry library. For instance, the backbone of the organic precursors can be altered by aliphatic or aromatics molecules with different chain length and functional group, thereby easily controlling the film properties.<sup>24</sup> However, the prerequisite for the MLD precursor such as high volatility, good thermal stability and reactivity should be ensured for a reproducible MLD growth.<sup>25</sup> MLD growth behavior is more complicated than ALD growth owing to the facts: i) the orientation of adsorbed molecules is complicated because the molecule can be bent over and tilted. This can terminate a new active site, hampering linear growth (double reactions)<sup>25,26</sup>, ii) bulky molecules aggravate steric hinderance effect, and iii) soft-saturation behavior because of noticeable molecule diffusion into porous polymer structure.<sup>27</sup> Another characteristic of MLD is that operating temperature of MLD processes is typically lower than ALD because of poor thermal stability of MLD precursors.

## 1.2 Area-Selective Deposition (ASD)

As feature size of state-of-the-art transistors approaches 5 nm or less, standard top-down lithographic patterning is encountering fundamental challenges in critical dimension such as edge

placement error, and line-edge roughness.<sup>28-30</sup> While advanced patterning processes such as self-aligned multi-patterning (SAMP), extreme ultraviolet (EUV) lithography, can address some of these challenges, high manufacturing costs, complicated process steps, and stochastic effects seem to be a bottleneck.<sup>28,31,32</sup>

As a path forward, bottom-up ASD enables to overcome these challenges.<sup>33,34</sup> Bottom-up ASD starts on a prepatterned substrate. On the prepatterned substrate, material A can be selectively deposited on growth-region whereas the deposition is inhibited on non-growth region. ASD is utilizing the dependence of inherent chemical reactivity on substrates. Whereas the pattern resolution of top-down processes is significantly dependent on the accuracy of the lithography, inherently self-aligned ASD is based on the chemical information on the substrates, offering precise pattern placement even less than 5 nm feature size. In addition, ASD process can simplify the manufacturing processes, greatly reducing the fabrication cost and chemical mechanical polishing (CMP) overburden.<sup>29,35</sup>

ASD is achieved when a heterogenous nucleation is formed on one surface vs. the other surface. From the thermodynamic perspective, Gibbs free energy ( $\Delta G$ ) is a useful parameter to predict the reaction propensity, but a kinetic aspect should be considered as well to fully understand ASD growth behavior. The selectivity is often quantified by comparing surface coverage which is directly related to nucleation. The selectivity,  $S$ , can be estimated by<sup>6,33</sup>

$$S(t_{growth}) = \frac{\theta_1 - \theta_2}{\theta_1 + \theta_2} \approx \frac{t_1 - t_2}{t_1 + t_2} \quad (\text{Eq 1.1})$$

where  $\theta_1$  and  $\theta_2$  is the measured surface coverage on the growth and non-growth surfaces, respectively, and,  $t_1$  and  $t_2$  is the thickness of films deposited on the growth and non-growth surfaces, respectively. Note that the value of  $S$  using the thickness values is usually larger (*i.e.*

better) than the selectivity by the surface coverages because the sensitivity of the surface coverage measurement is better than that of the thickness measurement: particularly, during the early nucleation stage. The value of  $S$  can be between 1 to 0, where  $S = 1$  for the perfect selectivity, and  $S = 0$  for the full selectivity loss ( $\theta_1 = \theta_2$ ). After the nuclei is fully coalesced, the surface coverage of  $\theta_1$  and  $\theta_2$  would be the same, whereas  $t_1 > t_2$ . Nonetheless, the error between  $\theta$  and  $t$  is small at the beginning of the nucleation where  $S$  is near 1. An analytical model is used to evaluate the quantification of ASD in **Chapter 3**.

Many approaches have been examined to enhance ASD. In an ideal case, no nucleation is observed on non-growth surface. However, the inherent ASD is limited to certain chemistry and the longer process would eventually generate the unwanted nuclei on the non-growth surface.<sup>16,33,36</sup> To suppress the unwanted nucleation, varied surface chemistry can be employed. This includes: i) surface activation using electron, ion, photon beams<sup>13,37,38</sup>, ii) surface passivation using self-assembly monolayers, and molecular inhibitors,<sup>39-41</sup> and iii) surface regeneration using intermittent etching.<sup>36,42,43</sup> Recently, orthogonal ASD is proposed using simultaneous deposition and etching, demonstrating the integration of two different ASDs.<sup>44</sup>

When it comes to investigating ASD, selective deposition is tested on two different blanket substrates. Once the results show good selectivity, the same ASD process is tested on prepatterned substrates. However, there are some challenges to transit from the blanket to the patterned wafers. For example, the loading effect, where the concentration gradient of the reactants can promote/hamper the nucleation, is substantial on the boundary of two different surfaces. This phenomenon is also associated with the feature shape effect. As the size and shape of the patterned wafers becomes more complex, reactant diffusion/transport is an important factor to achieve good ASD on the patterned substrates.<sup>6,16,27</sup>

ASD processes can be categorized into the material types being deposited: i) semiconductors, ii) dielectrics, and iii) metals. Semiconductor ASD has been widely used for front-end-of-line (FEOL) to obtain selective silicon epitaxy (SEG) for the source/drain contacts.<sup>45</sup> Based on the SEG process, many semiconductor ASDs including Ge,<sup>46</sup> GaAs,<sup>47</sup> SiC,<sup>48</sup> and SiGe<sup>49</sup> have been reported. In order to keep up with the line shrinkage less than 5 nm, many attentions have drawn to develop various dielectric and metal ASD processes. For the dielectric ASDs, hafnium oxide (HfO<sub>2</sub>) ASD<sup>50</sup> for high k and metal gate (HKMG) stacks, aluminum oxide (Al<sub>2</sub>O<sub>3</sub>)<sup>37,51</sup> as an etch stopper and fully-aligned *via* (FSAV),<sup>52</sup> low-k films and air gaps attract a great attention. Metal ASDs play an important role to scale down the interconnect. To reduce a substantial increase of RC delay,<sup>29,53</sup> the industry has demonstrated selective cobalt (Co) caps on Cu.<sup>54,55</sup> Nevertheless, Co needs seed/barrier layers which have high resistivity. To further decrease the RC delay, different metal ASDs including ruthenium,<sup>56</sup> molybdenum,<sup>57</sup> and more conductive seed/barrier layers<sup>58</sup> are explored. A systematic toolbox with new ASD capabilities on a wide range of surfaces is required for the future logic and memory applications.

### 1.3 Objective and Overview of Work

The main goal of this dissertation is to study area-selective deposition (ASD) of various inorganic and organic materials by using chemical vapor deposition (CVD), atomic layer deposition (ALD), and molecular layer deposition (MLD). For fundamental understanding of film nucleation and selectivity qualification, different surface-sensitive characterization methods as well as theoretical studies are used.

**Chapter 1** covers the general background of thin film deposition techniques and the importance of ASD in the semiconductor fabrication. **Chapter 2** describes the experimental and

analytical tools used for this work along with a brief operation mechanism. In **Chapter 3 and 4**, ASD of conjugated polymers including poly(3,4-ethylenedioxythiophene) (PEDOT), polyaniline (PANI), polypyrrole (PPY), and polythiophene (PTH) is investigated with MLD and CVD. A direct quantitative comparison of ASD between MLD and CVD is discussed with experimental and simulation results. **Chapter 5** describes the integration of two ASD processes on a single patterned substrate where self-aligned orthogonal growth is obtained, *i.e.* TiO<sub>2</sub> ASD on SiO<sub>2</sub> followed by W ASD on Si-H. **Chapter 6** shows cobalt metal ASD processes using bis(1,4-di-tert-butyl-1,3-diazadienyl)cobalt (CoDAD) and formic acid. In **Chapter 7**, tungsten metal ASD is explored by using repeated ALD and atomic layer etching (ALE).

## 1.4 References

- (1) Handbook of Thin Film Deposition, Fourth Edi.; Seshan, K., Schepis, D., Eds.; William Andrew, **2018**.
- (2) Devaray, P.; Hatta, S. F. W. M.; Wong, Y. H. An Overview of Conventional and New Advancements in High Kappa Thin Film Deposition Techniques in Metal Oxide Semiconductor Devices; Springer US, **2022**; Vol. 33.
- (3) Holloway, K.; Fryer, P. M. Tantalum and Niobium as a Diffusion Barrier between Copper and Silicon. *Appl. Phys. Lett.* **1990**, *57*, 1736–1738.
- (4) Fréty, N.; Bernard, F.; Nazon, J.; Sarradin, J.; Tedenac, J. C. Copper Diffusion into Silicon Substrates through TaN and Ta/TaN Multilayer Barriers. *J. Phase Equilibria Diffus.* **2006**, *27*, 590–597.
- (5) Rha, S. K.; Lee, W. J.; Lee, S. Y.; Hwang, Y. S.; Lee, Y. J.; Kim, D. Il; Kim, D. W.; Chun, S. S.; Park, C. O. Improved TiN Film as a Diffusion Barrier between Copper and Silicon. *Thin Solid Films* **1998**, *320*, 134–140.
- (6) Gladfelter, W. L. Selective Metallization by Chemical Vapor Deposition. *Chem. Mater.* **1993**, *5* (10), 1372–1388.
- (7) Hampden-Smith, M. J.; Kudas, T. T. Chemical Vapor Deposition of Metals : Part 1. An Overview of CVD Processes. *Chem. Vap. Depos.* **1995**, *1*, 8–23.
- (8) Kudas, T. T.; Hampden-Smith, M. J. The Chemistry of Metal CVD; VCH: Weinheim, **1994**.
- (9) Ritala, M.; Leskelä, M.; Dekker, J. P.; Mutsaers, C.; Soininen, P. J.; Skarp, J. Perfectly Conformal TiN and Al<sub>2</sub>O<sub>3</sub> Films Deposited by Atomic Layer Deposition. *Chem. Vap. Depos.* **1999**, *5*, 7–9.

- (10) Cremers, V.; Puurunen, R. L.; Dendooven, J. Conformality in Atomic Layer Deposition: Current Status Overview of Analysis and Modelling. *Appl. Phys. Rev.* **2019**, *6*, 021302.
- (11) Knoops, H. C. M.; Potts, S. E.; Bol, A. A.; Kessels, W. M. M. Atomic Layer Deposition; Kuech, T., Ed.; Elsevier, **2015**.
- (12) George, S. M.; Ott, A. W.; Klaus, J. W. Surface Chemistry for Atomic Layer Growth. *J. Phys. Chem.* **1996**, *100*, 13121–13131.
- (13) MacKus, A. J. M.; Verheijen, M. A.; Leick, N.; Bol, A. A.; Kessels, W. M. M. Influence of Oxygen Exposure on the Nucleation of Platinum Atomic Layer Deposition: Consequences for Film Growth, Nanopatterning, and Nanoparticle Synthesis. *Chem. Mater.* **2013**, *25*, 1905–1911.
- (14) Vandalon, V.; Kessels, W. M. M. Revisiting the Growth Mechanism of Atomic Layer Deposition of Al<sub>2</sub>O<sub>3</sub>: A Vibrational Sum-Frequency Generation Study. *J. Vac. Sci. Technol. A* **2017**, *35*, 05C313.
- (15) Datta, S.; Dutta, S.; Grisafe, B.; Smith, J.; Srinivasa, S.; Ye, H. Back-End-of-Line Compatible Transistors for Monolithic 3-D Integration. *IEEE Micro* **2019**, *39*, 8–15.
- (16) Parsons, G. N.; Clark, R. D. Area-Selective Deposition: Fundamentals, Applications, and Future Outlook. *Chem. Mater.* **2020**, *32*, 4920–4953.
- (17) Puurunen, R. L. Surface Chemistry of Atomic Layer Deposition: A Case Study for the Trimethylaluminum/Water Process. *J. Appl. Phys.* **2005**, *97*, 121301.
- (18) George, S. M. Atomic Layer Deposition: An Overview. *Chem. Rev.* **2010**, *110*, 111–131.
- (19) Yoshimura, T.; Tatsuura, S.; Sotoyama, W. Polymer Films Formed with Monolayer Growth Steps by Molecular Layer Deposition. *Appl. Phys. Lett.* **1991**, *59*, 482–484.

- (20) Seghete, D.; Davidson, B. D.; Hall, R. A.; Chang, Y. J.; Bright, V. M.; George, S. M. Sacrificial Layers for Air Gaps in NEMS Using Alucone Molecular Layer Deposition. *Sensors Actuators, A* **2009**, *155*, 8–15.
- (21) Yu, X.; Bobb-Semple, D.; Oh, I. K.; Liu, T. L.; Closser, R. G.; Trevillyan, W.; Bent, S. F. Area-Selective Molecular Layer Deposition of a Silicon Oxycarbide Low-k Dielectric. *Chem. Mater.* **2021**, *33*, 902–909.
- (22) Lee, S.; Kim, H. M.; Baek, G. H.; Park, J. S. Dry-Etchable Molecular Layer-Deposited Inhibitor Using Annealed Indicone Film for Nanoscale Area-Selective Deposition. *ACS Appl. Mater. Interfaces* **2021**, *13*, 60144–60153.
- (23) Zhou, H.; Bent, S. F. Molecular Layer Deposition of Functional Thin Films for Advanced Lithographic Patterning. *ACS Appl. Mater. Interfaces* **2011**, *3*, 505–511.
- (24) Nye, R. A.; Wang, S.; Uhlenbrock, S.; Smythe, J. A.; Parsons, G. N. In Situ Analysis of Growth Rate Evolution during Molecular Layer Deposition of Ultra-Thin Polyurea Films Using Aliphatic and Aromatic Precursors. *Dalt. Trans.* **2022**, *51*, 1838–1849.
- (25) George, S. M.; Dameron, A. A.; Yoon, B. Surface Chemistry for Molecular Layer Deposition of Organic and Hybrid Organic-Inorganic Polymers. *Acc. Chem. Res.* **2009**, *42*, 498–508.
- (26) Nye, R. A.; Kelliher, A. P.; Gaskins, J. T.; Hopkins, P. E.; Parsons, G. N. Understanding Molecular Layer Deposition Growth Mechanisms in Polyurea via Picosecond Acoustics Analysis. *Chem. Mater.* **2020**, *32*, 1553–1563.
- (27) Kim, J. S.; Parsons, G. N. Nanopatterned Area-Selective Vapor Deposition of PEDOT on SiO<sub>2</sub> vs Si-H: Improved Selectivity Using Chemical Vapor Deposition vs Molecular Layer Deposition. *Chem. Mater.* **2021**, *33*, 9221–9230.

- (28) Liu, E.; Lutker-Lee, K.; Lou, Q.; Chen, Y. M.; Raley, A.; Biolsi, P.; Yu, K. H.; Denbeaux, G. Line Edge Roughness Reduction for EUV Self-Aligned Double Patterning by Surface Modification on Spin-on-Carbon and Tone Inversion Technique. *J. Micro/Nanopatterning, Mater. Metrol.* **2021**, *20*, 1–11.
- (29) Clark, R.; Tapily, K.; Yu, K.; Hakamata, T.; Consiglio, S.; Meara, D. O.; Wajda, C.; Smith, J.; Leusink, G. Perspective : New Process Technologies Required for Future Devices and Scaling. *APL Mater.* **2018**, *6*, 058203.
- (30) Mulkens, J.; Slachter, B.; Kubis, M.; Tel, W.; Hinnen, P.; Maslow, M.; Dillen, H.; Ma, E.; Chou, K.; Liu, X.; Ren, W.; Hu, X.; Wang, F.; Liu, K. Holistic Approach for Overlay and Edge Placement Error to Meet the 5nm Technology Node Requirements. *Proc. SPIE* **2018**, *10585*, 105851L.
- (31) De Silva, A.; Meli, L.; Goldfarb, D. L.; Felix, N. M. Fundamentals of Resist Stochastics Effect for Single-Expose EUV Patterning. *Proc. SPIE* **2019**, *10957*, 109570F.
- (32) Raley, A.; Thibaut, S.; Mohanty, N.; Nakamura, S.; Raley, A.; Thibaut, S.; Mohanty, N.; Subhadeep, K.; Ko, A.; Meara, D. O.; Tapily, K.; Consiglio, S. Self-Aligned Quadruple Patterning Integration Using Spacer on Spacer Sub-32nm Pitch Applications. *Proc. SPIE* **2016**, *9782*, 97820F.
- (33) Parsons, G. N. Functional Model for Analysis of ALD Nucleation and Quantification of Area-Selective Deposition. *J. Vac. Sci. Technol. A* **2019**, *37*, 020911.
- (34) Mackus, A. J. M.; Merckx, M. J. M.; Kessels, W. M. M. From the Bottom-Up: Toward Area-Selective Atomic Layer Deposition with High Selectivity. *Chem. Mater.* **2019**, *31*, 2–12.

- (35) Dysard, J. M.; Brusica, V.; Feeney, P.; Grumbine, S.; Moeggenborg, K.; Whitener, G.; Ward, W. J.; Burns, G.; Choi, K. CMP Solutions for the Integration of High-K Metal Gate Technologies. *ECS Trans.* **2010**, *33*, 77–89.
- (36) Song, S. K.; Saare, H.; Parsons, G. N. Integrated Isothermal Atomic Layer Deposition/Atomic Layer Etching Super-Cycles for Area-Selective Deposition of TiO<sub>2</sub>. *Chem. Mater.* **2019**, *31*, 4793–4804.
- (37) Chalker, P. R.; Marshall, P. A.; Dawson, K.; Brunell, I. F.; Sutcliffe, C. J.; Potter, R. J. Vacuum Ultraviolet Photochemical Selective Area Atomic Layer Deposition of Al<sub>2</sub>O<sub>3</sub> Dielectrics. *AIP Adv.* **2015**, *5*, 017115.
- (38) Singh, J. A.; Thissen, N. F. W.; Kim, W.; Johnson, H.; Kessels, W. M. M.; Bol, A. A.; Bent, S. F.; Mackus, A. J. M. Area-Selective Atomic Layer Deposition of Metal Oxides on Noble Metals through Catalytic Oxygen Activation. *Chem. Mater.* **2018**, *30*, 663–670.
- (39) Junige, M.; George, S. M. Area-Selective Molecular Layer Deposition of Nylon 6,2 Polyamide: Growth on Carbon and Inhibition on Silica. *J. Vac. Sci. Technol. A* **2021**, *39*, 023204.
- (40) Pattison, T. G.; Hess, A. E.; Arellano, N.; Lanzillo, N.; Nguyen, S.; Bui, H.; Rettner, C.; Truong, H.; Friz, A.; Topuria, T.; Fong, A.; Hughes, B.; Tek, A. T.; DeSilva, A.; Miller, R. D.; Qiao, G. G.; Wojtecki, R. J. Surface Initiated Polymer Thin Films for the Area Selective Deposition and Etching of Metal Oxides. *ACS Nano* **2020**, *14*, 4276–4288.
- (41) Suh, T.; Yang, Y.; Zhao, P.; Lao, K. U.; Ko, H. Y.; Wong, J.; Distasio, R. A.; Engstrom, J. R. Competitive Adsorption as a Route to Area-Selective Deposition. *ACS Appl. Mater. Interfaces* **2020**, *12*, 9989–9999.

- (42) Saare, H.; Song, S. K.; Kim, J.-S.; Parsons, G. N. Effect of Reactant Dosing on Selectivity during Area-Selective Deposition of TiO<sub>2</sub> via Integrated Atomic Layer Deposition and Atomic Layer Etching. *J. Appl. Phys.* **2020**, *128*, 105302.
- (43) Vos, M. F. J.; Chopra, S. N.; Verheijen, M. A.; Ekerdt, J. G.; Agarwal, S.; Kessels, W. M. M.; Mackus, A. J. M. Area-Selective Deposition of Ruthenium by Combining Atomic Layer Deposition and Selective Etching. *Chem. Mater.* **2019**, *31*, 3878–3882.
- (44) Song, S. K.; Kim, J. S.; Margavio, H. R. M.; Parsons, G. N. Multimaterial Self-Aligned Nanopatterning by Simultaneous Adjacent Thin Film Deposition and Etching. *ACS Nano* **2021**, *15*, 12276–12285.
- (45) Joyce, B. D.; Baldrey, J. A. Selective Epitaxial Deposition of Silicon. *Nature* **1962**, *195*, 485–486.
- (46) Dumin, D. J. Selective Epitaxy Using Silane and Germane. *J. Cryst. Growth* **1971**, *8*, 33–36.
- (47) Rai-Choudhury, P.; Schroder, D. K. Selective Growth of Epitaxial Silicon and Gallium Arsenide. *J. Electrochem. Soc.* **1971**, *118*, 107.
- (48) Yih, P. H.; Li, J. P.; Steckl, A. J. SiC/Si Heterojunction Diodes Fabricated by Self-Selective and by Blanket Rapid Thermal Chemical Vapor Deposition. in *IEEE Transactions on Electron Devices*, **1994**, *41*, 281–287.
- (49) Bodnar, S.; Berranger, E. D.; Bouillon, P.; Mouis, M.; Skotnicki, T.; Regolini, J. L. Selective Si and SiGe Epitaxial Heterostructures Grown Using an Industrial Low-Pressure Chemical Vapor Deposition Module. *J. Vac. Sci. Technol. B Microelectron. Nanom. Struct.* **1997**, *15*, 712.

- (50) Stevens, E.; Tomczak, Y.; Chan, B. T.; Sanchez, E. A.; Parsons, G. N.; Delabie, A. Area-Selective Atomic Layer Deposition of TiN, TiO<sub>2</sub>, and HfO<sub>2</sub> on Silicon Nitride with Inhibition on Amorphous Carbon. *Chem. Mater.* **2018**, *30*, 3223–3232.
- (51) Saare, H.; Dianat, G.; Parsons, G. N. Comparative In Situ Study of the Initial Growth Trends of Atomic Layer-Deposited Al<sub>2</sub>O<sub>3</sub> Films. *J. Phys. Chem. C* **2022**, *126*, 7036-7046.
- (52) Juncker, A.; Clark, W.; Vincent, B.; Franke, J.-H.; Halder, S.; Lazzarino, F.; Murdoch, G. Self-Aligned Block and Fully Self-Aligned via for IN5 Metal 2 Self-Aligned Quadruple Patterning. *Proc. SPIE* **2018**, *10583*, 105830W.
- (53) Plombon, J. J.; Andideh, E.; Dubin, V. M.; Maiz, J. Influence of Phonon, Geometry, Impurity, and Grain Size on Copper Line Resistivity. *Appl. Phys. Lett.* **2006**, *89*, 2004–2007.
- (54) Breil, N.; Shemesh, D.; Fernandez, J.; Hung, R.; Bekiaris, N.; Tseng, J.; Naik, M.; Park, J. H.; Bakke, J.; Kumar, A.; Nafisi, K.; Litman, A.; Karnieli, A.; Kuchik, V.; Wachs, A.; Khasgiwale, N.; Chudzik, M. Electron Beam Detection of Cobalt Trench Embedded Voids Enabling Improved Process Control for Middle-Of-Line at the 7nm Node and Beyond. *2017 IEEE International Electron Devices Meeting (IEDM)*, **2017**, 349–352.
- (55) Auth, C.; Aliyarukunju, A.; Asoro, M.; Bergstrom, D.; Bhagwat, V.; Birdsall, J.; Bisnik, N.; Buehler, M.; Chikarmane, V.; Ding, G.; Fu, Q.; Gomez, H.; Han, W.; Hanken, D.; Haran, M.; Hatterndorf, M.; Heussner, R.; Hiramatsu, H.; Ho, B.; Jaloviar, S.; Jin, I.; Joshi, S.; Kirby, S.; Kosaraju, S.; Kothari, H.; Leatherman, G.; Lee, K.; Leib, J.; Madhavan, A.; Marla, K.; Meyer, H.; Mule, T.; Parker, C.; Parthasarathy, S.; Pelto, C.; Pipes, L.; Post, I.; Prince, M.; Rahman, A.; Rajamani, S.; Saha, A.; Dacuna Santos, J.; Sharma, M.; Sharma, V.; Shin, J.; Sinha, P.; Smith, P.; Sprinkle, M.; Amour, A. St.; Staus, C.; Suri, R.; Towner, D.; Tripathi, A.; Tura, A.; Ward, C.; Yeoh, A. A 10nm High Performance and Low-Power CMOS Technology Featuring 3rd

Generation FinFET Transistors, Self-Aligned Quad Patterning, Contact over Active Gate and Cobalt Local Interconnects. *2017 IEEE International Electron Devices Meeting (IEDM)*, **2017**, 673–676.

(56) Vega-Gonzalez, V.; Bekaert, J.; Kesters, E.; Le, Q. T.; Lorant, C.; Varela, P. O.; Teugels, L.; Heylen, N.; El-Mekki, Z.; Van Der Veen, M.; Webers, T.; Wilson, C. J.; Vats, H.; Rynders, L.; Cupak, M.; Uk-Lee, J.; Drissi, Y.; Halipre, L.; Charley, A. L.; Verdonck, P.; Witters, T.; Gompel, S. V.; Briggs, B.; Kimura, Y.; Jourdan, N.; Ciofi, I.; Gupta, A.; Contino, A.; Boccardi, G.; Lariviere, S.; Dupas, L.; De-Wachter, B.; Vancoille, E.; Decoster, S.; Lazzarino, F.; Ercken, M.; Debacker, P.; Kim, R.; Trivkovic, D.; Croes, K.; Leray, P.; Dillemans, L.; Chen, Y. F.; Tokei, Z.; Versluijs, J.; Lesniewska, A.; Paolillo, S.; Baert, R.; Puliyalil, H. Three-Layer BEOL Process Integration with Supervia and Self-Aligned-Block Options for the 3 Nm Node. *2019 IEEE International Electron Devices Meeting (IEDM)*, **2019**, 454–457.

(57) Tokei, Z.; Horiguchi, N. Scaling the BEOL – a toolbox filled with new processes, boosters and conductors <https://www.imec-int.com/en/imec-magazine/imec-magazine-september-2019/scaling-the-beol-a-toolbox-filled-with-new-processes-boosters-and-conductors>.

(58) Lo, C. L.; Zhang, S.; Shen, T.; Appenzeller, J.; Chen, Z. BEOL Compatible 2D Layered Materials as Ultra-Thin Diffusion Barriers for Cu Interconnect Technology. *2017 75th Annu. Device Res. Conf.* **2017**, 1–2.

## Chapter 2 Experimental Tools

### 2.1 Atomic Layer Deposition Reactor

ALD, MLD and CVD processes were performed in custom-built ALD reactors shown in **Figure 2.1**. With regard to the reactor geometry, there are two types of the reactors: 1) tubular and 2) sphere shape. The delivery line is consisted of ¼” stainless tube connected to reactants with a manual ball valve and a pneumatic diaphragm valve. Each line was purged by an inert gas (Ar or N<sub>2</sub>, 99.999%, Ar3 Gases), which passes through an Entegris Gatekeeper for additional purification. The gas flow was controlled by mass flow controller (MFC, MKS Instruments) and the pressure of the reactor was measured by either a baratron capacitance manometer (MKS Instruments) or a convectron Pirani gauge (The Granville-Phillips 275 Convectron, MKS Instruments). In this study, the working pressure was maintained at viscous flow regime (0.1 – 1 Torr) because viscous flow regime shows faster evacuation time and growth rate than the molecular flow regime.<sup>1,2</sup> The temperature of the main reactor was isothermal with the resistive heat tapes and the temperature of the delivery lines was set lower than the main chamber to prevent precursor condensation.

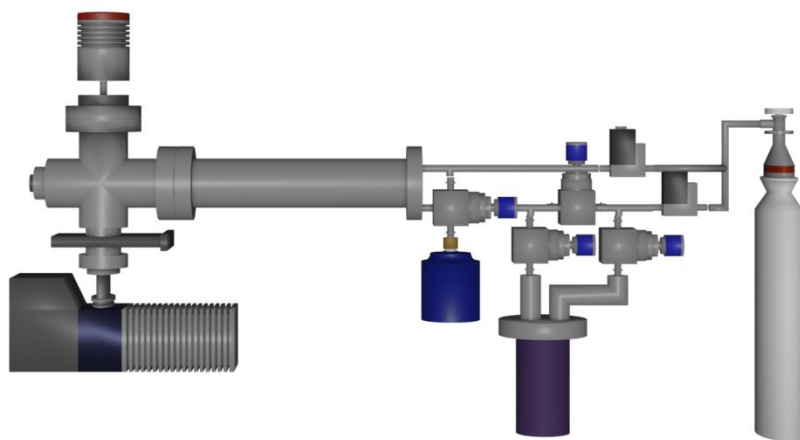


**Figure 2.1** Reactor Scheme.

As a reactor diagnostic, the pumping speed ( $S$ , l/s) and the residence time ( $\tau$ , sec) can be characterized by measuring the relationship between throughput ( $Q$ , torr·l/s) and pressure ( $P$ , torr). The residence time, defined as the time for the precursor to linger in the reactor, is an important parameter to determine the purge time. Ideally, the residence time should be lower to minimize the purge time for the ALD reaction. The throughput ( $Q$ ) and the residence time ( $\tau$ ) can be given as

$$Q = PS = \dot{n}RT \quad (\text{Eq 2.1})$$

$$\tau = \frac{V_R}{S} \quad (\text{Eq 2.2})$$

where  $P$  is the pressure of the reactor,  $T$  is the temperature of the reactor,  $R$  is the gas constant,  $\dot{n}$  is the molecular flow rate and  $V_R$  is the reactor volume. **Figure 2.2** and **Table 2.1** show the diagnostic comparison of different reactors: 1) PALDO, 2) WALDO, and 3) PALDI. From **Eq 2.1**, the pumping speed can be measured as a slope between  $Q$  and  $P$ . Considering that 1 standard cubic centimeters per minute (SCCM) = 0.0127 Torr·L·s<sup>-1</sup> and the volume of the reactor, the residence time can be estimated as shown in **Figure 2.2** and **Table 2.1**. For the pumping speed measurement, each reactor was pumped by the same type of rotary vane pump (Adixen 2021I, 5.8 L/s) filled with either fluorocarbon oil or hydrocarbon oil purged with a N<sub>2</sub> oil casing purge line. **Table 2.1** shows the correlation between the Al<sub>2</sub>O<sub>3</sub> growth rate and the residence time. As the residence time becomes longer, the longer purge time is required to achieve an ideal ALD growth rate (the ideal Al<sub>2</sub>O<sub>3</sub> growth rate would be 1.0 – 1.2 Å/cy). For enhancing the purge efficiency, a rotary pump with the fast pumping speed or the turbo pump with the throttle valve, and purging combined with the pump-down step would be performed. The inlet of the rotary pump was filtered with activated charcoal and sodasorb filters (Mass-Vac Inc.). It should be noted that using the filter traps

decreases the pumping speed (1-3 L/s vs. 5.8 L/s). Nonetheless, this is critical to enhance the lifetime of the pump. The filters and pump oil should be replaced once the working pressure and the leak up rate noticeably changes. To monitor the reactor condition, the leak-up rate where the pressure is monitored without pumping and flowing a gas and the base pressure where the reactor is pumped down from the working pressure for 60 s were recorded before and after the process. It is worthy to note that every reactor has virtual leaks such as degassing from the wall and gas trapped inside crevices so that the leak up rate could be substantially different depending on the ALD runs. In particular, the chemical degassing rate would be faster with higher temperatures. For example, on the PALDO reactor, the leak up rate at room temperature was less than 0.1 mT/s whereas it increased up to 10.0 mT/s immediately after increasing the temperature at 100 °C without any processes. As a different diagnostic test, dosing only trimethylaluminum (TMA) with the purge is helpful to figure out the moisture level of the reactor. Since TMA is extremely sensitive to the moisture, if there is any moisture inside the reactor, abnormally thick Al<sub>2</sub>O<sub>3</sub> film would be measured by spectroscopic ellipsometry whereas a reasonable growth would be 0.1-0.2 nm after dosing 100 cycle of TMA. In order to identify the exact leak-up point, helium leak testing with residual gas analyzer (RGA) and checking the bubbles with the leak check solution (Snoop, swagelok) can be useful. In terms of the reactor conditioning, baking the chamber at high temperatures (300-400 °C), coating the wall with thick Al<sub>2</sub>O<sub>3</sub> film (~50 nm) and physical cleaning with the alcohol and the vacuum cleaner can be carried out.

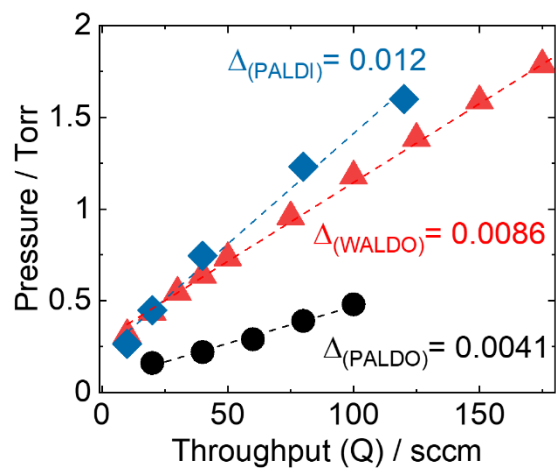


**Figure 2.2** Reactor pumping speed comparison.

**Table 2.1** Reactor diagnostic.

Reactor Name	PALDO	WALDO	PALDI
$\Delta = (\text{Pumping Speed})^{-1} (\text{Torr/sccm})^*$	0.0041	0.0086	0.012
$(\text{Pumping Speed})^{-1} (\text{Torr}/(\text{Torr}\cdot\text{L}\cdot\text{s}^{-1}))^*$	0.32	0.68	0.94
Pumping Speed (L/s)	3.10	1.48	1.06
Reactor Volume (L)	0.5	1.0	17.0
Residence time (s)	0.16	0.68	16.1
Leak up rate (mTorr/s)*	0.5 – 5.0	0.5 – 10.0	0.008 – 0.25
Base pressure (mTorr)	20 - 30	30 – 50	30 - 50
Growth rate ( $\text{\AA}/\text{cy}$ ) of $\text{Al}_2\text{O}_3$ ALD at 100-150 °C (TMA/ $\text{N}_2$ / $\text{H}_2\text{O}/\text{N}_2 = 0.2/60/0.2/60$ s)	1.2	1.1 - 1.2	1.4
* Leak up rate varies on the run due to the degassing after the process			
* 1 sccm = 0.0127 Torr·L·s <sup>-1</sup>			

## 2.2 Quartz Crystal Microbalance (QCM) Analysis

In-situ quartz crystal microbalance (QCM) was used to monitor a mass loading on a quartz crystal to understand the growth behavior during ALD, MLD, and CVD processes. QCM system is comprised of a probe body (desk, drawer and probe, Kurt Lesker), a 6 MHz gold coated crystal (Inficon or PhilipTech), a control box (Maxtek TM-400, Inficon SQM-160, and Inficon STM-2) and an oscillator. QCM is based on measuring the resonant frequency of a cut quartz (generally

AT quartz at  $\sim 35^\circ$ ) with an oscillator. From the Sauerbrey equation in **Eq 2.3**, the frequency change ( $\Delta f$ , Hz) is mathematically correlated with the mass change on the quartz crystal ( $\Delta m$ , ng).<sup>3,4</sup>

$$\Delta f = -\frac{2f_0^2}{A\sqrt{\mu\rho_q}}\Delta m = C\Delta m \quad (\text{Eq 2.3})$$

where  $f_0$  is the fundamental frequency ( $5.989 \times 10^6$  Hz),  $A$  is the surface area ( $0.357 \text{ cm}^2$ , area of backside electrode on the crystal),  $\mu$  is the shear modulus of quartz ( $2.947 \times 10^{11} \text{ g}\cdot\text{cm}^{-1}\cdot\text{s}^{-2}$ ),  $\rho_q$  is the density of quartz ( $2.648 \text{ g}\cdot\text{cm}^{-3}$ ) and  $C$  is the QCM constant ( $-0.2275 \text{ Hz}\cdot\text{ng}^{-1}$ ).

By using the density of the deposited film ( $\text{g}\cdot\text{cm}^{-3}$ ), the film thickness can be estimated during the deposition process in a real time. In this case, the mass change (ng) derived from the Sauerbrey equation should be divided by the active area ( $\text{ng}\cdot\text{cm}^{-2}$ ), thereby calculating the film thickness by the density and the mass change per area.

$$\frac{\Delta m}{A} = \frac{1}{A \cdot C} \Delta f \quad (\text{Eq 2.4})$$

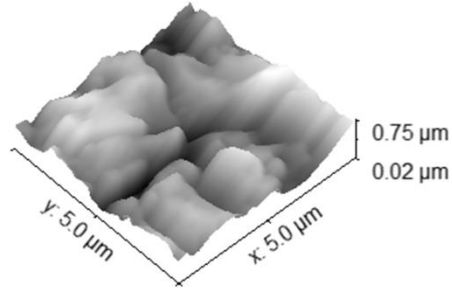
$$t = \frac{\Delta m}{A} \times \frac{1}{\rho_f} \quad (\text{Eq 2.5})$$

where  $\Delta m$  is the mass change from Eq 2.3,  $A$  is the surface area ( $0.357 \text{ cm}^2$ ) and  $C$  is the QCM constant ( $-0.2275 \text{ Hz}\cdot\text{ng}^{-1}$ ) and,  $t$  is the deposited film thickness,  $\rho_f$  is the deposited film density ( $\text{g}\cdot\text{cm}^{-3}$ ).

When it comes to measuring the QCM, two factors should be considered. The first thing is the exact surface area. Since the deposition occurs on both front and back crystals during the ALD

process and the assumption for **Eq 2.3-5** is that the film is only deposited on the front electrode, the backpurge (typically 15-25 sccm, giving ~150-250 mTorr pressure increase under 1 Torr working pressure) is required to prevent the deposition on the back electrode. It should be noted that if the working pressure is too low, for example 300 mTorr, the backpurge should be adjusted not to hinder the gas flow. The surface roughness of the crystal is also critical.<sup>5</sup> Two Au coated QCM crystals (unpolished, Inficon and polished, PhilipTech) were compared during 100 cycles of Al<sub>2</sub>O<sub>3</sub> ALD at 100 °C. **Figure 2.3** and **Table 2.2** shows the RMS of Au crystals and the mass change during TMA/H<sub>2</sub>O ALD cycles. The larger RMS can increase the actual surface area, leading to larger mass change (2.29 Å/cy using Al<sub>2</sub>O<sub>3</sub> density of 3.95 g/cm<sup>3</sup>), whereas the polished Au crystal shows reasonable growth rate (1.19 Å/cy).

Au (unpolished) - RMS : 122 nm



Au (polished) - RMS : 0.9 nm

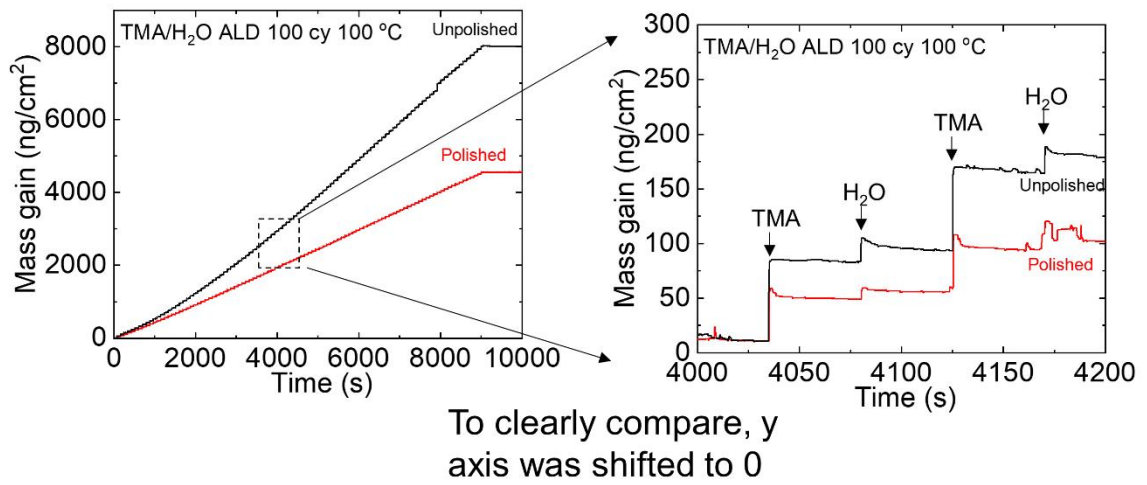
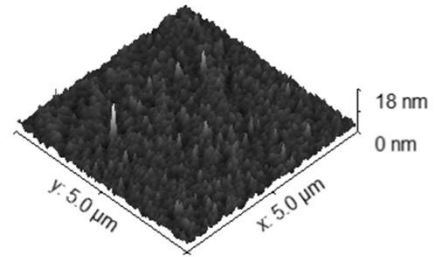


**Figure 2.3** QCM crystal roughness effect on mass gain during Al<sub>2</sub>O<sub>3</sub> ALD process.

**Table 2.2** Mass gain comparison on unpolished and polished QCM crystals

	Mass gain by TMA (ng/cm <sup>2</sup> )	Mass gain by H <sub>2</sub> O (ng/cm <sup>2</sup> )	Net mass change (ng/cm <sup>2</sup> )	GPC (Å/cy)*
On unpolished crystal	77.2	13.4	90.6	2.29
On polished crystal	39.6	7.5	47.1	1.19
* Assume Al <sub>2</sub> O <sub>3</sub> density = 3.95 g/cm <sup>3</sup>				

### 2.3 Spectroscopic Ellipsometry (SE)

Spectroscopic Ellipsometry (SE, alpha-SE ellipsometer, J.A. Woollam) was used to measure the film thickness and quantify the selectivity on the growth surface vs. the non-growth surface. The basic principle of SE is using the light reflection from various thin film stacks. To precisely track down the light reflection, the light is polarized into two planes (*S* and *P*) and two optical parameters (phase difference ( $\Delta$ ) and amplitude ratio ( $\Psi$ )) are collected as a function of wavelength (Generally 200 - 1700 nm). Based on the experimental raw data of  $\Delta$  and  $\Psi$ , the analytical model is used to fit the data in order to measure the film thickness as well as the optical constants (*n*, *k*). Since the measurement by SE is an indirect technique, users should carefully evaluate the fit accuracy between the experimental data and analytical fitting. This can be monitored by the mean-squared error (MSE). As a rule of thumb, good MSE should be lower than 4-5. It should be noted that if unknown materials are fit by SE, multi sample analysis (MSA) and comparing the SE results with other thickness measurement techniques (especially X-ray reflectivity and transmission electron microscopy) would be helpful.

$$MSE \propto \Sigma (Model - Exp)^2 \quad (\text{Eq 2.6})$$

Most of oxides, nitrides, fluorides, and carbides are transparent over the visible and near infrared wavelengths. For this reason, these films show normal dispersion where the refractive index decreases with increasing the wavelength. To describe the refractive index of the transparent films as a function of wavelength, the Cauchy dispersion relationship is generally used to fit the data. The Cauchy dispersion equation, given as

$$n(\lambda) = A + \frac{B}{\lambda^2} + \frac{C}{\lambda^4} \quad (\text{Eq 2.7})$$

where  $n$  is the refractive index of the film,  $\lambda$  is the wavelength (nm),  $A$ ,  $B$ , and  $C$  are the Cauchy parameters. In general, the refractive index is significantly dependent on parameter  $A$ . The estimated refractive index would be helpful to evaluate the deposited film quality. For instance, if  $\text{Al}_2\text{O}_3$  films are deposited by ALD run, the desirable refractive index would be 1.6 – 1.7 around 600 nm. If the obtained value is higher than this range, the deposited films would contain unexpected elements such as Ti and Zn from the  $\text{TiO}_2$  ( $n = 2.4 - 2.5$ ) and  $\text{ZnO}$  ( $n = 2.0$ ) residue in the reactor. However, when it comes to estimating the refractive index of the extremely thin films (less than 10 nm), it would be challenging to determine the precise optical constants.<sup>6</sup> In this case, measuring thicker films (more than 40-50 nm) would give better results.

For the light absorbing materials such as metals, semiconductors and conductive polymers, the careful fitting should be considered because the light absorption may distort the light reflection. To measure these materials, the fit can be conducted only at the transparent region. After fixing the film thickness, the model can be extended to all wavelengths fitting the optical constants. If

there is no transparent region, additional measurements including transmission measurement, inference enhancement, MSA, and different incident angles (45-90 °) would be necessary.<sup>7</sup> There are three primary models to fit the light absorbing films: direct fit for  $n$  and  $k$ , B-spline fit and oscillator model fit.<sup>6</sup>

As the light reflection is greatly dependent on the surface,  $\Delta$  and  $\Psi$  parameters can be used to quantify the film nucleation. While the detection resolution of SE is lower than the surface sensitive techniques including X-ray photoelectron spectroscopy, Auger electron spectroscopy and Rutherford backscattering spectroscopy, SE is a quick and simple method to characterize the extent of the film evolution. For in-situ SE, this would be especially helpful to study the selectivity and nucleation mechanism.

## 2.4 Profilometry

Profilometer (Dektak 150, Veeco) was used to measure the film thickness (0.03 - 10  $\mu\text{m}$ ). Step heights were made by the mechanical scratching with the end of spatula or tweezers. The radius of the stylus tip used was 12.5  $\mu\text{m}$  and the stylus force was set at 4 mg. In order to obtain high resolution, the typical measurement time is 200 – 300 s. After measurement, the results were leveled, and the step height was determined by the average step height (ASH) value. Measurements were averaged from the three different measurements using the automation measurement mode. It should be noted that the edge shape of the step is significantly dependent on the adhesion between a film and a substrate. If the film adhesion on the substrate is too strong to make a clear step height by the physical etching, chemical etching or lift-off would be considered.

## 2.5 X-Ray Photoelectron Spectroscopy (XPS)

X-ray photoelectron spectroscopy (XPS, Kratos Analytical Axis Ultra) with Al-K $\alpha$  gun was used to study the elemental composition and chemical state of deposited films. XPS is the implementation of the photoelectric effect where an incident x-ray bombards an electron out of the atom shell, ejecting the photoelectron. The relationship between the primary X-ray source and the energy of the photoelectrons is given as

$$E_b = h\nu - E_k - W \quad (\text{Eq 2.8})$$

where  $E_b$  and  $E_k$  are binding and the kinetic energy of the emitted photoelectron,  $h\nu$  is the photon energy, and  $W$  is the spectrometer work function. Al-K $\alpha$  and Mg-K $\alpha$  with line energies/line widths of 1486.6 eV/0.85 eV and 1253.6 eV/0.70 eV respectively, are commonly used as anode materials. The X-ray line width resolution can be further improved from 0.85 to 0.4 eV by implementing a quartz crystal monochromator. By using the monochromator, satellite peaks and the Bremsstrahlung continuum can be effectively removed.

For the XPS, the attenuation length ( $\lambda$ ) of the photoelectron which indicates the distance before the electron is being inelastically scattered is typically under 10 nm range. This gives high surface sensitivity of XPS. Another important capability of the XPS is that it can distinguish the chemical state of the film. By using peak fitting and deconvolution by CASA XPS software, the detailed chemical information such as the extent of oxidation, chlorination and fluorination can be characterized. Regarding the peak deconvolution, due to the doublet of p and d orbitals, the observed energy shows pairs of peaks: the area ratio of (p $_{1/2}$ , p $_{3/2}$ ), (d $_{3/2}$ , d $_{5/2}$ ), (f $_{5/2}$ , f $_{7/2}$ ) are 1:2, 2:3, and 3:4, respectively. For this study, peak positions are calibrated by referencing either the

adventitious C 1s peak at 285 eV or O 1s peak at 531 eV. For example, **Figure 2.4** shows the peak deconvolution of Sb 3d and O 1s of polypyrrole on Si substrate by using 9.34 eV for peak distance and 1.5 for the relative intensity between Sb 3d<sub>5/2</sub> and Sb 3d<sub>3/2</sub>.

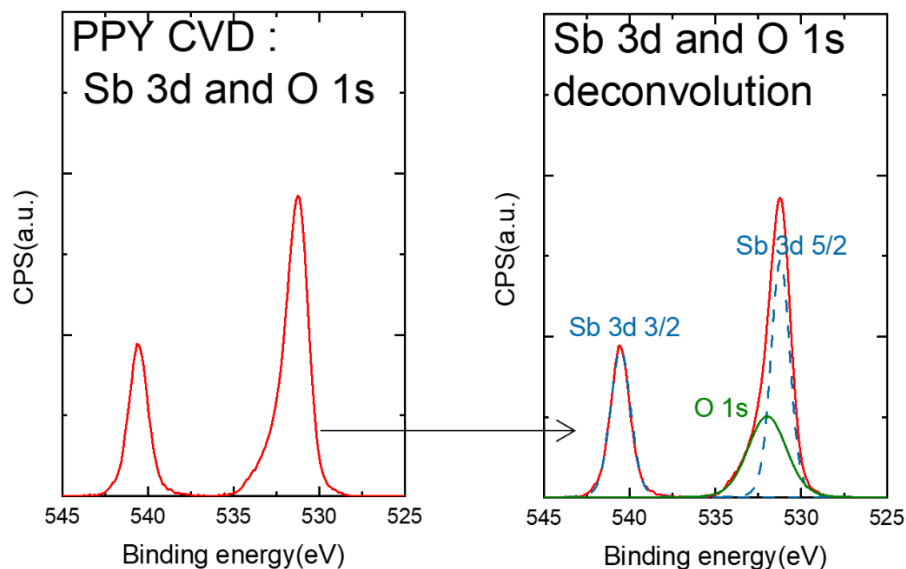


**Figure 2.4** High resolution XPS scan of Sb 3d/O 1s for polypyrrole film on Si substrate by CVD at 50 °C.

## 2.6 X-Ray Reflectivity (XRR)

X-ray reflectivity (XRR, Rigaku Smartlab X-ray diffractometer) using Cu K $\alpha$  radiation with parallel beam geometry at an angle of incidence of 0 to 4 was used to measure the film thickness, density, and roughness. While the acquisition and data analysis of the XRR requires more time than SE, it shows better resolution (0.1-400 nm) and measures the properties of light absorbing and opaque films. Similar to SE, the model fit is pivotal to obtain accurate results. The XRR data is fitted with the Genx software. The model is composed of a deposited film/substrate

(generally Si or SiO<sub>2</sub>) with interface roughness, density, and film thickness as fitting parameters. In the model, the figure of merit (FOM) is used for the parameter indicating the difference between the simulation and measured values. For the log FOM mode, the acceptable FOM value would be less than 0.08.

The principle of XRR is using the X-ray reflection on the sample stack with grazing angles (0 to 10 °) in Bragg Brentano ( $\theta$ - $2\theta$ ) configuration. Since the angle of the incident light is extremely small, X-rays yield total external reflection if the grazing angle  $\theta$  is smaller than the critical angle  $\theta_c$ . The critical angle  $\theta_c$  (usually 0.2 – 0.5 °) is given as

$$\theta_c = \sqrt{2\delta} \quad (\text{Eq 2.9})$$

where  $\delta$  is the real component of the complex refractive describing the dispersive of the wave-matter interaction. The value of  $\delta$  is determined by the X-ray wavelength and the density of the films which are associated with the electron density. The critical angle of material increases with higher density. Above the critical angle, X-ray reflection occurs at the surface and all the interfaces, giving an interference patterns, so called Kiessig fringes. Analyzing these oscillations can provide the information including the film thickness, density and roughness. As the film is thicker, the oscillation period is shorter. Film roughness can be estimated in two ways: the intensity decay at higher angles is associated with the roughness of the top surface (Larger roughness leads to faster intensity drop), and the larger interface roughness causes smoother fringes.<sup>8</sup>

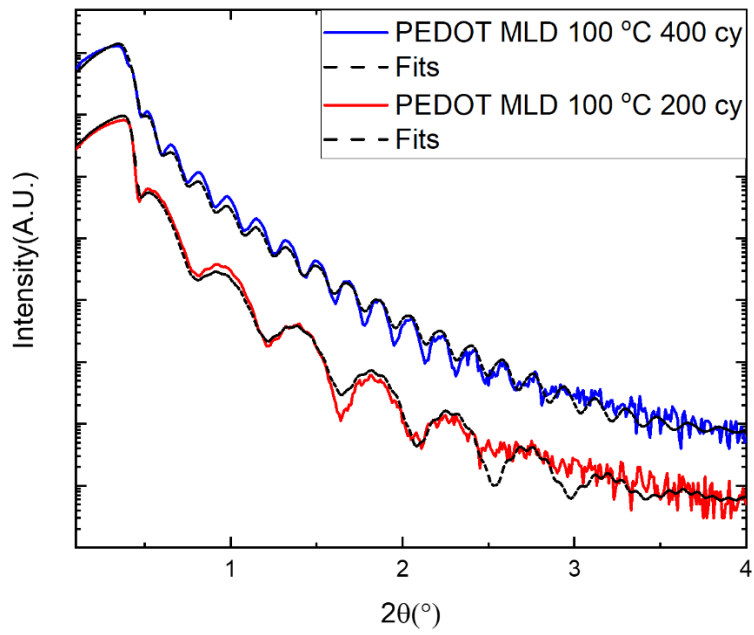


**Figure 2.5** X-ray reflectivity pattern of 200 and 400 cycles of PEDOT MLD on thermal SiO<sub>2</sub> (100 nm)/Si at 100 °C

**Table 2.3** Summary of the parameters resulting from the fitting of the XRR data

		Thickness (nm)	Density (g/cm <sup>3</sup> )	Roughness (nm)	Thickness measured by Ellipsometry (nm)
PEDOT MLD 100 °C 200 cy	PEDOT	19.45	1.73	0.96	16.8
	SiO <sub>2</sub>	100.4	2.20	0.49	
	Si substrate	-	2.30	0.001	
PEDOT MLD 100 °C 400 cy	PEDOT	48.4	1.72	0.80	47.7
	SiO <sub>2</sub>	98.0	2.20	0.77	
	Si substrate	-	2.32	0.21	

## 2.7 Scanning Electron Microscopy (SEM)

Scanning electron microscopy (SEM, FEI Verios 460L) operated at 2-30 kV with 0.7 nm resolution was used for the surface characterization and thickness measurements. Different modes including plane-, angle-, and cross-section-view were utilized. For the angle-view, tilt angle at  $\pm 8^\circ$  was used. In general, 2 kV was used to clearly observe the surface morphology, whereas for measuring the nuclei on the surface, high voltage at 5-10 kV with high current of 10 nA was used. In order to measure the ASD on patterned wafers, back scatter electron (BSE) mode can be beneficial if the mass of deposited materials is dramatically different.

## 2.8 Transmission Electron Microscopy (TEM)

Transmission electron microscopy (TEM, FEI Talos F200X) operated at 200 kV with 0.12 nm resolution was used to characterize the ASD on patterned wafers. Dual beam focused ion beam

(FIB, FEI Quanta 3D FEG instrument) operated at 30 keV with 7 nm resolution for the ion column and at 30 keV with 1.2 nm resolution for the SEM column was used to prepare TEM samples.  $\sim 3.2$   $\mu\text{m}$  of Pt capping layer was pre-deposited and  $20 \mu\text{m} \times 2 \mu\text{m}$  area was lifted out by a  $\text{Ga}^+$  ion. After a final milling with 5 kV at 48 pA ion emission current, the thickness of TEM samples was  $\sim 100$  nm. Samples were thinned to a thickness of  $\sim 100$  nm with a final milling step of 5 kV at 48 pA ion emission current. After the lift-out, the specimen was placed onto a 3 mm diameter of Cu TEM grid using a micromanipulator. The TEM camera (ThermoFisher Ceta camera) acquires  $4\text{k} \times 4\text{k}$  images. Energy-dispersive X-ray spectroscopy (EDX) elemental mappings were measured using scanning transmission electron microscopy (STEM). The STEM mode was measured by high-angle annular dark-field (HAADF) detector with a camera length of  $\sim 100$  mm. The Talos TEM uses the Super-X EDX system, which is composed of four in-column EDX detectors with a collection angle of  $\sim 0.9$  sr. Typical STEM EDX collection parameters yielded a beam current of 350 pA and each EDX collection time exceeded 5 min.

## 2.9 Four Point Probe

Four point probe method (RM 3-AR, Jandell) was used to characterize the electrical resistivity of the films. The four point probe technique separately measures voltage and current, thus eliminating the probe and contact resistance for the measurement. For each measurement, voltage was measured with forward and reverse current directions with sweeping mode to check the contact between the tip and the sample. If the measured voltages by forward/reverse directions are not identical, the sample height and tip conditions should be checked again. After confirming the contact, film sheet resistance ( $R_s$ ,  $\Omega/\square$ ) was measured with 1 mm probe spacing ( $s = 1$  mm). Note that for the Jandell's program, the sheet resistance value is automatically calculated with a

correction factor of 4.5324 with V/I. Depending on the sample geometries such as the film thickness, the sample size, and the probe spacing, various correction factors can be considered.<sup>9</sup> To validate the accuracy of the obtained results, a custom-built four-point probe (Tushar K. Ghosh group in college of textiles) with 2mm spacing and Keithley 2400 source meter from was also measured, showing the similar results. Based on the sheet resistance, the resistivity ( $\rho$ ) and conductivity ( $\sigma$ ) can be given as

$$\rho [\Omega \cdot cm] = R_s \frac{A}{l} = R_s \frac{wt}{l} \quad (\text{Eq 2.10})$$

$$\sigma [S \cdot cm^{-1}] = \frac{1}{\rho} \quad (\text{Eq 2.11})$$

where  $A$  is the cross-section area of the sample,  $l$ ,  $w$ , and  $t$  is the length, width and thickness of the sample, respectively. Assuming the sample is square ( $l = w$ ),  $\rho = R_s \cdot t$ .

## 2.10 Fourier Transform Infrared Spectroscopy (FTIR)

Fourier Transform Infrared Spectroscopy (FTIR, Thermo Scientific Nicolet 6700 spectrometer) was used to characterize the chemical properties of the film. Under a dry air purge, spectra were measured in an absorption mode with 200 scans at  $4 \text{ cm}^{-1}$  resolution from  $4000$  to  $400 \text{ cm}^{-1}$ . FTIR is measuring multiple frequencies of light simultaneously and the measured data is processed with a Fourier transform. There are various vibrational modes including stretching, bending, scissoring, rocking and twisting modes. Since the absorption band is dependent on the chemical bonding, FTIR is significantly useful to identify the chemical species of the deposited films.

## 2.11 References

- (1) Cremers, V.; Puurunen, R. L.; Dendooven, J. Conformality in Atomic Layer Deposition: Current Status Overview of Analysis and Modelling. *Appl. Phys. Rev.* **2019**, *6*, 021302.
- (2) George, S. M. Atomic Layer Deposition: An Overview. *Chem. Rev.* **2010**, *110*, 111–131.
- (3) Sauerbrey, G. The Use of Quarts Oscillators for Weighing Thin Layers and for Microweighing. *Z. Phys.* **1959**, *155*, 206–222.
- (4) Mecea, V. M. From Quartz Crystal Microbalance to Fundamental Principles of Mass Measurements. *Anal. Lett.* **2005**, *38*, 753–767.
- (5) Elam, J. W.; Groner, M. D.; George, S. M. Viscous Flow Reactor with Quartz Crystal Microbalance for Thin Film Growth by Atomic Layer Deposition. *Rev. Sci. Instrum.* **2002**, *73*, 2981–2987.
- (6) Tompkins, H. G.; Hilfiker, J. N. Spectroscopic Ellipsometry : Practical Application to Thin Film Characterization; Momentum Press: New York, **2016**.
- (7) Pettersson, L. A. A.; Carlsson, F.; Inganäs, O.; Arwin, H. Spectroscopic Ellipsometry Studies of the Optical Properties of Doped Poly(3,4-Ethylenedioxythiophene): An Anisotropic Metal. *Thin Solid Films* **1998**, *313–314*, 356–361.
- (8) Ribera, R. C. Growth and Thermal Oxidation of Ru and ZrO<sub>2</sub> Thin Films as Oxidation Protective Layers. Roger Coloma Ribera, University of Twente, **2017**.
- (9) Smits, F. M. Measurement of Sheet Resistivities with the Four-Point Probe. *Bell Syst. Tech. J.* **1958**, *37*, 711–718.

## Chapter 3 Nanopatterned Area-Selective Vapor Deposition of PEDOT on SiO<sub>2</sub> vs. Si-H: Improved Selectivity using Chemical Vapor Deposition vs. Molecular Layer Deposition

The following work is a reprint published in *Chem. Mater.* **2021**, *33*, 9221–9230.

### 3.1 Abstract

Area-selective deposition (ASD) of polymers is expected to be useful for self-aligned patterning of nucleation inhibitors, sacrificial layers, and air-gap materials during future bottom-up nanoscale materials fabrication. This work describes a simple, rapid, and effective method to achieve inherent ASD of poly(3,4-ethylenedioxythiophene) (PEDOT) on SiO<sub>2</sub> vs. hydrogen-terminated silicon (Si-H) substrates *via* molecular layer deposition (MLD) and chemical vapor deposition (CVD) using 3,4-ethylenedioxythiophene (EDOT) as a reactive monomer and SbCl<sub>5</sub> as an oxidant for polymerization. Film thickness measured by spectroscopic ellipsometry indicates the MLD process can obtain ~35 nm of deposition with a selectivity of 90%, *i.e.*,  $t_{S=0.90} \approx 35$  nm, which is better than many other reports of inorganic or organic material ASD. Furthermore, we show that under CVD conditions, the selectivity is further improved, *i.e.*,  $t_{S=0.90} \approx 55.4$  nm and that CVD can achieve ASD at an overall rate more than 100 times faster than MLD for the same ASD thickness, allowing 30 nm of ASD to be achieved in less than 10 s of process time. The selective growth of PEDOT on SiO<sub>2</sub> vs. Si-H is ascribed to the localized reduction of the SbCl<sub>5</sub> on the Si-H surface, thereby inhibiting EDOT polymerization in that region. The high selectivity allows us to observe and analyze lateral “mushroom” overgrowth and compare ASD growth rates on blanket vs. patterned wafers. Overall, results suggest that CVD may have distinct advantages over MLD or atomic layer deposition (ALD) for other ASD applications.

### 3.2 Introduction.

Photolithography is routinely used in electronics manufacturing to transform uniform blanket metal and dielectric thin films into complex line and space patterns that are aligned with underlying features to create complex nanostructured circuits. Using extreme UV (EUV) lithography, features can be printed with a width approaching 10 nm, but inherent stochastics in the process lead to unwanted variations in feature size (*i.e.*, critical dimension error), as well as errors in feature alignment (*i.e.*, edge placement error) when printing lines on top of each other.<sup>1-4</sup> As a means to augment photolithography and achieve improved precision, researchers are exploring vapor-based area-selective deposition (ASD), where thin-film materials are built up only in predetermined regions on a starting patterned surface.<sup>3-10</sup> Area-selective epitaxy, for example, is widely used to create self-aligned source/drain transistor contacts, but the substrate-dependent chemical reactions require temperatures in excess of 800 °C under near-equilibrium conditions.<sup>4</sup> <sup>11</sup> However, during back-end processing, unwanted metal diffusion can occur near 400 °C. Therefore, to form self-aligned metal and dielectric features within back-end circuitry, new ASD processing methods and materials are needed at a temperature less than 400 °C.

Low-temperature ASD can be achieved by chemical vapor deposition (CVD), atomic layer deposition (ALD), and molecular layer deposition (MLD), with most recent attention focused on area-selective ALD.<sup>3-10</sup> While studies of ASD metals and dielectrics are most common, ASD of polymers is also expected to play an important role in bottom-up synthesis as nucleation inhibitors, low-k layers, and air-gap materials.<sup>12-15</sup> Previous studies of polymer CVD include several examples of substrate-preferential growth.<sup>16-19</sup> Using a thermally-excited reaction initiator, conjugated poly(p-phenylene vinylene) (PPV) and nonconjugated parylene N and parylene C were found to preferentially grow on hydroxylated silicon oxide (Si-OH) with minimal growth on iron

and other transition metals.<sup>17,18</sup> Based on growth rates and surface topology, inhibition on the metal was ascribed to quenching of activated monomers by available surface charge, forming a thin passivation layer that impeded subsequent reaction. Similarly, area-selective CVD of poly(azomethine) was achieved on Si-OH *vs.* hydrogen-terminated silicon (Si-H), but details of the related mechanism and the extent of selectivity were not well identified.<sup>19</sup>

Patterned growth of conductive poly(3,4-ethylenedioxythiophene) (PEDOT) films has also been achieved under CVD conditions, where an oxidant such as iron(III) p-toluenesulfonate (Fe(III) tosylate) was placed on a surface and exposed to reactive 3,4-ethylenedioxythiophene (EDOT) monomer. The polymerization selectively proceeded in the regions containing the oxidant, producing ~12-18 nm of PEDOT film.<sup>20,21</sup> Features with lateral resolution as small as 250 nm were tested, but the extent of unwanted nonselective growth was not fully quantified.

In addition to CVD, ASD of polymers has also been studied by MLD, a stepwise sequence for organic film deposition analogous to ALD. Using MLD,<sup>22-27</sup> a polyurea layer up to ~6 nm in thickness was achieved on Si-OH, with minimal growth on copper that was passivated by an octadecylphosphonic acid self-assembled monolayer (SAM).<sup>22</sup> Surface passivation by SAMs has also been used for ASD of poly-p-xylylene<sup>23</sup> and silicon oxycarbide (SiCO),<sup>24</sup> in both cases enabling ~5 nm of ASD. In another study, selectivity up to ~17 nm was shown for ASD of polyimide (nylon 6,2) on amorphous carbon (a-C) *vs.* SiO<sub>2</sub> passivated with dimethylamino-trimethylsilane (DMA-TMS).<sup>25</sup> Area-selective MLD of polyimide has also been achieved on Cu *vs.* SiO<sub>2</sub>, where the copper surface catalytically promotes localized polymerization. The process allowed as much as 130 nm of selectively deposited polymer, possibly due to copper diffusion to the top of the growing film.<sup>26</sup> In addition to vapor processing, ASD of polymers has also been

explored by spin-coating,<sup>27</sup> where surface-dependent dewetting of semifluorinated poly(acrylate) allows selective coating on Cu *vs.* SiO<sub>2</sub>.

Vacuum-based PEDOT deposition provides advantages over conventional solution-based processes in terms of crystallinity, conductivity, and conformal coating on three-dimensional (3D) substrates. PEDOT vapor deposition occurs *via* oxidative surface polymerization (*i.e.*, oxidative CVD, oCVD), where an oxidant species delivered to the growth surface promotes polymerization of adsorbed EDOT monomer. Since the rate of polymerization depends on the surface concentration and reactivity of the oxidant, the choice of oxidant is important in the overall deposition process. A range of oxidants, including FeCl<sub>3</sub>,<sup>28–30</sup> CuCl<sub>2</sub>,<sup>31</sup> Br<sub>2</sub>,<sup>32</sup> VOCl<sub>3</sub><sup>33</sup> and SbCl<sub>5</sub><sup>33</sup> have been investigated for PEDOT oCVD. In addition, MoCl<sub>5</sub><sup>34</sup> and SbCl<sub>5</sub><sup>35</sup> have been implemented for oxidative MLD (oMLD). Generally, the more volatile SbCl<sub>5</sub> and VOCl<sub>3</sub> oxidants show better process reliability.

This work describes inherent PEDOT ASD on SiO<sub>2</sub> *vs.* Si-H *via* oMLD and oCVD using SbCl<sub>5</sub> as an oxidant and presents several scientifically novel findings. Specifically, we show a unique capability for the inherent ASD of a conjugated polymer, PEDOT, with favorable deposition on SiO<sub>2</sub> *vs.* Si-H surfaces, achieving ~30 nm of selective deposition, which exceeds that of most ASD reports of metals and dielectrics.<sup>4</sup> Additionally, we provide a direct quantitative comparison of ASD using MLD and CVD, showing that the CVD process enhances selectivity. A mechanism for selectivity loss is proposed, where the Si-H surface promotes the reduction of the SbCl<sub>5</sub> inhibiting subsequent EDOT polymerization. In addition, we report feature size-dependent ASD growth comparing growth rate dependence on blanket and patterned surfaces, including features as small as ~100 nm, with less growth observed on patterned wafers *vs.* blanket wafers under the same deposition conditions. The high selectivity allows us to observe the extent of lateral

“mushroom” growth, indicating that the growth of PEDOT on the exposed SiO<sub>2</sub> may not be completely uniform in all directions. Overall, the results show feasible ASD of PEDOT on nanoscale-patterned surfaces, thereby expanding the range of materials available for advanced deposition-based patterning.

### 3.3 Experimental Section

#### 3.3.1 Deposition Reactants

The EDOT monomer (3,4-ethylenedioxythiophene, 97%, Alfa Aesar) and antimony pentachloride (SbCl<sub>5</sub>, 99%, Alfa Aesar) were used as received without further purification. All materials were transferred into glass and stainless steel vessels in a nitrogen-purged glovebox. Nitrogen gas (N<sub>2</sub>, 99.999%, Arc3 Gases) purified with an inert gas filter (GateKeeper, Entegris) was used as a reactant carrier and purge gas.

#### 3.3.2 Deposition Substrates

Silicon (boron-doped Si (100), 6–10 Ω·cm, WRS Materials) and silicon dioxide (SiO<sub>2</sub>, 100 nm of thermally grown SiO<sub>2</sub> on boron-doped Si (100), WRS Materials) were cut into ~1 cm × 1 cm coupons. Line-patterned Si-H/SiO<sub>2</sub> samples with half-pitch of ~3 μm and height of ~100 nm were prepared by optical lithography of thermally oxidized Si wafers. Coplanar Si-H/SiO<sub>2</sub> line-patterned samples with half-pitch of ~130 nm and topographical Si-H/SiO<sub>2</sub> line-patterned samples with half-pitch of ~200 nm and height of ~100 nm were provided by collaborators. Before deposition, all silicon, SiO<sub>2</sub>, and patterned wafers were cleaned in a hot piranha bath (1:1 = H<sub>2</sub>SO<sub>4</sub>/H<sub>2</sub>O<sub>2</sub> by volume ratio) for 30 min, rinsed with deionized (DI) water, and dried with N<sub>2</sub>, forming surface silicon hydroxide. To form hydrogen-terminated silicon (Si-H), silicon and

patterned wafers were dipped into 5% hydrogen fluoride (HF) aqueous solution for 30 s, rinsed with DI water for 30 s, and dried with N<sub>2</sub>. To minimize surface oxidation and contamination, the HF treatment was conducted immediately before use.

### 3.3.3 Reactor Design and Reaction Sequence

PEDOT deposition was performed in a home-built, isothermal, and viscous-flow ALD reactor described previously.<sup>5</sup> The reaction chamber was a stainless steel cylinder with ~4 cm inner diameter and ~60 cm length. The sample deposition zone was defined by the substrate holder with ~30 cm long and ~4 cm wide, placed approximately in the middle of the reaction chamber. The reactor was heated resistively using PID controllers, and the temperature was set at 100–150 °C. The chamber was pumped by a rotary vane pump (Adixen 2021I, 21 m<sup>3</sup>/h) filled with fluorocarbon oil and was equipped with a N<sub>2</sub> oil casing purge line. The inlet of the rotary pump was filtered through activated charcoal and sodasorb filters (Mass-Vac Inc.). The working pressure, measured with a N<sub>2</sub> flow rate of 135 standard cubic centimeters per minute (sccm), was ~1 Torr. N<sub>2</sub> and reactant flow were controlled by computer-controlled pneumatic diaphragm valves. The EDOT reactant vessel was arranged as a bubbler container and heated to 80 °C. Upon EDOT delivery, the reactor pressure increased by ~30 mTorr. The SbCl<sub>5</sub> vessel was arranged as a direct port to the N<sub>2</sub> carrier line and was heated to either 40 or 50 °C, as described below. When heated at 50 °C, the SbCl<sub>5</sub> delivery led to a pressure increase of ~30 mTorr. At 40 °C, the pressure increase was ~10 mTorr. For some experiments, the deposition was repeated in a second home-built reactor with similar geometry and design, and consistent results were obtained.

Prior to loading substrates into the reactor, the chamber was conditioned with 50 cycles of Al<sub>2</sub>O<sub>3</sub> ALD using trimethylaluminum (TMA, 98%, Strem Chemicals) and DI H<sub>2</sub>O. The Al<sub>2</sub>O<sub>3</sub>

ALD sequence followed TMA/N<sub>2</sub>/H<sub>2</sub>O/N<sub>2</sub> = 0.1/60/0.1/60 s at 100 °C, leading to 4.5 ± 0.5 nm of Al<sub>2</sub>O<sub>3</sub> on Si-OH.

After reactor wall conditioning, substrates were loaded into the reactor and exposed to N<sub>2</sub> flow for 30 min to reach thermal equilibrium with the reactor walls. For the ASD growth by MLD, two conditions were studied for the SbCl<sub>5</sub> dose. Under high dose conditions shown in **Figure 3.2a**, the SbCl<sub>5</sub> source was held at 50 °C, and the dose time was 0.5 s/cycle. The reactant dose sequence followed: SbCl<sub>5</sub>/N<sub>2</sub>/EDOT/N<sub>2</sub> = 0.5/60/2/60 s. For low dose conditions shown in **Figure 3.2b**, the SbCl<sub>5</sub> temperature was set at 40 °C, and the dose time was 0.1 s/cycle, and the corresponding sequence was SbCl<sub>5</sub>/N<sub>2</sub>/EDOT/N<sub>2</sub> = 0.1/60/2/60 s. For ASD growth by the CVD process, EDOT (reactant vessel held at 80 °C) and SbCl<sub>5</sub> (vessel held at 40 °C) were simultaneously dosed using N<sub>2</sub> flow at 150 °C. The flow rates of N<sub>2</sub> were controlled independently through the EDOT and SbCl<sub>5</sub> delivery lines and an additional N<sub>2</sub> purge line, with flow rates of EDOT/SbCl<sub>5</sub>/N<sub>2</sub> = 6/20/30 sccm, respectively, producing a reactor pressure of 370 mTorr.

### 3.3.4 Sample Characterization

Quartz crystal microbalance (QCM) was used to measure the mass uptake in situ during MLD. A QCM probe body (Kurt Lesker) with a 6 MHz gold-coated crystal sensor (Inficon) was loaded into the reactor and allowed to stabilize at the reactor temperature. The resonant frequency of the crystal was recorded with a control box (Maxtek TM-400) through a home-designed LabVIEW program and converted to mass change (ng/cm<sup>2</sup>) with the Sauerbrey equation.<sup>36</sup> The crystal holder was modified to allow 25 sccm of N<sub>2</sub> to purge the back side of the crystal to prevent deposition in the electrical contact regions.

PEDOT thickness was monitored by ex situ spectroscopic ellipsometry (SE,  $\alpha$ -SE ellipsometer, J.A. Woollam). Measurements were performed at an incidence angle of  $70^\circ$ , with a spectral range of 300–900 nm. Due to the optical anisotropy of PEDOT, biaxial b-spline models, transmission data, and multisample analysis were used for SE fitting.<sup>37</sup> In addition to SE analysis, the same samples measured by SE were characterized by X-ray reflectivity (XRR, Rigaku SmartLab X-ray Diffractometer) using Cu K $\alpha$  radiation with parallel beam geometry at an angle of incidence of 0–4 and cross-sectional scanning electron microscopy (SEM, FEI Verios 460L) operated at 2–30 kV with 0.7 nm resolution to confirm the data's accuracy. The XRR data was fit with the software GenX. The thickness differences between XRR, SE, and SEM results were less than 3 nm. The thickness results reported here were the average of three samples separately placed on the sample holder, and each sample was measured at three different locations.

PEDOT growth and nucleation were characterized by plan-view SEM and X-ray photoelectron spectroscopy (XPS, Kratos Analytical Axis Ultra) with an Al K $\alpha$  (1486.6 eV) gun. Peak positions were calibrated by referencing the adventitious C 1s peak to 285.0 eV. **Figure 3.10** shows high-resolution XPS data in the Cl 2p, C 1s, Sb 3d, O 1s, and Si 2p regions collected from PEDOT deposited on SiO<sub>2</sub> and Si-H after 50, 100, 200, and 400 MLD cycles. The elemental compositions determined from the XPS results are given in **Table 3.3**.

PEDOT ASD on Si-H/SiO<sub>2</sub> line-patterned wafers were characterized by transmission electron microscopy (TEM, FEI Talos F200X) operated at 200 kV with 0.12 nm resolution and by SEM. Dual-beam focused ion beam (FIB, FEI Quanta 3D FEG instrument) with 7 nm resolution at 30 keV for the ion column and 1.2 nm resolution at 30 keV for the SEM column was used for TEM sample preparation.  $\sim 3.2 \mu\text{m}$  of Pt capping layer was coated, and a  $20 \times 2 \mu\text{m}$  region was milled out by Ga<sup>+</sup> ions. Samples were thinned to a thickness of  $\sim 100$  nm, with a final milling step

of 5 kV at 48 pA ion emission current. After the lift-out, the specimen was transferred onto a 3 mm diameter Cu TEM grid using a micromanipulator. The TEM camera was a Thermo Fisher Ceta camera that acquires  $4 \times 4$  k images. Energy-dispersive X-ray spectroscopy (EDX) elemental mappings were collected using scanning transmission electron microscopy (STEM). In STEM mode, the high-angle annular dark-field imaging (HAADF) detector with a camera length of  $\sim 100$  mm was used. Typical STEM EDX collection parameters yielded a beam current of 350 pA, and each EDX collection time was longer than 5 min.

### 3.4 Results and Discussion

For this study, PEDOT films were deposited in a custom hot-wall tubular flow reactor under both MLD and CVD conditions. For MLD, the reactor was heated to 100 °C, and MLD was performed using sequential doses of EDOT and  $\text{SbCl}_5$  vapors separated by purging with continuously flowing  $\text{N}_2$ . The MLD reactant dose time sequence was  $\text{SbCl}_5/\text{N}_2/\text{EDOT}/\text{N}_2 = 0.1/60/2/60$  s. The mass uptake was monitored using QCM, and results are shown in **Figure 3.1a**. For this test, the deposition was performed for 100 cycles, and for clarity, the data in **Figure 3.1a** shows results collected during the final 12 cycles. Before deposition, the QCM crystal and the chamber walls were preconditioned by coating with 50 cycles of ALD  $\text{Al}_2\text{O}_3$  at 100 °C. **Figure 3.1b** shows an expanded view of one representative cycle. The  $\text{SbCl}_5$  dose leads to a relatively large mass increase, and the following EDOT dose produces a smaller mass increase followed by some mass decrease. The results are consistent with the overall reaction mechanism shown in **Figure 3.1c**.<sup>34,35</sup> During exposure, the  $\text{SbCl}_5$  physisorbs on the growth surface. During the subsequent exposure of the EDOT monomer, the  $\text{SbCl}_5$  promotes oxidative polymerization to form PEDOT, along with desorption of  $\text{SbCl}_x$  and HCl byproducts. The relatively large mass increase

during the  $\text{SbCl}_5$  dose and the net mass loss during the EDOT dose reflect the larger molecular weight of the antimony chloride reactant ( $\text{SbCl}_5$ : 299.02 g/mol) and vapor product ( $\text{SbCl}_x + \text{HCl}$ ), respectively, relative to the EDOT monomer (EDOT: 142.17 g/mol).

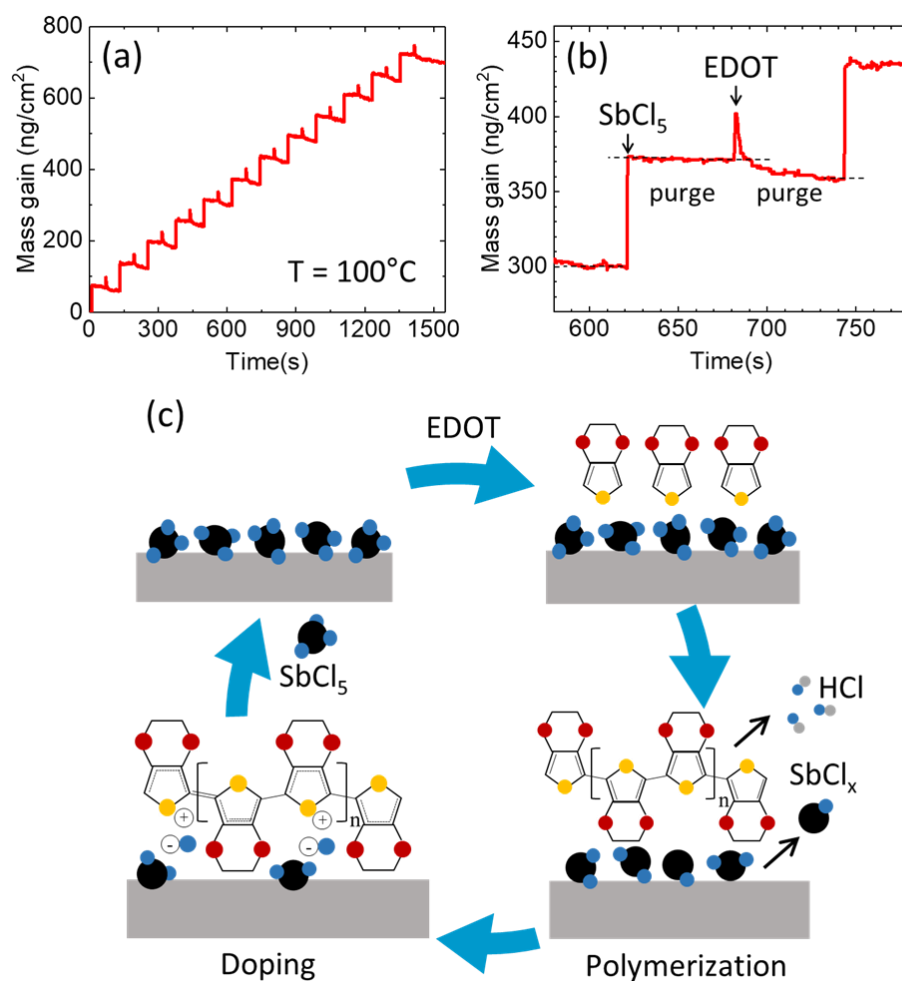


**Figure 3.1** (a) Quartz crystal microbalance mass uptake during PEDOT MLD cycles using EDOT and SbCl<sub>5</sub> at 100 °C, (b) enlarged view of (a) showing a large mass uptake during the SbCl<sub>5</sub> and a slight mass decrease during the EDOT dose, and (c) proposed reaction scheme for the PEDOT oMLD process.

### 3.4.1 Area-Selective MLD of PEDOT on Blanket Substrates

To explore the substrate dependence of PEDOT deposition, the reactor was loaded with two different silicon wafer coupons; one was coated with 100 nm of thermally grown silicon

dioxide (SiO<sub>2</sub>) cleaned by piranha treatment, and a second silicon piece was treated with piranha cleaning, followed by a dilute HF dip to form a hydrogen-terminated surface (Si-H). **Figure 3.2** shows the resulting thickness vs. cycle measured by SE on these two wafer pieces. The dashed lines through the data are fits to an analytical model for nucleation and island growth discussed below and in the Supporting Information (**Figure 3.8**).<sup>4,38</sup> The thickness per cycle was measured under various reactant dose conditions, and results are given in **Figure 3.9**. For **Figure 3.9a**, the SbCl<sub>5</sub> exposure dose was set to 0.5 s/cycle, whereas for **Figure 2b**, the SbCl<sub>5</sub> dose was 0.1 s/cycle (see Experimental Section). In **Figure 3.2a**, PEDOT thickness on SiO<sub>2</sub> increases linearly with a slope of ~0.32 nm/cycle. On Si-H substrates, less growth is observed, consistent with inhibited nucleation. In **Figure 3.2b**, using the smaller SbCl<sub>5</sub> dose, after some inhibition, the thickness on SiO<sub>2</sub> increases linearly with a rate of ~0.12 nm/cycle, and again, less growth is observed on Si-H. The decrease in growth rate using the smaller SbCl<sub>5</sub> dose is consistent with previous studies, where the thickness per cycle during PEDOT oMLD was limited by SbCl<sub>5</sub>.<sup>35</sup> Even when growth was limited by SbCl<sub>5</sub>, we observed good uniform deposition under MLD conditions at 100 °C in our tubular hot-wall reactor system. For a deposition thickness of ~30 nm, the thickness across the 2 cm wide and 10 cm long growth zone was uniform within ± 2 nm. Repeating the process in a second custom reactor with the similar design also showed good uniformity (20 ± 3 nm) across the 2 cm wide and 30 cm long growth zone.

We further tested film growth on Si-H and SiO<sub>2</sub> at different deposition temperatures. Using fixed reactant dose conditions (*i.e.*, the same as used at 100 °C for the samples in **Figure 3.2a**), increasing the deposition temperature to 125 and 150 °C led to a net decrease in growth rate on both SiO<sub>2</sub> and Si-H (**Figure 3.9c**). This trend is consistent with other MLD processes and is correlated with an increased rate in reactant desorption at higher temperatures.<sup>34,35,39–41</sup> The

difference in growth rates on SiO<sub>2</sub> and Si-H was most pronounced at 100 °C, so this temperature was used for subsequent tests.

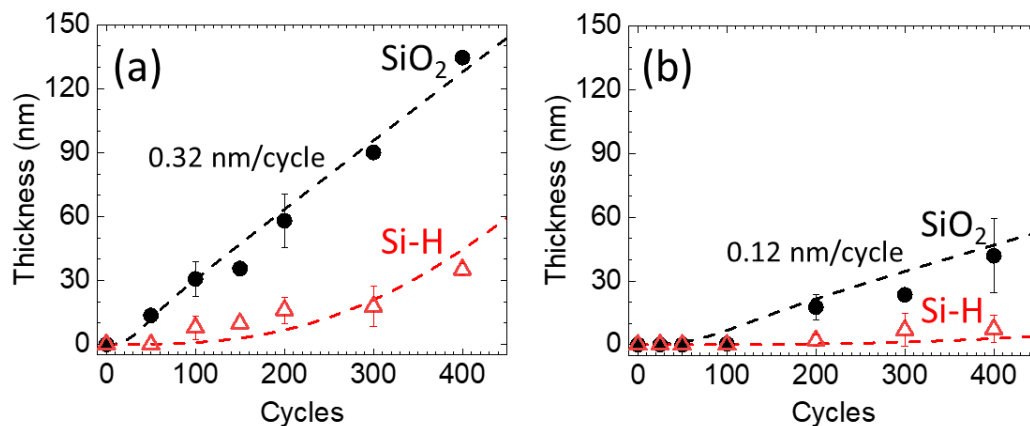


**Figure 3.2** PEDOT film thickness vs. MLD cycles at 100 °C on SiO<sub>2</sub> and Si-H using (a) SbCl<sub>5</sub>/N<sub>2</sub>/EDOT/N<sub>2</sub> = 0.5/60/2/60 s and (b) SbCl<sub>5</sub>/N<sub>2</sub>/EDOT/N<sub>2</sub> = 0.1/60/2/60 s. The dashed lines are fits to an analytical model described in the text.

Film thickness on SiO<sub>2</sub> after 200 and 400 cycles at 100 °C with SbCl<sub>5</sub> dose = 0.1 s was measured by SE, cross-sectional SEM, and XRR. The cross-sectional SEM images in **Figure 3.3a,b** show 18.2 and 44.3 nm after 200 and 400 cycles, respectively, which are reasonably consistent with 16.8 and 47.4 nm measured by SE, and 19.5 and 48.4 nm determined by XRR. (**Table 3.2**). The films deposited on SiO<sub>2</sub> and Si-H at 100 °C were also analyzed by XPS, and the spectra collected in the sulfur 2p region are shown in **Figure 3.3c,d**. (Additional XPS data can be found in **Figure 3.10** and **Table 3.3**). On SiO<sub>2</sub>, a weak signal due to sulfur is observed after 50 and 100 cycles, with a stronger peak observed after 200 and 400 cycles. On the Si-H, a weak peak is

visible after 200 cycles, with a stronger peak present after 400 cycles. These results are consistent with the thickness data in **Figure 3.2b**, as well as plan-view SEM images in **Figure 3.11**.

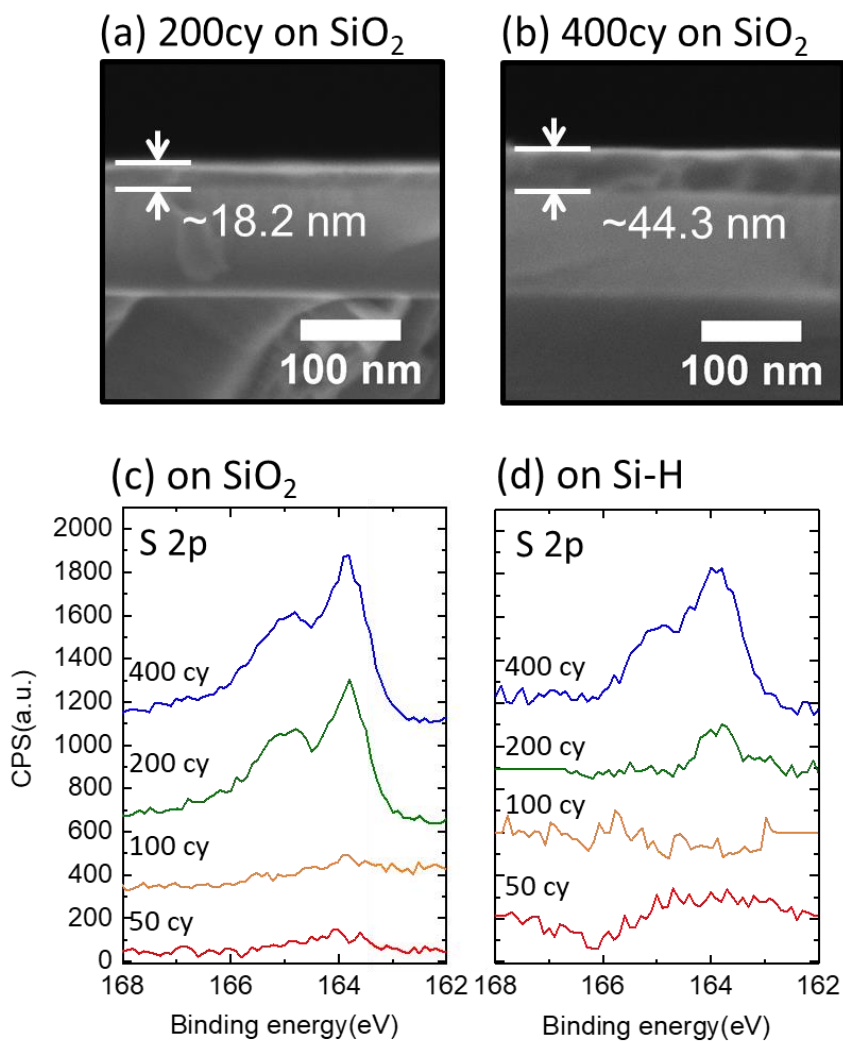


**Figure 3.3** Cross-sectional SEM images of films deposited on SiO<sub>2</sub> using (a) 200 and (b) 400 cycles of MLD. XPS spectra collected in the S 2p region on (c) SiO<sub>2</sub> and (d) Si-H after 50, 100, 200, and 400 cycles of MLD.

### 3.4.2 Area-Selective MLD on Patterned Substrates

As shown in **Figure 3.2b**, at 100 °C with an  $\text{SbCl}_5$  dose time of 0.1 s/cycle, 200 cycles of MLD PEDOT can produce  $\sim 15$  nm of deposition on a blanket  $\text{SiO}_2$  wafer with minimal growth on Si-H. Using the same conditions, deposition was performed for 200 and 400 cycles on Si-H/ $\text{SiO}_2$  line/space patterns with  $\sim 3$   $\mu\text{m}$  half-pitch, used previously in our lab.<sup>5,42-44</sup> **Figure 3.4a,b** shows plan-view SEM images, where the top portion of the frame corresponds to the  $\text{SiO}_2$ , and the bottom portion is the Si-H region. After 200 MLD cycles, a rough texture is seen on the  $\text{SiO}_2$ , consistent with PEDOT growth. In contrast, on the Si-H region, the surface appears smooth with no distinct nuclei visible. After 400 cycles, both regions show similar surface texture, consistent with loss of selectivity and growth of PEDOT on the Si-H. These results agree well with SE, XPS, and SEM results in **Figures 3.2 and 3.3, and 3.11**, showing highly selective nucleation and growth of PEDOT on  $\text{SiO}_2$  vs. Si-H.

Cross-sectional STEM images of the patterned samples after 200 MLD cycles are given in **Figure 3.4c,d**. The images show  $\sim 7.8$  nm of PEDOT on  $\text{SiO}_2$ , with no visible nuclei on the neighboring Si-H surface. The corresponding EDX elemental map in **Figure 3.4e** shows sulfur (from the PEDOT) only on the  $\text{SiO}_2$  region, verifying ASD of PEDOT on  $\text{SiO}_2$  vs. Si-H. After 200 cycles, the PEDOT thickness of  $\sim 7.8$  nm on the  $\text{SiO}_2$  region of the patterned substrates is substantially smaller than the  $\sim 17$  nm thickness obtained under the same conditions on blanket  $\text{SiO}_2$  wafers (**Figure 3.2b**). During ASD, reactant gradients are expected to develop due to surface diffusion and spatially dependent reactant consumption, leading to feature-dependent growth rates.<sup>44,45</sup>

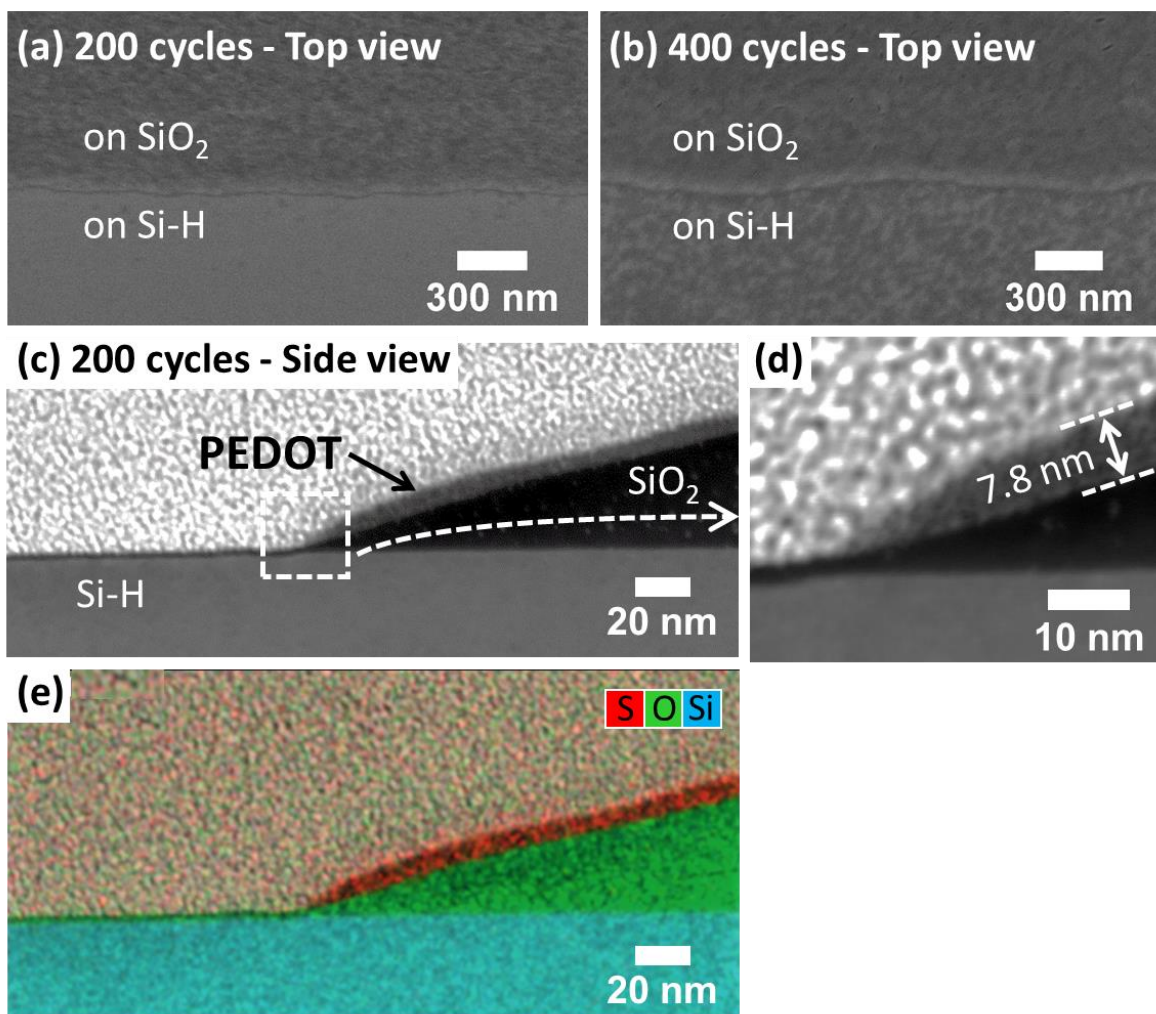


**Figure 3.4** Plan-view SEM images for (a) 200 and (b) 400 MLD cycles at 100 °C on Si-H/SiO<sub>2</sub> substrates. Cross-sectional STEM images for (c) 200 MLD cycles at 100 °C on Si-H/SiO<sub>2</sub> substrates, (d) enlarged view of (c), and (e) EDX elemental mapping of the corresponding region. All samples were deposited on 3 μm Si-H/SiO<sub>2</sub> line/space-patterned wafers.

### 3.4.3 Area-Selective CVD of PEDOT on Blanket Substrates

As another test, we studied film deposition under CVD conditions. In this case, the EDOT and SbCl<sub>5</sub> reactants were allowed to flow simultaneously and continuously into the heated tubular

reactor. At 100 °C, film growth was nonuniform, with substantial growth near the beginning of the growth zone, consistent with facile reactant adsorption. Increasing the reaction temperature to 150 °C led to good uniform growth across the 30 cm length of the substrate holder in the reactor deposition zone. The improved uniformity suggests that for the reactant pressure and dose conditions used, the higher temperature leads to a more optimized balance between the rates of reactant adsorption/desorption and the rate of deposition.

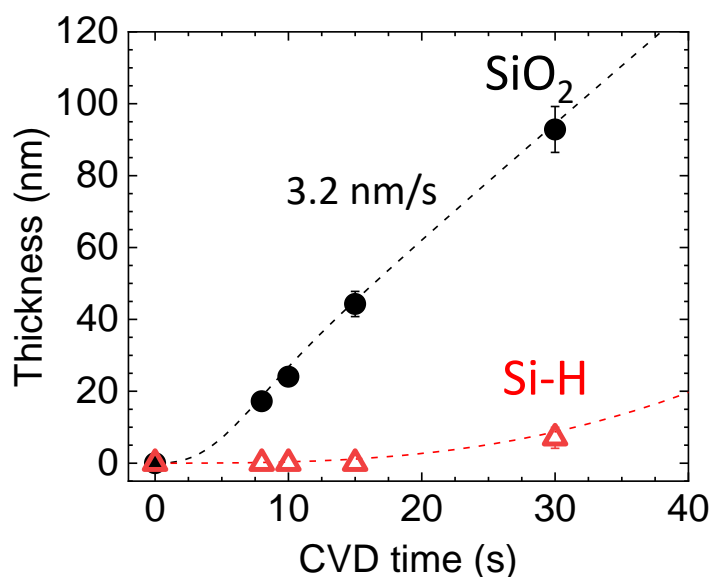


**Figure 3.5** PEDOT film thickness vs. CVD process time at 150 °C on SiO<sub>2</sub> and Si-H under 0.37 Torr. The dashed lines are fits to an analytical model described in the text.

Using CVD conditions at 150 °C, the film thickness was measured by SE after various deposition times on blanket SiO<sub>2</sub> and Si-H substrates, and the results are shown in **Figure 3.5**. On SiO<sub>2</sub>, after a short incubation time, the film thickness increases linearly as a function of time with a rate of 3.2 nm/s. On Si-H, however, SE analysis shows no measurable PEDOT growth after 15

s, with some growth after 30 s. The dashed lines correspond to a fit to the island growth model.<sup>38</sup> As shown in Figure 5, 15 s of CVD leads to no measurable PEDOT on Si-H while the SiO<sub>2</sub> surface shows ~40 nm of growth. On both substrates, the surface of PEDOT films is fairly conformal (RMS = 0.18–0.58 nm), as shown in **Table 3.4**. Comparing the CVD results in **Figure 3.5** to the MLD results in **Figure 3.2**, MLD achieved ~15 nm of PEDOT ASD on SiO<sub>2</sub> before measurable growth appeared on Si-H, whereas the CVD process allowed more than 40 nm of selective growth. A more detailed comparison of MLD and CVD results is discussed below.

#### 3.4.4 Area-Selective CVD on Patterned Substrates

To fully explore the CVD process, deposition was also tested on nanoscale Si-H/SiO<sub>2</sub> line/space patterns using deposition times of 10, 15, and 30 s at 150 °C. Patterned substrates included coplanar Si-H/SiO<sub>2</sub> lines with SiO<sub>2</sub> line width of 130 nm, separated by exposed silicon regions with a width between 130 and 500 nm. We also used topographical Si-H/SiO<sub>2</sub> line patterns, with SiO<sub>2</sub> lines of ~200 nm width and ~100 nm thickness, spaced 200 nm apart on silicon (*i.e.*, 200 nm half-pitch). On the coplanar Si-H/SiO<sub>2</sub> surfaces in **Figure 3.6a,b**, 10 s of CVD leads to ~29.5 nm of PEDOT on the SiO<sub>2</sub> regions, with no visible nuclei on Si-H. Likewise, on the topographical features in **Figure 3.6c**, the film thickness on the top and side of the SiO<sub>2</sub> is ~22.4 nm, with no PEDOT visible on Si-H. After 15 s of deposition, the coplanar features in **Figure 3.6d,e** show 36 nm of ASD PEDOT on SiO<sub>2</sub>, and Figure 6f shows 31.3 nm of ASD on the nonplanar substrates. After 30 s of growth, corresponding images in **Figure 3.6g-i** show 78 and 82 nm of PEDOT on SiO<sub>2</sub>, respectively. In the images, 30 s of deposition leads to visible nuclei and bridging between features, indicating selectivity loss. On the patterned wafers, the values for

film thickness correspond to a linear CVD growth rate of  $\sim 2.6$  nm/s on SiO<sub>2</sub>, which is less than 3.2 nm/s obtained on blanket SiO<sub>2</sub> substrates in Figure 5 using the same growth conditions.

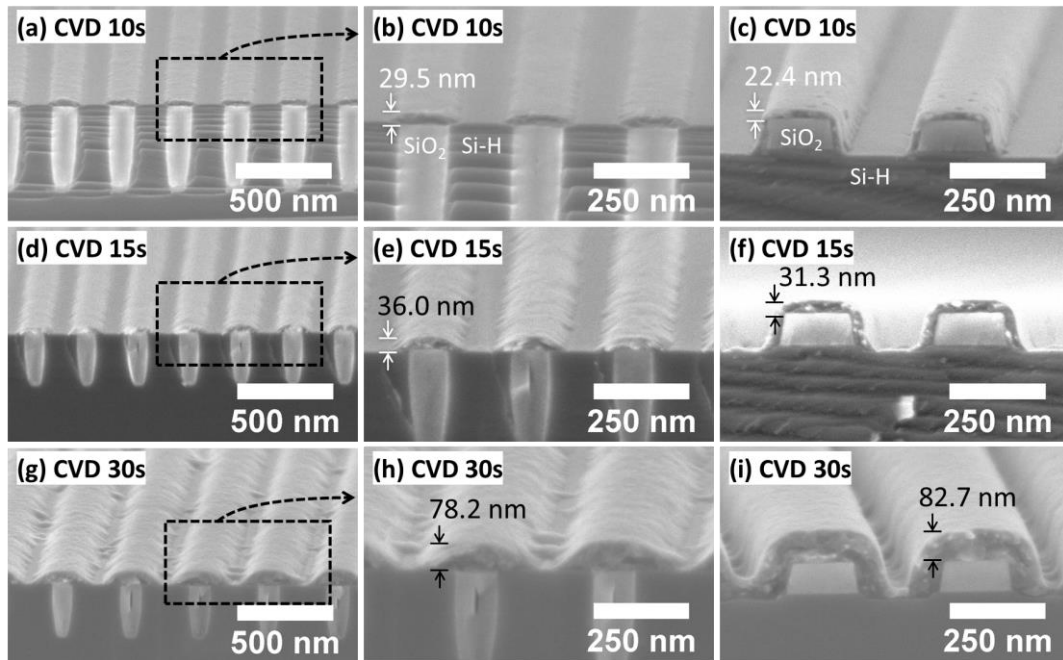


**Figure 3.6** Angled-view SEM images of PEDOT CVD on Si-H/SiO<sub>2</sub>-patterned wafers at 150 °C for (a–c) = 10 s, (d–f) 15 s, and (g–i) 30 s.

#### 3.4.5 Vertical vs. Lateral Growth

On the planar substrates in **Figure 3.6**, mushroom growth is observed, where the PEDOT growth on the SiO<sub>2</sub> extends laterally over the top of the adjacent Si-H region. **Figure 3.7** shows the mushroom growth after 15 and 30 s of CVD in more detail. If the growth proceeds only on SiO<sub>2</sub> with a rate that is uniform in all directions, the distance that the lateral growth extends on top of the Si-H is expected to be the same as the net vertical film thickness on the SiO<sub>2</sub>. After both 15 and 30 s, the distance of the lateral growth over the Si-H region coincides well with the total

thickness on top of the SiO<sub>2</sub>. However, the thickness of the overgrowth appears to be tapered, whereas a uniform growth rate is expected to produce a more rounded edge. To fully understand feature shape evolution during ASD, feature-dependent deposition rates should be considered.

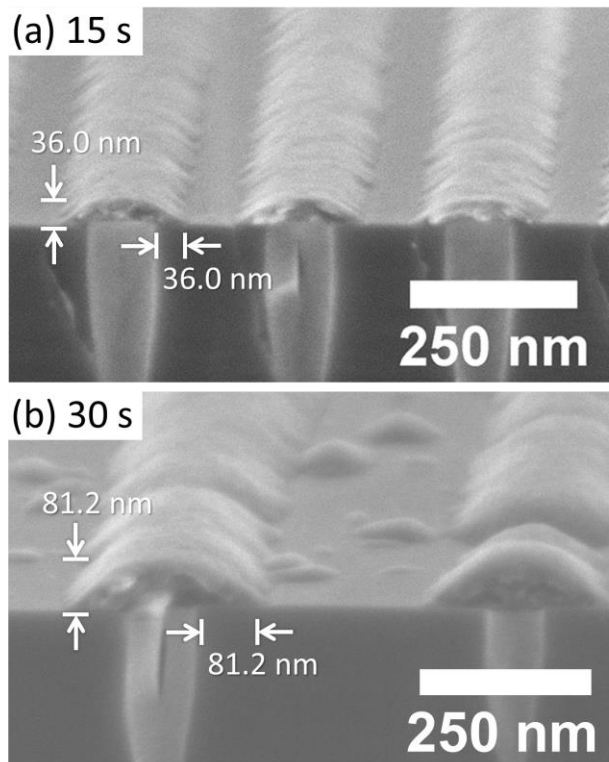


**Figure 3.7** Angled-view SEM images of PEDOT CVD at 150 °C for (a) 15 s on a coplanar 130 nm SiO<sub>2</sub>/130 nm Si-H line-patterned wafer and (b) 30 s on a coplanar 130 nm SiO<sub>2</sub>/430 nm Si-H line-patterned wafer. The PEDOT growth on SiO<sub>2</sub> extends laterally over the top of the adjacent Si-H, and the distance of the lateral growth is approximately equal to the vertical growth thickness.

### 3.4.6 Mechanism for PEDOT Selectivity on SiO<sub>2</sub> vs. Si-H

To understand the ASD results, we considered several mechanisms that enable preferential deposition of PEDOT on SiO<sub>2</sub> vs. Si-H. Based on the general deposition mechanism in **Figure 3.1**, PEDOT film growth proceeds *via* reduction of the SbCl<sub>5</sub> and concomitant EDOT oxidative polymerization. Therefore, two possible mechanisms could account for the observed lack of PEDOT nucleation on Si-H vs. SiO<sub>2</sub>: (1) the adsorption energy for SbCl<sub>5</sub> on Si-H is much smaller than that on SiO<sub>2</sub>, leading to preferential desorption from the Si-H vs. SiO<sub>2</sub> surface; and/or (2) the SbCl<sub>5</sub> readily adsorbs on both Si-H and SiO<sub>2</sub>, but on Si-H, the adsorbed Sb species is unable to oxidize the EDOT monomer, leading to preferential growth on SiO<sub>2</sub>.

Considering the first possible mechanism, **Figure 3.2** shows that decreasing the SbCl<sub>5</sub> dose leads to less film growth, but the extent of selectivity hardly changes (*i.e.*, the change in growth is similar for both the SiO<sub>2</sub> and Si-H substrates), suggesting that a large difference in reactant adsorption is not a key factor. For the second possible mechanism, we used thermodynamic reaction analysis (HSC Chemistry 7.1)<sup>46</sup> to examine possible reactions for SbCl<sub>5</sub> with silicon and silicon oxide. It is important to note that, in general, experiments do not always yield the expected thermodynamic product because kinetic barriers may limit the rate of product formation. As shown in **Figure 3.12**, when SbCl<sub>5</sub> is exposed to solid silicon, the overall reaction energetics favor the reduction of the SbCl<sub>5</sub> to form Si-Cl bonds. On SiO<sub>2</sub>, however, while some disproportionation of SbCl<sub>5</sub> may occur, the SbCl<sub>5</sub> is not expected to react with the silicon oxide surface. Therefore, a likely explanation for the observed substrate-dependent PEDOT growth is that on the Si-H surface, the SbCl<sub>5</sub> promotes a redox reaction, chlorinating the Si-H and reducing the SbCl<sub>5</sub> to SbCl<sub>x</sub>. In the reduced form, the adsorbed SbCl<sub>x</sub> on the silicon is unable to oxidize the EDOT monomer, thereby inhibiting PEDOT polymerization. On the SiO<sub>2</sub>, physisorbed SbCl<sub>5</sub> remains available to oxidize

the EDOT, thereby enabling PEDOT ASD. Further evidence to support the second mechanism can be obtained from careful inspection of XPS results in **Figure 3.10g**, where after 50 cycles of PEDOT MLD, the XPS spectrum shows evidence for Sb present on the Si-H. This indicates that Sb adsorption on Si-H is favorable, showing that PEDOT growth is likely impeded by the reduction of  $\text{SbCl}_5$  rather than the  $\text{SbCl}_5$  adsorption difference on  $\text{SiO}_2$  and Si-H surfaces.

On the silicon surface, the thermodynamic analysis in **Figure 3.12** also indicates the  $\text{SbCl}_5$  can react with silicon to form volatile  $\text{SiCl}_4$  (*i.e.*, silicon etching). To examine possible effects of silicon etching, Si-H/ $\text{SiO}_2$ -patterned wafers were exposed to multiple doses of only  $\text{SbCl}_5$ . As shown in the STEM image in **Figure 3.13**, extended  $\text{SbCl}_5$  exposure led to silicon etching, particularly in the region adjacent to the  $\text{SiO}_2$  line. The enhanced etching at the feature edge is ascribed to excess  $\text{SbCl}_5$  available in this region. Since the  $\text{SbCl}_5$  is less reactive on the  $\text{SiO}_2$ , the  $\text{SbCl}_5$  adsorbed on  $\text{SiO}_2$  can move to the Si-H region by surface diffusion and/or by desorption and gas-phase transport. As a result, the enhanced  $\text{SbCl}_5$  flux increases the extent of etching at the Si-H/ $\text{SiO}_2$  boundary. Other feature and shape-dependent phenomena have also been ascribed to surface and gas-phase transport, which changes the local reactant concentration and supersaturation during ASD.<sup>4,45</sup>

#### 3.4.7 Quantified Selectivity and Comparison of MLD vs. CVD

While many methods are known for ASD using ALD, MLD, and CVD,<sup>4</sup> direct comparisons of ALD (or MLD) and CVD processes for ASD are not widely reported. The data in **Figures 3.2 and 3.5** allows us to estimate a value for selectivity,  $S$ , that can be compared for the MLD and CVD processes. Selectivity is formally defined by the ratio of thermodynamic driving force for nucleation on the growth and nongrowth surfaces.<sup>38,47</sup> Commonly, the driving force is

assumed to be proportional to nucleation rate, which in turn is taken to correlate with  $\theta_1$  and  $\theta_2$ , the surface coverage on the desired growth surface and the nongrowth surface, respectively. Because the coverage on the nongrowth surface depends on the extent of desired film growth, the selectivity is given as a function of the thickness on the desired growth surface,  $S(t_{growth})$

$$S(t_{growth}) = \frac{\theta_1 - \theta_2}{\theta_1 + \theta_2} \approx \frac{t_1 - t_2}{t_1 + t_2} \quad (\text{Eq 3.1})$$

As shown in the equation,  $S(t_{growth})$  can also be estimated from the measured film thickness on the growth ( $t_1 = t_{growth}$ ) and nongrowth ( $t_2$ ) surfaces. However, using the thickness values, the value of  $S$  will be larger (*i.e.*, better) than the value obtained using the surface coverages.

To compare the selectivity for the different conditions studied, we utilized a quantitative nucleation model and two figures of merit,<sup>38</sup>  $S_t=10$  nm, defined as the selectivity when the desired film thickness is 10 nm, and  $t_s=0.9$ , the deposited film thickness when selectivity is 0.9 (see Supporting Information). The resulting values for selectivity obtained from the data in **Figures 3.2 and 3.5** are summarized in **Table 3.1**. Notably, we find that the selectivity for both the MLD and CVD PEDOT processes is larger compared to most previous reports of inorganic and organic ASD.<sup>24,25,27,43</sup> Furthermore, noteworthy is the total time required for these processes. For the MLD conditions used in **Figure 3.2a,b**, *i.e.*, 30 and 100 MLD cycles, respectively (not optimized for process speed), the total process time was ~60 and 200 minutes, respectively. In contrast, for the CVD process in **Figure 3.5**, ~10 nm of ASD PEDOT requires less than 5 s of process time. We also investigated the relationship between  $\text{SbCl}_5$  total exposure time and PEDOT growth rate by CVD and MLD processes in **Figure 3.10**. Clearly, CVD enables a decrease in the  $\text{SbCl}_5$  exposure time with a faster growth rate on  $\text{SiO}_2$  surfaces.

**Table 3.1** Quantitative Comparison of PEDOT ASD *via* MLD *vs.* CVD.

Method	Deposition Rate <sup>a</sup>	Selectivity Parameter <sup>b</sup>	Approximate total deposition time for 10 nm of ASD <sup>c</sup>
MLD	0.32 nm/cycle	$t_{s=0.9}$ 35.4 nm	60 min
		$S_{t=10nm}$ 0.933	
MLD	0.12 nm/cycle	$t_{s=0.9}$ 35.5 nm	200 min
		$S_{t=10nm}$ 0.933	
CVD	3.2 nm/s	$t_{s=0.9}$ 55.4 nm	0.1 min
		$S_{t=10nm}$ 0.989	

<sup>a</sup>Linear deposition rate on the receptive SiO<sub>2</sub> surface from model fits (**Figure 3.9**).

<sup>b</sup>Parameters are outputs from model fits (**Figure 3.9**).

<sup>c</sup>Time estimated from graphs of thickness *vs.* cycle (or time) (**Figure 3.9**) on blanket wafers using the processes described (not optimized for process speed).

### 3.5 Summary

This work describes the inherent area-selective deposition of PEDOT on SiO<sub>2</sub> *vs.* Si-H surfaces *via* MLD and CVD using EDOT as a reactive monomer and SbCl<sub>5</sub> as an oxidant for polymerization. Results confirmed that both MLD and CVD can induce preferential deposition of PEDOT onto SiO<sub>2</sub> *vs.* Si-H. The observed slow nucleation on Si-H was ascribed to the reduction of the SbCl<sub>5</sub> on the Si-H surface, thereby inhibiting oxidative polymerization. Using the film thickness values measured by SE for MLD PEDOT at 100 °C on blanket SiO<sub>2</sub> and Si-H surfaces, a fit to a quantitative nucleation model indicated that the MLD process could achieve ~35 nm of deposition with a selectivity of 90%, *i.e.*,  $t_{s=0.90} \approx 35$  nm. When the same process conditions were

applied to patterned line/space Si-H/SiO<sub>2</sub> substrates with ~6 μm full pitch (*i.e.*, 3 μm SiO<sub>2</sub> spaces separated by 3 μm Si-H lines), less net film thickness was obtained on SiO<sub>2</sub>.

Using CVD conditions at 150 °C, we also observed favorable ASD of PEDOT on SiO<sub>2</sub> *vs.* Si-H, with overall selectivity that exceeded the selectivity by MLD. Specifically, using values of thickness *vs.* deposition time measured on blanket wafers, the model fit indicated that ~55 nm of ASD could be achieved at  $S = 0.9$ , *i.e.*,  $t_{S=0.90} \approx 55.4$  nm. When ASD was performed on patterned Si-H/SiO<sub>2</sub> wafers using CVD, the extent of film deposition was less than that observed on blanket wafers using the same CVD conditions, but the decrease was smaller than that observed for MLD processes.

Comparing the MLD and CVD processes, the CVD enabled better selectivity than the MLD. Particularly noteworthy is the difference in total process time needed. To achieve 10 nm of ASD, the CVD process was more than 100 times faster than MLD under the process conditions studied. This result suggests that for other ASD materials, CVD processes may be better than ALD. Furthermore, using patterned substrates with coplanar Si-H/SiO<sub>2</sub>-patterned regions, the extent of lateral PEDOT overgrowth, *i.e.*, “mushrooming” was observed and measured. The distance that the PEDOT grew in the lateral direction from the SiO<sub>2</sub> over top of the adjacent Si-H region matched well with the vertical film thickness on the SiO<sub>2</sub>. However, the cross-sectional shape of the overgrowth appeared tapered instead of the rounded shape expected if the PEDOT grew uniformly in all directions on the SiO<sub>2</sub>.

The mechanisms leading to the observed differences in film growth rates on the blanket and patterned wafers and the extent and shape of mushroom lateral overgrowth were not well defined, but they are likely related to surface and gas-phase transport effects previously described to account for feature and size-dependent deposition rates during ASD.<sup>44,45</sup>

### 3.6 Supporting Information

#### 3.6.1 Definition of Selectivity( $S(t_{growth})$ ), and Area-Selective Deposition Figures of Merit

During area-selective deposition (ASD), a value for selectivity,  $S$ , is formally defined by the ratio of thermodynamic driving force for nucleation on the growth and non-growth surfaces.<sup>38,47</sup> Commonly, the driving force is assumed to be proportional to nucleation rate, which in turn is taken to correlate with the fractional surface coverage,  $\theta$ , versus reaction time, *i.e.* number of cycles,  $n$ , so that  $S=S(n)$ . During ASD, we are usually interested in optimizing the film thickness on the desired growth surface,  $t_{growth}$ , which is typically measured as a function of cycles (or time):  $t_{growth}(n)$ . Therefore, selectivity is suitably analyzed as a function of  $t_{growth}$ :  $S(t_{growth}) = ((\theta_1 - \theta_2) / ((\theta_1 + \theta_2)))$  where  $\theta_1$  and  $\theta_2$  are the surface coverage on the desired growth surface and the non-growth surface, respectively.<sup>4,38,47</sup> To compare two processes, for any value of  $t_{growth}$ , the process that allows a larger value of  $S$  is more favorable. A problem with this definition is that surface coverage is not always easy to measure. Therefore,  $S(t_{growth})$  is sometimes estimated from the ratio of the film thickness on the growth ( $t_1 = t_{growth}$ ) and non-growth ( $t_2 = t_{non-growth}$ ) surfaces:  $S \approx ((t_1 - t_2) / ((t_1 + t_2)))$ . It is important to note that for any values of  $\theta_1$  and  $\theta_2$ , the value for  $S(t_{growth})$  obtained using the corresponding values of  $t_1$  and  $t_2$  will be larger (*i.e.* better) than that the value obtained using the surface coverages.

Using the above equations, values for  $S(t_{growth})$  can be obtained directly from experimental data. The expected trend for  $S(t_{growth})$  as well as insight into mechanisms for unwanted nucleation can also be obtained using an analytical model for nucleation and growth evolution summarized below.<sup>4,38</sup>

Generally, a single “figure of merit” makes it easier to quantitatively compare different processes.<sup>38</sup> As an example selectivity figure of merit, we identify a target thickness on the desired

growth surface, *e.g.*  $t_{growth} = 10 \text{ nm}$ , and report the selectivity achieved at that thickness, *i.e.*  $S(t = 10 \text{ nm})$ . As an alternative figure of merit, we select an example target selectivity, *e.g.*  $S = 0.9$ , and report the thickness on the desired growth surface for that target selectivity, *i.e.*  $t(S=0.9)$ . Using this scheme, depending on the application, other target values for  $t_{growth}$  or  $S$  could also be used to define other associated figures of merit.

### 3.6.2 Nucleation Model Description

The nucleation and growth evolution model follows a procedure described previously<sup>4,38</sup> to identify the expected trend for film thickness *vs.* deposition cycle (or time) on the desired growth and non-growth surfaces. In the model, the film thickness deposited per cycle, given as  $\dot{G}$  [nm/cycle] (for ALD or MLD), or [nm/s] (for CVD), is assumed to be uniform in any direction and constant on any receptive surface. The value for  $\dot{G}$  is obtained experimentally as the thickness/cycle (during ALD or MLD) or thickness/s (during CVD) during steady linear growth on a receptive surface. For the results shown here,  $\dot{G}$  is the slope in the linear region of the thickness *vs.* cycle (or time) during PEDOT deposition on SiO<sub>2</sub>. On the non-growth surface, deposition is assumed to begin at randomly distributed nucleation sites which may be present on the starting surface, and/or generated during the deposition process. The density of nucleation sites on the starting surface is denoted as  $\hat{N}$  [sites/nm<sup>2</sup>] and the rate of nucleation site generation is denoted as  $\dot{N}$  [sites/nm<sup>2</sup> cycle] (during MLD) or [sites/nm<sup>2</sup> s] (during CVD), and the values of  $\hat{N}$  and  $\dot{N}$  are fitting parameters in the model.

When deposition begins on the non-growth surface, the model assumes that the nuclei grow as hemispheres with radius increasing at  $\dot{G}$  [nm/cycle]. As nuclei grow, the coalescence is modeled using the Avrami formalism<sup>4,38</sup> to obtain values for surface coverage *vs.* cycle (or time). Integration

of the surface coverage gives the net volume of material deposited on the substrate surface. The film thickness is defined to be the total volume of deposited material per unit area of the planar substrate surface.

### 3.6.3 Model Fitting and Results

The value of  $\hat{G}$  first is determined by fitting the measured thickness vs. cycle (or time) on the growth surface. The values for  $\hat{N}$  and/or  $\dot{N}$  are adjusted until the model output provides a reasonable visible match to the thickness data on the non-growth surface. The values of  $\theta_1$  and  $\theta_2$  versus cycle or time are used to calculate  $S_{(t_{growth})}$ . For simplicity, the fits reported here were obtained by adjusting the value of  $\hat{N}$  with  $\dot{N} = 0$ . Fits were also examined by setting  $\dot{N} = 0$  and adjusting  $\hat{N}$ , and the resulting fits showed similar overall trends. To better distinguish the mechanism for unwanted nucleation, (*i.e.* nucleation sites on the starting non-growth surface vs. nucleation site generation during deposition) the fitting requires more extensive data sets and systematic model output analysis.

Thickness vs. MLD cycle measured by spectroscopic ellipsometry (SE) from **Figure 3.2** is replotted in **Figure 3.9**, including lines from the model fits. The corresponding plots of  $S_{(t_{growth})}$  are also shown, calculated using  $\theta_1$  and  $\theta_2$  (solid lines) and  $t_1$  and  $t_2$  (dashed lines). As noted above, the dashed line using  $t_1$  and  $t_2$  overestimates the values of  $S$ . The solid red dots are the values of  $S$  calculated using  $t_1$  and  $t_2$  measured by SE. For small values of  $t_1$  and  $t_2$ , the accuracy of the SE measurement tends to skew the values for  $S$ , giving values that are much smaller than the expected model trend.

For the MLD data using  $\text{SbCl}_5 = 0.5$  s/cycle, the fit in Figure 2 and S1 corresponds to  $\hat{G} = 0.32$  nm/cycle, and  $\hat{N} = 1.3 \times 10^{-5}$  sites/nm<sup>2</sup>, with  $\dot{N} = 0$ . If nucleation sites are present on the starting

nongrowth surface, we expect that changing the deposition conditions should not substantially change the value of  $\hat{N}$ . Therefore, to fit the thickness data obtained using  $\text{SbCl}_5 = 0.1$  s/cycle, we first fit the growth rate on  $\text{SiO}_2$  and obtained to  $\dot{G} = 0.12$  nm/cycle and calculated the expected thickness vs. cycle on Si-H assuming  $\hat{N} = 1.3 \times 10^{-5}$  sites/nm<sup>2</sup>, *i.e.* the value obtained when  $\text{SbCl}_5 = 0.5$  s/cycle. The resulting model output in **Figures 3.2b and 3.9b** agree reasonably well with the measured data. Likewise, the data collected under CVD conditions was also fit using the model, giving  $\dot{G} = 3.2$  nm/s. Then, using the same value for  $\hat{N} = 1.3 \times 10^{-5}$  sites/nm<sup>2</sup>, the output thickness on Si-H was larger than observed experimentally. A reasonable fit was obtained using  $\hat{N} = 5.0 \times 10^{-6}$  sites/nm<sup>2</sup>, *i.e.* a smaller number of nucleation sites. Since the CVD process is much faster than the MLD process, the smaller value for  $\hat{N}$  for CVD suggests that nucleation site generation may be important. However, as noted above, unambiguous analysis of the nucleation mechanism will require more data to obtain more accurate fits. The figures of merit values  $S_{t=10nm}$  and  $t_{S=0.9}$  corresponding to these data sets are given in **Table 3.1**.

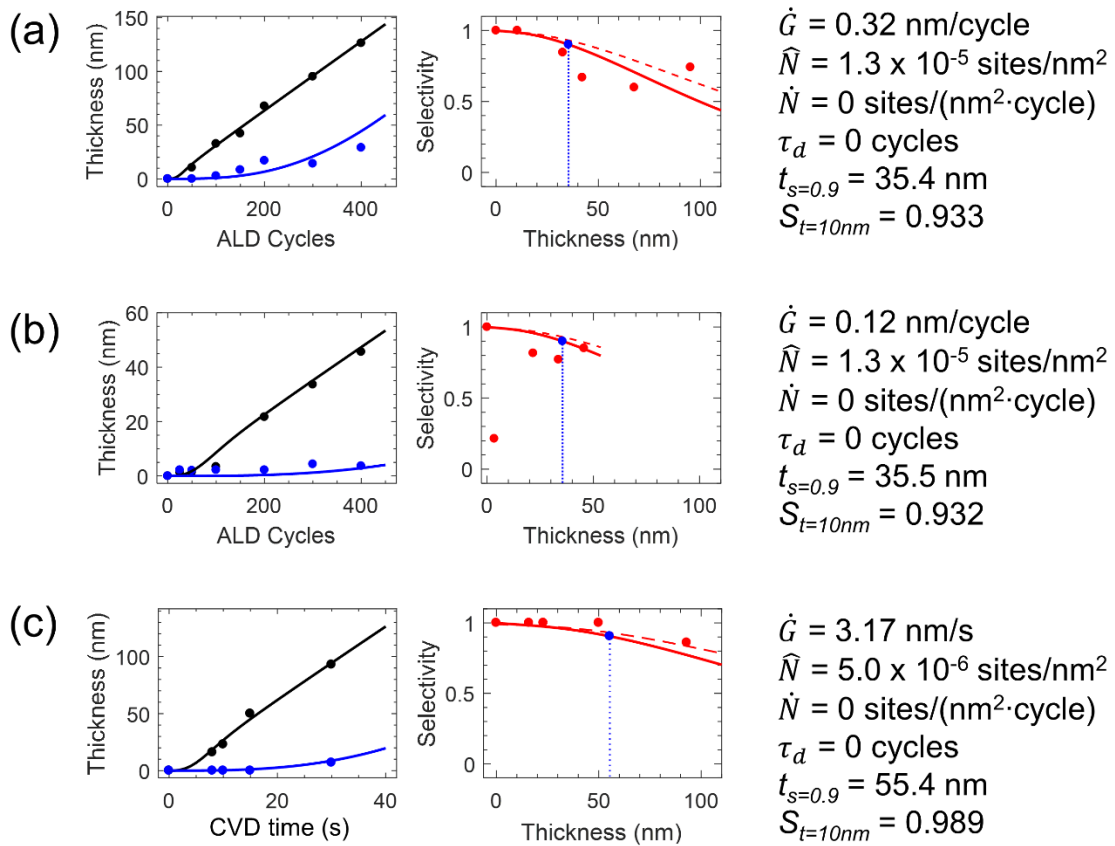


**Figure 3.8** PEDOT ASD experimental results along with model output fits using (a) MLD with  $\text{SbCl}_5 = 0.5$  s/cycle at  $100^\circ\text{C}$ , (b) MLD with  $\text{SbCl}_5 = 0.1$  s/cycle at  $100^\circ\text{C}$ , and (c) CVD conditions at  $150^\circ\text{C}$ . The model parameters corresponding to the resulting line fits are also given for each data set.

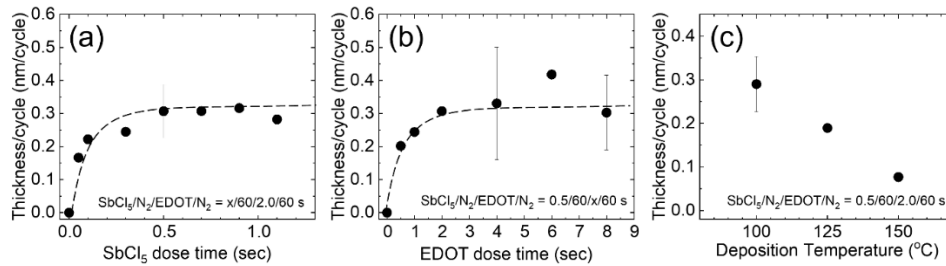


**Figure 3.9** The effect of reactant dose times of (a) SbCl<sub>5</sub> and (b) EDOT on PEDOT growth on SiO<sub>2</sub> at 100 °C. EDOT dose was held constant at 2.0 s for (a) and SbCl<sub>5</sub> dose time was held constant 0.5 s for (b). Dashed lines in (a) and (b) are drawn as guides to the eye. Panel (c) shows the thickness/cycle at different temperatures using the dose conditions indicated. All data were measured by spectroscopic ellipsometry and the error bar was from the standard deviation of three separate measurements.

**Table 3.2** PEDOT thickness on SiO<sub>2</sub> measured by SE, XRR and SEM. Films were deposited on SiO<sub>2</sub> at 100 °C using SbCl<sub>5</sub>/N<sub>2</sub>/EDOT/N<sub>2</sub> = 0.1/60/2/60 s.

MLD Cycles	Thickness (nm) measured by:		
	SE	X-ray Reflectivity	Cross-sectional SEM
200 cy	16.8 nm	19.5 nm	18.2 nm
400 cy	47.7 nm	48.4 nm	44.3 nm

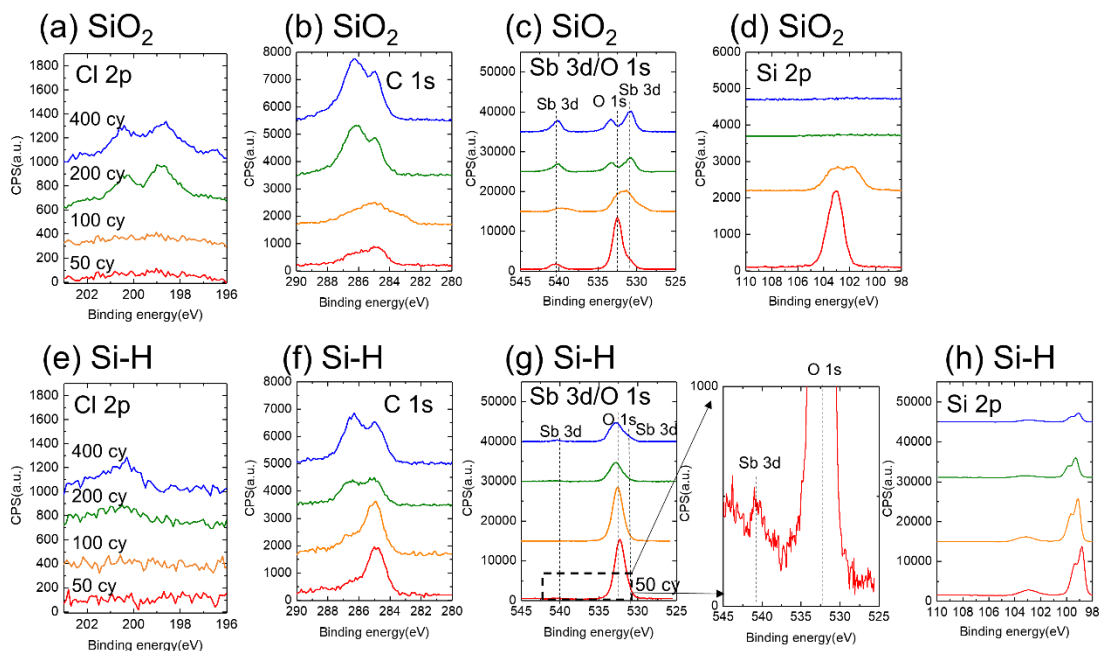


**Figure 3.10** High resolution XPS scans of (a) Cl 2p, (b) C 1s (c) Sb 3d/O 1s, (d) Si 2p on SiO<sub>2</sub> substrates and (e) Cl 2p, (f) C 1s, (g) Sb 3d/O 1s, (h) Si 2p on Si-H substrates for various MLD cycles at 100 °C. To clearly see the peak change, each spectrum was offset on the y-axis. Peak positions were calibrated by referencing the adventitious C 1s peak to 285.0 eV. Note that for the Sb 3d peak deconvolution, Sb 3d<sub>5/2</sub> and 3d<sub>3/2</sub> peaks were separated by 9.32 eV with a relative intensity of 3 to 2.

**Table 3.3** Elemental composition from XPS analysis. Values are given in atomic %.

Substrate	MLD cycles	C 1s	Si 2p	Sb 3d	O 1s	Cl 2p	S 2p	F 1s
SiO <sub>2</sub>	25	10.2	35.9	1.4	52.2	0.4	0.0	-
	50	14.6	32.7	1.6	49.3	1.4	0.5	-
	100	26.9	25.1	1.8	42.3	1.8	2.0	-
	200	60.9	3.1	3.9	16.0	7.0	9.2	-
	400	62.0	2.6	4.4	16.8	5.7	8.5	-
Si-H	25	16.9	78.4	0.0	4.5	0.1	0.2	-
	50	12.0	55.9	0.1	32.0	0.1	0.0	-
	100	15.3	53.1	0.1	31.5	0.0	0.0	-
	200	23.8	46.4	0.2	24.8	2.4	1.0	1.5
	400	43.2	21.3	0.5	26.7	2.0	6.3	-

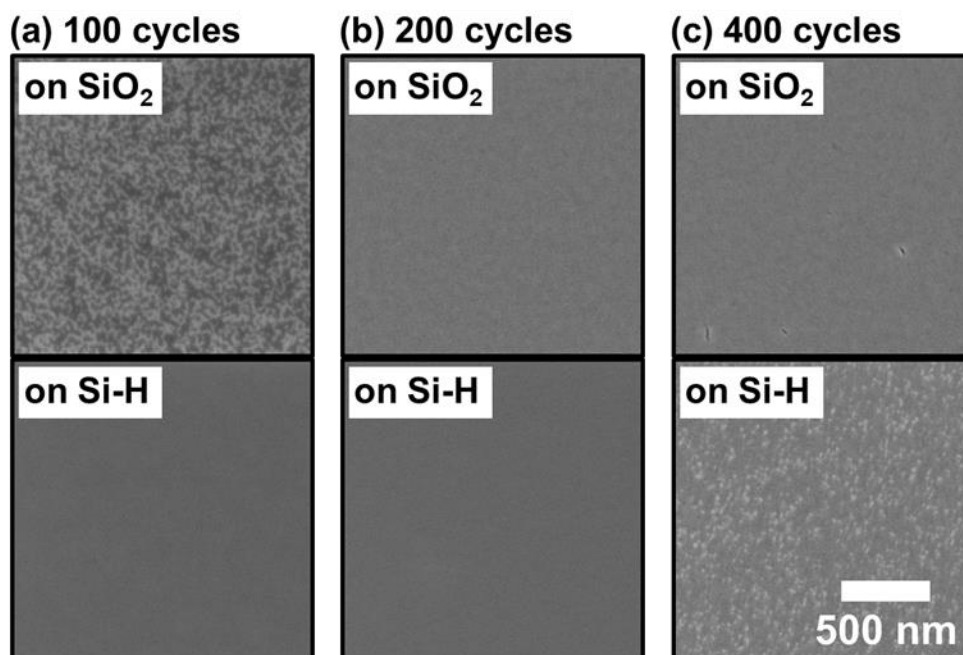


**Figure 3.11** Plan-view SEM images of PEDOT films formed using (a) 100, (b) 200, and (c) 400 MLD cycles on SiO<sub>2</sub> and Si-H at 100 °C. After 100 cycles on SiO<sub>2</sub>, panel (a) shows non-uniform surface structure, consistent with PEDOT nuclei. As MLD cycles increase to 200 and 400 cycles, the surface texture on the SiO<sub>2</sub> becomes more uniform, consistent with nuclei coalescence and uniform growth. On the Si-H substrates, no PEDOT nuclei are observed after 100 or 200 MLD cycles. After 400 cycles, white particles appear on the surface, consistent with PEDOT nucleation.

**Table 3.4** PEDOT surface roughness on SiO<sub>2</sub> and Si-H by AFM. Each RMS is the average of three measurements scanned over 2 x 2 μm.

Substrate	CVD time (sec)	RMS (nm)
SiO <sub>2</sub>	8	0.416 ± 0.029
	10	0.461 ± 0.007
	15	0.500 ± 0.016
Si-H	0 (bare)	0.098 ± 0.015
	8	0.208 ± 0.042
	10	0.582 ± 0.643
	15	0.179 ± 0.087

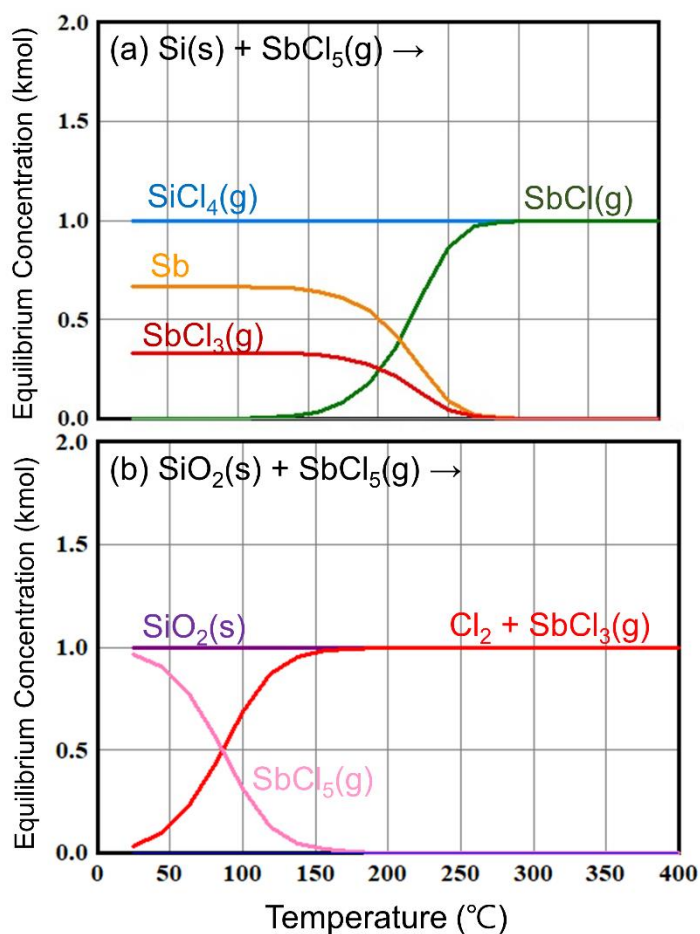


**Figure 3.12** Thermodynamic analysis (HSC Chemistry 7.1) showing the expected equilibrium species concentrations at 1 Torr at temperatures between 25 and 400 °C for: (a) 1 kmol of Si<sub>(s)</sub> + 1 kmol of SbCl<sub>5(g)</sub>; and (b) 1 kmol of SiO<sub>2(s)</sub> + 1 kmol of SbCl<sub>5(g)</sub>. The plots show that SbCl<sub>5</sub> is expected to react with silicon, but no reaction is expected on SiO<sub>2</sub>.

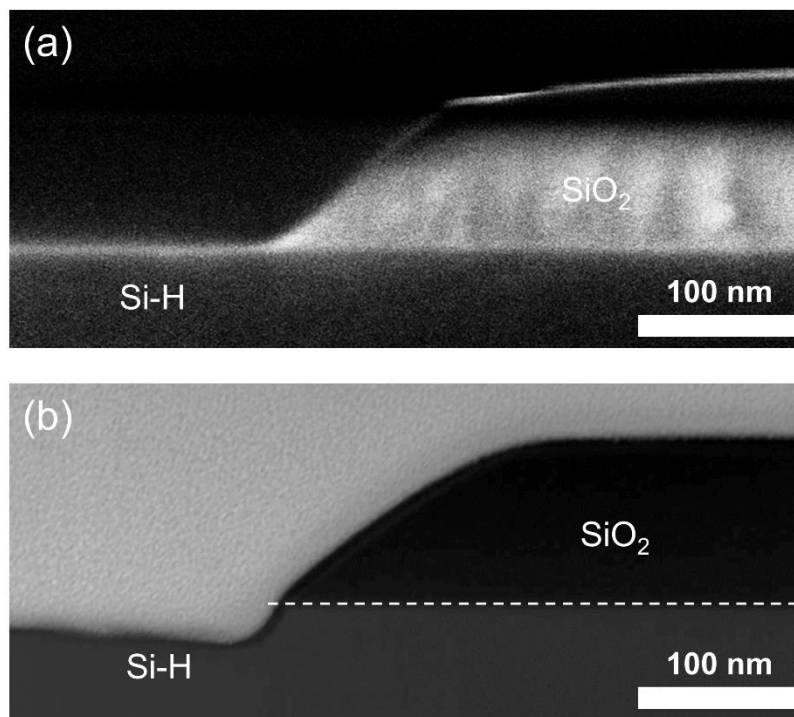


**Figure 3.13** Cross-sectional SEM images of bare Si-H/ SiO<sub>2</sub> patterned substrates and cross-sectional STEM image of the Si-H/SiO<sub>2</sub> patterned substrates after multiple doses of SbCl<sub>5</sub> (without EDOT exposure) at 100 °C. Sample-to-sample variation in the starting pattern production process causes differences in the SiO<sub>2</sub> edge profile shape. The SbCl<sub>5</sub> doses led to loss of silicon, with more etching at the Si-H/SiO<sub>2</sub> boundary region. The extent of SbCl<sub>5</sub> exposure was larger than that used for ASD of PEDOT shown in **Figure 3.4**. For this test, the SbCl<sub>5</sub> doses were performed with PEDOT coated on the inner reactor walls, rather than the typical Al<sub>2</sub>O<sub>3</sub> prepared during chamber conditioning. We find that the PEDOT on the reactor wall absorbs SbCl<sub>5</sub> during the dose period and releases it during the purge, leading to a larger SbCl<sub>5</sub> dose than expected.

### 3.7 References

- (1) Shchegrov, A. V.; Leray, P.; Paskover, Y.; Yerushalmi, L.; Megged, E.; Grauer, Y.; Gronheid, R. On Product Overlay Metrology Challenges in Advanced Nodes. *Proc. SPIE* **2020**, *11325*, No. 113251P.
- (2) Hiromatsu, T.; Ohkubo, R.; Maeda, H.; Fukui, T.; Shishido, H.; Ono, K.; Hashimoto, M. Continuous Challenges for next Era of Lithography. *Proc. SPIE* **2019**, *11177*, No. 1117705.
- (3) Clark, R.; Tapily, K.; Yu, K.; Hakamata, T.; Consiglio, S.; Meara, D. O.; Wajda, C.; Smith, J.; Leusink, G. Perspective : New Process Technologies Required for Future Devices and Scaling. *APL Mater.* **2018**, *6*, No. 058203.
- (4) Parsons, G. N.; Clark, R. D. Area-Selective Deposition: Fundamentals, Applications, and Future Outlook. *Chem. Mater.* **2020**, *32*, 4920–4953.
- (5) Song, S. K.; Saare, H.; Parsons, G. N. Integrated Isothermal Atomic Layer Deposition/Atomic Layer Etching Supercycles for Area-Selective Deposition of TiO<sub>2</sub>. *Chem. Mater.* **2019**, *31*, 4793–4804.
- (6) Vos, M. F. J.; Chopra, S. N.; Verheijen, M. A.; Ekerdt, J. G.; Agarwal, S.; Kessels, W. M. M.; Mackus, A. J. M. Area-Selective Deposition of Ruthenium by Combining Atomic Layer Deposition and Selective Etching. *Chem. Mater.* **2019**, *31*, 3878–3882.
- (7) Carlsson, J. O. Selective Vapor-Phase Deposition on Patterned Substrates. *Crit. Rev. Solid State Mater. Sci.* **1990**, *16*, 161–212.
- (8) Soethoudt, J.; Hody, H.; Spampinato, V.; Franquet, A.; Briggs, B.; Chan, B. T.; Delabie, A. Defect Mitigation in Area-Selective Atomic Layer Deposition of Ruthenium on Titanium Nitride / Dielectric Nanopatterns. *Adv. Mater. Interfaces* **2019**, *6*, No. 1900896.

- (9) Merkx, M. J. M.; Sandoval, T. E.; Hausmann, D. M.; Kessels, W. M. M.; Mackus, A. J. M. Mechanism of Precursor Blocking by Acetylacetone Inhibitor Molecules during Area-Selective Atomic Layer Deposition of SiO<sub>2</sub>. *Chem. Mater.* **2020**, *32*, 3335–3345.
- (10) Cao, K.; Cai, J.; Chen, R. Inherently Selective Atomic Layer Deposition and Applications. *Chem. Mater.* **2020**, *32*, 2195–2207.
- (11) Radamson, H. H.; He, X.; Zhang, Q.; Liu, J.; Cui, H.; Xiang, J.; Kong, Z.; Xiong, W.; Li, J.; Gao, J.; Yang, H.; Gu, S.; Zhao, X.; Du, Y.; Yu, J.; Wang, G. Miniaturization of CMOS. *Micromachines* **2019**, *10*, No. 293.
- (12) Pattison, T. G.; Hess, A. E.; Arellano, N.; Lanzillo, N.; Nguyen, S.; Bui, H.; Rettner, C.; Truong, H.; Friz, A.; Topuria, T.; Fong, A.; Hughes, B.; Tek, A. T.; DeSilva, A.; Miller, R. D.; Qiao, G. G.; Wojtecki, R. J. Surface Initiated Polymer Thin Films for the Area Selective Deposition and Etching of Metal Oxides. *ACS Nano* **2020**, *14*, 4276–4288.
- (13) Mohabir, A. T.; Tutuncuoglu, G.; Weiss, T.; Vogel, E. M.; Filler, M. A. Bottom-Up Masking of Si/Ge Surfaces and Nanowire Heterostructures via Surface-Initiated Polymerization and Selective Etching. *ACS Nano* **2020**, *14*, 282–288.
- (14) Wang, M.; Wang, X.; Moni, P.; Liu, A.; Kim, D. H.; Jo, W. J.; Sojoudi, H.; Gleason, K. K. CVD Polymers for Devices and Device Fabrication. *Adv. Mater.* **2017**, *29*, No. 1604606
- (15) Uzunlar, E.; Kohl, P. A. Size-Compatible, Polymer-Based Air-Gap Formation Processes, and Polymer Residue Analysis for Wafer-Level MEMS Packaging Applications. *J. Electron. Packag.* **2015**, *137*, No. 041001.
- (16) Huang, Z.; Wang, P.; Macdiarmid, A. G.; Xia, Y.; Whitesides, G. Selective Deposition of Conducting Polymers on Hydroxyl-Terminated Surfaces with Printed Monolayers of Alkylsiloxanes as Templates. *Langmuir* **1997**, *13*, 6480–6484.

- (17) Vaeth, K. M.; Jensen, K. F. Transition Metals for Selective Chemical Vapor Deposition of Parylene-Based Polymers. *Chem. Mater.* **2000**, *12*, 1305–1313.
- (18) Vaeth, K. M.; Jackman, R. J.; Black, A. J.; Whitesides, G. M.; Jensen, K. F. Use of Microcontact Printing for Generating Selectively Grown Films of Poly(p-Phenylene Vinylene) and Parylenes Prepared by Chemical Vapor Deposition. *Langmuir* **2000**, *16*, 8495–8500.
- (19) Yoshimura, T.; Terasawa, N.; Kazama, H.; Naito, Y.; Suzuki, Y.; Asama, K. Selective Growth of Conjugated Polymer Thin Films by the Vapor Deposition Polymerization. *Thin Solid Films* **2006**, *497*, 182–184.
- (20) Brooke, R.; Evans, D.; Dienel, M.; Hojati-Talemi, P.; Murphy, P.; Fabretto, M. Inkjet Printing and Vapor Phase Polymerization: Patterned Conductive PEDOT for Electronic Applications. *J. Mater. Chem. C* **2013**, *1*, 3353–3358.
- (21) O’Connell, C. D.; Higgins, M. J.; Nakashima, H.; Moulton, S. E.; Wallace, G. G. Vapor Phase Polymerization of EDOT from Submicrometer Scale Oxidant Patterned by Dip-Pen Nanolithography. *Langmuir* **2012**, *28*, 9953–9960.
- (22) Prasittichai, C.; Zhou, H.; Bent, S. F. Area Selective Molecular Layer Deposition of Polyurea Films. *ACS appl. Mater. Interfaces* **2013**, *5*, 13391–13396.
- (23) Bally-Le Gall, F.; Friedmann, C.; Heinke, L.; Arslan, H.; Azucena, C.; Welle, A.; Ross, A. M.; Wöll, C.; Lahann, J. Free-Standing Nanomembranes Based on Selective CVD Deposition of Functional Poly-p-Xylylenes. *ACS Nano* **2015**, *9*, 1400–1407.
- (24) Yu, X.; Bobb-Semple, D.; Oh, I. K.; Liu, T. L.; Closser, R. G.; Trevillyan, W.; Bent, S. F. Area-Selective Molecular Layer Deposition of a Silicon Oxycarbide Low-k Dielectric. *Chem. Mater.* **2021**, *33*, 902–909.

- (25) Junige, M.; George, S. M. Area-Selective Molecular Layer Deposition of Nylon 6,2 Polyamide: Growth on Carbon and Inhibition on Silica. *J. Vac. Sci. Technol. A* **2021**, *39*, No. 023204.
- (26) Zhang, C.; Vehkamäki, M.; Pietikäinen, M.; Leskelä, M.; Ritala, M. Area-Selective Molecular Layer Deposition of Polyimide on Cu through Cu-Catalyzed Formation of a Crystalline Interchain Polyimide. *Chem. Mater.* **2020**, *32*, 5073–5083.
- (27) Zhang, Y.; Discekici, E. H.; Burns, R. L.; Somervell, M. H.; Hawker, C. J.; Bates, C. M. Single-Step, Spin-on Process for High Fidelity and Selective Deposition. *ACS Appl. Polym. Mater.* **2020**, *2*, 481–486.
- (28) Lock, J. P.; Im, S. G.; Gleason, K. K. Oxidative Chemical Vapor Deposition of Electrically Conducting Poly(3,4-Ethylenedioxythiophene) Films. *Macromolecules* **2006**, *39*, 5326–5329.
- (29) Moni, P.; Lau, J.; Mohr, A. C.; Lin, T. C.; Tolbert, S. H.; Dunn, B.; Gleason, K. K. Growth Temperature and Electrochemical Performance in Vapor-Deposited Poly(3,4-Ethylenedioxythiophene) Thin Films for High-Rate Electrochemical Energy Storage. *ACS Appl. Energy Mater.* **2018**, *1*, 7093–7105.
- (30) Wang, X.; Zhang, X.; Sun, L.; Lee, D.; Lee, S.; Wang, Mi.; Zhao, J.; Shao-Horn, Y.; Dinca, M.; Palacios, T.; Gleason, K. K. High Electrical Conductivity and Carrier Mobility in oCVD PEDOT Thin Films by Engineered Crystallization and Acid Treatment. *Sci. Adv.* **2018**, *4*, No. eaat5780.
- (31) Im, S. G.; Kusters, D.; Choi, W.; Baxamusa, S. H.; van de Sanden, M. C. M.; Gleason, K. K. Conformal Coverage of Poly(3,4-Ethylenedioxythiophene) Films with Tunable Nanoporosity. *ACS Nano* **2008**, *2*, 1959–1967.

- (32) Chelawat, H.; Vaddiraju, S.; Gleason, K. Conformal, Conducting Poly(3,4-Ethylenedioxythiophene) Thin Films Deposited Using Bromine as the Oxidant in a Completely Dry Oxidative Chemical Vapor Deposition Process. *Chem. Mater.* **2010**, *22*, 2864–2868.
- (33) Kaviani, S.; Mohammadi Ghaleni, M.; Tavakoli, E.; Nejati, S. Electroactive and Conformal Coatings of Oxidative Chemical Vapor Deposition Polymers for Oxygen Electroreduction. *ACS Appl. Polym. Mater.* **2019**, *1*, 552–560.
- (34) Atanasov, S. E.; Losego, M. D.; Gong, B.; Sachet, E.; Maria, J. P.; Williams, P. S.; Parsons, G. N. Highly Conductive and Conformal Poly(3,4-Ethylenedioxythiophene) (PEDOT) Thin Films via Oxidative Molecular Layer Deposition. *Chem. Mater.* **2014**, *26*, 3471–3478.
- (35) Volk, A. A.; Kim, J.-S.; Jamir, J.; Dickey, E. C.; Parsons, G. N. Oxidative Molecular Layer Deposition of PEDOT Using Volatile Antimony(V) Chloride Oxidant. *J. Vac. Sci. Technol. A* **2021**, *39*, No. 032413.
- (36) Sauerbrey, G. The Use of Quarts Oscillators for Weighing Thin Layers and for Microweighing. *Z. Phys.* **1959**, *155*, 206–222.
- (37) Pettersson, L. A. A.; Carlsson, F.; Inganäs, O.; Arwin, H. Spectroscopic Ellipsometry Studies of the Optical Properties of Doped Poly(3,4-Ethylenedioxythiophene): An Anisotropic Metal. *Thin Solid Films* **1998**, *313–314*, 356–361.
- (38) Parsons, G. N. Functional Model for Analysis of ALD Nucleation and Quantification of Area-Selective Deposition. *J. Vac. Sci. Technol. A* **2019**, *37*, No. 020911.
- (39) Putkonen, M.; Harjuoja, J.; Niinisto, L. Atomic Layer Deposition of Polyimide Thin Films. *J. Mater. Chem.* **2007**, *17*, 664–669.
- (40) Du, Y.; George, S. M. Molecular Layer Deposition of Nylon 66 Films Examined Using in Situ FTIR Spectroscopy. *J. Phys. Chem. C* **2007**, *111*, 8509–8517.

- (41) Nye, R. A.; Kelliher, A. P.; Gaskins, J. T.; Hopkins, P. E.; Parsons, G. N. Understanding Molecular Layer Deposition Growth Mechanisms in Polyurea via Picosecond Acoustics Analysis. *Chem. Mater.* **2020**, *32*, 1553–1563.
- (42) Saare, H.; Song, S. K.; Kim, J.-S.; Parsons, G. N. Effect of Reactant Dosing on Selectivity during Area-Selective Deposition of TiO<sub>2</sub> via Integrated Atomic Layer Deposition and Atomic Layer Etching. *J. Appl. Phys.* **2020**, *128*, No. 105302
- (43) Song, S. K.; Kim, J.; Margavio, H. R. M.; Parsons, G. N. Multimaterial Self-Aligned Nanopatterning by Simultaneous Adjacent Thin Film Deposition and Etching. *ACS Nano* **2021**, *15*, 12276–12285.
- (44) Kalanyan, B.; Lemaire, P. C.; Atanasov, S. E.; Ritz, M. J.; Parsons, G. N. Using Hydrogen to Expand the Inherent Substrate Selectivity Window during Tungsten Atomic Layer Deposition. *Chem. Mater.* **2016**, *28*, 117–126.
- (45) Fitch, J. T.; Denning, D. J.; Beard, D. The Pattern Dependence of Selectivity in Low Pressure Selective Epitaxial Silicon Growth. *J. Electron. Mater.* **1992**, *21*, 455–462.
- (46) Roine, A.; Kotiranta, T.; Eerola, H.; Lamberg, P. *HSC Chemistry, Version 7.1*. Otkukumpu Research Oy, Pori **2002**.
- (47) Gladfelter, W. L. Selective Metallization by Chemical Vapor Deposition. *Chem. Mater.* **1993**, *5*, 1372–1388.

## Chapter 4 Area-Selective Deposition of Conjugated Polymers

### 4.1 Abstract

Area-selective deposition (ASD) plays an important role for advanced electronic devices by using bottom-up self-aligned deposition. Specifically, ASD of organic materials can be utilized for nucleation inhibitors, sacrificial layers, and air-gap materials for next-generation nanoscale processing. This work introduces fundamental growth behavior of various conjugated polymers including polypyrrole, polythiophene and polyaniline *via* oxidative molecular layer deposition and chemical vapor deposition. Effects of process parameters on film properties are described and ASD behavior of different polymers are quantitatively characterized. This finding offers a fundamental understanding of conjugated polymer depositions and a new perspective for developing organic ASD capabilities.

### 4.2 Introduction

Area-selective deposition (ASD) of polymers provides high-quality organic films with nano-scale thickness precision. ASD of polymers can be generally obtained by chemical vapor deposition (CVD) and molecular layer deposition (MLD). Selective polymer deposition is based on chemical specificity led by substrate-dependent physical or chemical adsorption. Since the smallest feature size of the semiconductor transistor approaches 5 nm regime, ASD of various organic materials can be one of the promising candidates to overcome the limitation of the current photolithographic alignments. Specifically, selectively deposited organic films can serve as nucleation inhibitors, blocking masks, air-gap materials, and low-k materials to address the critical dimension error, line-edge roughness, chemical mechanical polishing overburden, and high cost of extreme ultraviolet (EUV) processes.<sup>1-7</sup>

In a range of fields including nano-electronics,<sup>8-11</sup> biomaterials,<sup>12,13</sup> and catalyst,<sup>14,15</sup> ASD of polymers has been investigated. Previous ASD of polymers include poly(p-phenylene vinylene)(PPV), parylene N, parylene C on hydroxyl silicon oxide (Si-OH) vs. transition metals, and poly(azomethine) on Si-OH vs. hydrogen-terminated silicon (Si-H) by CVD processes.<sup>10,11,16</sup> ASD of polyurea,<sup>17,18</sup> poly-p-xylylene,<sup>13</sup> silicon oxycarbide (SiCO),<sup>4</sup> poly(3,4-ethylenedioxythiophene) (PEDOT),<sup>1</sup> polyimide<sup>19</sup> and polyamide<sup>2</sup> was demonstrated *via* MLD processes by passivating the non-growth surface with organic inhibitors. In **Chapter 3**, inherent PEDOT ASD was achieved on Si-OH vs. Si-H using 3,4-ethylenedioxythiophene (EDOT) monomer and antimony pentachloride (SbCl<sub>5</sub>) using oxidative MLD and CVD processes. Significant improved ASD of PEDOT can be obtained by CVD (~30 nm) vs. MLD (~8 nm) as shown in **Figure 3.4-6** due to the fast reaction by CVD processes. This result indicates that similar ASD could be achieved for different conjugated polymers using the oxidative polymerization with different monomers and the same oxidant (SbCl<sub>5</sub>). This work shows ASD of various conjugated polymers including polypyrrole (PPY), polyaniline (PANI), and polythiophene (PTH). ASD is compared using MLD and CVD processes, providing the comparative studies of monomer effects on ASD of conjugated polymers.

## 4.3 Experimental Section

### 4.3.1 Substrate preparation

Boron-doped Si (100) 6-10  $\Omega\cdot\text{cm}$  was used for substrates. The Si wafers were cleaned by piranha solution (H<sub>2</sub>O<sub>2</sub>:H<sub>2</sub>SO<sub>4</sub>=1:1 volumetric ratio) for 15 min, rinsed with deionized (DI) water, and dried with N<sub>2</sub> gas. To prepare for hydrogen-terminated Si (Si-H), piranha-cleaned Si wafers

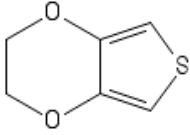
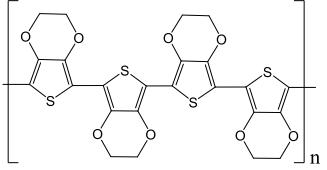
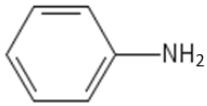
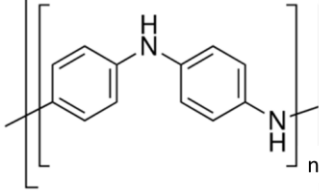
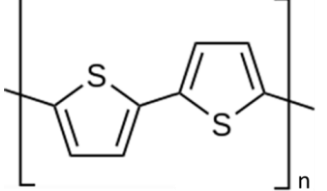
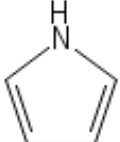
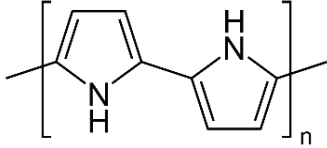
were dipped for 30 s in dilute hydrofluoric acid (HF, 5 vol%, Sigma-Aldrich), followed by DI rinsing, and dried with N<sub>2</sub> gas.

#### 4.3.2 Reactor and Process Sequence

Conjugated polymer deposition was conducted in a home-built tubular hot-walled isothermal viscous-flow ALD reactor of 60 cm length and 4 cm diameter under constant temperature (25 – 250 °C) using PID controllers shown in **Figure 2.1**. High purity nitrogen (>99.999 %, Arc3 Gases) was used for purge gas and purified using an inert gas filter (Gate-Keeper, Entegris). The base pressure of the reactor (WALDO) was 20-30 mTorr and the working pressure was 1 Torr with a carrier gas flow rate of 135 standard cubic centimeters per minute (sccm).

The EDOT (3,4-ethylenedioxythiophene, 97%, Alfa Aesar), aniline (99.8%, Fisher Scientific), pyrrole (98%, Sigma-Aldrich), thiophene (99%, Sigma-Aldrich) monomers and antimony pentachloride (SbCl<sub>5</sub>, 99%, Alfa Aesar) were used as received without further purification. All materials were transferred into glass and stainless-steel vessels in a nitrogen-purged glovebox. **Table 4.1** shows the basic chemical information of monomers.

**Table 4.1** Basic chemical properties of different monomers.

	Molecular weight (g·mol <sup>-1</sup> )	Vapor pressure (Torr at 25 °C)	Monomer Structure	Polymer Structure
EDOT	142.2	0.28		
Aniline	93.1	0.73		
Thiophene	84.1	81.7		
Pyrrole	67.1	12.2		

Considering that the vapor pressure of aniline is 0.73 Torr at 25 °C which is similar to EDOT, the aniline monomer was heated between 40 – 80 °C with direct flow over of N<sub>2</sub> gas: EDOT monomer was heated at 80 °C with a bubbler setup to boost the delivery of the monomer. Pyrrole and thiophene were delivered at room temperature with direct flow over of N<sub>2</sub> gas due to the high vapor pressure. All ALD processes were controlled by a custom LABVIEW program.

Before the film deposition, sample substrates were loaded into the reactor for 30 min to reach the thermal equilibrium with the chamber temperature. Note that for the  $\text{SbCl}_5$ , the heating temperature varied between 40 and 50 °C and even at the same heating temperature, the actual dose of the  $\text{SbCl}_5$  was dependent on the reactivity of the oxidant; therefore, a very careful control is needed to deliver a consistent dose of the  $\text{SbCl}_5$  reactant.

#### 4.3.3 Characterization Methods

In-situ quartz crystal microbalance (QCM) was used to understand the growth behavior. 6 MHz gold-coated crystal (Inficon) was used with a QCM probe body (Kurt Lesker) and a control box (TM-400, Maxtek). Before the measurement, the QCM probe was loaded into a reactor under a steady  $\text{N}_2$  flow at least 120 min for stabilization.  $\text{N}_2$  back-side purge was used to protect the rear side of electrical contact with 42.5 sccm of  $\text{N}_2$  flow. The measured resonant frequency of the crystal was converted to mass change per an active surface area ( $\text{ng}/\text{cm}^2$ ) using the Sauerbrey equation.<sup>20,21</sup> For the data conversion, MATLAB was used to calculate the net mass gain per cycle (CVD time). The thickness of conjugated polymers was measured by ex situ spectroscopic ellipsometry (SE,  $\alpha$ -SE ellipsometer, J.A. Woollam) with an incidence angle of 70 ° and a spectral range of 300–900 nm. Given that the structure of PPY, PANI, and PTH is analogous to PEDOT (conjugated polymer), the same SE model used for PEDOT in **Chapter 3** was employed for fitting. X-ray photoelectron spectroscopy (XPS, Kratos Analytical Axis Ultra) with an Al  $K\alpha$  (1486.6 eV) gun was used to analyze the chemical composition of the films. Peak positions were calibrated by referencing the adventitious C 1s peak to 285.0 eV. The sheet resistance ( $R_s$ ,  $\Omega/\square$ ) of the film was measured with a four-point-probe (RM 3-AR, Jandell) with 1 mm probe spacing ( $s = 1$  mm). The sample size is  $\sim 1$  cm x 1 cm ( $d = 1$  cm) and the correction factor of 4.5324 with  $V/I$  was used to

calculate the sheet resistance. Note that for more accurate correction factor, the relationship between the film thickness ( $t$ ), the probe spacing ( $s$ ), and sample size ( $d$ ) should be considered.<sup>22,23</sup> Fourier transform infrared spectroscopy (FTIR, Nicolet 6700 FT-IR, Thermos Scientific) with a deuterated triglycine sulfate detector was used to characterize the film composition. The measurements were operated in transmission mode with 200 scans at  $4\text{ cm}^{-1}$  resolution from 4000 to  $400\text{ cm}^{-1}$  with a dry air purge.

#### 4.4 Results and Discussion

Polypyrrole (PPY), polythiophene (PTH), and polyaniline (PANI) were deposited by using pyrrole, thiophene, and aniline monomers with the  $\text{SbCl}_5$  oxidant through MLD and CVD processes. The basic growth behavior of PPY, PTH and PANI is described, and ASD properties are characterized.

##### 4.4.1 Polypyrrole deposition

Based on PEDOT ASD on Si-OH vs. Si-H surfaces in **Chapter 3**, a growth of polypyrrole (PPY) was tested using pyrrole monomer and  $\text{SbCl}_5$  oxidant. QCM was used for confirming the growth by CVD process in which the monomer and  $\text{SbCl}_5$  were simultaneously delivered. **Figure 4.1** shows the mass uptake for the PPY growth by CVD for 60 s. As a control experiment, the mass changes during only pyrrole or  $\text{SbCl}_5$  dose are also shown. While no mass change is observed for the pyrrole dose, slight mass increase of  $\sim 50\text{ ng/cm}^2$  is measured for the  $\text{SbCl}_5$  dose, led by the physisorption of the oxidant on the surface. Compared to the control experiment, the big mass increase of  $\sim 12000\text{ ng/cm}^2$  is obtained during the PPY CVD growth. Immediately after the doses

of the reactants, the unreacted reactants were removed by the purging gas, showing gradual mass decrease and after 120 s of the purge, the mass change reaches plateau.

The effect of reactant dose time on net film growth was studied for MLD processes at 125 °C. In this test, the  $\text{SbCl}_5$  and pyrrole source were held at 50 and 25 °C, respectively and the thickness of PPY films on Si-OH substrates were measured by SE. Data in **Figure 4.2a** corresponds to various  $\text{SbCl}_5$  dose conditions :  $\text{SbCl}_5/\text{N}_2/\text{Pyrrole}/\text{N}_2 = x/10/2.0/10$  s for 200 cycles, with  $x$  adjusted between 0 and 4.0 s and **Figure 4.2b** corresponds to various pyrrole dose conditions:  $\text{SbCl}_5/\text{N}_2/\text{Pyrrole}/\text{N}_2 = 1.0/10/x/10$  s for 200 cycles, with  $x$  adjusted between 0 and 4.0 s. **Figure 4.2c** displays that increasing purge times decrease the net growth rate. Considering that the reaction of oxidative conjugated polymer relies on the physisorption of  $\text{SbCl}_5$  oxidant on the surface, the physisorbed  $\text{SbCl}_5$  oxidant would be gradually desorbed with the longer purge time, resulting in lower net growth rate. The effect of the reactant dose times on PPY growth illustrates that the PPY growth is soft-saturated behavior: in particular, the  $\text{SbCl}_5$  dose time and the purge time are critically important to determine the net growth rate. Even though the results on **Figure 4.2a,b** seem to be saturated, the growth rate largely changed with different purge time and  $\text{SbCl}_5$  dose time. In general, the growth behavior of conjugated polymers studied here (PEDOT, PPY, PANI and PTH) by vapor-based oxidation polymerization using the  $\text{SbCl}_5$  oxidant exhibited similar trend, implying that controlling of the  $\text{SbCl}_5$  dose is a key factor to achieve more reproducible results. One condition was used to observe the growth as a function of MLD cycles in **Figure 4.2d**:  $\text{SbCl}_5/\text{N}_2/\text{Pyrrole}/\text{N}_2 = 1.0/10/2.0/10$  s at 125 °C. The result exhibits the linear growth rate of 0.6 Å/cycle.

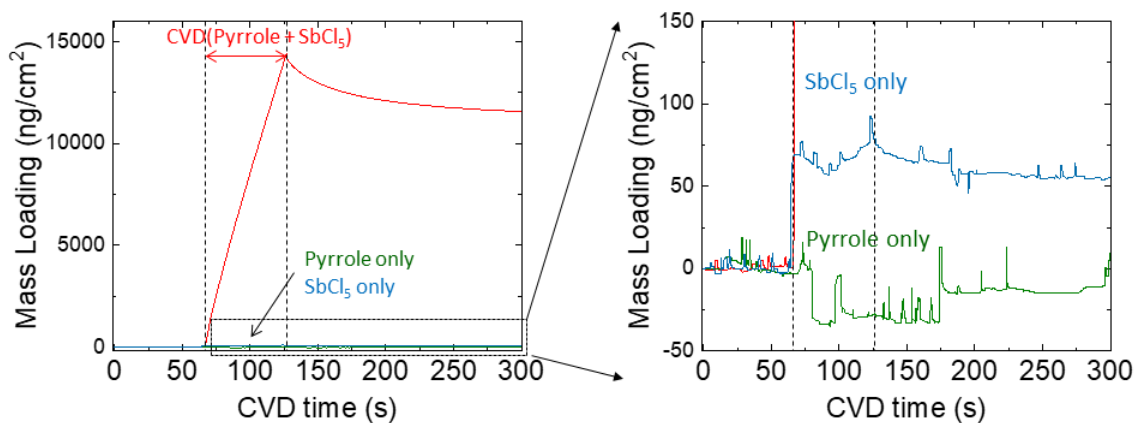


**Figure 4.1** Quartz crystal microbalance mass uptake during PPY CVD process using pyrrole and  $\text{SbCl}_5$  at  $175\text{ }^\circ\text{C}$ . As a control experiment, the mass uptake was measured during only dose of pyrrole or  $\text{SbCl}_5$ , indicating no noticeable mass change during separate dose of the reactant.

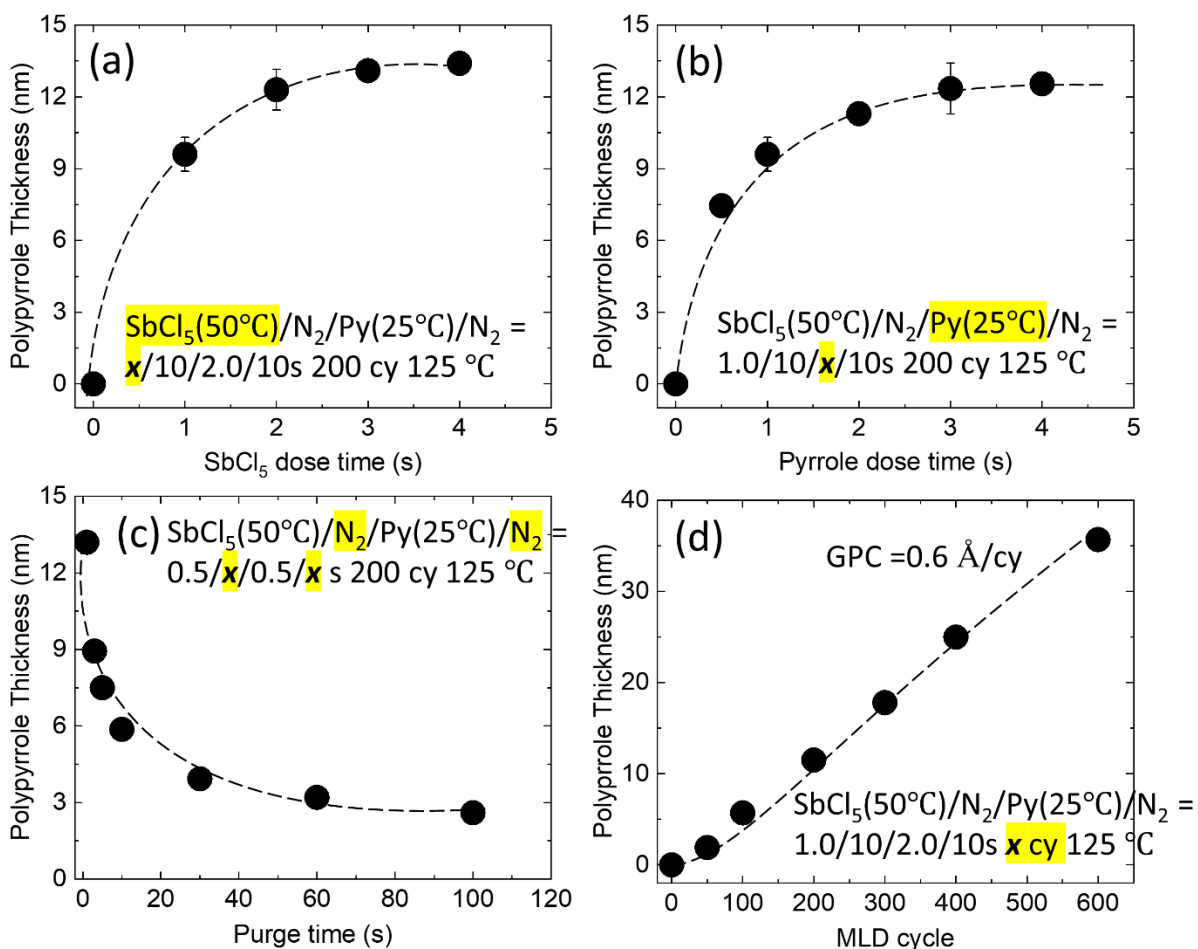


**Figure 4.2** The effect of reactant dose times of (a) SbCl<sub>5</sub> and (b) Pyrrole on the growth rate of PPY deposited on Si-OH at 125 °C. Pyrrole dose was held constant 2 s for (a) and SbCl<sub>5</sub> dose time was held constant at 1 s for (b). The effect of purge time on the growth rate of PPY. PPY thickness at 125 °C as a function of MLD cycles on Si-OH. SbCl<sub>5</sub> and pyrrole doses were held constant at 0.5 and 0.5 for (c), and 1 and 2 s for (d), respectively. All thicknesses were measured by spectroscopic ellipsometry and the error bar was from multiple sets average. Lines were drawn as guides to the eye.

**Figure 4.3** displays the temperature dependence of PPY growth on Si-OH by MLD and CVD processes. MLD and CVD processes were conducted in the same reactor, and the only difference between MLD and CVD processes is whether the reactants were delivered separately (MLD) or simultaneously (CVD). The condition of MLD experiment was  $\text{SbCl}_5/\text{N}_2/\text{Pyrrole}/\text{N}_2 = 1.0/10/2.0/10$  s with varied MLD cycle and temperature. The thickness of PPY films on Si-OH significantly decreases with increasing MLD temperature in **Figure 4.3a**. This phenomenon is widely reported in MLD processes, ascribed to faster monomer desorption at higher temperatures.<sup>1,24-28</sup> Furthermore, the  $\text{SbCl}_5$  oxidant would be decomposed at higher temperatures. From this regard, the lower growth rate of PPY with increasing temperatures can be explained by both pyrrole monomer desorption and  $\text{SbCl}_5$  decomposition. For the CVD processes, the deposition time was fixed at 15 s with various temperatures. **Figure 4.3b** shows that plateau growth is observed between 100 and 200 °C, whereas the growth rate rapidly decreases at 25 and 300 °C. This is associated with fast condensation reaction at 25 °C where most of reactants would be reacted near the inlet of the reactor and fast desorption of the reactants at higher temperatures where no reaction occurs. **Figure 4.3c** indicates the substrate boat used. Note that the size of the main chamber (60 cm length and 4 cm diameter) and the boat (30 cm length and 2 cm width). For each run, three set of samples were loaded with distance of 9 cm to study the thickness gradient of the reaction. In **Figure 4.3b**, the error bar at lower chamber temperatures increases, suggesting that the condensation reaction becomes dominant with decreasing temperature. In order to obtain more uniform growth with higher net growth rate, 150 – 200 °C would be reasonable for PPY deposition *via* CVD.

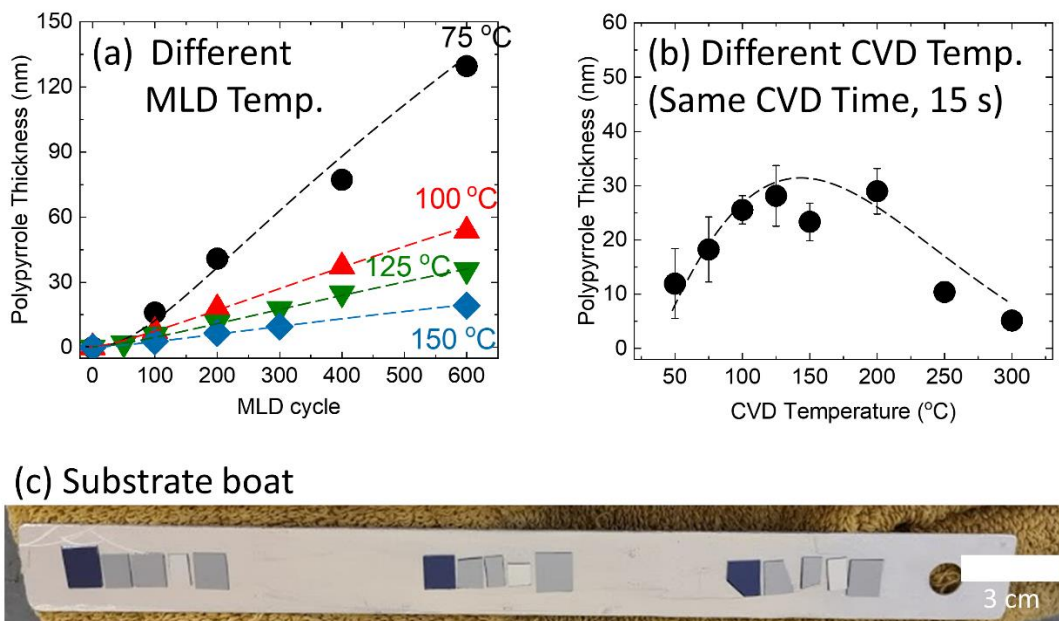


**Figure 4.3** (a) PPY film thickness as a function of MLD deposition temperature on Si-OH using  $\text{SbCl}_5/\text{N}_2/\text{Pyrrole}/\text{N}_2 = 1.0/10/2.0/10$  s. (b) PPY film thickness as a function of CVD deposition temperature on Si-OH. The CVD deposition time and the working pressure were held at 15 s and 1 Torr, respectively. For both MLD and CVD processes, the  $\text{SbCl}_5$  and pyrrole source temperatures were held at 50 and 25 °C, respectively. (c) Three samples were loaded with distance of 9 cm to test the thickness gradient of the reactor. All thicknesses were measured by spectroscopic ellipsometry and the error bar was from multiple sets average. Lines were drawn as guides to the eye.

FTIR was used to confirm the film composition by MLD and CVD at different temperatures as shown in **Figure 4.4**. To clearly observe the signal of the film out of the Si-OH substrate, all the spectra were normalized by the Si-Si peak at  $610\text{ cm}^{-1}$  which is the largest peak and subtracted to the spectrum of bare Si-OH. The spectra of film deposition at lower temperatures

(50-125 °C) exhibit characteristic PPY peaks including the bands at 1548, 1477, 1290, 1189, 1045, and 911  $\text{cm}^{-1}$ .<sup>29-31</sup> The bands at 1548 and 1477  $\text{cm}^{-1}$  are corresponding to C-C stretching vibrations and C-N stretching vibrations of the pyrrole rings, respectively. The band at 1290  $\text{cm}^{-1}$  is attributed to C-H or C-N in-plane deformation modes. The peak at 1189  $\text{cm}^{-1}$  indicates the presence of breathing vibrations of the pyrrole rings. C-H and N-H in-plane deformation vibrations are observed at 1045  $\text{cm}^{-1}$ . The peak at 911  $\text{cm}^{-1}$  is due to C-H out-of-plane deformation vibrations of the ring. With increasing temperatures, the PPY peaks becomes gradually smaller, illustrating that the structure of the PPY films changed.

**Figure 4.4a** shows the photographic image of profilometer measurement. To verify the accuracy of the thickness data measured by SE, the profilometer was used. Step height was made by removing the PPY films from the Si substrate with the end of a tweezer. While the smooth step curve is observed for PPY film deposited at 50 °C by CVD, no step height is observed for PPY films deposited at 150 °C. This is due to the higher adhesion between deposited PPY films and Si substrates at higher temperature, which is associated with the structure change observed in FTIR spectra in **Figure 4.3**. **Table 4.2** indicates that the thickness of PPY films by CVD at 50 °C measured is 38.3 nm, consistent with the thickness of 33.6 nm measured by profilometer. In addition, the conductivity of the PPY film at lower temperature (50 °C) is 18 S/cm, whereas the conductivity of PPY film deposited at higher temperature (150 °C) is out of range. This is related to the structure change in the band between 1600 – 900  $\text{cm}^{-1}$  in the IR spectra. IR spectra also show that the background of absorption near 4000 – 2000  $\text{cm}^{-1}$  for conductive PPY films is higher than non-conductive films.<sup>30</sup> This could be due to the electron scattering (Drude model) at higher vibration energy.

**Figure 4.6** and **Table 4.3** show high resolution scan of C 1s, N 1s, Cl 2p and Sb 3d/O 1s for PPY films by CVD at different temperatures. Peak positions were calibrated by using the adventitious C 1s peak to 285.0 eV. For a peak deconvolution between O 1s, Sb 3d<sub>5/2</sub>, and Sb 3d<sub>3/2</sub>, Sb 3d<sub>5/2</sub> and 3d<sub>3/2</sub> peaks were separated by 9.34 eV with a relative intensity of 3 to 2. No noticeable change is observed for C 1s, N 1s and Sb 3d peaks at different temperatures in terms of peak shifts and atomic composition except relatively higher Sb ratio for the film deposited at 50 °C. Cl 2p peaks show a significant intensity decrease of Cl 2p<sub>3/2</sub> at 198 eV with increasing deposition temperatures, suggesting that Cl<sup>-</sup> concentration decreases.<sup>32,33</sup> This is consistent with FTIR and conductivity results in **Figure 4.4** and **Table 4.2**.

The surface roughness of PPY films on Si-OH was characterized by AFM. Compared to RMS of bare Si-OH (0.13 nm), the PPY films are conformal (RMS = 0.33 - 2.51 nm) in **Table 4.3**. The largest RMS value (2.51 nm) is obtained for PPY films deposited by CVD at 25 °C, suggesting that the fast condensation reaction becomes dominant with decreasing temperature.

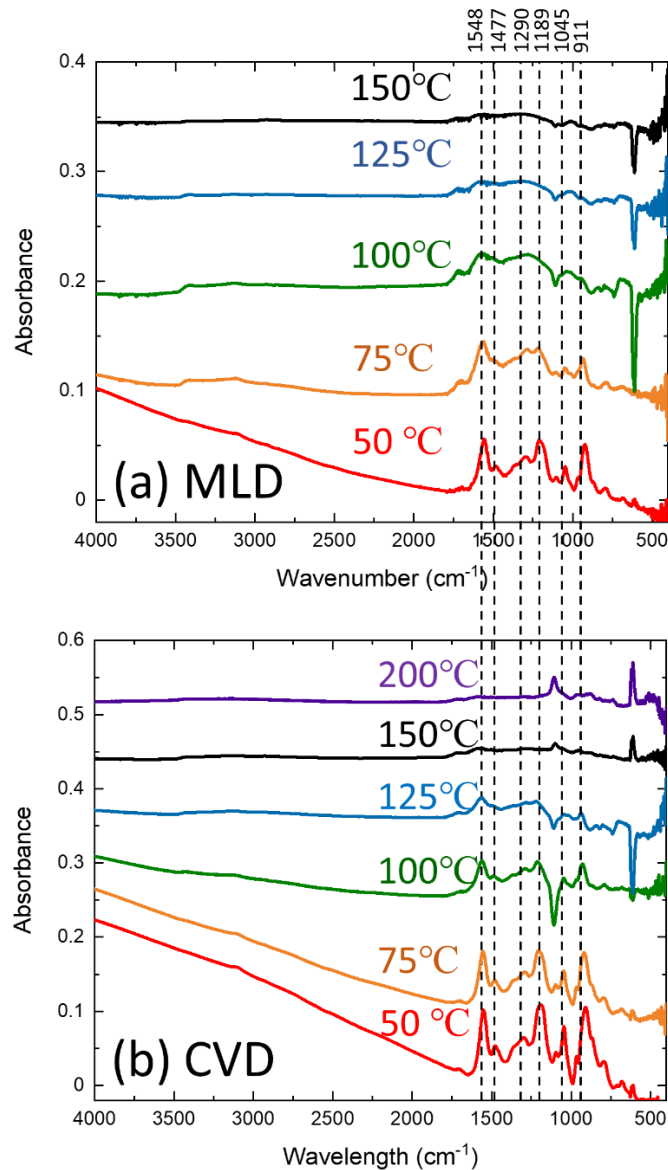


**Figure 4.4** FTIR spectra of PPY on double-side polished Si-OH at different (a) MLD temperatures and (b) CVD temperatures. All the spectra were normalized by the Si-Si peak ( $\sim 610\text{ cm}^{-1}$ ) and subtracted to the bare Si-OH spectra. MLD samples were deposited following  $\text{SbCl}_5/\text{N}_2/\text{Py}/\text{N}_2 = 1.0/10/2.0/10\text{s}$ . Same samples were measured for **Figure 4.4, 6 and 7**.

**Table 4.2** The conductivity and thickness of PPY films by CVD at 50 and 150 °C. For the thickness measurement, SE and profilometer were compared.

	PPY CVD 50 °C	PPY CVD 150 °C
Conductivity (S/cm)	18	Out of range
Thickness by SE (nm)	$38.3 \pm 1.5$	N/A
Thickness by profilometer (nm)	$33.6 \pm 1.8$	Can't measure

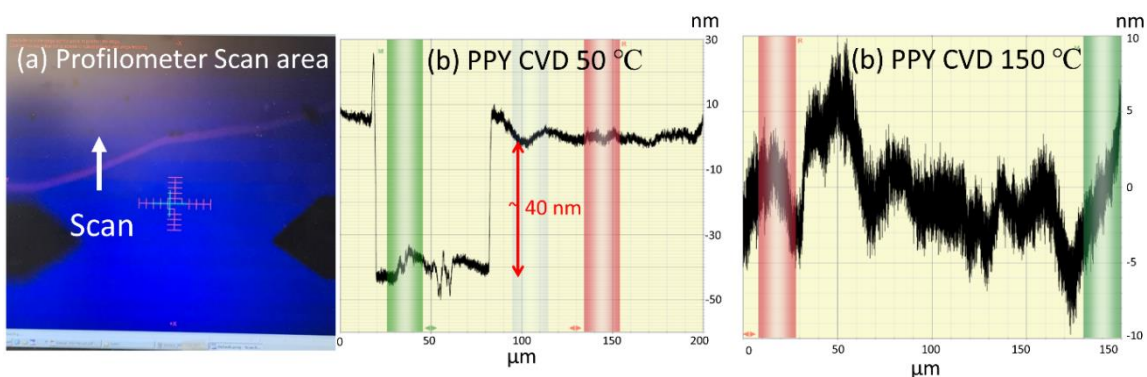


**Figure 4.5** (a) Snapshot of profilometer scan region, and step height measured by profilometer of (a) PPY CVD at 50 °C and (b) PPY CVD at 150 °C. Step height was made by scratching the surface with the tweezers. Panel (b) shows a clear step height whereas panel (c) shows no step height due to the strong adhesion of deposited film on the substrate.

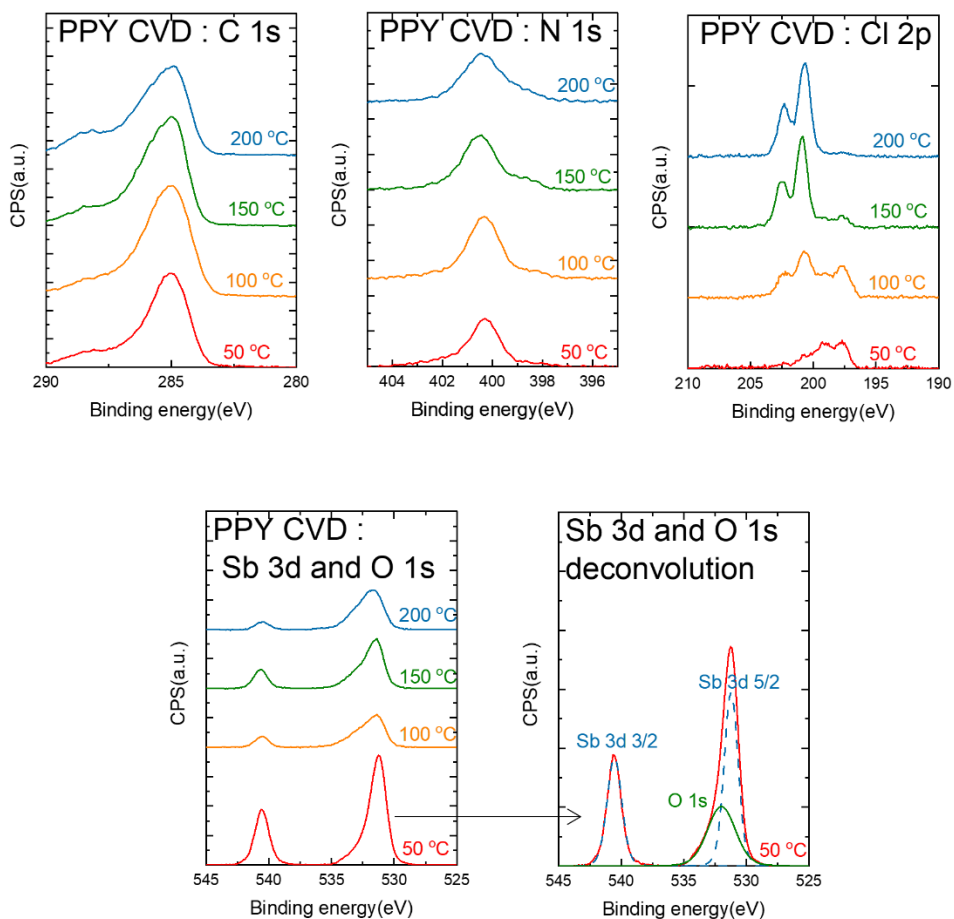


**Figure 4.6** High resolution XPS scans of C 1s, N 1s, Cl 2p, and Sb 3d/O 1s after PPY deposition on Si-OH at different CVD temperatures. For a peak deconvolution of Sb 3d and O 1s, a peak distance of 9.34 eV and a relative intensity of 1.5 between Sb 3d<sub>5/2</sub> and Sb3d<sub>3/2</sub> were used.

**Table 4.3** Elemental composition from XPS analysis and RMS values from AFM results for PPY on Si-OH with various MLD and CVD temperatures. XPS values are given in atomic %.

Depo. condition	Cl 2p	C 1s	Si 2p	N 1s	Sb 3d <sub>5/2</sub>	O 1s	RMS (nm)
18 nm MLD 50 °C	3.94	62.13	0.77	10.76	4.43	17.96	0.58 ± 0.05
47 nm MLD 100 °C	8.52	67.08	0.00	12.58	1.76	10.07	0.33 ± 0.00
14 nm MLD 150 °C	11.7	63.35	0.81	12.76	0.81	10.57	0.41 ± 0.02
45 nm CVD 50 °C	2.48	62.18	0.00	10.37	5.10	19.87	2.51 ± 0.27
48 nm CVD 100 °C	4.36	70.38	0.00	12.19	0.83	12.24	0.75 ± 0.05
42 nm CVD 150 °C	4.18	67.89	0.00	12.11	1.47	14.35	0.56 ± 0.05
21 nm CVD 200 °C	4.57	63.96	0.00	12.32	0.63	18.51	0.41 ± 0.01

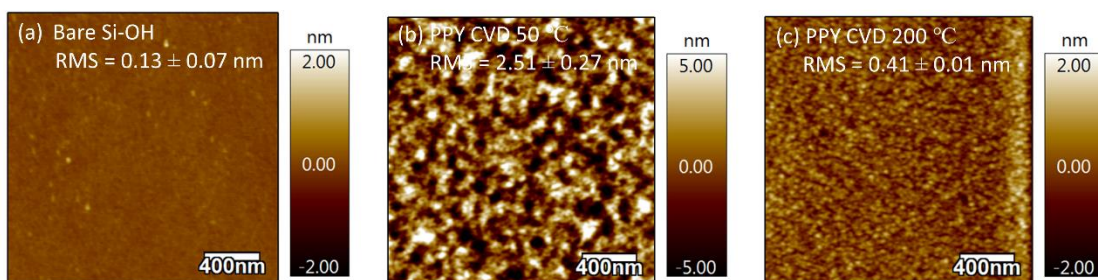


**Figure 4.7** AFM images of (a) bare Si-OH, PPY deposited on Si-OH by CVD processes at (b) 50 °C and (c) 200 °C. Each RMS value is the average of three different measurements.

#### 4.4.2 Polythiophene Deposition

Polythiophene (PTH) was deposited by using thiophene (TH) monomer and  $\text{SbCl}_5$  oxidant. **Figure 4.8a, b** show the thickness of PTH as a function of MLD cycles and CVD times. The MLD process followed:  $\text{SbCl}_5/\text{N}_2/\text{Thiophene}/\text{N}_2 = 0.5/1.0/0.1/1.0$  s. The PTH deposition exhibits highly temperature dependent growth: above room temperature, no deposition is observed for both MLD and CVD processes.<sup>34</sup> This would be due to the fast desorption rate of the thiophene monomer at higher temperatures. Likewise, more desorption occurs with longer purge time, observing less net deposition with increasing the purge time.

**Figure 4.9** and **Table 4.4** display XPS results of a PPY film by CVD for 45 s. Similar to the Sb 3d/O 1s deconvolution of PPY films, the same split conditions were used. Considering the thickness of PTH (15 nm), the small silicon intensity of 1.27 at% is measured. The PTH film shows good conformality (RMS = 0.41 nm) and high resistivity (out of range measured by four-point-probe). This is also confirmed by the absence of  $\text{Cl}^-$  on the Cl 2p in **Figure 4.9**.

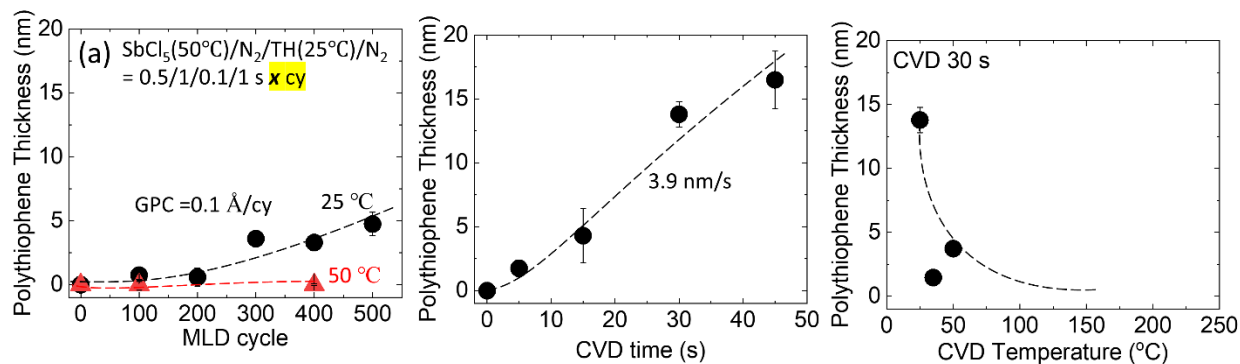


**Figure 4.8** (a) Polythiophene (PTH) thickness as a function of MLD cycles on Si-OH at 25 and 50 °C. The MLD sequence followed:  $\text{SbCl}_5(50^\circ\text{C})/\text{N}_2/\text{thiophene}(25^\circ\text{C})/\text{N}_2 = 0.5/1.0/0.1/1.0$  s. (b) PTH thickness as a function of CVD time on Si-OH at 25 °C. (c) The effect of CVD temperatures on PTH thickness after 30 s of CVD process time. All thicknesses were measured by spectroscopic ellipsometry and the error bar was from multiple sets average. Lines were drawn as guides to the eye.

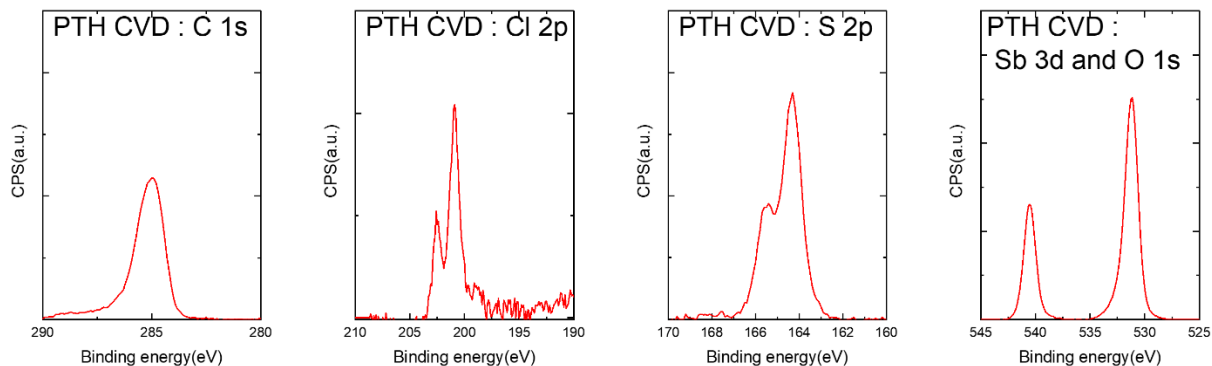


**Figure 4.9** High resolution XPS scans of C 1s, Cl 2p, S 2p and Sb 3d/O 1s after PTH deposition on Si-OH at 25 °C. For a peak deconvolution of Sb 3d and O 1s, a peak distance of 9.34 eV and a relative intensity of 1.5 between Sb 3d<sub>5/2</sub> and Sb3d<sub>3/2</sub> were used.

**Table 4.4** Elemental composition from XPS analysis and RMS values from AFM results for PTH on Si-OH at 25 °C by CVD. XPS values are given in atomic %.

Deposition condition	Cl 2p	C 1s	Si 2p	S 2p	Sb 3d <sub>5/2</sub>	O 1s	RMS (nm)
15 nm PTH CVD 25 °C	2.16	52.46	1.27	10.16	8.80	25.15	0.41 ± 0.08

#### 4.4.3 Polyaniline Deposition

Polyaniline (PANI) was deposited by using aniline (Ani) monomer and SbCl<sub>5</sub> oxidant. In comparison with pyrrole and thiophene monomers which were held at room temperature, the aniline monomer was heated between 40-80 °C with direct flow over of N<sub>2</sub> gas. **Figure 4.10a** displays the purge time effect on net PANI growth. Analogous to PPY and PTH growth, PANI growth rate decreases with increasing purge time, illustrating that the film growth is dependent on the physisorption of SbCl<sub>5</sub> oxidant. Note that the purge time effect on the PANI growth rate becomes substantial at higher temperatures (>100 °C). In order to keep reasonable growth rate above 100 °C, the purge time was fixed at 10 s for **Figure 4.10b, c**. **Figure 4.10b** describes the PANI growth as a function of MLD cycles using SbCl<sub>5</sub>/N<sub>2</sub>/Aniline/N<sub>2</sub> = 0.1/10/0.1/10 s at 75 °C, showing the linear growth rate of 5.9 Å/cycle. **Figure 4.10c** indicates the temperature dependence of the PANI growth by MLD processes. The MLD conditions were followed: SbCl<sub>5</sub>/N<sub>2</sub>/Aniline/N<sub>2</sub> = 0.1/10/0.1/10 s for 50 cycles. The result shows similar trend with PPY growth, exhibiting lower growth rate at higher temperatures due to the monomer desorption. For CVD processes, the deposition time was held at 30 s with various temperatures in **Figure 4.10d**. Significant large thickness gradient is observed at 75 °C, whereas the growth rate greatly decreases at 25 and 175

°C, consistent with PPY CVD results in **Figure 4.3b**. Note that the growth rate of PANI by CVD is extremely sensitive to source temperature at lower temperature regime ( $< 75$  °C). This might be due to the fast reaction between aniline and  $\text{SbCl}_5$  at this temperature window, therefore careful temperature control required to achieve reproducible processes.

**Figure 4.11** shows vibrational spectrum to evaluate the film composition at different temperatures. The results depict characteristic PANI peaks at 3377, 3081, 1611, 1586, 1497, 1318, 1250, 1158 and 812  $\text{cm}^{-1}$ .<sup>35-38</sup> The peaks at 3377 and 3081  $\text{cm}^{-1}$  show N-H stretching and C-H stretching vibrational mode from aromatic ring. The bands at 1611 and 1178  $\text{cm}^{-1}$  are associated with delocalization effects of semiquinone radicals ( $-\text{C}=\text{C}-$ ) and C-H in-plane ring deformation/ring-amine stretching vibration, respectively. Quinoid and benzenoid ring stretching vibrations are confirmed at 1586 and 1497  $\text{cm}^{-1}$ . The spectra at 1318 and 1250  $\text{cm}^{-1}$  are owing to C-N stretching mode of aromatic amine structure. C-H in-plane/C-H out-of-plane bending vibration of aromatic ring is observed at 812  $\text{cm}^{-1}$ . Note that the thickness of PANI films deposited at 25, 75, 125 and 175 °C is 10, 500, 500, 180 nm, respectively. Due to thinner thickness of PANI film at 25 °C, the FTIR spectrum signal is mainly from the Si-OH substrate. Given that SE model fit is difficult to estimate thick PANI samples ( $> 100$  nm), profilometer was used to measure thickness of thicker films. The same samples were used for FTIR, AFM and XPS in **Figure 4.11-13**.

The surface roughness of PANI films on Si-OH was evaluated by AFM as shown in **Figure 4.12** and **Table 4.5**. The fast condensation reaction at 75 °C facilitates the bubble formation, having the height of  $\sim 400$  nm and the RMS of 164 nm. Larger scan size ( $50 \mu\text{m} \times 50 \mu\text{m}$ ) was used to capture the large bubbler formation. Even at lower temperature (25 °C), the slower growth rate leads to smoother surface than 75 °C. At higher temperatures, more smooth surfaces are observed.

Since the surface roughness increases with the rate of the condensation reaction, decreasing the growth rate at lower temperatures would be helpful to obtain smoother PANI films.

High resolution XPS results are shown in **Figure 4.13 and Table 4.5**. No substantial peak shifts are observed for C 1s, N 1s, and Sb 3d/O 1s, implying no chemical change with different CVD temperatures. However, Cl 2p peak at 198 eV gradually decreases with higher temperatures, leading to lower Cl<sup>-</sup> dopants. In terms of elemental composition, larger Sb components are observed for the films deposited at lower temperatures. The large deviation of Sb ratio at different temperatures is attributed to the temperature dependence of the PANI growth rate. Given that the growth behavior of PANI films in the range of 25-75 °C markedly changes depending on the source temperature, careful process control is substantially critical to obtain reproducible film growth.

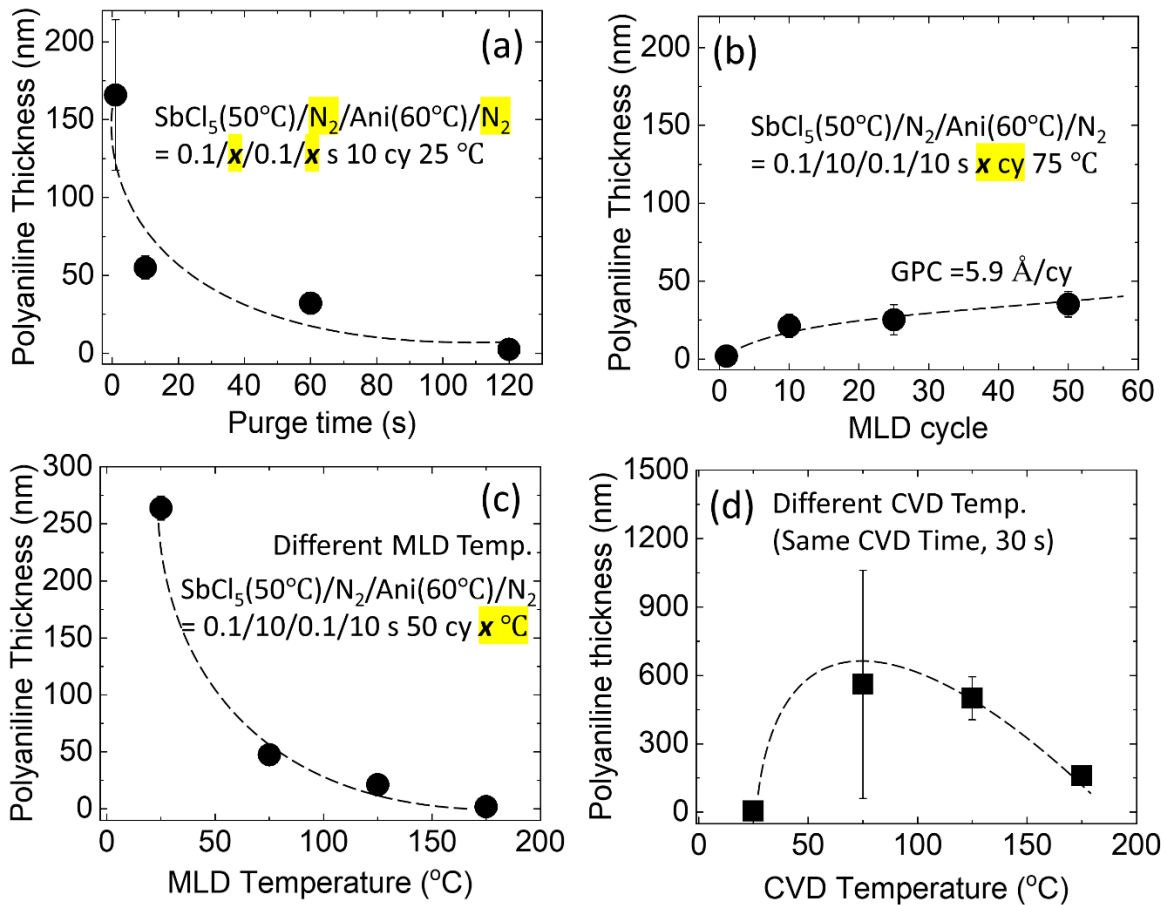


**Figure 4.10** (a) The effect of purge time on the growth rate of polyaniline (PANI) on Si-OH at 25 °C.  $\text{SbCl}_5$  and aniline dose times were held constant 0.1 s. (b) PANI thickness as a function of MLD cycles on Si-OH at 75 °C. The effect of (c) MLD and (d) CVD temperatures on PANI thickness on Si-OH. For (b) and (c), the MLD sequence followed:  $\text{SbCl}_5(50^\circ\text{C})/\text{N}_2/\text{aniline}(60^\circ\text{C})/\text{N}_2 = 0.1/10/0.1/10$  s. For (d), CVD process time was held at 30 s. All thicknesses were measured by spectroscopic ellipsometry and the error bar was from multiple sets average. Lines were drawn as guides to the eye.

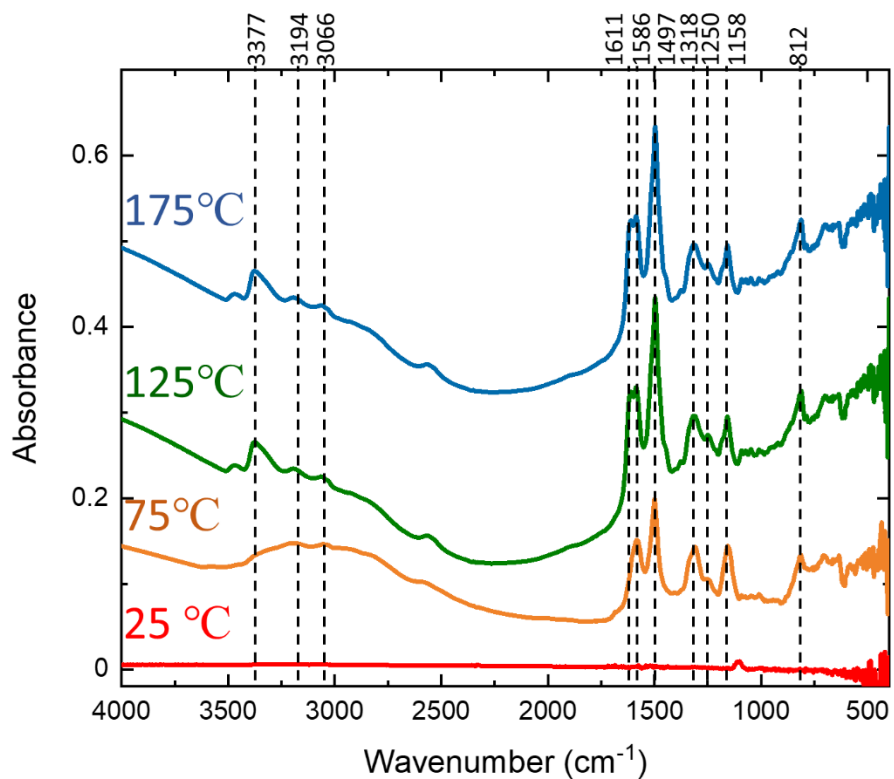


**Figure 4.11** FTIR spectra of PANI on double-side polished Si-OH at different CVD. All the spectra were normalized by the Si-Si peak ( $\sim 610\text{ cm}^{-1}$ ) and subtracted to the bare Si-OH spectra. Same samples were used for **Figure 4.11, 12 and 13**.

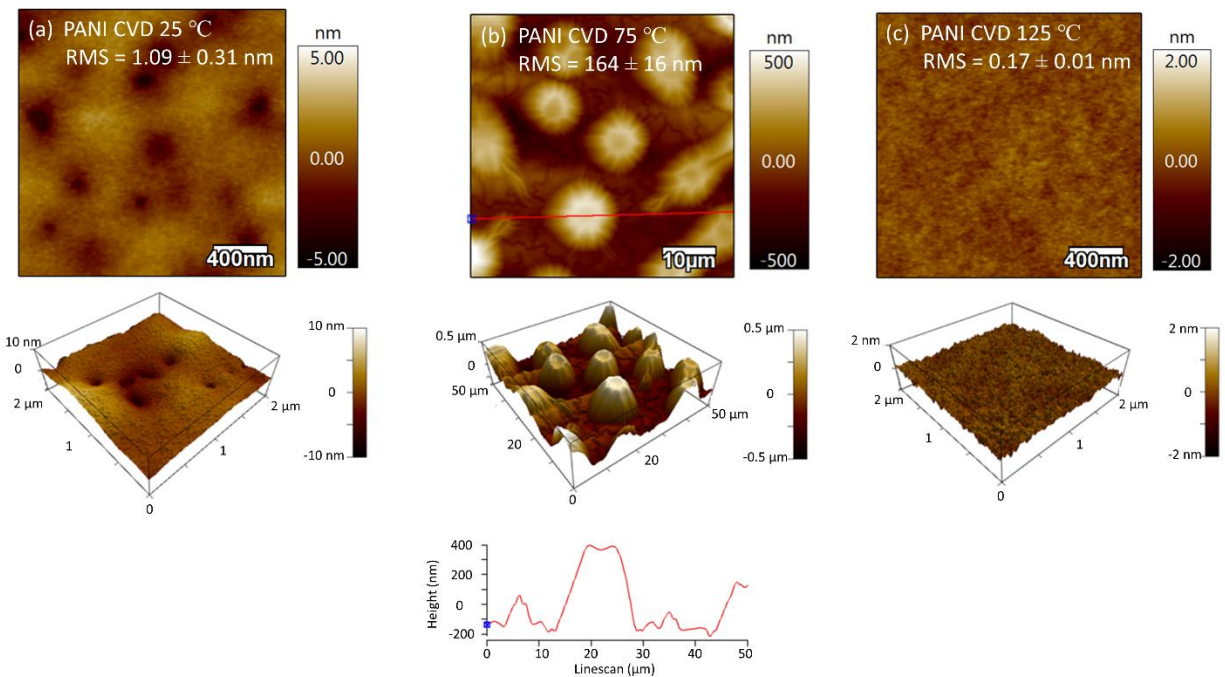


**Figure 4.12** AFM images of PPY deposited on Si-OH by CVD processes at (a) 25 °C, (b) 75 °C and (c) 125 °C. Each RMS value is the average of three different measurements. For (b), red line on 2D mapping indicates the linescan on the bottom of 3D mapping.

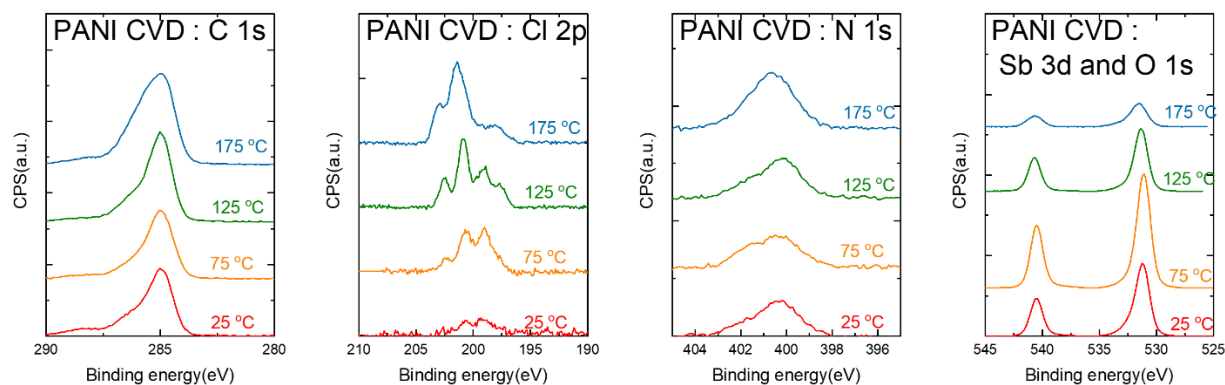


**Figure 4.13** High resolution XPS scans of C 1s, N 1s, Cl 2p, and Sb 3d/O 1s after PANI deposition on Si-OH at different CVD temperatures. For a peak deconvolution of Sb 3d and O 1s, a peak distance of 9.34 eV and a relative intensity of 1.5 between Sb 3d<sub>5/2</sub> and Sb3d<sub>3/2</sub> were used.

**Table 4.5** Elemental composition from XPS analysis and RMS values from AFM results for PANI on Si-OH with various CVD temperatures. XPS values are given in atomic %.

Deposition condition	Cl 2p	C 1s	Si 2p	N 1s	Sb 3d <sub>5/2</sub>	O 1s	RMS (nm)
10 nm CVD 25 °C	1.23	46.42	12.01	5.79	8.03	26.53	1.09 ± 0.31
500 nm CVD 75 °C	2.88	46.13	0.00	6.15	13.88	30.96	164 ± 16.1
500 nm CVD 125 °C	4.26	61.09	0.00	7.29	7.90	19.45	0.17 ± 0.01
180 nm CVD 175 °C	3.84	74.21	0.00	9.07	2.66	10.22	0.52 ± 0.03

#### 4.4.5 Area-selective Deposition of Conjugated Polymers

To study the substrate-dependent growth of PPY, two different silicon wafers were loaded into a reactor; 100 nm of thermally grown silicon dioxide (SiO<sub>2</sub>) cleaned by piranha treatment, and a silicon piece was treated with piranha cleaning, followed by a dilute HF dip to form a hydrogen-terminated surface (Si-H). **Figure 4.14a-d** depict the thickness of PPY as a function of MLD cycles at different MLD temperatures between 75 and 150 °C. The condition of MLD experiment was SbCl<sub>5</sub>/N<sub>2</sub>/Pyrrole/N<sub>2</sub> = 1.0/10/2.0/10 s. All the results were measured by SE and each measurement is the average of three different samples. Throughout all temperature regimes, less PPY growth is observed on Si-H, which is similar with PEDOT ASD in **Chapter 3**. As the chamber temperature increases, the growth rate on both surfaces decreases, decreasing the PPY selectivity between SiO<sub>2</sub> and Si-H surfaces. In order to explore different substrate dependence of PPY growth, PPY was deposited at 125 °C on 82 nm of low-k, 150 nm of SiN, 5 nm of TiN, and 15 nm of Ru as shown in **Figure 4.14e**, showing similar growth with SiO<sub>2</sub> substrates. Different substrates, including W and SiC surfaces which is not shown here, also exhibit similar trend, illustrating that PPY growth is only inhibited on Si-H surfaces. However, different growth is observed on Cu and Co substrates due to the chlorination reaction between Cu/Co and SbCl<sub>5</sub> oxidants. **Figure 4.16** shows cross-sectional SEM of Cu substrates after SbCl<sub>5</sub> exposure. With the exposure of SbCl<sub>5</sub> on Cu surface, 35 nm of Cu films are expanded to ~150 nm with forming CuCl<sub>x</sub>. Considering the molar concentration of Cu should be conserved,  $t_{\text{Cu}} \cdot \rho_{\text{Cu}} / M_{\text{Cu}} = t_{\text{CuCl}_x} \cdot \rho_{\text{CuCl}_x} / M_{\text{CuCl}_x}$  where  $t_{\text{Cu}} = 35 \text{ nm}$ ,  $\rho_{\text{Cu}} = 8.96 \text{ g/cm}^3$ ,  $\rho_{\text{CuCl}} = 4.14 \text{ g/cm}^3$ ,  $\rho_{\text{CuCl}_2} = 3.39 \text{ g/cm}^3$ ,  $M_{\text{Cu}} = 63.55 \text{ g/mol}$ ,  $M_{\text{CuCl}} = 98.99 \text{ g/mol}$ , and  $M_{\text{CuCl}_2} = 134.5 \text{ g/mol}$ , respectively. If all Cu films were converted to CuCl and CuCl<sub>2</sub>, the thickness would be 118 or 195.8 nm, respectively. This implies that the converted layer is composed of CuCl/CuCl<sub>2</sub> mixture (~6:4 ratio). To prevent the fast chlorination reaction, barrier layer such as

TaN would be necessary for the  $\text{SbCl}_5$  based oxidative polymerization. Otherwise, different reaction using plasma-enhanced radical would be helpful to bypass the undesirable reaction on Cu and Co surfaces.

**Figure 4.14f** shows the temperature dependence of PPY growth at different CVD temperatures ranging from 50 to 300 °C. At lower growth temperatures ( $T < 100$  °C), PPY selectivity on  $\text{SiO}_2$  vs. Si-H is small and depending on the sample position, higher PPY growth is observed on Si-H vs.  $\text{SiO}_2$ . This is associated with the fast condensation reaction, driven by the reactor geometry rather than the chemical reaction propensity of the substrates. At middle temperature regime ( $100 < T < 200$  °C), higher selectivity is obtained on  $\text{SiO}_2$  vs. Si-H, consistent with PEDOT ASD. At higher temperature regime ( $T > 200$  °C), PPY selectivity dramatically decreases owing to the lower overall growth rate at higher temperatures. To compare the temperature effect of MLD and CVD on PPY selectivity, a value for selectivity,  $S$ , in **Eq 1.1**, was implemented in **Figure 4.15**. The value of  $S$  can be between 1 to 0, where  $S = 1$  for the perfect selectivity, and  $S = 0$  for the full selectivity loss ( $\theta_1 = \theta_2$ ). In **Figure 4.15a**,  $S$  was plotted as a function of the thickness of PPY at different MLD temperatures. For better ASD processes,  $S$  value should be near 1 as increasing the thickness of PPY films. While similar trend is confirmed at 75, 100, and 125 °C, the selectivity dropped at 150 °C due to the decreased growth rate at higher temperatures. **Figure 4.15b** indicates the CVD temperature effects on PPY ASD. As illustrated in **Figure 4.14f**, three different regimes are confirmed for PPY CVD processes: i) no/reverse selectivity on  $\text{SiO}_2$  vs. Si-H ( $T < 100$  °C), showing negative selectivity, ii) good selectivity on  $\text{SiO}_2$  vs. Si-H ( $100 < T < 200$  °C), and iii) poor selectivity ( $T > 200$  °C). The highest selectivity of PPY films were achieved at 200 °C, but similar selectivity would be achieved near  $200 \pm 25$  °C. Note that the ASD temperature regime would change depending on the  $\text{SbCl}_5$  source condition. Similar

to PEDOT ASD processes, higher PPY ASD was obtained by CVD *vs.* MLD processes, attributed by the fast reaction rate of CVD processes.

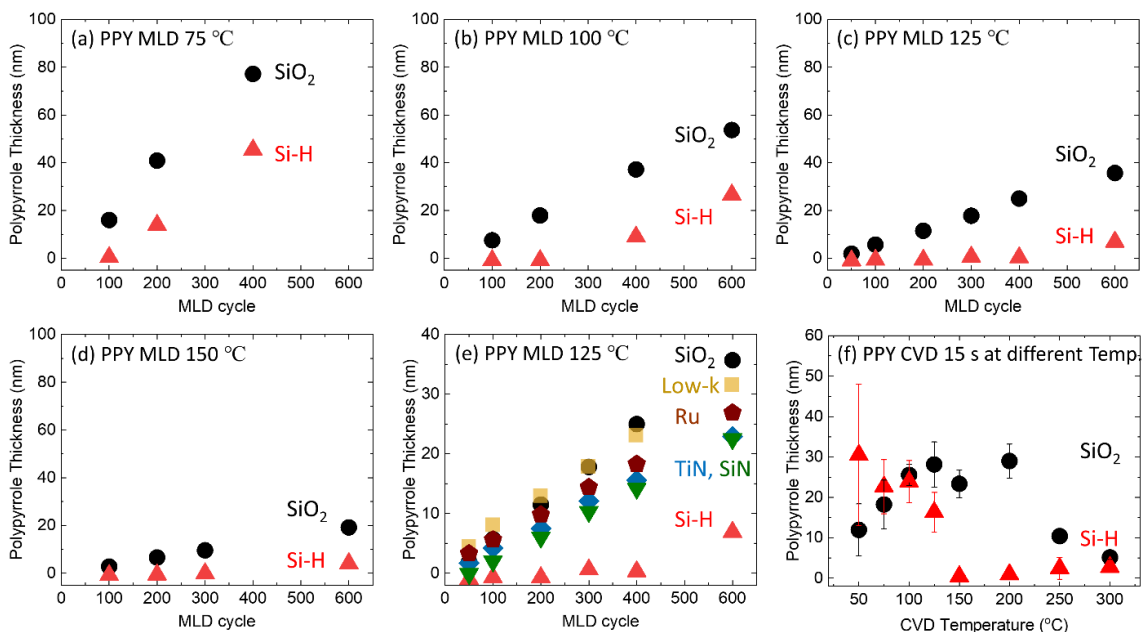


**Figure 4.14** Area-selective deposition (ASD) of polypyrrole (PPY) on SiO<sub>2</sub> *vs.* Si-H as a function of MLD cycle at (a) 75, (b) 100, (c) 125, and (d) 150 °C. (e) Substrate selectivity of PPY as a function of MLD cycles at 125 °C. All MLD processes followed: SbCl<sub>5</sub>/N<sub>2</sub>/Pyrrrole/N<sub>2</sub> = 1.0/10/2.0/10 s. (f) ASD of PPY by CVD at different temperatures (50 – 300 °C) on SiO<sub>2</sub> *vs.* Si-H. CVD deposition time was held at 15 s. All thicknesses were measured by spectroscopic ellipsometry and the error bar was from multiple sets average.

**Figure 4.17** shows the summary of conjugated polymers ASD by CVD processes. All monomers including EDOT, pyrrole, thiophene and aniline were polymerized by the SbCl<sub>5</sub> oxidant. Regarding PEDOT ASD on SiO<sub>2</sub> *vs.* Si-H, the delayed PEDOT nucleation on Si-H is due to the SbCl<sub>5</sub> reduction on Si-H surfaces, showing 40 nm PEDOT ASD. PPY ASD indicates similar

ASD behavior (~30 nm ASD) whereas lower ASD is obtained for PTH (~7 nm ASD) and PANI (~ 5 nm ASD) growth. PTH and PANI growth are highly temperature dependent. For PTH growth, the chamber temperature should be kept at 25 °C and the fast condensation reaction dominates the film growth, possibly decreasing the selective  $\text{SbCl}_5$  reduction on Si-H surfaces. For the similar reason, PANI ASD is difficult to control. The growth rate of PANI rapidly changes depending on the source temperature of  $\text{SbCl}_5$  and aniline. Below the threshold source temperatures which can be varied at reactor temperature, no growth would occur on both surfaces, whereas rapid nucleation would be observed on both substrates above the threshold point. More rigorous studies to find out the relationship between the source delivery and the growth rate would be helpful to enhance PANI ASD, but this work illustrates that PEDOT and PPY shows more reproducible and better ASD compared to PANI.

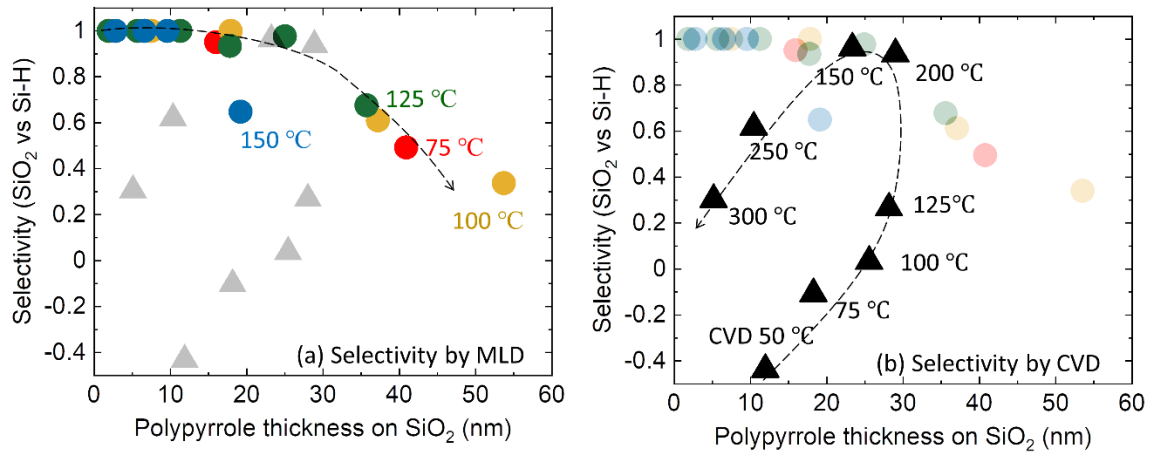


**Figure 4.15** Polypyrrole (PPY) selectivity as a function of the thickness of PPY on SiO<sub>2</sub> at (a) various MLD temperatures and (b) CVD temperatures. Selectivity was calculated based on the thickness data measured by spectroscopic ellipsometry and Eq. (1.1).

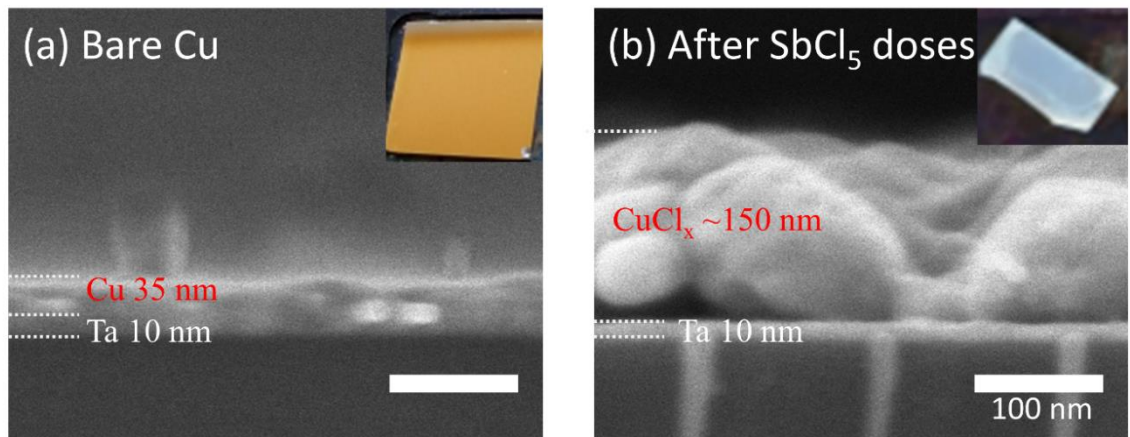


**Figure 4.16** Cross-sectional SEM images of (a) bare Cu and (b) after 50 cycles of (SbCl<sub>5</sub>(40 °C)/N<sub>2</sub> = 0.1/60 s) doses on Cu substrates. All scales are the same. Top right of each image shows the photographic image of each sample, describing the surface color change.

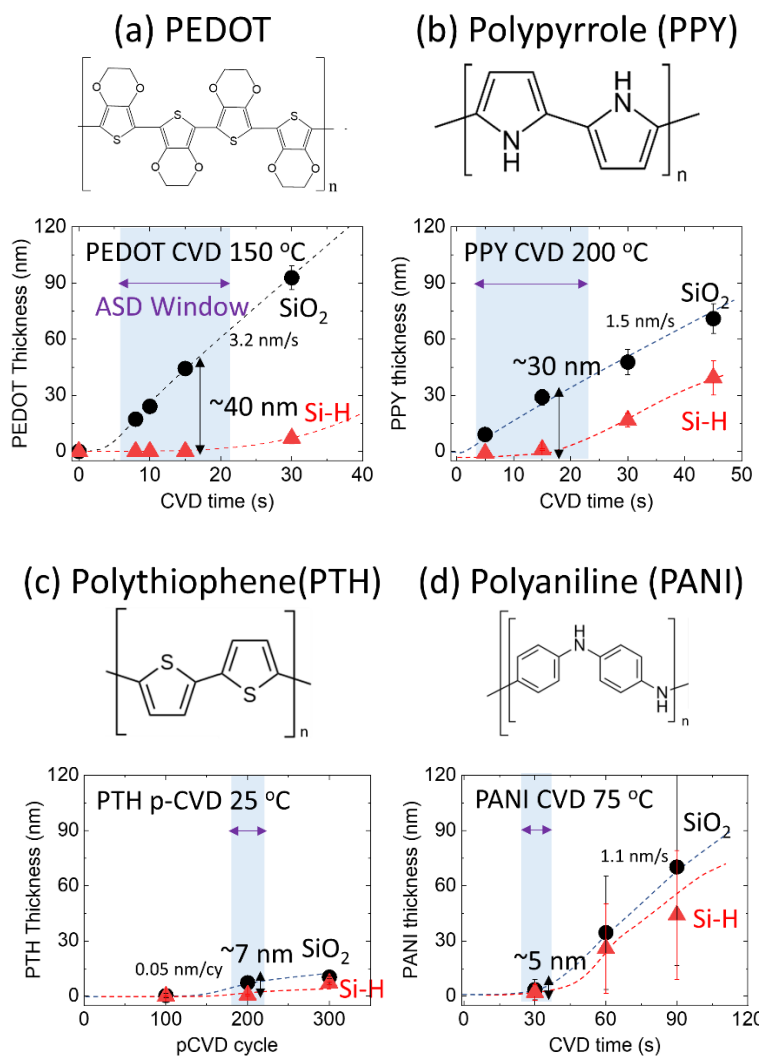


**Figure 4.17** Area-selective deposition of (a) PEDOT, (b) PPY, (c) PTH, and (d) PANI with various CVD temperatures. Blue highlighted region indicates selective window on SiO<sub>2</sub> vs. Si-H. For PTH, pulse CVD was used to improve the film uniformity. All thicknesses were measured by spectroscopic ellipsometry and the error bar was from multiple sets average. Lines were drawn as guides to the eye.

## 4.5 Summary

Basic growth behavior of a range of conjugated polymers including polypyrrole (PPY), polythiophene (PTH), and polyaniline (PANI) was investigated by CVD and MLD processes using various monomers and  $\text{SbCl}_5$  oxidant. The effect of reactants on net growth rate of PPY films described soft-saturated behavior, illustrating that the film deposition rate relies on the balance between reactant dose and purge time. In terms of purge time, shorter purge time was necessary for PPY (10 s), PTH (1 s) and PANI (10 s) to obtain reasonable growth rate compared to PEDOT (60 s). Otherwise, longer purge time substantially decreased the growth rate. This is mainly associated with the fact that the  $\text{SbCl}_5$  oxidant sticks on the surface *via* physisorption during oxidative polymerization, suggesting controlling the physisorbed  $\text{SbCl}_5$  oxidant is critical to obtain good reproducibility.

The film growth rate of PPY, PTH and PANI during MLD processes decreased with increasing the reactor temperatures, attributed to the faster desorption of monomers and decomposition of the oxidant at higher temperatures. In particular, PTH process showed highly temperature dependent growth, requiring room temperature for deposition. For the CVD processes of PPY, the growth rate was steady between 100 and 200 °C, whereas the growth rate decreased at 25 and 300 °C. This is due to fast condensation reaction at 25 °C where most of reactants would be consumed near the inlet of the reactor and faster monomer desorption at 300 °C. While conductive PPY films (~16 S/cm) were achieved at lower deposition temperatures ( $T < 100$  °C), non-conductive films were obtained at higher temperatures. This is also consistent with FTIR results, exhibiting noticeable peak change above 150 °C. The CVD process of PANI films showed large growth variation depending on temperatures, affecting film roughness and composition ratio.

Due to the fast growth rate at 75 °C, the surface roughness was 164 nm relative to ~ 1 nm at different temperatures. Despite different surface roughness and Sb atomic ratio, the FTIR peaks were independent on different temperatures (75 – 175 °C), showing good thermal stability of PANI films.

Area-selective deposition (ASD) of PPY, PTH and PANI was studied. While the nucleation of PPY films was observed on various substrates including SiO<sub>2</sub>, Ru, low-k, TiN, SiN, W, and SiC, the film growth was impeded only on Si-H surfaces, consistent with PEDOT ASD in **Chapter 3**. This is explained by the selective SbCl<sub>5</sub> reduction on Si-H surface. Undesirable chlorination reaction occurred on Cu and Co by reacting with SbCl<sub>5</sub> oxidant. A value for selectivity, *S*, was employed to evaluate PPY ASD on SiO<sub>2</sub> vs. Si-H by MLD and CVD processes. PPY ASD by MLD decreased at higher temperature (150 °C) and CVD yielded better PPY ASD than MLD processes. For CVD processes, ASD behavior dramatically changed depending on the chamber temperature, potentially beneficial for controlling selectivity.

Compared to PEDOT ASD of 40 nm on SiO<sub>2</sub> vs. Si-H, similar ASD of 30 nm was achieved for PPY, whereas lower ASD of 7 and 5 nm was obtained for PTH and PANI, respectively. The underlying reason of poor ASD for PTH and PANI films would be a difficulty to control the chemical reaction. Regarding PTH growth, temperature restriction which should be near room temperature resulted in the fast condensation reaction, decreasing the selective SbCl<sub>5</sub> reduction on Si-H surfaces. From a similar perspective, PANI growth was challenging to achieve reliable growth rate. More systematic studies to control the reactant delivery and growth rate would be helpful to improve ASD of PTH and PANI films. Overall, this work provides an important insight into developing various polymer ASD using MLD and CVD for bottom-up nanoscale fabrication.

#### 4.6 References

- (1) Kim, J. S.; Parsons, G. N. Nanopatterned Area-Selective Vapor Deposition of PEDOT on SiO<sub>2</sub> vs Si-H: Improved Selectivity Using Chemical Vapor Deposition vs Molecular Layer Deposition. *Chem. Mater.* **2021**, *33*, 9221–9230.
- (2) Junige, M.; George, S. M. Area-Selective Molecular Layer Deposition of Nylon 6,2 Polyamide: Growth on Carbon and Inhibition on Silica. *J. Vac. Sci. Technol. A* **2021**, *39*, 023204.
- (3) Lee, S.; Kim, H. M.; Baek, G. H.; Park, J. S. Dry-Etchable Molecular Layer-Deposited Inhibitor Using Annealed Indicone Film for Nanoscale Area-Selective Deposition. *ACS Appl. Mater. Interfaces* **2021**, *13*, 60144–60153.
- (4) Yu, X.; Bobb-Semple, D.; Oh, I. K.; Liu, T. L.; Closser, R. G.; Trevillyan, W.; Bent, S. F. Area-Selective Molecular Layer Deposition of a Silicon Oxycarbide Low-k Dielectric. *Chem. Mater.* **2021**, *33*, 902–909.
- (5) Merckx, M. J. M.; Sandoval, T. E.; Hausmann, D. M.; Kessels, W. M. M.; Mackus, A. J. M. Mechanism of Precursor Blocking by Acetylacetone Inhibitor Molecules during Area-Selective Atomic Layer Deposition of SiO<sub>2</sub>. *Chem. Mater.* **2020**, *32*, 3335–3345.
- (6) Suh, T.; Yang, Y.; Zhao, P.; Lao, K. U.; Ko, H. Y.; Wong, J.; Distasio, R. A.; Engstrom, J. R. Competitive Adsorption as a Route to Area-Selective Deposition. *ACS Appl. Mater. Interfaces* **2020**, *12*, 9989–9999.
- (7) Pattison, T. G.; Hess, A. E.; Arellano, N.; Lanzillo, N.; Nguyen, S.; Bui, H.; Rettner, C.; Truong, H.; Friz, A.; Topuria, T.; Fong, A.; Hughes, B.; Tek, A. T.; DeSilva, A.; Miller, R. D.; Qiao, G. G.; Wojtecki, R. J. Surface Initiated Polymer Thin Films for the Area Selective Deposition and Etching of Metal Oxides. *ACS Nano* **2020**, *14*, 4276–4288.

- (8) Huang, Z.; Wang, P.; Macdiarmid, A. G.; Xia, Y.; Whitesides, G. Selective Deposition of Conducting Polymers on Hydroxyl-Terminated Surfaces with Printed Monolayers of Alkylsiloxanes as Templates. *Langmuir* **1997**, *13*, 6480–6484.
- (9) Vaeth, K. M.; Jensen, K. F. Selective Growth of Poly(p-Phenylene Vinylene) Prepared by Chemical Vapor Deposition. *Adv. Mater.* **1999**, *11*, 814–820.
- (10) Vaeth, K. M.; Jensen, K. F. Transition Metals for Selective Chemical Vapor Deposition of Parylene-Based Polymers. *Chem. Mater.* **2000**, *12*, 1305–1313.
- (11) Vaeth, K. M.; Jackman, R. J.; Black, A. J.; Whitesides, G. M.; Jensen, K. F. Use of Microcontact Printing for Generating Selectively Grown Films of Poly(p-Phenylene Vinylene) and Parylenes Prepared by Chemical Vapor Deposition. *Langmuir* **2000**, *16*, 8495–8500.
- (12) Hsien-Yeh Chen, Joseph Hermes Lai, Xuwei Jiang, and J. L. Substrate-Selective Chemical Vapor Deposition of Reactive Polymer Coatings. *Adv. Mater.* **2008**, *20*, 3474–3480.
- (13) Bally-Le Gall, F.; Friedmann, C.; Heinke, L.; Arslan, H.; Azucena, C.; Welle, A.; Ross, A. M.; Wöll, C.; Lahann, J. Free-Standing Nanomembranes Based on Selective CVD Deposition of Functional Poly-p-Xylylenes. *ACS Nano* **2015**, *9*, 1400–1407.
- (14) Hermes, S.; Schröder, F.; Chelmowski, R.; Wöll, C.; Fischer, R. A. Selective Nucleation and Growth of Metal-Organic Open Framework Thin Films on Patterned COOH/CF<sub>3</sub>-Terminated Self-Assembled Monolayers on Au(111). *J. Am. Chem. Soc.* **2005**, *127*, 13744–13745.
- (15) Zhuang, J. L.; Kind, M.; Grytz, C. M.; Farr, F.; Diefenbach, M.; Tussupbayev, S.; Holthausen, M. C.; Terfort, A. Insight into the Oriented Growth of Surface-Attached Metal-Organic Frameworks: Surface Functionality, Deposition Temperature, and First Layer Order. *J. Am. Chem. Soc.* **2015**, *137*, 8237–8243.

- (16) Yoshimura, T.; Terasawa, N.; Kazama, H.; Naito, Y.; Suzuki, Y.; Asama, K. Selective Growth of Conjugated Polymer Thin Films by the Vapor Deposition Polymerization. *Thin Solid Films* **2006**, *497*, 182–184.
- (17) Hashemi, F. S. M.; Prasittichai, C.; Bent, S. F. A New Resist for Area Selective Atomic and Molecular Layer Deposition on Metal-Dielectric Patterns. *J. Phys. Chem. C* **2014**, *118*, 10957–10962.
- (18) Prasittichai, C.; Zhou, H.; Bent, S. F. Area Selective Molecular Layer Deposition of Polyurea Films. *ACS appl. Mater. Interfaces* **2013**, *5*, 13391–13396.
- (19) Zhang, C.; Vehkamäki, M.; Pietikäinen, M.; Leskelä, M.; Ritala, M. Area-Selective Molecular Layer Deposition of Polyimide on Cu through Cu-Catalyzed Formation of a Crystalline Interchain Polyimide. *Chem. Mater.* **2020**, *32*, 5073–5083.
- (20) Sauerbrey, G. The Use of Quarts Oscillators for Weighing Thin Layers and for Microweighing. *Z. Phys.* **1959**, *155*, 206–222.
- (21) Mecea, V. M. From Quartz Crystal Microbalance to Fundamental Principles of Mass Measurements. *Anal. Lett.* **2005**, *38*, 753–767.
- (22) Fabretto, M.; Zuber, K.; Jariego-Moncunill, C.; Murphy, P. Measurement Protocols for Reporting PEDOT Thin Film Conductivity and Optical Transmission: A Critical Survey. *Macromol. Chem. Phys.* **2011**, *212*, 2173–2180.
- (23) Smits, F. M. Measurement of Sheet Resistivities with the Four-Point Probe. *Bell Syst. Tech. J.* **1958**, *37*, 711–718.
- (24) Putkonen, M.; Harjuoja, J.; Niinisto, L. Atomic Layer Deposition of Polyimide Thin Films. *J. Mater. Chem.* **2007**, *17*, 664–669.

- (25) Du, Y.; George, S. M. Molecular Layer Deposition of Nylon 66 Films Examined Using in Situ FTIR Spectroscopy. *J. Phys. Chem. C* **2007**, *111*, 8509–8517.
- (26) Atanasov, S. E.; Losego, M. D.; Gong, B.; Sachet, E.; Maria, J. P.; Williams, P. S.; Parsons, G. N. Highly Conductive and Conformal Poly(3,4-Ethylenedioxythiophene) (PEDOT) Thin Films via Oxidative Molecular Layer Deposition. *Chem. Mater.* **2014**, *26*, 3471–3478.
- (27) Nye, R. A.; Kelliher, A. P.; Gaskins, J. T.; Hopkins, P. E.; Parsons, G. N. Understanding Molecular Layer Deposition Growth Mechanisms in Polyurea via Picosecond Acoustics Analysis. *Chem. Mater.* **2020**, *32*, 1553–1563.
- (28) Volk, A. A.; Kim, J.-S.; Jamir, J.; Dickey, E. C.; Parsons, G. N. Oxidative Molecular Layer Deposition of PEDOT Using Volatile Antimony(V) Chloride Oxidant. *J. Vac. Sci. Technol. A* **2021**, *39*, 032413.
- (29) Stejskal, J.; Trchová, M.; Bober, P.; Morávková, Z.; Kopecký, D.; Vršata, M.; Prokeš, J.; Varga, M.; Watzlová, E. Polypyrrole Salts and Bases: Superior Conductivity of Nanotubes and Their Stability towards the Loss of Conductivity by Deprotonation. *RSC Adv.* **2016**, *6*, 88382–88391.
- (30) Mohammadi, A.; Hasan, M. A.; Liedberg, B.; Lundström, I.; Salaneck, W. R. Chemical Vapour Deposition (CVD) of Conducting Polymers: Polypyrrole. *Synth. Met.* **1986**, *14*, 189–197.
- (31) Hitoshi, K.; Osamu, N.; Tomoko, M.; Seishi, H.; Hiroshi, K. Fourier Transform Infrared Spectroscopy Study of Conducting Polymer Poly Pyrrole: Higher Order Structure of Electrochemically Synthesized Film. *J. Phys. Chem.* **1991**, *95*, 6014–6016.
- (32) Lee, S.; Borrelli, D. C.; Jo, W. J.; Reed, A. S.; Gleason, K. K. Nanostructured Unsubstituted Polythiophene Films Deposited Using Oxidative Chemical Vapor Deposition: Hopping Conduction and Thermal Stability. *Adv. Mater. Interfaces* **2018**, *5*, 1–8.

- (33) Im, S. G.; Gleason, K. K.; Olivetti, E. A. Doping Level and Work Function Control in Oxidative Chemical Vapor Deposited Poly (3,4-Ethylenedioxythiophene). *Appl. Phys. Lett.* **2007**, *90*, 152112.
- (34) Nejati, S.; Lau, K. K. S. Chemical Vapor Deposition Synthesis of Tunable Unsubstituted Polythiophene. *Langmuir* **2011**, *27*, 15223–15229.
- (35) Smolin, Y. Y.; Soroush, M.; Lau, K. K. S. Oxidative Chemical Vapor Deposition of Polyaniline Thin Films. *Beilstein J. Nanotechnol.* **2017**, *8*, 1266–1276.
- (36) Industrial, Z. Vibrational Spectra and Structure of Polyaniline and Related Compounds. *Synth. Met.* **1989**, *29*, E303-312.
- (37) Neugebauer, H.; Neckel, A. In Situ FTIR Measurements of Polyaniline in the Non-Metallic Phase. *Synth. Met.* **1989**, *29*, E185-192.
- (38) Ping, Z. On the Base-Acid Transitions of Polyaniline Base-Acid Transition in the Emeraldine Form of Polyaniline. *J. Chem. Soc., Faraday Trans* **1996**, *92*, 3063–3067.

## Chapter 5 Multimaterial Self-Aligned Nanopatterning by Simultaneous Adjacent Thin

### Film Deposition and Etching

The following work is a reprint published in *ACS Nano* **2021**, *15*, 12276–12285. S.K. Song and J. Kim are co-first authors on this work and J. Kim contributed to Tungsten deposition and thin film characterization using TEM.

#### 5.1 Abstract

Printed component sizes in electronic circuits are approaching 10 nm, but inherent variability in feature alignment during photolithography poses a fundamental barrier for continued device scaling. Deposition-based self-aligned patterning is being introduced, but nuclei defects remain an overarching problem. This work introduces low-temperature chemically self-aligned film growth *via* simultaneous thin film deposition and etching in adjacent regions on a nanopatterned surface. During deposition, nucleation defects are avoided in nongrowth regions because deposition reactants are locally consumed *via* sacrificial etching. For a range of materials and process conditions, thermodynamic modeling confirms that deposition and etching are both energetically favorable. We demonstrate nanoscale patterning of tungsten at 220 °C with simultaneous etching of TiO<sub>2</sub>. Area selective deposition (ASD) of the sacrificial TiO<sub>2</sub> layer produces an orthogonal sequence for self-aligned patterning of two materials on one starting pattern, *i.e.*, TiO<sub>2</sub> ASD on SiO<sub>2</sub> followed by W ASD on Si–H. Experiments also show capacity for self-aligned dielectric patterning *via* favorable deposition of AlF<sub>3</sub> on Al<sub>2</sub>O<sub>3</sub> at 240 °C with simultaneous atomic layer etching of sacrificial ZnO. Simultaneous deposition and etching provides opportunities for low-temperature bottom-up self-aligned patterning for electronic and other nanoscale systems.

## 5.2 Introduction

The smallest printed features in semiconductor manufacturing are currently less than 15 nm.<sup>1</sup> Continued scaling poses significant problems in material patterning and feature alignment.<sup>1-4</sup> Techniques to create small features are well-developed, but a key barrier is the limited ability to control minute variations in feature pattern alignment. Devices are constructed with hundreds of layers of patterned metals and dielectrics, and achieving circuit performance requires the conductors and insulators in each layer to be precisely registered as they form on top of each other. Patterns that are misaligned by only a few nanometers (a distance corresponding to  $\sim 10$  atoms in crystalline silicon) can lead to faults including electrical shorts, open circuits, and excess resistance.<sup>4</sup> To avoid metal diffusion, reaction temperature during “back-end” fabrication is limited to  $<400$  °C,<sup>3</sup> putting stringent demands on surface chemical processes. Advanced 13.5 nm extreme UV (EUV) lithography can address some of these challenges, but equipment costs are expected to be substantial,<sup>5</sup> especially when multiple EUV steps are needed. Also, alignment problems will become more acute in future 3D devices being considered to overcome impending obstacles of silicon memory density and computing energy consumption.<sup>1</sup>

To overcome inherent variability and stochastics in lithography, new self-alignment methods are needed where the chemistry of the underlying surface can guide the placement of overlying material layers. Self-aligned ASD uses surface chemistry to promote deposition in predetermined growth regions and minimize growth in adjacent nongrowth regions. At  $<400$  °C, ASD can proceed using chemical vapor deposition (CVD)<sup>3,6-11</sup> or atomic layer deposition (ALD).<sup>12-16</sup> In these methods, the vapor-phase reactants are generally selected to favor net deposition; *i.e.*, the Gibbs free energy change for deposition is negative,  $\Delta G < 0$ .<sup>17,18</sup> However, the strong reaction energetics is problematic for ASD because it leads to creation of unwanted

nucleation defects. Surface passivation layers or other means can slow the rate of nucleation, but unwanted nuclei eventually form, leading to undesired growth and loss of self-alignment. During “front-end” processing, temperatures can exceed 700 °C, and selective silicon epitaxy is widely used to self-align the source/drain contacts to silicon channels. Using high temperatures, defect nuclei are effectively avoided by optimizing reaction thermodynamics.<sup>8-11,19-21</sup> For selective silicon epitaxy, a single set of gas-phase precursors (often including a mixture of chlorosilanes, HCl, and hydrogen) can allow favorable silicon film growth on receptive regions, while, in neighboring regions, the same reactants favor formation of only volatile silicon products, such as SiCl<sub>2</sub>.<sup>11,20</sup> In this way, self-aligned selective epitaxy avoids defects using thermodynamically favorable reactions that locally consume the deposition reactant in the regions where growth is not desired.

Several vapor/surface exchange and conversion reaction mechanisms are known where material deposition simultaneously liberates another volatile species at the surface deposition site.<sup>22-24</sup> In contrast, low-temperature surface reactions that achieve simultaneous delocalized deposition and etching in neighboring regions on a patterned surface are not well known.

In this work, we demonstrate low-temperature (<400 °C) self-aligned deposition using a single set of vapor-phase reactants to achieve deposition in a desired growth region while simultaneously etching a neighboring sacrificial surface in a nongrowth region. The primary example reported here shows self-limiting ALD with simultaneous continuous chemical vapor etching (CVE), and an alternate example shows ALD with simultaneous self-limiting atomic layer etching (ALE). Akin to high-temperature selective epitaxy reactions, the resulting net deposition is inherently self-aligned with the prepatterned starting surface because the etching reaction locally consumes the deposition reactant, thereby avoiding unwanted nuclei.

Starting with a patterned surface with exposed hydrogen-terminated silicon (Si-H) and TiO<sub>2</sub> regions, we show that sequential exposures of SiH<sub>4</sub> and WF<sub>6</sub> at 220 °C produce self-aligned growth of tungsten only on the silicon, while simultaneously, on the neighboring TiO<sub>2</sub>, the WF<sub>6</sub> preferentially reacts to form volatile WO<sub>2</sub>F<sub>2</sub> and TiF<sub>4</sub>, thereby avoiding tungsten metal growth. At the reaction temperature, the deposition and etching rates are sufficient to avoid accumulation of unwanted W metal until the sacrificial layer is consumed. By creating the starting pattern using ASD of TiO<sub>2</sub> on SiO<sub>2</sub>,<sup>16</sup> we establish a primary experimental demonstration of multiple-material orthogonal area-selective deposition.<sup>25</sup> Using a combination of thermodynamic modeling and experiments, we further show that self-aligned deposition and etching can be extended to a range of other material systems and show experimental results confirming that deposition of AlF<sub>3</sub> dielectric can proceed with atomic layer etching of ZnO.

### 5.3 Experimental Section

#### 5.3.1 Substrate Preparation.

For all deposition studies reported here, each run was performed using wafer pieces with Si-H/SiO<sub>2</sub> patterns and/or separate blanket Si-H and Si-OH pieces, with both pieces always present in the deposition chamber. Surfaces designated as “Si-OH” consist of piranha cleaned silicon producing hydroxyl termination, whereas surfaces designated as “SiO<sub>2</sub>” are thermally oxidized silicon, also with hydroxyl termination. “Si-H” surfaces are formed by dipping the Si-OH in 5% HF for 30 s, producing hydrogen termination. Before deposition, lithographically patterned Si-H/SiO<sub>2</sub> substrates were prepared by piranha cleaning and HF dipping of Si/SiO<sub>2</sub>. The piranha solution was prepared by mixing 30% hydrogen peroxide (electronic grade, J.T. Baker) and 98% sulfuric acid (certified ACS plus, Fisher Chemical) with 1:1 volume ratio.

A boron-doped silicon (100) wafer with 5–10  $\Omega\cdot\text{cm}$  resistivity was cleaved into small pieces (10 mm  $\times$  10 mm). These wafer pieces were cleaned with the piranha solution for 15 min, rinsed with deionized (DI) water, and stored in a DI water filled glass vial. They served as our oxide-terminated blanket silicon substrates (Si–OH) after being rinsed with DI water and dried with  $\text{N}_2$  flow.

Hydrogen-terminated blanket silicon (Si–H) samples were prepared from the Si–OH pieces described above by employing a 30 s dip in 5% HF solution, a 30 s rinse in flowing DI water, and then drying with  $\text{N}_2$ . The Si–H substrates were always loaded into the reactor within 10 min after preparation. Si/SiO<sub>2</sub> line patterned substrates were prepared by photolithographic wet etching of 100 nm thick thermally grown silicon dioxide (SiO<sub>2</sub>) on silicon wafers. The pattern consists of long (>10 mm) alternating lines of SiO<sub>2</sub> and Si, each 3  $\mu\text{m}$  wide for a 6  $\mu\text{m}$  pitch. The wafer was cleaved into small pieces (10 mm  $\times$  10 mm) and prepared immediately prior to loading, as described above for Si–H sample preparation. The 200 nm half-pitch patterned samples were provided by industry and prepared in the same way.

### 5.3.3 TiO<sub>2</sub> ALD/ALE Supercycles Condition.

TiO<sub>2</sub> ALD was performed using 99% pure TiCl<sub>4</sub> (Strem Chemicals) and deionized water (DI water), and the ALE was performed using 99.999% pure WF<sub>6</sub> (Galaxy Chemicals) and 99.9% pure BCl<sub>3</sub> (Matheson). The ALD/ALE supercycles were conducted in a custom-built tubular hot-walled isothermal viscous-flow ALD reactor, further notified as “TiO<sub>2</sub> reactor”, under constant wall temperature (150 °C) and pressure (0.9–1.1 Torr) with 150 sccm of 99.999% pure N<sub>2</sub> (Arc3 Gases) as a carrier gas. One TiO<sub>2</sub> ALD cycle was defined as “TiCl<sub>4</sub> pulse (0.1 s) → N<sub>2</sub> purge (45 s) → H<sub>2</sub>O pulse (0.05 s) → N<sub>2</sub> purge (45 s)” and one TiO<sub>2</sub> ALE cycle was defined as “WF<sub>6</sub> pulse (0.1 s) → N<sub>2</sub> purge (45 s) → BCl<sub>3</sub> pulse (1 s) → N<sub>2</sub> purge (45 s)”. One TiO<sub>2</sub> ALD/ALE supercycle consisted of 30 cycles of TiCl<sub>4</sub>/H<sub>2</sub>O (for TiO<sub>2</sub> ALD) followed by 7 cycles of WF<sub>6</sub>/BCl<sub>3</sub> (TiO<sub>2</sub> ALE). The supercycles were performed in a single reactor at a fixed temperature of 150 °C. Using 12 or 20 supercycles produced ~11.5 and ~16.4 nm of TiO<sub>2</sub> on Si–OH, respectively, with less than 1.9 nm of TiO<sub>2</sub> on exposed Si–H surfaces.

### 5.3.4 W ALD Cycles Condition.

W ALD, using 2% SiH<sub>4</sub> (Custom Gas Solution) and 99.999% pure WF<sub>6</sub> (Galaxy Chemicals), was performed in a separate custom-built tubular hot-walled isothermal viscous-flow ALD reactor, further notified as “W reactor”, under constant wall temperature (220 °C) and pressure (2.0–2.4 Torr) with 210 sccm of 99.999% pure Ar (Arc3 gases) as a carrier gas. One W ALD cycle was define as “SiH<sub>4</sub> pulse (45 s) → Ar purge (45 s) → WF<sub>6</sub> pulse (1 s) → Ar purge (45 s)”. W film was deposited on prepared substrates by running W ALD 10–20 cycles. In this experiment, we first performed Al<sub>2</sub>O<sub>3</sub> ALD to initialize the internal surface of the hot-walled reactor and the surface of the QCM crystal. Trimethylaluminum (TMA; 98%, Strem Chemicals)

and DI water were used for the Al<sub>2</sub>O<sub>3</sub> ALD to initialize the wall condition of the W reactor between batches. One cycle of TMA/H<sub>2</sub>O was defined as “TMA pulse (0.1 s) → Ar purge (45 s) → H<sub>2</sub>O pulse (0.1 s) → Ar purge (45 s)”, and 25 cycles of TMA/H<sub>2</sub>O were used for the initialization.

### 5.3.5 Integrated Sequence of “TiO<sub>2</sub> ALD/ALE → HF Dipping → W ALD”.

Prepared blanket Si–OH and Si–H samples as well as Si–H/SiO<sub>2</sub>-patterned substrates were loaded into the TiO<sub>2</sub> reactor and allowed to reach thermal equilibrium for 60 min under 150 sccm of N<sub>2</sub> flow at 150 °C wall temperature. TiO<sub>2</sub> ALD/ALE 12 or 20 supercycles were performed for TiO<sub>2</sub> ASD on SiO<sub>2</sub>. Following TiO<sub>2</sub> ASD, the samples were removed from the reactor, dipped into 5% HF for 5 s, rinsed with flowing DI H<sub>2</sub>O for 30 s, and dried with N<sub>2</sub> flow in atmospheric conditions to remove undesired oxides on Si–H surfaces. Next, the samples were loaded into the W reactor and allowed to reach thermal equilibrium for 30 min with 210 sccm of Ar flow at 220 °C wall temperature. Subsequently, 10–20 W ALD cycles were carried out at 220 °C to selectively deposit W film on Si–H.

### 5.3.6 HF/TMA Exposures on ZnO and Al<sub>2</sub>O<sub>3</sub>.

Hydrogen fluoride pyridine (~70% HF + ~30% pyridine, Sigma-Aldrich) was used as the HF source. One cycle of HF/TMA exposure was defined as “HF pulse (2 s) → N<sub>2</sub> purge (90 s) → TMA pulse (1 s) → N<sub>2</sub> purge (90 s)”, and 15 cycles of HF/TMA exposure were performed at 240 °C after either ZnO or Al<sub>2</sub>O<sub>3</sub> predeposition on QCM crystals at 150 °C.

95% pure diethylzinc (DEZ) from Strem Chemicals and DI water were used to deposit ZnO films on QCM crystals. One cycle of DEZ/H<sub>2</sub>O was defined as “DEZ pulse (0.5 s) → N<sub>2</sub> purge

(60 s) → H<sub>2</sub>O pulse (0.1 s) → N<sub>2</sub> purge (60 s)", and 100 cycles of DEZ/H<sub>2</sub>O exposure at 150 °C were performed before the HF/TMA exposures at 240 °C.

One cycle of TMA/H<sub>2</sub>O was defined as "TMA pulse (0.5 s) → N<sub>2</sub> purge (60 s) → H<sub>2</sub>O pulse (0.1 s) → N<sub>2</sub> purge (60 s)", and 100 cycles of TMA/H<sub>2</sub>O exposure at 150 °C were performed before the HF/TMA exposures at 240 °C.

### 5.3.7 Characterization.

For monitoring mass uptake on TiO<sub>2</sub> or W films during deposition, a quartz crystal microbalance probe (Kurt Lesker) with a 6 MHz gold-coated crystal sensor (Inficon) was inserted into the reactor and kept in the reactor at least 120 min to be thermally stabilized. To avoid deposition on the exposed electrical contacts, the backside of the crystal was purged with 25 sccm of carrier gas flow during the measurement. In situ mass loading (ng/cm<sup>2</sup>) was obtained by electronic data acquisition.

W or TiO<sub>2</sub> thickness was measured by ex situ spectroscopic ellipsometry (alpha-SE ellipsometer, J.A. Woollam) in the 380–890 nm of wavelength ( $\lambda$ ) at 70 ° incident angle. A Cauchy model provided from J.A. Woollam was used to calculate the TiO<sub>2</sub> thickness. The values for W thickness were estimated by correlating ellipsometry parameters  $\Delta$  and  $\Psi$  collected at  $\lambda = 700$  nm to film thickness.<sup>31</sup>

Chemical composition of obtained TiO<sub>2</sub> and W films was characterized using ex situ X-ray photoelectron spectroscopy (XPS, Kratos Analytical Axis Ultra) with an Al K $\alpha$  (1486.6 eV) gun (operating at 15 kV and 10 mA). A neutralizer was used to reduce the charging effect. Survey and high-resolution scans were carried out for C 1s, O 1s, F 1s, Cl 2p, Ti 2p, W 4f, W 4d, B 1s, and Si 2p. Casa XPS software was used to process the collected raw data, and peak positions were

calibrated with the adventitious C 1s peak as 284.8 eV. The high-resolution and survey scans were used to obtain atomic concentrations (at. %).

Angled- and top-view images of patterned samples were obtained using field emission scanning electron microscopy (SEM, FEI Verios 460L). A high-current Ga<sup>+</sup> liquid metal focused ion beam (FIB; FEI Quanta 3D FEG) was used to prepare samples for TEM. The dual beam FIB provided 7 nm resolution at 30 keV for the ion column and 1.2 nm resolution at 30 keV for the SEM column. Prior to the lift-out, samples were coated with a Pt capping layer with thickness of ~3.2 μm. The Ga<sup>+</sup> ion source was used to mill-out a 20 μm × 2 μm region, followed by a final milling to ~100 nm thickness using of 5 kV at 48 pA ion emission current. The TEM specimen was then removed from the sample using a micromanipulator and placed directly onto a 3 mm diameter Cu TEM grid. Cross-sectional images of patterned samples were collected by transmission electron microscopy (TEM; FEI Talos F200X) operated at 200 kV with 0.12 nm resolution. The TEM camera (ThermoFisher Ceta) acquired images with 4k × 4k resolution. Energy-dispersive X-ray spectroscopy element mapping was performed using scanning transmission electron microscopy (STEM). In STEM mode, the HAADF images were acquired with camera length of ~100 mm. The FEI Talos F200X TEM uses the Super-X EDX system, which is comprised of four in-column EDX detectors with a collection angle of ~0.9 sr. The typical parameters for STEM-EDX used a beam current of 350 pA, and each EDX collection time exceeded 5 min.

#### 5.4 Results and Discussion

The reaction scheme for self-aligned pattern generation using simultaneous deposition and etching is shown in **Figure 5.1a**. For this example system, a surface with open Si-H and TiO<sub>2</sub>

regions is exposed to multiple cycles of SiH<sub>4</sub>/WF<sub>6</sub> co-reactants separated by Ar purge at 220 °C, resulting in W deposition on the Si–H region and simultaneous etching of the sacrificial TiO<sub>2</sub>. We performed *in situ* QCM experiments to monitor the surface mass change on two different surfaces exposed to the same reaction conditions, and results are given in **Figure 5.1b**. For this study, a QCM crystal was pretreated *in situ* with 25 cycles of Al<sub>2</sub>O<sub>3</sub> ALD to create a surface receptive to W growth, similar to QCM crystals coated with silicon.<sup>26</sup> This was followed immediately in the same reactor by 20 cycles of sequential SiH<sub>4</sub>/Ar/WF<sub>6</sub>/Ar exposures at 220 °C.<sup>27</sup>

The blue line in **Figure 5.1b** shows the mass change (ng/cm<sup>2</sup>) during the SiH<sub>4</sub>/WF<sub>6</sub> cycles, indicating that after a few initial cycles this process gives net atomic layer deposition of tungsten on Al<sub>2</sub>O<sub>3</sub>. Consistent with previous studies,<sup>26</sup> after ~5 cycles of growth initiation on Al<sub>2</sub>O<sub>3</sub>, mass increases linearly with cycles, which on the basis of the density of W correlates to a W growth rate of ~0.5 nm/cycle. The black line in **Figure 5.1b** gives the mass change collected during 20 cycles of SiH<sub>4</sub>/Ar/WF<sub>6</sub>/Ar under identical reactor conditions, except, for this case, the QCM crystal was prepared by coating with 200 cycles of TiO<sub>2</sub> ALD using TiCl<sub>4</sub>/H<sub>2</sub>O doses at 220 °C. The results show a small mass gain due to initial uptake of tungsten and fluorine, followed by net mass loss, consistent with TiO<sub>2</sub> etching *via* reaction with WF<sub>6</sub> to form volatile WF<sub>2</sub>O<sub>2</sub> (g).<sup>28,29</sup> Using the density of TiO<sub>2</sub>, the mass change correlates with a loss of ~2 nm during the 20 cycles, for an average of ~0.1 nm/cycle.<sup>28,29</sup>

**Figure 5.1b** also includes schematics of the reactions corresponding to the QCM results, and **Figure 5.1c and d** show corresponding thermodynamic equilibrium analysis of the expected reactions and reaction products.<sup>30</sup> When SiH<sub>4</sub> and WF<sub>6</sub> react on a receptive growth surface, the net Gibbs free energy change (black line in **Figure 5.1c**) shows large  $-\Delta G$  values across a wide temperature range. The SiH<sub>4</sub> acts as a reducing agent, with some Si–H remaining on the surface

after exposure. The surface Si–H is then available to promote reduction and net deposition during the WF<sub>6</sub> exposure step.<sup>27,31</sup> This produces the stepwise mass uptake observed in the QCM data. On the TiO<sub>2</sub> surface, however, etching reactions become available. In **Figure 5.1c**, the red line shows the overall Gibbs free energy change when SiH<sub>4</sub> and WF<sub>6</sub> react with TiO<sub>2</sub>. For temperatures above 75 °C, a favorable reaction ( $\Delta G < 0$ ) yields volatile TiF<sub>4</sub> and WF<sub>2</sub>O<sub>2</sub>, with no net reaction for the SiH<sub>4</sub>. Because SiH<sub>4</sub> does not react on TiO<sub>2</sub> at low temperature, surface Si–H groups are not available to reduce the WF<sub>6</sub>, thereby promoting WF<sub>6</sub> to react and be consumed by the etch reaction. Likewise, **Figure 5.1d** gives the expected equilibrium product concentrations when WF<sub>6</sub> reacts with TiO<sub>2</sub> at different temperatures. At 220 °C, the expected products are TiF<sub>4</sub> and WF<sub>2</sub>O<sub>2</sub> vapors. Some tungsten oxide solid may also be expected, but oxide buildup is avoided due to continued formation of WF<sub>2</sub>O<sub>2</sub> (g) as a volatile etch product.<sup>28,29</sup> For the SiH<sub>4</sub>/WF<sub>6</sub> reaction on TiO<sub>2</sub>, the QCM results in **Figure 5.1b** are consistent with negligible reaction during SiH<sub>4</sub> and net mass loss during the WF<sub>6</sub> dose. XPS surface analysis results **Figure 5.6** further confirm minimal reaction with SiH<sub>4</sub>.

We also used ellipsometry and XPS to analyze simultaneous deposition and etching reactions during SiH<sub>4</sub>/WF<sub>6</sub> exposure on Si–H and TiO<sub>2</sub> surfaces. On patterned wafers discussed below, Si–H and TiO<sub>2</sub> surfaces are formed by applying TiO<sub>2</sub> ASD to Si–H/SiO<sub>2</sub> patterns. This is followed by W ASD, producing a multiple-material orthogonal ASD sequence<sup>25</sup> (*i.e.*, TiO<sub>2</sub> ASD on SiO<sub>2</sub> followed by W ASD on Si–H). Therefore, for ellipsometry and XPS analysis, the starting Si–H and TiO<sub>2</sub> samples also were prepared by TiO<sub>2</sub> ASD, following the same procedure used below for Si–H/TiO<sub>2</sub>-patterned wafers. Specifically, a pair of silicon wafer pieces, one with silicon oxide (Si–OH) and one with Si–H termination, were simultaneously exposed to TiO<sub>2</sub> ASD at 150 °C using a “supercycle” sequence, including TiO<sub>2</sub> ALD cycles with periodic atomic layer etching

steps.<sup>16</sup> This was followed by a 5 s dip in dilute (5%) HF solution and immediate transfer to the SiH<sub>4</sub>/WF<sub>6</sub> reactor. The intermediate HF dip step facilitated the desired W nucleation on Si-H and removed ~5 nm of the deposited TiO<sub>2</sub> layer (**Figure 5.7** and **Table 5.4**). The procedure was also tested without any intermediate treatment and with intermediate H<sub>2</sub>/Ar plasma exposure. As discussed in the **Supporting Information**, samples without HF treatment or with H<sub>2</sub>/Ar plasma exposure showed an unfavorable delay in W growth on the Si-H. Therefore, the HF dip was used for further analysis.

After TiO<sub>2</sub> ASD on Si-OH and Si-H, ellipsometry data (**Table 5.4**) shows TiO<sub>2</sub> thickness of 16.4 nm on the Si-OH and ~1.9 nm on the Si-H. After HF, ellipsometry showed no oxide on Si-H, with 11.4 nm of TiO<sub>2</sub> on the Si-OH, indicating a loss of ~5 nm of TiO<sub>2</sub>. After simultaneous exposure to 15 cycles of SiH<sub>4</sub>/WF<sub>6</sub> at 220 °C, the Si-H sample showed a net growth of 9.7 nm of W, while the TiO<sub>2</sub> film showed a net thickness decrease of ~1.1 nm. Using newly prepared Si-H and TiO<sub>2</sub> samples, the experiment was repeated using 20 cycles of SiH<sub>4</sub>/WF<sub>6</sub>. On Si-H, 20 SiH<sub>4</sub>/WF<sub>6</sub> cycles produced 12.6 nm of W, with a net TiO<sub>2</sub> thickness decrease of ~1.4 nm.

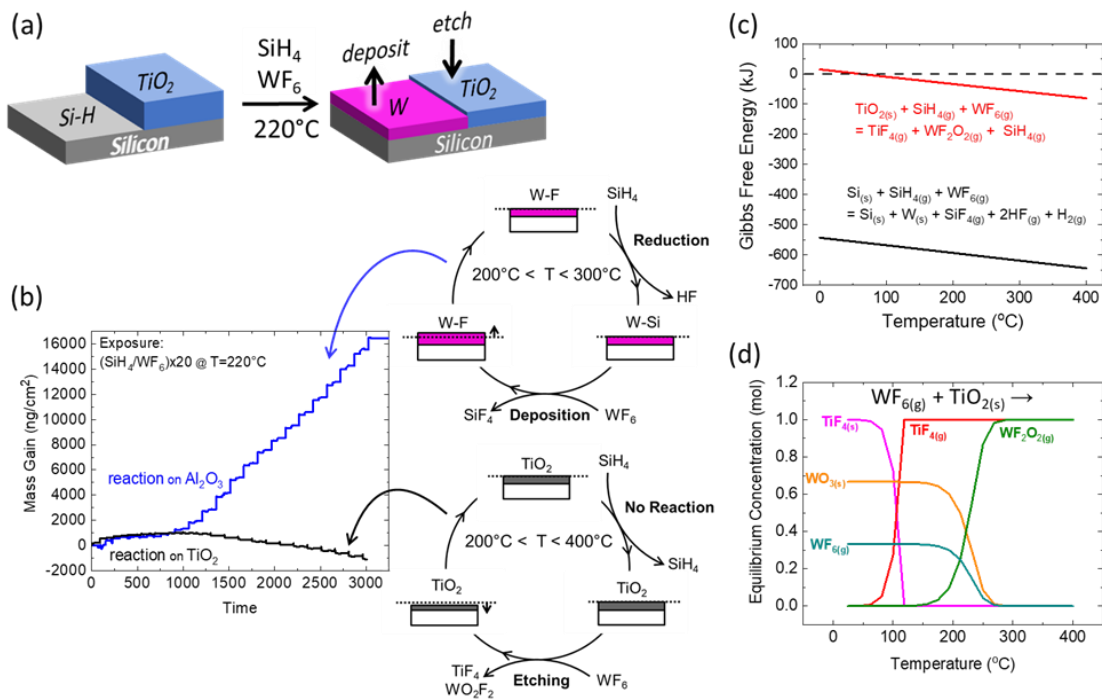


**Figure 5.1** Schematic for self-aligned patterning using simultaneous deposition and etching: (a) starting Si–H/TiO<sub>2</sub> pattern exposed to a set of reactants (in this example, SiH<sub>4</sub>/WF<sub>6</sub> in an ALD-type reaction sequence for 20 cycles), yielding W growth on silicon, with no growth in the TiO<sub>2</sub> region due to simultaneous TiO<sub>2</sub> etching. (b) Mass change (ng/cm<sup>2</sup>) measured by QCM during SiH<sub>4</sub>/WF<sub>6</sub> exposures (SiH<sub>4</sub>/Ar/WF<sub>6</sub>/Ar = 45/45/1/60 s) at 220 °C, along with the expected reactions during SiH<sub>4</sub> and WF<sub>6</sub> exposure steps on W and on TiO<sub>2</sub> surfaces. The indicated product species are from thermodynamic analysis. A QCM precoated with Al<sub>2</sub>O<sub>3</sub> shows net mass gain indicating favorable ALD of W (blue line). On the basis of the density of W, the growth rate is ~0.5 nm/cycle. Under identical conditions, a QCM crystal precoated with TiO<sub>2</sub> shows net mass loss corresponding to etching (black line), with an etch rate of ~0.1 nm/cycle. (c) Overall Gibbs free energy change for SiH<sub>4</sub>/WF<sub>6</sub> reactions on TiO<sub>2</sub> (red) and Si (black) surfaces, consistent with the QCM results in panel b. (d) Thermodynamic equilibrium product compositions for WF<sub>6</sub> reacting with an equimolar composition of TiO<sub>2</sub>, further supporting simultaneous deposition and etching.

The measured thickness change indicates the SiH<sub>4</sub>/WF<sub>6</sub> allowed simultaneous deposition and etching, consistent with QCM in **Figure 5.1**. From the thickness data, the W deposition rate is ~0.6 nm/cycle and the etch rate of the TiO<sub>2</sub> is ~0.1 nm per ALD cycle, in reasonable agreement with the deposition rate of ~0.5 nm/cycle and etch rate of ~0.1 nm/cycle estimated from the QCM results in **Figure 5.1b**. Under the conditions used, this etching rate is sufficient to avoid W growth.

For this approach to be useful, it should be compatible with different methods to form patterned sacrificial materials. A possible issue is that the rate of etching will depend on the process used to form the sacrificial layer. For example, using TiO<sub>2</sub> deposited by physical vapor deposition, initial experiments show a slower etch rate. The slower etching consumes less reactant, and therefore promotes unwanted deposition. To address this, the process provides flexibility to allow tuning of the relative deposition and etching rates. For the W/TiO<sub>2</sub> system, increasing substrate temperature from 220 to 275 °C does not substantially change the W deposition rate,<sup>27</sup> but a larger etching rate is observed (**Table 5.5**), thereby allowing process adjustment and optimization.

The same blanket samples used for thickness measurement were also analyzed by XPS to evaluate the surface element composition after SiH<sub>4</sub>/WF<sub>6</sub> treatment, and results are shown in **Table 5.1**. As expected, all samples show oxygen and carbon resulting from exposure to the ambient between deposition and analysis. On the Si-H surface, both 15 and 20 SiH<sub>4</sub>/WF<sub>6</sub> cycles lead to strong W signals, consistent with expected W deposition on the receptive Si-H. Also as expected, the signal from Ti 2p was below the detection limit (<0.1 at. %). A small Si signal after SiH<sub>4</sub>/WF<sub>6</sub> is ascribed to remnant surface silicon from the silane reducing agent. On the TiO<sub>2</sub> surface, the SiH<sub>4</sub>/WF<sub>6</sub> leads to a small amount of W (~2.5–4.1 at. %), ascribed to formation of tungsten oxides, as expected from the thermodynamic analysis shown in **Figure 5.1d**.<sup>29</sup> We also note that the amount of W on TiO<sub>2</sub> does not increase when the number of W ALD cycles increases from 15 to

20, further indicating that tungsten oxide does not accumulate on the TiO<sub>2</sub>.<sup>28,29</sup> This small amount of tungsten oxide on the TiO<sub>2</sub> can be effectively removed by exposing the surface to BCl<sub>3</sub> vapor at the reaction temperature (**Table 5.6**).

**Table 5.1** XPS atomic fraction (at.%) measured on Si-H and TiO<sub>2</sub> before and after exposure to 15 or 20 cycles of SiH<sub>4</sub>/WF<sub>6</sub> at 220 °C.<sup>a</sup>

Surface	SiH <sub>4</sub> /WF <sub>6</sub> @ 220 °C	XPS atomic fraction (at.%)							
		Ti 2p	W 4d	Si 2p	O 1s	F 1s	Cl 2p	B 1s	C 1s
Si-H	none	0	0	79.2	7.5	1.2	0	0	12.1
	15 cycles	0	20.2	1.5	53.7	0.3	0	0	24.3
	20 cycles	0	22.2	2.6	47.4	0	0	0	27.8
TiO <sub>2</sub>	none	18.0	0.4	0	48.5	6.8	0.7	4.9	20.7
	15 cycles	17.7	4.1	0.2	55	2.1	0.4	3	17.5
	20 cycles	15.1	2.5	1.6	52	1.3	0	2.5	25

<sup>a</sup>The starting Si-H and TiO<sub>2</sub> were prepared by exposing Si-H or Si-OH wafers to TiO<sub>2</sub> ALD/ALE supercycles,<sup>16</sup> following the same procedure applied to Si-H/SiO<sub>2</sub> patterned wafers discussed in the text.

We applied this approach on microscale and nanoscale line/space patterns. Microscale-patterned substrates, used previously for ASD studies,<sup>16,31,32</sup> consisted of 3 μm wide SiO<sub>2</sub> lines, ~100 nm thick, separated by 3 μm of exposed Si-H (*i.e.*, 6 μm full-pitch). To form the patterned sacrificial TiO<sub>2</sub> layers, Si-H/SiO<sub>2</sub> samples were coated at 150 °C by ASD TiO<sub>2</sub> using a supercycle sequence as mentioned above. A sequence of 20 supercycles produced ~16.4 nm of TiO<sub>2</sub> atop the SiO<sub>2</sub> regions, with minimal TiO<sub>2</sub> on adjacent Si-H regions.<sup>16</sup> After TiO<sub>2</sub> ASD, samples were treated with a 5 s dip in dilute (5%) HF solution and immediately transferred to the SiH<sub>4</sub>/WF<sub>6</sub>

reactor to perform the second ASD step using simultaneous W deposition and TiO<sub>2</sub> etching. This sequence of TiO<sub>2</sub> ASD on SiO<sub>2</sub> followed by W ASD on Si-H provides an experimental demonstration of multiple-material orthogonal ASD.<sup>25</sup>

The resulting microscale self-aligned W/TiO<sub>2</sub> patterns are shown in **Figures 5.2 and 5.3**. **Figure 5.2b** shows cross-sectional STEM images and corresponding STEM-EDX data after treating the TiO<sub>2</sub>/Si-H pattern with 15 cycles of SiH<sub>4</sub>/WF<sub>6</sub> at 220 °C. A tungsten film with thickness of  $7.0 \pm 0.4$  nm (given as the mean of 8 measurements  $\pm$  1 standard deviation) is visible only on the Si-H region, and the TiO<sub>2</sub> is visible only atop the SiO<sub>2</sub>. The remaining ASD TiO<sub>2</sub> layer is  $4.9 \pm 0.3$  nm thick, indicating that the HF dip + SiH<sub>4</sub>/WF<sub>6</sub> treatment removed  $\sim$ 11 nm of TiO<sub>2</sub>. The experiment was repeated on another TiO<sub>2</sub>/Si-H substrate with  $\sim$ 16.4 nm of ASD TiO<sub>2</sub>, except for the second ASD step; the SiH<sub>4</sub>/WF<sub>6</sub> exposure was performed for 20 cycles. **Figure 5.2c** shows the resulting STEM and STEM-EDX images. In this case, the samples show  $10.0 \pm 0.6$  nm of W on Si-H, with no visible TiO<sub>2</sub> on the SiO<sub>2</sub>. The 20 W ALD cycles were sufficient to completely remove the sacrificial TiO<sub>2</sub>, while simultaneously depositing 10 nm of W in the neighboring Si-H regions.

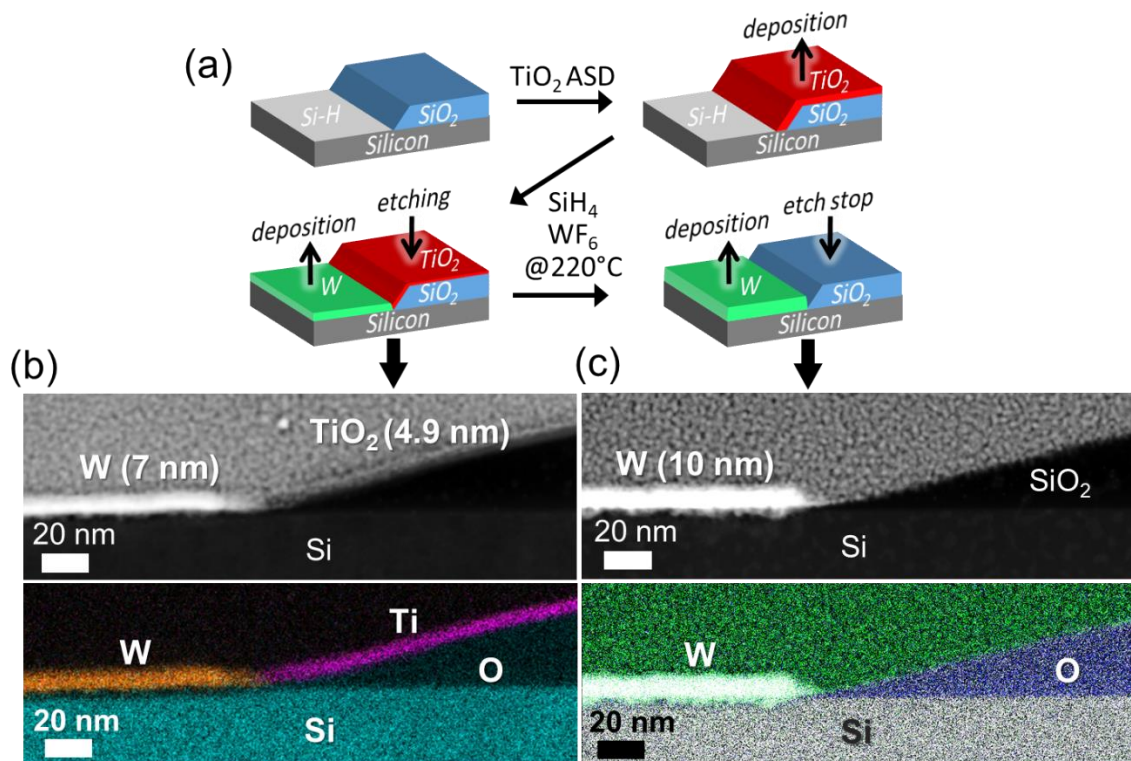


**Figure 5.2** Self-aligned orthogonal micro-scale patterning of TiO<sub>2</sub> and W films: (a) schematic sequence used for preparation of patterned sacrificial TiO<sub>2</sub> layer, followed by simultaneous deposition and etching to form the self-aligned W and TiO<sub>2</sub>; (b) cross-sectional STEM and STEM-EDX after 15 SiH<sub>4</sub>/WF<sub>6</sub> cycles; and (c) data collected from an identical sample after 20 SiH<sub>4</sub>/WF<sub>6</sub> cycles. The images show the SiH<sub>4</sub>/WF<sub>6</sub> cycles produce net W deposition in exposed Si-H regions, with simultaneous etching of the sacrificial TiO<sub>2</sub> layer.

Comparing the thicknesses of the TiO<sub>2</sub> and W films in **Figure 5.2** to those measured by ellipsometry on blanket substrates following identical process conditions, the patterned wafers show somewhat thinner W layers. The patterned wafers also show net thinner TiO<sub>2</sub> layers compared to the blanket samples. This thinner TiO<sub>2</sub> layer may result from faster etching on the patterned surface. Mechanisms leading to pattern-dependent deposition and etching rates are well-known during ASD<sup>3,9,31,33</sup> and generally relate to gas-transport and surface diffusion effects that alter the local reactant concentration and supersaturation across the sample surface. As discussed below, understanding pattern-dependent reaction rates remains an overarching issue for self-aligned deposition-based patterning.

The self-aligned patterned samples shown in **Figure 5.2** were also analyzed by angled-view SEM, and images are presented in **Figure 5.3**. **Figure 5.3a** shows a control Si-H/SiO<sub>2</sub> wafer (with no TiO<sub>2</sub> initially present) treated with 20 cycles of SiH<sub>4</sub>/WF<sub>6</sub>. The SiH<sub>4</sub>/WF<sub>6</sub> produces a cohesive W film on Si-H, and the rough texture on SiO<sub>2</sub> is consistent with W nuclei.<sup>31</sup> **Figure 5.3b** shows the sample from **Figure 5.2b**, corresponding to Si-H/TiO<sub>2</sub> after 15 cycles of SiH<sub>4</sub>/WF<sub>6</sub>. Both the TiO<sub>2</sub> and W regions appear smooth, with no visible W nuclei on the TiO<sub>2</sub>. **Figure 5.3c** shows the sample from **Figure 5.2c**, identical except after 20 SiH<sub>4</sub>/WF<sub>6</sub> cycles. Some particles appear in the SiO<sub>2</sub> region likely corresponding to W nuclei that are expected to form after complete consumption of the TiO<sub>2</sub>. Similarly sized nuclei (10–20 nm) formed during ASD were previously analyzed using SEM-EDX, but sensitivity was limited by the small volume of the nuclei.<sup>16</sup>

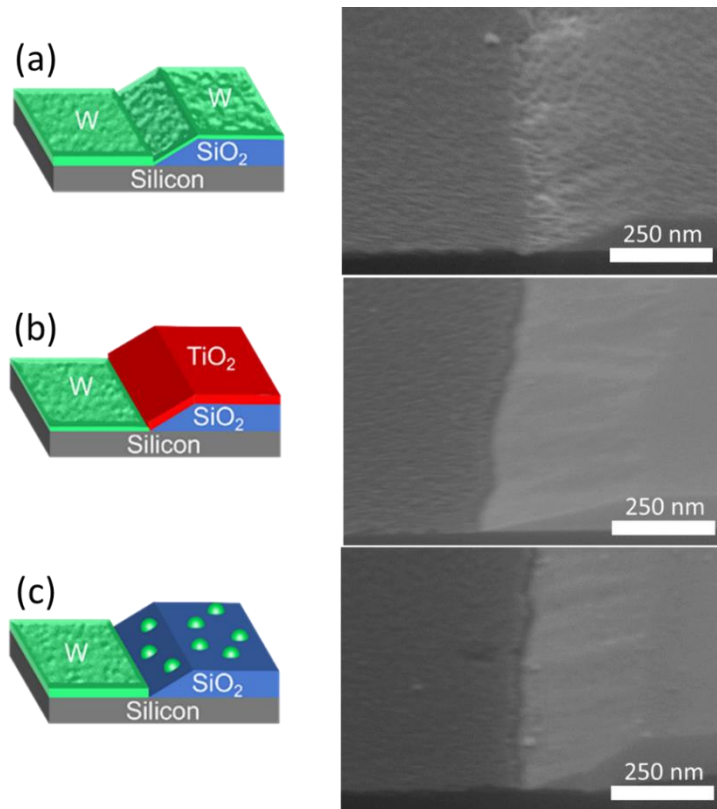


**Figure 5.3** Angled view SEM for: (a) Si-H/SiO<sub>2</sub> patterns with no TiO<sub>2</sub> present after 20 cycles of SiH<sub>4</sub>/WF<sub>6</sub>, indicating W deposition on both of Si-H and SiO<sub>2</sub>; (b) the sample from **Figure 5.2b**, showing surface texture consistent with W deposition on Si-H and simultaneous etching of the TiO<sub>2</sub>; and (c) the sample from **Figure 5.2c** showing a small number of W nuclei on SiO<sub>2</sub>, consistent with consumption of the TiO<sub>2</sub> sacrificial layer.

We further confirmed that the approach could extend to nano-scaled patterns, and results are given in **Figure 5.4**. The figure includes a schematic diagram, along with corresponding STEM and STEM-EDX images of self-aligned W and TiO<sub>2</sub> on ~200 nm of Si-H/SiO<sub>2</sub>-patterned substrates (~400 nm full-pitch) using the same condition as for samples in **Figure 5.2b**. Four neighboring features in **Figure 5.4b** show consistent pattern duplication, with an expanded higher resolution view of one example region in **Figure 5.4c, d**. The sequence yielded  $6.1 \pm 0.5$  nm of W on the Si-H region and  $5.8 \pm 0.3$  nm of TiO<sub>2</sub> on the SiO<sub>2</sub>. These values are reasonably similar to those in **Figure 5.2b** obtained on the 3  $\mu$ m features.

Careful inspection of the high-resolution images shows that the TiO<sub>2</sub> layer may be thinner on top of the corner edge of the SiO<sub>2</sub>, possibly indicating faster TiO<sub>2</sub> etching on exposed corners. The high-resolution images also show uniform W thickness on the exposed silicon, with no visible W nuclei on the TiO<sub>2</sub>. The TiO<sub>2</sub>/W feature edge boundaries appear well-defined, but understanding feature development at the atomic scale remains a challenge. **Figure 5.8** shows additional TEM/STEM images of self-aligned nanopatterned W/TiO<sub>2</sub> samples.

This work presents simultaneous deposition and etching as a route for direct-patterned area-selective deposition. Also importantly, as shown in **Figures 5.2 and 5.4**, we show that the starting sacrificial pattern can be formed by area-selective deposition, thereby confirming experimental feasibility for orthogonal multiple-material patterning<sup>25</sup> as a step forward in bottom-up nanomaterial surface synthesis.

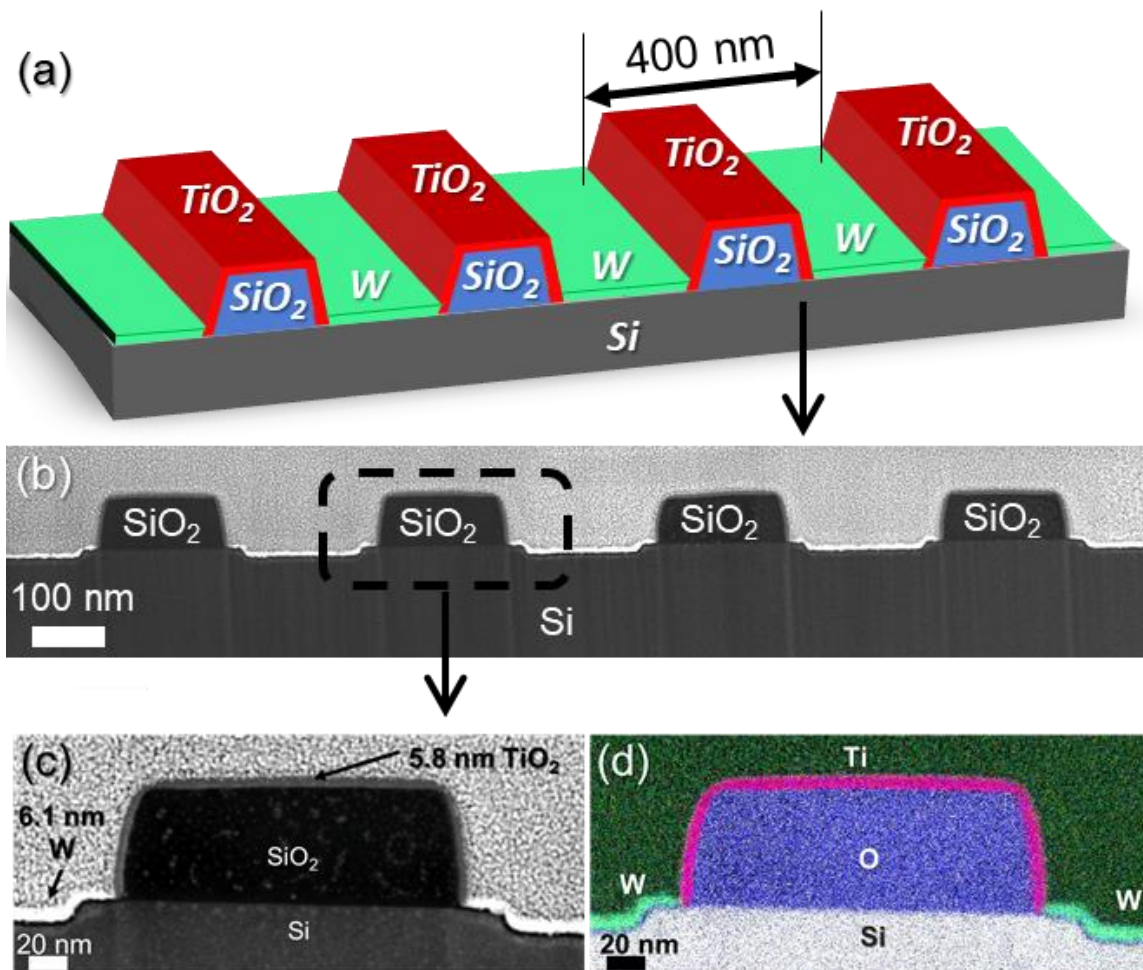


**Figure 5.4** (a) Broad-view schematic of the orthogonal selective deposition of W and  $\text{TiO}_2$  on Si-H/ $\text{SiO}_2$  patterned surfaces (200 nm width and  $\sim 100$  nm height) after  $\text{TiO}_2$  20 supercycles and W 15 cycles; (b) cross-sectional STEM of the multiple patterns; (c) zoom-in view of one pattern from (b); (d) STEM-EDX corresponding to image (c).

#### 5.4.1 Extension to Other Material Systems.

In addition to the W/TiO<sub>2</sub> system, thermodynamic modeling<sup>30</sup> and published rate data indicate that simultaneous deposition and etching can be achieved for a range of other deposition and sacrificial materials. Examples are presented in **Table 5.2**. The table include calculated values of the Gibbs free energy changes for atomic layer deposition and etching and the approximate overlapping temperature range, where both reactions are expected to be energetically favorable. Where available, the table also includes experimental values for atomic layer deposition and etching rates at an example temperature within the favorable temperature range. For some systems, a range of etch rates is reported because etch kinetics can depend strongly on detailed process conditions. The etching rates (nm/cycle) correspond to the expected thickness loss during the simultaneous atomic layer deposition cycle. We further note that, for some materials sets, reaction thermodynamics may favor simultaneous deposition and etching but slow reaction kinetics may make them experimentally difficult. The deposition reactions are expected to proceed on any receptive surface where etching does not occur.

As one example, data in **Table 5.2** indicate that, with use of trimethylaluminum (TMA) and hydrogen fluoride (HF) as co-reactants at 240 °C, a receptive surface (such as Al<sub>2</sub>O<sub>3</sub>)<sup>34</sup> is expected to yield favorable deposition of AlF<sub>3</sub>. Further, when a ZnO surface is exposed to these same conditions, reaction energetics favors ZnO atomic layer etching, producing volatile dimethyl zinc, dimethyl aluminum fluoride, and water.<sup>35</sup>

To confirm the feasibility of the AlF<sub>3</sub> and ZnO system, we used QCM analysis to observe mass changes on different surfaces exposed to HF/TMA and results are shown in **Figure 5.5**. For these data, the experimental procedure follows that was used to collect data in **Figure 5.1**. First, a QCM crystal was precoated with ALD Al<sub>2</sub>O<sub>3</sub> at 150 °C to be receptive to AlF<sub>3</sub>, followed by

exposure to repeated doses of HF and TMA at 240 °C. The data in **Figure 5.5** show stepwise mass gain, consistent with ALD of  $\text{AlF}_3$ .<sup>34</sup> Also in **Figure 5.5**, a second QCM crystal was precoated with ZnO at 150 °C and then exposed to HF/TMA under identical conditions at 240 °C. The QCM results show clear mass loss, consistent with ZnO etching.<sup>35</sup> Therefore, the concept demonstrated above for simultaneous deposition and etching can also be extended to other ASD material systems, including  $\text{AlF}_3$  on  $\text{Al}_2\text{O}_3$  with sacrificial etching of neighboring ZnO.

**Table 5.2** A partial list of example material systems showing thermodynamic feasibility for self-aligned patterning *via* simultaneous deposition and etching.

ASD Material	Sacrificial Material	Reactants	T range (°C)	Expected Reactions		Example T (°C)	Rate (nm/cycle)	$\Delta G$ (kJ/mol) @ T (°C)	Ref.
W	TiO <sub>2</sub>	SiH <sub>4</sub> WF <sub>6</sub>	200 - 300	Deposition	$\text{SiH}_{4(g)} + \text{WF}_{6(g)} \rightarrow \text{W}_{(s)} + \text{SiF}_{4(g)} + 2\text{HF}_{(g)} + \text{H}_{2(g)}$	220	0.58	-598	This work, 3
				Etching	$\text{TiO}_{2(s)} + \text{WF}_{6(g)} \rightarrow \text{TiF}_{4(g)} + \text{WO}_2\text{F}_{2(g)}$				0.02 — 0.2
WO <sub>3</sub>	TiO <sub>2</sub>	SiH <sub>4</sub> WF <sub>6</sub> H <sub>2</sub> O	200 - 275	Deposition	$\text{SiH}_{4(g)} + \text{WF}_{6(g)} + 3\text{H}_2\text{O}_{(g)} \rightarrow \text{WO}_{3(s)} + \text{SiF}_{4(g)} + 2\text{HF}_{(g)} + 4\text{H}_{2(g)}$	220	0.58	-653	3,5
				Etching	$\text{TiO}_{2(s)} + \text{WF}_{6(g)} \rightarrow \text{TiF}_{4(g)} + \text{WO}_2\text{F}_{2(g)}$				0.02 — 0.2
WO <sub>3</sub>	TiN	H <sub>2</sub> O SiH <sub>4</sub> WF <sub>6</sub>	200 - 275	Deposition	$\text{SiH}_{4(g)} + \text{WF}_{6(g)} + 3\text{H}_2\text{O}_{(g)} \rightarrow \text{WO}_{3(s)} + \text{SiF}_{4(g)} + 2\text{HF}_{(g)} + 4\text{H}_{2(g)}$	220	0.58	-653	3,5
				Etching	$\text{TiN}_{(s)} + 2\text{H}_2\text{O}_{(g)} + \text{WF}_{6(g)} \rightarrow \text{TiF}_{4(g)} + \text{WO}_2\text{F}_{2(g)} + \text{NH}_3(g) + 0.5\text{H}_{2(g)}$				0.02 — 0.2
WS <sub>2</sub>	TiO <sub>2</sub>	WF <sub>6</sub> H <sub>2</sub> S	250 - 300	Deposition	$\text{WF}_{6(g)} + 3\text{H}_2\text{S}_{(g)} \rightarrow \text{WS}_{2(s)} + 6\text{HF}_{(g)} + 0.5\text{S}_{2(g)}$	300	~ 0.1	-205	6
				Etching	$\text{TiO}_{2(s)} + \text{WF}_{6(g)} \rightarrow \text{TiF}_{4(g)} + \text{WO}_2\text{F}_{2(g)}$				~ 0.3
AlF <sub>3</sub>	ZnO	HF TMA	200 - 250	Deposition	$3\text{HF}_{(g)} + \text{Al}(\text{CH}_3)_3(g) \rightarrow \text{AlF}_{3(s)} + 3\text{CH}_4(g)$	220	~ 0.05	-701	7
				Etching	$\text{ZnO}_{(s)} + 2\text{HF}_{(g)} + 2\text{Al}(\text{CH}_3)_3(g) \rightarrow \text{Zn}(\text{CH}_3)_2(g) + 2\text{AlF}(\text{CH}_3)_2(g) + \text{H}_2\text{O}_{(g)}$				0.11
AlF <sub>3</sub>	Ga <sub>2</sub> O <sub>3</sub>	HF TMA	200 - 250	Deposition	$3\text{HF}_{(g)} + \text{Al}(\text{CH}_3)_3(g) \rightarrow \text{AlF}_{3(s)} + 3\text{CH}_4(g)$	250	~ 0.05	-699	7
				Etching	$\text{Ga}_2\text{O}_3(s) + 6\text{HF}_{(g)} + 4\text{Al}(\text{CH}_3)_3(g) \rightarrow 3\text{H}_2\text{O}_{(g)} + 2\text{GaF}(\text{CH}_3)_2(g) + 4\text{AlF}(\text{CH}_3)_2(g)$				~ 0.082
Si <sub>3</sub> N <sub>4</sub>	HfO <sub>2</sub>	HF SiCl <sub>4</sub> NH <sub>3</sub>	300 - 350	Deposition	$3\text{SiCl}_{4(g)} + 4\text{NH}_3(g) \rightarrow \text{Si}_3\text{N}_{4(s)} + 12\text{HCl}_{(g)}$	350	0.2	-104	10
				Etching	$\text{HfO}_{2(s)} + 4\text{HF}_{(g)} + \text{SiCl}_{4(g)} \rightarrow 2\text{H}_2\text{O}_{(g)} + \text{SiF}_{4(g)} + \text{HfCl}_{4(g)}$				0.005
SnS	HfO <sub>2</sub>	HF Sn(acac) <sub>2</sub> H <sub>2</sub> S	200 - 250	Deposition	$\text{Sn}(\text{acac})_2(g) + \text{H}_2\text{S}_{(g)} \rightarrow \text{SnS}_{(s)} + 2\text{H}(\text{acac})_{(g)}$	200	0.019	< 0	12
				Etching	$\text{HfO}_{2(s)} + 4\text{HF}_{(g)} + 4\text{Sn}(\text{acac})_2(g) \rightarrow \text{Hf}(\text{acac})_4(g) + 4\text{SnF}(\text{acac})_{(g)} + 2\text{H}_2\text{O}_{(g)}$				0.006
SnS	Al <sub>2</sub> O <sub>3</sub>	HF Sn(acac) <sub>2</sub> H <sub>2</sub> S	200 - 250	Deposition	$\text{Sn}(\text{acac})_2(g) + \text{H}_2\text{S}_{(g)} \rightarrow \text{SnS}_{(s)} + 2\text{H}(\text{acac})_{(g)}$	200	0.019	< 0	12
				Etching	$\text{Al}_2\text{O}_3(s) + 6\text{HF}_{(g)} + 6\text{Sn}(\text{acac})_2(g) \rightarrow 2\text{Al}(\text{acac})_3(g) + 6\text{SnF}(\text{acac})_{(g)} + 3\text{H}_2\text{O}_{(g)}$				0.023

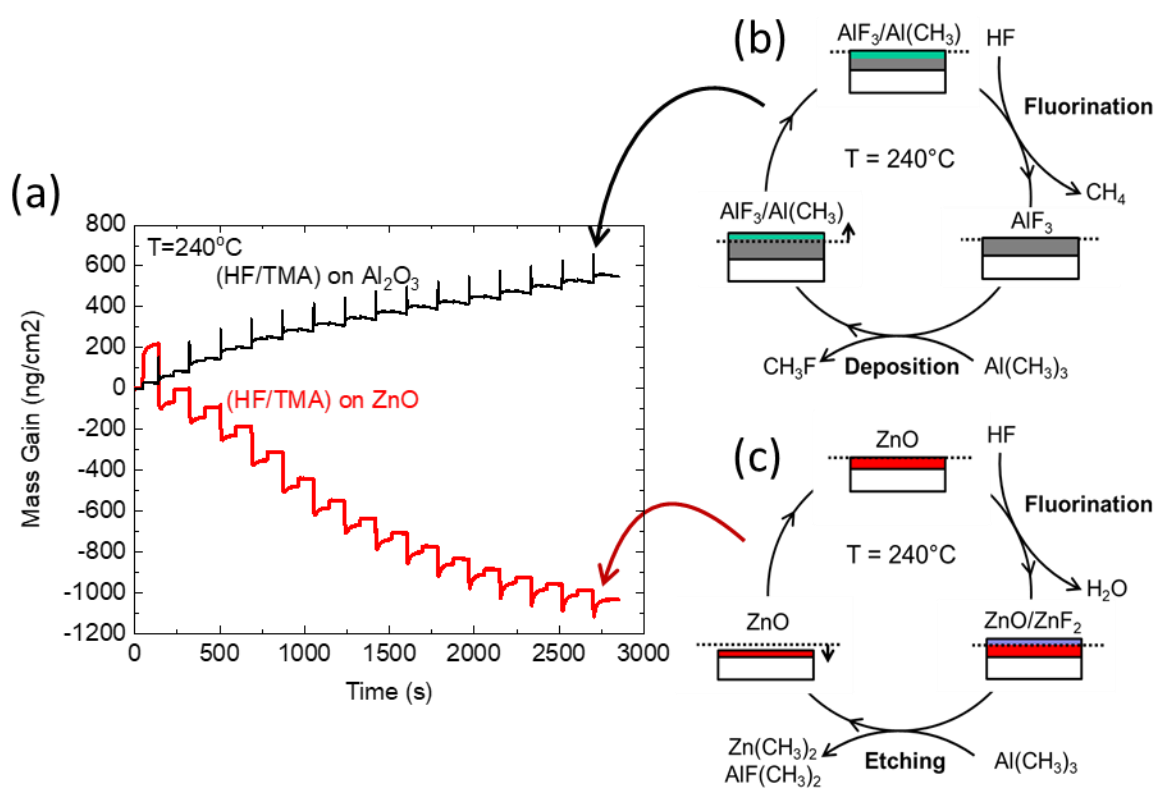


**Figure 5.5** (a) Collected QCM mass gain data from Al<sub>2</sub>O<sub>3</sub> or ZnO precoated crystals during 15 cycles of (HF/TMA) exposures. (b) AIF<sub>3</sub> deposition mechanism on Al<sub>2</sub>O<sub>3</sub> surface and (c) ZnO atomic layer etching mechanism on ZnO during 15 HF/TMA cycles. Reaction schemes indicate the expected dominant products from thermodynamic analysis.

## 5.5 Summary

In summary, our findings highlight the importance of thermodynamically designed surface chemistry for nanoscale self-aligned thin film patterning. Counterintuitively, results show that, at low temperatures, using a single set of reactants, it is possible for both deposition and etching to be favored at the same time on different regions of an exposed patterned surface. This means that unwanted nucleation, a broad problem in area-selective deposition, can be avoided because the etching reaction locally consumes the nucleation reactants. This approach to avoid unwanted nucleation may be useful for low-temperature self-aligned patterning in back-end electronics manufacturing and other nanoscale material systems. As one key prospect, we show a sequence of two deposition processes can orthogonally self-align two different materials in different regions on a single starting patterned substrate.

Our findings also reveal several challenges and remaining problems. One challenge is that reaction conditions should allow the etching and deposition rates to be balanced so that the etching rate is sufficient to consume the gas-phase reactants and avoid unwanted nucleation, with fast enough deposition to develop the desired pattern thickness. Also, while we show the approach works using tungsten and  $\text{TiO}_2$ , which are important materials in semiconductor processing, semiconductor device manufacturers are seeking self-aligned patterning solutions for a broad and expanding set of materials. Discovering additional material systems will require more extensive modeling and may include the design of new precursors and reactants. Another important outstanding problem is to what extent this process can apply to features approaching atomic scale dimensions. Results show uniform patterning at the 200 nm scale, but we see that etching and deposition rates may depend on feature shape and size. Further scaling will require better understanding of these effects.

Eventually, scaling of deposition-based self-aligned patterning to single-atom dimensions will allow ultimate precision in materials fabrication. Achieving this feat using designed surface chemistry will be a critical step toward producing large numbers of devices in parallel across large surface areas under conditions using limited thermal exposure.

## 5.6 Supporting Information

### 5.6.1 Effect of intermediate surface treatments (H<sub>2</sub>+Ar plasma and HF dip) on W growth

To achieve multi-material orthogonal area-selective deposition of W and TiO<sub>2</sub> on Si-H/SiO<sub>2</sub> patterns, the surface condition of the Si-H surface (*i.e.* the TiO<sub>2</sub> non-growth surface and W growth surface) after the TiO<sub>2</sub> ALD/ALE is important for favorable W growth. After multiple TiO<sub>2</sub> ALD/ALE supercycles, the Si-H surface can lose surface hydrogen termination allowing some surface oxidation.<sup>16,42</sup> The loss of hydrogen can allow partial oxidation of the Si-H during the water dose used for TiO<sub>2</sub> ALD (*i.e.* TiCl<sub>4</sub>/H<sub>2</sub>O), and this oxidation may inhibit the subsequent W growth, producing a net reduced rate of W ALD.<sup>43,44</sup>

Inhibited W growth in the Si-H region following TiO<sub>2</sub> ASD is observed in the experimental spectroscopic ellipsometry and XPS data in **Figure 5.7** and **Table 5.3**. **Figure 5.7a** shows spectroscopic ellipsometry parameter delta measured at 700 nm ( $\Delta_{700\text{nm}}$ ) on the Si-H samples after different surface treatments. Immediately following a 30 s dip in dilute HF solution, a clean Si-H surface shows  $\Delta_{700\text{nm}} = 178 \pm 1$  (1st data point on the left). After performing 10 cycles of W ALD on the clean Si-H at 220 °C, the  $\Delta$  parameter decreases to  $\Delta_{700\text{nm}} = 158 \pm 2$ .<sup>31</sup> However, if the clean Si-H is first exposed to 12 supercycles of ASD TiO<sub>2</sub> by ALD/ALE at 150 °C,<sup>16</sup> the same 10 cycles SiH<sub>4</sub>/WF<sub>6</sub> W ALD shows  $\Delta_{700\text{nm}} = 170$ , consistent with less W deposition.<sup>31</sup> In this case, the TiO<sub>2</sub> ALD/ALE produces a minimal amount of TiO<sub>2</sub> on the Si-H,<sup>5</sup> but the surface damage inhibits

subsequent W growth. Similar trends are shown in the XPS results in **Table 5.3**. After TiO<sub>2</sub> ALD/ALE, treating the surface with 10 cycles of SiH<sub>4</sub>/WF<sub>6</sub> (*i.e.* Si-H + TiO<sub>2</sub> + W) leads to only a small amount of W (3.7 at.%).

To improve the extent of W growth on Si-H after TiO<sub>2</sub> ALD/ALE, we compared samples prepared with three different sequences: 1) “TiO<sub>2</sub> + W”; 2) “TiO<sub>2</sub> + H<sub>2</sub>\* + W”; and 3) “TiO<sub>2</sub> + HF + W”. The TiO<sub>2</sub> treatment consisted of 12 ALD/ALE supercycles at 150 °C, and the W step was 10 cycles of SiH<sub>4</sub>/WF<sub>6</sub> at 220°C. We examined two intermediate steps between the TiO<sub>2</sub> and W steps: “H<sub>2</sub>\*” = 4% H<sub>2</sub>/Ar plasma for 300 s with 10 Watts power; and “HF” = 5 s dip in dilute 5% HF solution. As shown in **Figure 5.7a** using H<sub>2</sub>\* as the intermediate step (*i.e.* Si-H + TiO<sub>2</sub> + H<sub>2</sub>\* + W), ellipsometry showed  $\Delta_{700\text{nm}} = 167$ , whereas the HF dip (*i.e.* Si-H + TiO<sub>2</sub> + HF + W) produced  $\Delta_{700\text{nm}} = 161$ , indicating improved W growth with the HF treatment. **Figure 5.7b** shows XPS W 4d spectra for the samples prepared without intermediate treatment and with H<sub>2</sub>\* and HF intermediate treatment. The largest W signal is obtained using the HF intermediate treatment. The surface composition of each sample obtained by XPS is given in **Table 5.3**, further showing the HF step provides the most favorable W growth on Si-H after TiO<sub>2</sub> ALD/ALE.

While the HF treatment promotes favorable W growth on the Si-H surface, it is also expected to affect the deposited TiO<sub>2</sub> surface. To better understand the effect of the intermediate HF dipping treatment on the TiO<sub>2</sub>, we started with blanket Si-OH and Si-H substrates and treated them both to the same TiO<sub>2</sub> + HF + W treatments, producing net TiO<sub>2</sub> growth on the Si-OH and net W growth on the Si-H. After each process step, we measured the resulting thickness of TiO<sub>2</sub> (on Si-OH substrate) and W (on the Si-H substrate), and results are shown in **Figure 5.7c**. Note that W thickness is estimated by matching measured  $\Delta_{700\text{nm}}$  with published thickness *vs.*  $\Delta_{700\text{nm}}$  relation.<sup>31</sup> The TiO<sub>2</sub> step produced ~11.5 nm of TiO<sub>2</sub> on Si-OH. The HF dip etched ~ 2.1 nm of

this  $\text{TiO}_2$ . Then, the W sequence etched  $\sim 1$  nm of  $\text{TiO}_2$ , and simultaneously deposited  $\sim 5$  nm of W. On a similar sample without intermediate HF treatment, the W film thickness was  $\sim 2$  nm after 10  $\text{SiH}_4/\text{WF}_6$  cycles.

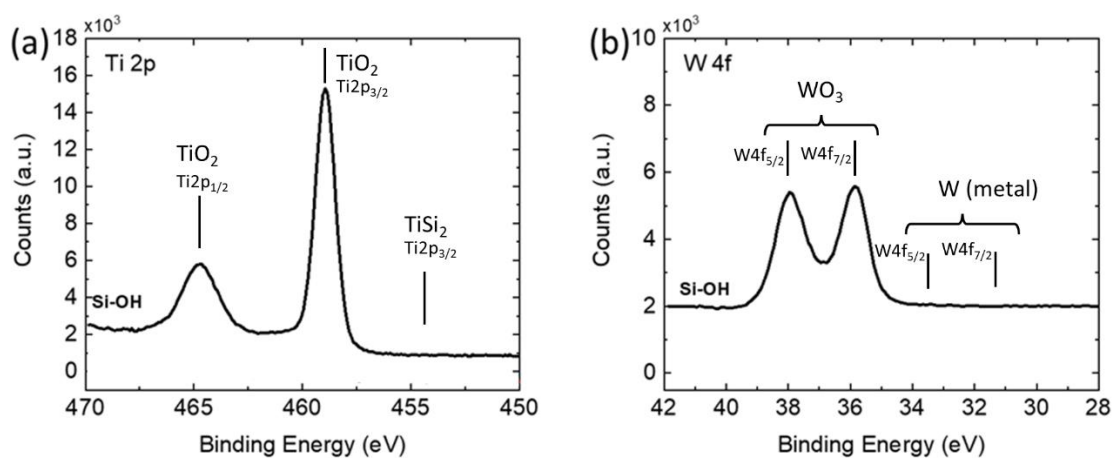


**Figure 5.6** XPS spectra collected from blanket Si-OH wafers after  $\text{TiO}_2$  deposition at  $150^\circ\text{C}$  followed by  $\text{SiH}_4/\text{WF}_6$  at  $220^\circ\text{C}$ . The  $\text{TiO}_2$  was done using 20 ALD/ALE supercycles, leading to favorable  $\text{TiO}_2$  growth on the Si-OH. The  $\text{SiH}_4/\text{WF}_6$  was performed for 15 cycles. (a) Ti 2p region showing  $\text{TiO}_2$  with no signal for  $\text{TiSi}_2$ , consistent with no reaction during the  $\text{SiH}_4$  dose step. (b) W 4f spectra showing some  $\text{WO}_3$  present after  $\text{SiH}_4/\text{WF}_6$  at  $220^\circ\text{C}$ . The thin residual  $\text{WO}_3$  layer does not accumulate during  $\text{SiH}_4/\text{WF}_6$  treatment, and can be removed by exposure to  $\text{BCl}_3$  (**Table 5.5**).<sup>16,29</sup>

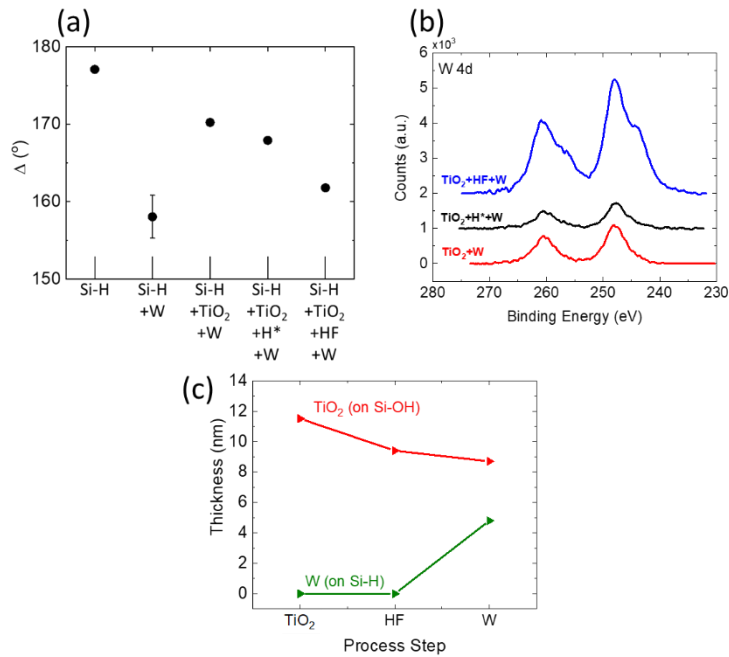


**Figure 5.7** (a) Ellipsometry delta parameter ( $\Delta$ ) at  $\lambda = 700$  nm on Si-H substrates after various treatments: “Si-H” = starting Si-H surface prepared by treating Si-OH with 30 s dip in dilute (5%) HF; “Si-H + W” = HF dip + W (*i.e.* no TiO<sub>2</sub> ALD/ALE); “Si-H + TiO<sub>2</sub> + W” = no intermediate treatment between TiO<sub>2</sub> and W; “Si-H + TiO<sub>2</sub> + H\* + W” = intermediate treatment with 4% H<sub>2</sub>/Ar plasma for 300 s at 10 watts. “Si-H + TiO<sub>2</sub> + HF + W” = intermediate treatment with 5 s dip in dilute 5% HF. A smaller value for  $\Delta$  corresponds to a thicker W film. The TiO<sub>2</sub> treatment was 12 ALD/ALE supercycles at 150°C, and the W step was 10 cycles of SiH<sub>4</sub>/WF<sub>6</sub> at 220°C. The 12 TiO<sub>2</sub> ALD/ALE supercycles leads to minimal TiO<sub>2</sub> on Si-H, but surface damage can influence subsequent W nucleation and growth.<sup>13</sup> After TiO<sub>2</sub> deposition, the HF dip allowed the largest amount of W growth on Si-H during the SiH<sub>4</sub>/WF<sub>6</sub>. (b) XPS W 4d spectra collected from the last 3 samples in (a). The largest W signal is observed for the sample treated with the intermediate HF dip. (c) TiO<sub>2</sub> and W thickness on Si-OH and Si-H substrates, respectively, after each step during the TiO<sub>2</sub> ALD/ALE + HF + W ALD sequence. The HF dip etched a small amount of TiO<sub>2</sub>, but the TiO<sub>2</sub> thickness was sufficient to enable sacrificial etching during W deposition.

**Table 5.3** XPS atomic concentration (%) data collected from Si-H substrates after TiO<sub>2</sub> (= 12 supercycles of TiO<sub>2</sub> ALD/ALE at 150 °C) and W (= 10 cycles of SiH<sub>4</sub>/WF<sub>6</sub> at 220 °C). The effect of two treatments, “H<sub>2</sub>\*” and “HF”, between the TiO<sub>2</sub> and W steps was tested. “H<sub>2</sub>\*” = 4% H<sub>2</sub>/Ar plasma for 300 s at 10 watts; and “HF” = 5 s dip in dilute 5% HF. The HF dip allowed the most substantial growth of W.

Surface	XPS atomic concentration (at. %)							
	Ti 2p	W 4d	Si 2p	O 1s	F 1s	Cl 2p	B 1s	C 1s
Si-H + TiO <sub>2</sub> + W	0	3.7	43.4	23.0	0.4	0	8.0	21.5
Si-H + TiO <sub>2</sub> + H <sub>2</sub> * + W	0	2.6	41.7	24.6	1.3	0.2	6	23.6
Si-H + TiO <sub>2</sub> + HF + W	0	18.5	20.9	39.6	0.1	0	0	21.0

**Table 5.4** Thickness of TiO<sub>2</sub> or W measured by ellipsometry on blanket Si-H and Si-OH substrates after TiO<sub>2</sub> deposition at 150 °C followed by SiH<sub>4</sub>/WF<sub>6</sub> at 220 °C. Between TiO<sub>2</sub> and W steps, the samples received a 5 s dip in dilute HF. The Si-H and Si-OH substrates were treated simultaneously to each reaction. The TiO<sub>2</sub> was done using 20 ALD/ALE supercycles at 150 °C, leading to ASD of TiO<sub>2</sub> predominantly on Si-OH. The SiH<sub>4</sub>/WF<sub>6</sub> was performed for 15 cycles. A second pair of substrates was also prepared with ASD TiO<sub>2</sub>, and those samples were treated with 20 SiH<sub>4</sub>/WF<sub>6</sub> cycles. The W thickness is determined with ellipsometry using a correlation between delta value and thickness.<sup>31</sup>

Treatment	Si-H substrate		Si-OH substrate	
	Coating	Thickness (nm)	Coating	Thickness (nm)
TiO <sub>2</sub> : 20 supercycles @ 150°C	TiO <sub>2</sub>	1.9	TiO <sub>2</sub>	16.4
+ HF dip	--	0	TiO <sub>2</sub>	11.4
+ SiH <sub>4</sub> /WF <sub>6</sub> : 15 cycles @ 220°C	W	9.7	TiO <sub>2</sub>	10.3
+ SiH <sub>4</sub> /WF <sub>6</sub> : 20 cycles @ 220°C	W	12.6	TiO <sub>2</sub>	10.0

**Table 5.5** Surface composition determined by XPS for Si-H and TiO<sub>2</sub> after exposure to SiH<sub>4</sub>/WF<sub>6</sub> at 220 °C and after exposing the same samples to 5 doses of BCl<sub>3</sub> gas. Each BCl<sub>3</sub> dose included 1 s BCl<sub>3</sub> exposure and 45 s N<sub>2</sub> purge. The TiO<sub>2</sub> was deposited on Si-OH using 20 ALD/ALE supercycles at 150 °C. Before the SiH<sub>4</sub>/WF<sub>6</sub> treatment, the Si-H surface was also exposed to the same TiO<sub>2</sub> treatment of 20 ALD/ALE supercycles at 150 °C. Results show a large W signal on Si-H due to W deposition, with some residual W on TiO<sub>2</sub> due to residual WO<sub>3</sub> vapor etching intermediate. After BCl<sub>3</sub> treatment, the WO<sub>3</sub> signal is smaller, consistent with WO<sub>3</sub> etching by BCl<sub>3</sub>. The W surface on Si-H showed no B after the BCl<sub>3</sub> treatment.

Surface	Treatment	XPS atomic concentration (at. %)							
		Ti 2p	W 4d	Si 2p	O 1s	F 1s	Cl 2p	B 1s	C 1s
Si-H	10 SiH <sub>4</sub> /WF <sub>6</sub>	0.0	18.5	20.9	39.6	0.1	0.0	0.0	21.0
	10 SiH <sub>4</sub> /WF <sub>6</sub> + 5 BCl <sub>3</sub>	0.0	18.9	24.6	35.6	0.9	1.0	0.0	19.1
TiO <sub>2</sub>	10 SiH <sub>4</sub> /WF <sub>6</sub>	16.1	3.0	2.7	51.6	2.1	0.8	4.0	19.7
	10 SiH <sub>4</sub> /WF <sub>6</sub> + 5 BCl <sub>3</sub>	19.1	1.9	1.9	45.7	2.3	1.2	6.6	21.4

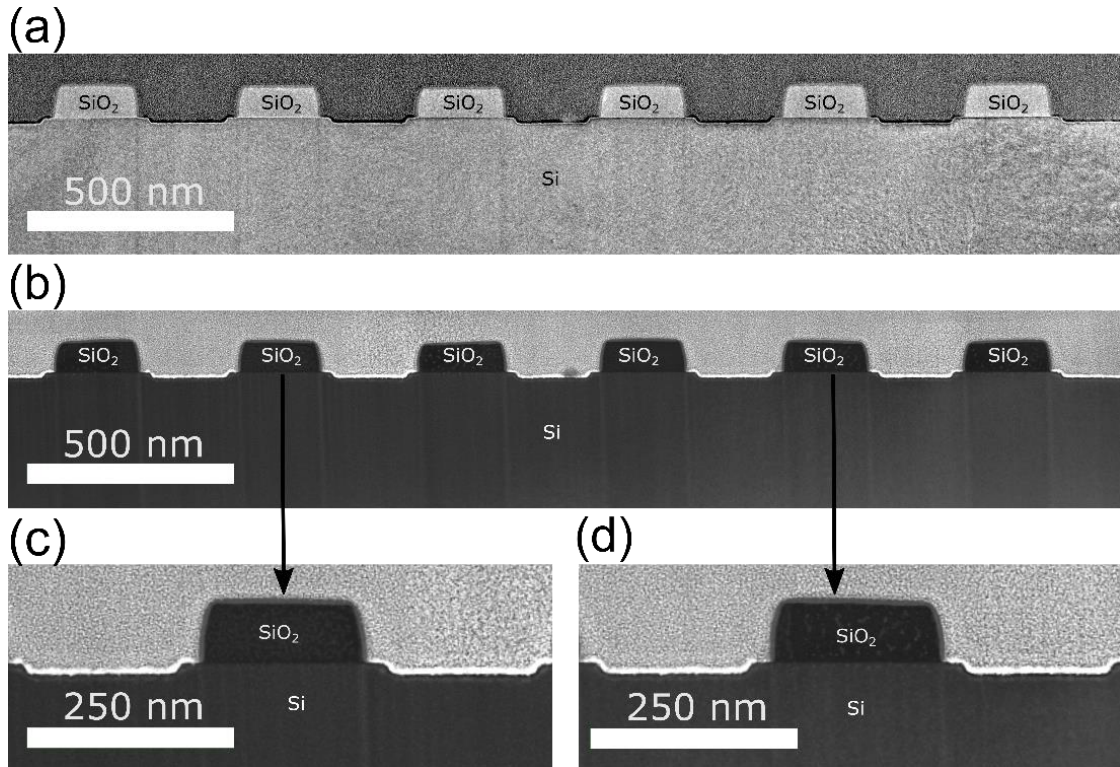


**Figure 5.8** TEM/STEM images of self-aligned nano-patterned W and TiO<sub>2</sub> formed by simultaneous deposition and etching, prepared using the same conditions as used for the images in **Figure 5.4**: (a) bright field TEM; and (b) STEM images of W/TiO<sub>2</sub> on Si-H/SiO<sub>2</sub> nano-patterned substrates; (c) and (d) high magnification view of two different regions from image (b).

## 5.7 References

- (1) Decadal Plan for Semiconductors; Semiconductor Industry Association, Semiconductor Research Corp., 2021. [www.src.org/decadal-plan](http://www.src.org/decadal-plan) (accessed 2021-06-16).
- (2) Clark, R.; Tapily, K.; Yu, K.-H.; Hakamata, T.; Consiglio, S.; O'Meara, D.; Wajda, C.; Smith, J.; Leusink, G. Perspective: New Process Technologies Required for Future Devices and Scaling. *APL Mater.* **2018**, *6*, 058203.
- (3) Parsons, G. N.; Clark, R. D. Area-Selective Deposition: Fundamentals, Applications, and Future Outlook. *Chem. Mater.* **2020**, *32*, 4920–4953.
- (4) Mohanty, N.; Smith, J. T.; Huli, L.; Pereira, C.; Raley, A.; Kal, S.; Fonseca, C.; Sun, X.; Burns, R. L.; Farrell, R. A.; Hetzer, D. R.; Metz, A. W.; Ko, A.; Scheer, S. A.; Biolsi, P.; DeVillers, A. EPE Improvement Thru Self-Alignment via Multi-Color Material Integration. In *Optical Microlithography XXX*; Erdmann, A., Kye, J., Eds.; The International Society for Optics and Photonics (SPIE), 2017; Vol. 10147, p 1014704.
- (5) Levinson, H. J. The Potential of EUV Lithography. In *35th European Mask and Lithography Conference (EMLC 2019)*; Behringer, U. F., Finders, J., Eds.; The International Society for Optics and Photonics (SPIE), 2019; Vol. 1117702, p 2.
- (6) Bally-Le Gall, F.; Friedmann, C.; Heinke, L.; Arslan, H.; Azucena, C.; Welle, A.; Ross, A. M.; Wöll, C.; Lahann, J. Free-Standing Nanomembranes Based on Selective CVD Deposition of Functional Poly-p-Xylylenes. *ACS Nano* **2015**, *9*, 1400–1407.
- (7) Gladfelter, W. L. Selective Metallization by Chemical Vapor Deposition. *Chem. Mater.* **1993**, *5*, 1372–1388.
- (8) Claassen, W. A. P.; Bloem, J. The Nucleation of CVD Silicon on SiO<sub>2</sub> and Si<sub>3</sub>N<sub>4</sub> Substrates: I. The System at High Temperatures. *J. Electrochem. Soc.* **1980**, *127*, 194–202.

- (9) Fitch, J. T.; Denning, D. J.; Beard, D. The Pattern Dependence of Selectivity in Low Pressure Selective Epitaxial Silicon Growth. *J. Electron. Mater.* **1992**, *21*, 455–462.
- (10) Hartmann, J. M.; Bertin, F.; Rolland, G.; Laugier, F.; Semeria, M. N. Selective Epitaxial Growth of Si and SiGe for Metal Oxide Semiconductor Transistors. *J. Cryst. Growth* **2003**, *259*, 419–427.
- (11) Gates, S. M. Surface Chemistry in the Chemical Vapor Deposition of Electronic Materials. *Chem. Rev.* **1996**, *96*, 1519–1532.
- (12) Minaye Hashemi, F. S.; Prasittichai, C.; Bent, S. F. Self-Correcting Process for High Quality Patterning by Atomic Layer Deposition. *ACS Nano* **2015**, *9*, 8710–8717.
- (13) Mameli, A.; Merckx, M. J. M.; Karasulu, B.; Roozeboom, F.; Kessels, W. E. M. M.; MacKus, A. J. M. Area-Selective Atomic Layer Deposition of SiO<sub>2</sub> Using Acetylacetone as a Chemoselective Inhibitor in an ABC-Type Cycle. *ACS Nano* **2017**, *11*, 9303–9311.
- (14) Pattison, T. G.; Hess, A. E.; Arellano, N.; Lanzillo, N.; Nguyen, S.; Bui, H.; Rettner, C.; Truong, H.; Friz, A.; Topuria, T.; Fong, A.; Hughes, B.; Tek, A. T.; DeSilva, A.; Miller, R. D.; Qiao, G. G.; Wojtecki, R. J. Surface Initiated Polymer Thin Films for the Area Selective Deposition and Etching of Metal Oxides. *ACS Nano* **2020**, *14*, 4276–4288.
- (15) Cho, T. H.; Farjam, N.; Allemang, C. R.; Pannier, C. P.; Kazyak, E.; Huber, C.; Rose, M.; Trejo, O.; Peterson, R. L.; Barton, K.; Dasgupta, N. P. Area-Selective Atomic Layer Deposition Patterned by Electrohydrodynamic Jet Printing for Additive Manufacturing of Functional Materials and Devices. *ACS Nano* **2020**, *14*, 17262–17272.
- (16) Song, S. K.; Saare, H.; Parsons, G. N. Integrated Isothermal Atomic Layer Deposition/Atomic Layer Etching Super-Cycles for Area-Selective Deposition of TiO<sub>2</sub>. *Chem. Mater.* **2019**, *31*, 4793–4804.

- (17) Leskelä, M.; Ritala, M. Atomic Layer Deposition (ALD): From Precursors to Thin Film Structures. *Thin Solid Films* **2002**, *409*, 138–146.
- (18) Parsons, G. N.; George, S. M.; Knez, M. Progress and Future Directions for Atomic Layer Deposition and ALD-Based Chemistry. *MRS Bull.* **2011**, *36*, 865–871.
- (19) Holleman, J. Selective Chemical Vapor Deposition. In *Chemical Physics of Thin Film Deposition Processes for Micro- and Nano-Technologies*; Pauleau, Y., Ed.; Springer: New York, 2002; pp 171–198. DOI: 10.1007/978-94-010-0353-7\_8
- (20) Madar, R.; Bernard, C. Thermodynamic Modeling of Selective Chemical Vapor Deposition Processes in Microelectronic Silicon. *J. Vac. Sci. Technol., A* **1990**, *8*, 1413–1421.
- (21) Carlsson, J. O. Selective Vapor-Phase Deposition on Patterned Substrates. *Crit. Rev. Solid State Mater. Sci.* **1990**, *16*, 161–212.
- (22) Juppo, M.; Vehkamäki, M.; Ritala, M.; Leskelä, M. Deposition of Molybdenum Thin Films by an Alternate Supply of MoCl<sub>5</sub> and Zn. *J. Vac. Sci. Technol., A* **1998**, *16*, 2845–2850.
- (23) Myers, T. J.; Cano, A. M.; Lancaster, D. K.; Clancey, J. W.; George, S. M. Conversion Reactions in Atomic Layer Processing with Emphasis on ZnO Conversion to Al<sub>2</sub>O<sub>3</sub> by Trimethylaluminum. *J. Vac. Sci. Technol., A* **2021**, *39*, 021001.
- (24) Agbenyeke, R. E.; Han, S. H.; Park, B. K.; Chung, T.-M.; Lee, Y. K.; Kim, C. G.; Han, J. H. Simultaneous Etching of Underlying Metal Oxide and Sulfide Thin Films during Cu<sub>2</sub>S Atomic Layer Deposition. *Appl. Surf. Sci.* **2020**, *524*, 146452.
- (25) Haukka, S. P.; Matero, R. H.; Tois, E.; Niskanen, A.; Tuominen, M.; Huotari, H.; Pore, V. J. Dual Selective Deposition. U.S. Patent Application US 2015/0299848 A1, 2015.
- (26) Lemaire, P. C.; King, M.; Parsons, G. N. Understanding Inherent Substrate Selectivity during Atomic Layer Deposition: Effect of Surface Preparation, Hydroxyl Density, and Metal Oxide

Composition on Nucleation Mechanisms during Tungsten ALD. *J. Chem. Phys.* **2017**, *146*, 052811.

(27) Kalanyan, B.; Losego, M. D.; Oldham, C. J.; Parsons, G. N. Low-Temperature Atomic Layer Deposition of Tungsten Using Tungsten Hexafluoride and Highly-Diluted Silane in Argon. *Chem. Vap. Deposition* **2013**, *19*, 161–166.

(28) Lemaire, P. C.; King, M.; Parsons, G. N. Understanding Inherent Substrate Selectivity during Atomic Layer Deposition: Effect of Surface Preparation, Hydroxyl Density, and Metal Oxide Composition on Nucleation Mechanisms during Tungsten ALD. *J. Chem. Phys.* **2017**, *146*, 052811.

(29) Lemaire, P. C.; Parsons, G. N. Thermal Selective Vapor Etching of TiO<sub>2</sub>: Chemical Vapor Etching via WF<sub>6</sub> and Self-Limiting Atomic Layer Etching Using WF<sub>6</sub> and BCl<sub>3</sub>. *Chem. Mater.* **2017**, *29*, 6653–6665.

(30) Roine, A.; Kotiranta, T.; Eerola, H.; Lamberg, P. *HSC Chemistry, Ver. 7.1*; Otkukumpu Research Oy: Pori, Finland, 2002.

(31) Kalanyan, B.; Lemaire, P. C.; Atanasov, S. E.; Ritz, M. J.; Parsons, G. N. Using Hydrogen to Expand the Inherent Substrate Selectivity Window during Tungsten Atomic Layer Deposition. *Chem. Mater.* **2016**, *28*, 117–126.

(32) Atanasov, S. E.; Kalanyan, B.; Parsons, G. N. Inherent Substrate-Dependent Growth Initiation and Selective-Area Atomic Layer Deposition of TiO<sub>2</sub> Using “Water-Free” Metal-Halide/Metal Alkoxide Reactants. *J. Vac. Sci. Technol., A* **2016**, *34*, 01A148.

(33) Creighton, J. R. A Mechanism for Selectivity Loss during Tungsten CVD. *J. Electrochem. Soc.* **1989**, *136*, 271.

- (34) Lee, Y.; DuMont, J. W.; Cavanagh, A. S.; George, S. M. Atomic Layer Deposition of AlF<sub>3</sub> Using Trimethylaluminum and Hydrogen Fluoride. *J. Phys. Chem. C* **2015**, *119*, 14185–14194.
- (35) Zywojko, D. R.; George, S. M. Thermal Atomic Layer Etching of ZnO by a “Conversion-Etch” Mechanism Using Sequential Exposures of Hydrogen Fluoride and Trimethylaluminum. *Chem.Mater.* **2017**, *29*, 1183–1191.
- (36) Warren, A.; Nylund, A.; Olefjord, I. Oxidation of Tungsten and Tungsten Carbide in Dry and Humid Atmospheres. *Int. J. Refract. Hard Met.* **1996**, *14*, 345–353.
- (37) Scharf, T. W.; Prasad, S. V.; Mayer, T. M.; Goeke, R. S.; Dugger, M. T. Atomic Layer Deposition of Tungsten Disulphide Solid Lubricant Thin Films. *J. Mater. Res.* **2004**, *19*, 3443–3446.
- (38) Lee, Y.; Johnson, N. R.; George, S. M. Thermal Atomic Layer Etching of Gallium Oxide Using Sequential Exposures of HF and Various Metal Precursors. *Chem. Mater.* **2020**, *32*, 5937–5948.
- (39) Klaus, J. W.; Ott, A. W.; Dillon, A. C.; George, S. M. Atomic Layer Controlled Growth of Si<sub>3</sub>N<sub>4</sub> Films Using Sequential Surface Reactions. *Surf. Sci.* **1998**, *418*, L14–L19.
- (40) Lee, Y.; Huffman, C.; George, S. M. Selectivity in Thermal Atomic Layer Etching Using Sequential, Self-Limiting Fluorination and Ligand-Exchange Reactions. *Chem. Mater.* **2016**, *28*, 7657–7665.
- (41) Kim, J. Y.; George, S. M. Tin Monosulfide Thin Films Grown by Atomic Layer Deposition Using Tin 2,4-Pentanedionate and Hydrogen Sulfide. *J. Phys. Chem. C* **2010**, *114*, 17597–17603.
- (42) Sreejith, K.; Pillai, C. G. S. IR Study on the Effect of Chloride Ion on Porous Silicon. *Appl. Surf. Sci.* **2006**, *252*, 8399–8403.

(43) Chang, K. M.; Wang, S. W.; Li, C. H.; Tsai, J. Y.; Yeh, T. H. Reduction of Selectivity Loss Probability on Dielectric Surface during Chemical Vapor Deposition of Tungsten Using Fluorinated Oxide and Removing Silanol Units on Dielectric Surface. *Jpn. J. Appl. Phys.*, **1996**, *35*, 6555–6561.

(44) Kobayashi, N.; Nakamura, Y.; Goto, H.; Homma, Y. In Situ Infrared Reflection and Transmission Absorption Spectroscopy Study of Surface Reactions in Selective Chemical Vapor Deposition of Tungsten Using  $WF_6$  and  $SiH_4$ . *J. Appl. Phys.* **1993**, *73*, 4637.

## **Chapter 6 Cobalt metal deposition using bis(1,4-di-tert-butyl-1,3-diazadienyl)cobalt and formic acid with atomic layer deposition and chemical vapor deposition**

### 6.1 Abstract

With the miniaturization of a transistor less than 10 nm, the size effects of tungsten and copper metallization lead to substantial electrical loss owing to the electron scattering and larger barrier/seed layer ratio compared to metal fill. Cobalt metal would address this challenge due to its good conductivity and electromigration. This work illustrates cobalt metal deposition using bis(1,4-di-tert-butyl-1,3-diazadienyl)cobalt (CoDAD) and formic acid with atomic layer deposition (ALD) and chemical vapor deposition (CVD). To understand the basic growth behavior, various process conditions such as precursor temperatures, dose and purge times are investigated. The results indicate that the growth of CoDAD/F.A process is dominated by CVD growth. Film composition measured by x-ray photoelectron spectroscopy (XPS) exhibits area-selective deposition of cobalt on metal films including copper and gold vs. hydrogen-terminated silicon (Si-H) and titanium dioxide (TiO<sub>2</sub>). This work describes which factor is important to obtain more consistent and reproducible results.

### 6.2 Introduction

As a miniaturization of an integrated circuit, the RC delay is a rate limiting step for circuit delay. When the linewidths are less than 10 nm, circuit resistance substantially increases mainly due to electron scattering.<sup>1</sup> To overcome this challenge, Co metal capping and liners for Cu interconnect are widely investigated on the back-end-of-the-line (BEOL) manufacturing processes.<sup>2-4</sup> In addition to good conductivity, Co exhibits greater resistance to electromigration

and lower diffusion into Si than Cu.<sup>5-7</sup> Aside from BEOL applications, Co thin films have been employed for various applications including CoSi<sub>2</sub> conversion coatings,<sup>8</sup> magneto-optic recording media,<sup>9,10</sup> and wear-resistant coatings.<sup>11</sup>

When it comes to general metal ALD processes, reduction reaction is frequently used to obtain metal films from inorganic or metalorganic precursors. Depending on the chemical properties and decomposition pathways of precursors, the combination of metal precursors and reducing agents should be considered.<sup>12,13</sup> For metal-organic CVD (MOCVD) processes, Co<sup>+0</sup> precursor is preferable in terms of process simplicity and high purity film.<sup>14,15</sup> Even though many Co ALD processes are originated from conventional Co CVD processes, Co precursors with higher oxidation state is necessary for step-growth processes: otherwise, the self-limiting reaction would be difficult. Layer-by-layer growth takes advantages over CVD processes due to good step coverage with precise thickness control. Various Co precursors with oxidation states ranging from +1 to +2 containing carbonyl,<sup>16-19</sup> cyclopentadienyl (Cp),<sup>18-20</sup> and amidinate (AMD)<sup>21,22</sup> have been studied with different reducing agents such as H<sub>2</sub>, NH<sub>3</sub>, dimethylhydrazine (DMHz), t-butylamine, diethylamine, and formic acid.

Among many Co metal ALD studies, there are few works focusing on ASD processes. Chabal group reported Co metal ASD processes using (Bu-AllylCo(CO)<sub>3</sub>) and DMHz.<sup>23,24</sup> Co thin films were selectively grown on H-terminated Si surfaces (Si-H) relative to SiO<sub>2</sub> surfaces (SiO<sub>2</sub>) with the growth rate of 0.5 Å/cycle at 140 °C. Selective Co growth was led by the surface reaction energy differences between Co source and Si-H vs. SiO<sub>2</sub>. However, the detailed process characteristics such as ALD temperature, selectivity window, and saturation behavior was not reported. Ekerdt group developed Co ASD processes using bis(N-tert-butyl-N'-ethylpropionamidinato) cobalt(II) (CoAMD) and H<sub>2</sub>.<sup>2,3</sup> By using selective decomposition of

CoAMD on Cu substrates, 3 nm of Co was predominantly deposited on Cu surface compared to SiO<sub>2</sub> and porous low-k carbon doped oxide (CDO) at 165 °C. In order to obtain high selectivity, surface passivation with trimethylchlorosilane and hexamethyldisilazane are required to deactivate reactive sites on dielectric surface and the process shows slow growth rate of 0.03 Å/cycle.

Recently, Winter group found out Co metal ALD using bis(1,4-di-tert-butyl-1,3-diazadienyl)cobalt (Co-DAD) and formic acid or t-butylamine.<sup>25-28</sup> The growth rate was 0.95 Å/cycle between 170 and 180 °C ALD window temperature. Under this process, Co films were selectively grown on noble metal substrates such as Ru, Cu, and Pt relative to Si substrate. The substrate selectivity was attributed by the selective decomposition of formic acid on noble metals.<sup>29, 30</sup> Nonetheless, there was no convincing data to illustrate the relationship between the role of formic acid and AS-ALD on noble metals and no in-depth ASD studies regarding selectivity behavior and ALD processes were reported. The current work explores the understanding of ALD Co film growth using Co-DAD and formic acid; specifically, the main goal is to clarify the selective growth behavior of Co film and the primary role of formic acid on ASD processes. In order to define the standard ALD growth conditions, Co-DAD and formic dose/purge time as well as the source and chamber temperature are varied.

## 6.3 Experimental Section

### 6.3.1 Substrate preparation

Boron-doped Si (100) 6-10 Ω·cm, 100 nm thermal SiO<sub>2</sub> on Si, 50 nm Cu/TaN deposited by PVD on Si, 80 nm Au deposited by thermal evaporation and 27 nm Pt /10 nm Ti deposited by thermal evaporation on Si and 8 nm TiO<sub>2</sub> deposited by ALD on Si were used for substrates. The Si and SiO<sub>2</sub> wafers were cleaned by piranha solution (H<sub>2</sub>O<sub>2</sub>/H<sub>2</sub>SO<sub>4</sub> : 1:1 volume ratio) for 15 min,

rinsed with deionized (DI) water, and stored in DI water. Prior to loading the samples, Si wafers were dried with N<sub>2</sub> gas. To prepare for hydrogen-terminated Si (Si-H), piranha-cleaned Si wafers were dipped for 30 s in dilute hydrofluoric acid (HF, 5 vol%, Sigma-Aldrich), followed by DI rinsing, and dried with N<sub>2</sub> gas.

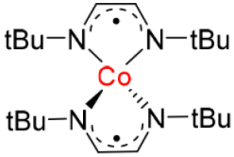
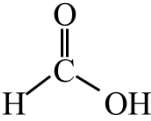
### 6.3.2 Reactor and Process Sequence

Co deposition was performed in a home-built tubular hot-walled isothermal viscous-flow ALD reactor of 60 cm length and 4 cm diameter under constant temperature (140–200 °C) using PID controllers shown in **Figure 6.1**. High purity nitrogen (>99.999 %, Arc3 Gases) was used for purge gas and purified using an inert gas filter (Gate-Keeper, Entegris). The base pressure of the system (WALDO) was 20-30 mTorr and the working pressure was 1 Torr with a carrier gas flow rate of 135 standard cubic centimeters per minute (sccm).

Bis(1,4-di-tert-butyl-1,3-diazadienyl)cobalt (Co-DAD, EMD Chemicals Inc.) and formic acid(99.0%, Fisher Chemical) were used as received without further purification. It is reported that Co-DAD sublimates at 115 °C/0.05 Torr with ~ 95 % recovery, showing 50 mTorr vapor pressure at 115 °C and melting point and decomposition temperature is 175 and 235 °C, respectively.<sup>28</sup> In order to increase solid Co-DAD delivery to the chamber, the customized bubbler flow was implemented for Co-DAD line. The Co-DAD source temperature was varied 90 - 150 °C based on the sublimation and melting point of the Co-DAD. Due to the high vapor pressure of formic acid (33 Torr at 20 °C), formic acid was delivered at room temperature with direct flow over of N<sub>2</sub> gas. All ALD processes were controlled by a custom LABVIEW program. Before the Co film deposition, sample substrates were loaded into the reactor for 30 min to reach the thermal

equilibrium with the chamber. Various reactants dose/purge conditions of Co-DAD/N<sub>2</sub>/Formic acid/N<sub>2</sub> (1-60/60-240/0.1-1.0/60-240 s) were examined to understand the growth behavior.

**Table 6.1** Basic chemical properties of precursors for Cobalt deposition.<sup>28</sup>

Chemical	Structure	B.P. (°C)	M.P. (°C)	Sublimation	Vapor pressure	Decomp. Temp.
Co-DAD [Bis(1,4-di-tert-butyl-1,3-diazabutadienyl)cobalt(II)]		-	175	115 °C @ 50 mTorr	2.48~5.13 Torr @ 115 °C	235 °C
Formic acid		101	8	-	33 Torr @ 20 °C	-

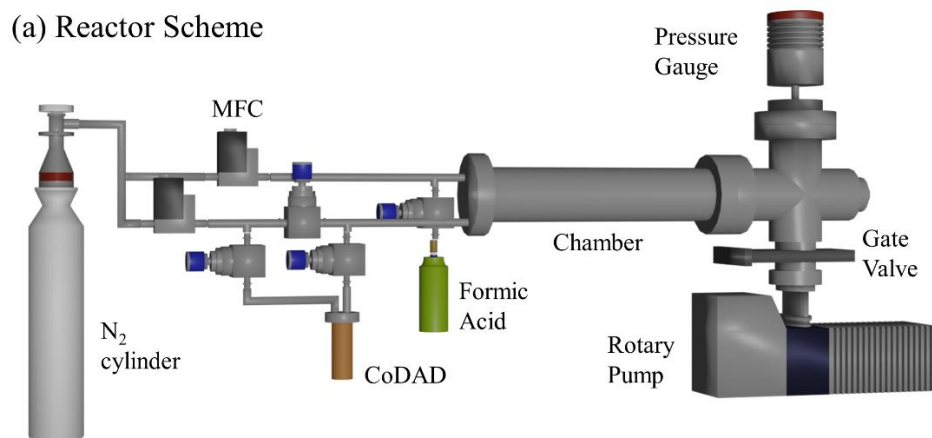


**Figure 6.1** (a) A reactor scheme and (b) photographic images of the reactor.

### 6.3.3 Characterization Methods

In order to evaluate the film growth rate, mass change was monitored by in-situ quartz crystal microbalance (QCM). 6 MHz gold-coated crystal sensor (Inficon) was installed on a QCM probe body (Kurt Lesker) and loaded into the reactor at the reaction temperature under a steady N<sub>2</sub> flow at least 120 min for stabilization. To prevent deposition on the electrical contact, back-side N<sub>2</sub> purge was used, corresponding to ~250 mTorr pressure increase with 42.5 sccm of N<sub>2</sub> flow.

Co film thickness and morphology was characterized by scanning electron microscopy (SEM, FEI Verios 460L). Chemical composition was evaluated by ex-situ X-ray photoelectron spectroscopy (XPS, Kratos Analytical Axis Ultra) with Al-Kalpa (1486.6 eV) gun. Survey scans and high-resolution scans for each component were collected. Peak calibration was conducted by using the adventitious C 1s peak to 285.0 eV. For the peaks showing weak C 1s peak, O 1s peak to 531.0 eV was used for the calibration. The sheet resistance ( $R_s$ ,  $\Omega/\square$ ) of the film was measured with a four-point-probe (RM 3-AR, Jandel) with 1 mm probe spacing ( $s = 1$  mm). The sample size was ~ 2 cm x 2 cm ( $d = 2$  cm) and the correction factor of 4.5324 with  $V/I$  was used to calculate the sheet resistance. For more accurate correction factor, the relationship between the film thickness ( $t$ ),  $s$ , and  $d$  should be considered.

## 6.4 Results and Discussion

### 6.4.1 Basic Growth Behavior

**Table 6.1** shows the basic properties of CoDAD and formic acid (F.A). While the F.A. has high vapor pressure (33 Torr at 20 °C), the solid CoDAD requires high temperature (~100 °C) to be delivered. In principle, heating temperature of the precursor can increase near its decomposition

temperature, but there are two factors to consider when heating the precursor at higher temperatures: i) Precursor will be decomposed faster at higher temperatures even if the temperature is below its decomposition temperature, and ii) The ALD diaphragm valve can't go above 120 °C (low temp) and 200 °C (high temp), respectively. In this regard, the precursor temperature can't go above 200 °C.

To test the CoDAD dosing behavior, the pressure change during DAD dose was measured with different heating temperatures (90 – 130 °C). **Figure 6.2** shows 10 cycles of DAD/N<sub>2</sub>/F.A/N<sub>2</sub> = (30/60/0.1/60 s) where DAD was heated at 123 °C. ~10 mTorr and ~30 mTorr of pressure increase are observed during DAD and F.A doses, respectively. For F.A dose, the needle throttle valve was used to adjust the precursor dosing. DAD pressure change is constant regardless of temperature change.

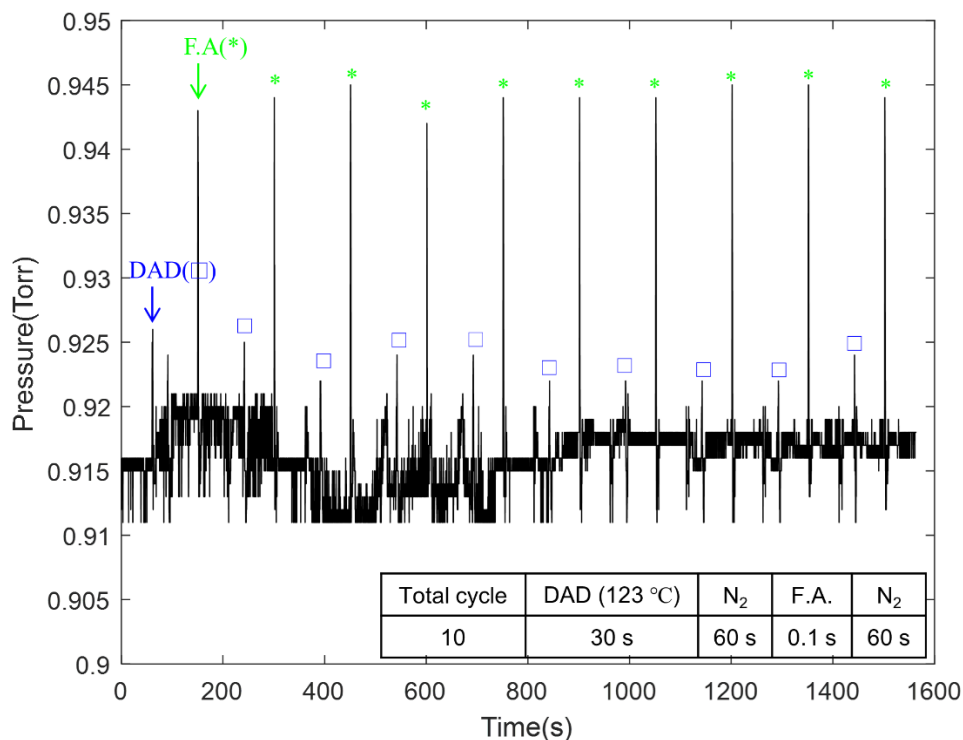


**Figure 6.2** Pressure profile during 10 cycles of CoDAD/N<sub>2</sub>/Formic acid/N<sub>2</sub> = 30/60/0.1/60 s.

After checking the pressure increase of CoDAD and F.A, QCM analysis was used to study the relationship between the growth rate and operation conditions including working pressure, temperatures, precursor exposure times, and purge times. **Figure 6.3** exhibits mass change by QCM using CoDAD(heated at 100 °C)/N<sub>2</sub>/F.A/N<sub>2</sub> = 10/60/0.1/60 s for 50 cycles at 180 °C. The mass change linearly increases with number of deposition cycles as shown in **Figure 6.3a**. **Figure 6.3b** indicates a magnified view of the mass uptake during single cycle. During the CoDAD dose, the mass rapidly increases, whereas the mass slightly decreases during the F.A dose. To clearly see the net mass uptake per each dose, MATLAB was used to calculate the net mass change as shown in **Figure 6.3c**. By using the bulk cobalt density of 8.9 g/cm<sup>3</sup> and the average net mass

change per one ALD cycle ( $49.23 \text{ ng/cm}^2$ ) shown in **Eq. 2.5**, the estimated growth rate from the QCM results is  $0.55 \text{ \AA/cycle}$ .

Since the dose time of CoDAD (more than 10 s) is relatively longer than the general ALD dose conditions (less than 1 s), different purge conditions were investigated. **Figure 6.4** illustrates the mass uptake during 10 s of CoDAD dose followed by different purge times for 50 cycles. Obviously, combining the standard  $\text{N}_2$  purge step with the pump step where only the gate valve is open without the  $\text{N}_2$  flow shows more consistent net mass change even if the total purge time is the same of 60 s (**Figure 6.4a vs. b**). Longer pump/purge steps in **Figure 6.4c** indicates more consistent results. This would be a good way how to enhance the purge efficiency.

Longer purge times for the F.A (240 vs. 60 s in **Figure 6.5**) shows higher growth rate. No such trend is observed on the longer purge time for the CoDAD (240 vs. 60 s), showing no obvious change for the growth rate. This might be due to the fact that the rate limiting step of this reaction is the F.A, thereby longer F.A purge time giving more reaction time to increase its growth rate.

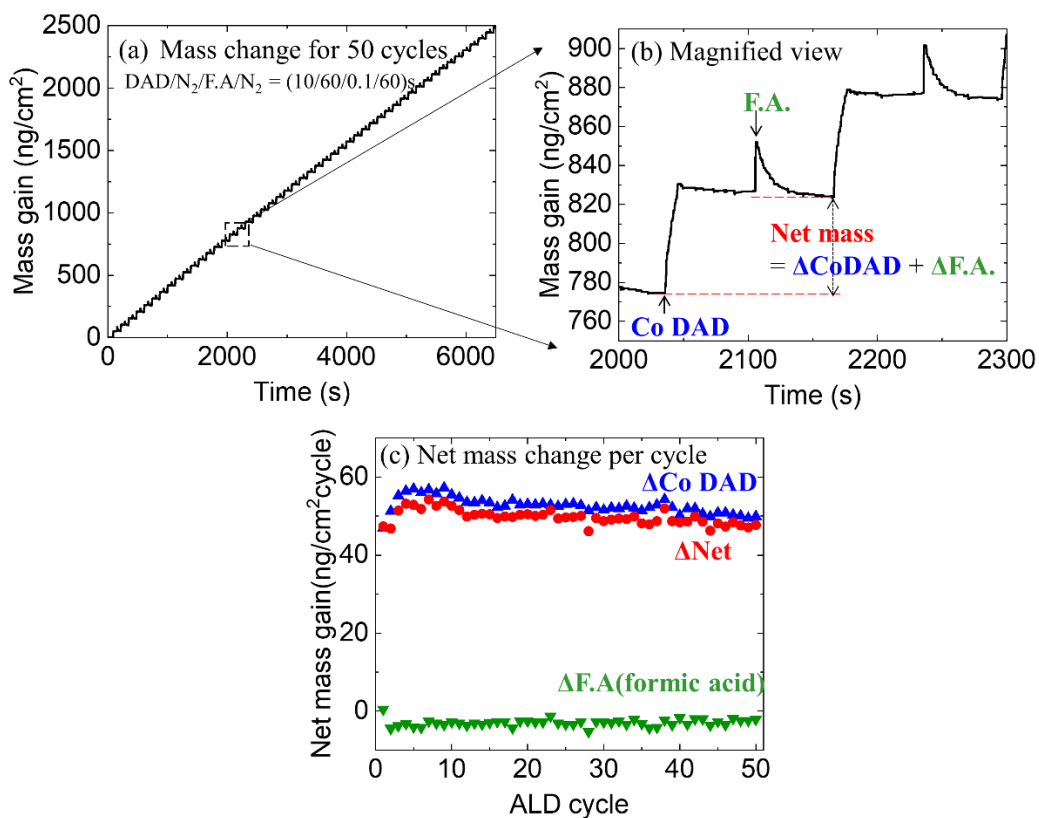


**Figure 6.3** QCM analysis during CoDAD (heated at 100 °C)/N<sub>2</sub>/F.A./N<sub>2</sub> = 10/60/0.1/60 s for 50 cycles at 180 °C and (b) an enlarged view of (a) showing large mass uptake during Co-DAD and slight mass decrease during formic acid dose, and (c) the net mass change per each cycle. A blue square shows the net mass change during CoDAD dose, a green triangle shows the net mass change during F.A. dose, and a red plus indicates the sum of CoDAD and F.A. during single cycle.

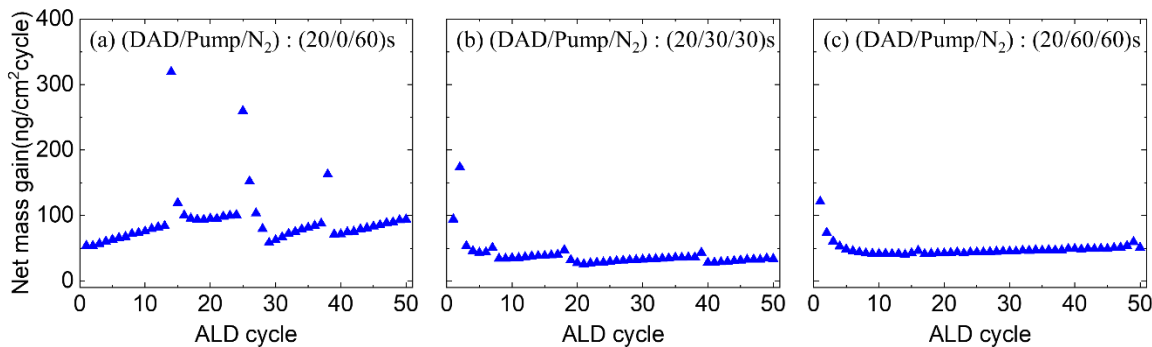


**Figure 6.4** Purge effects on the QCM mass change.

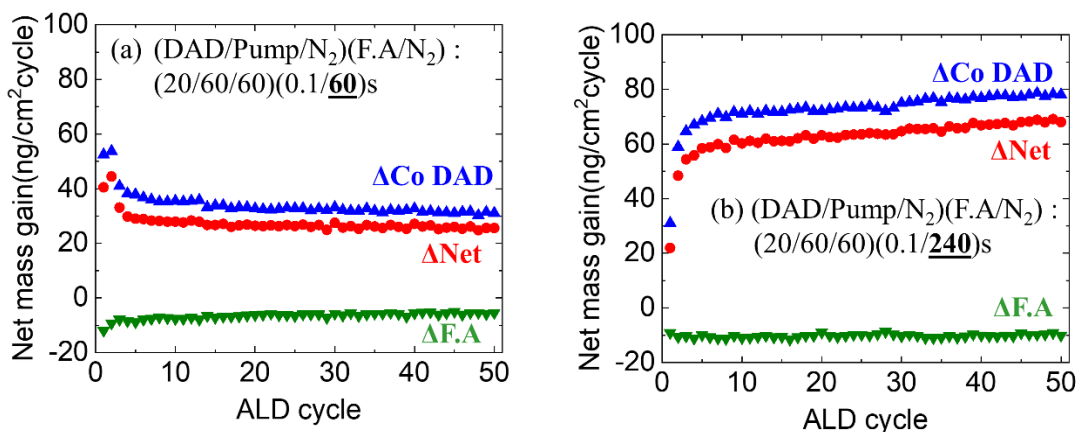


**Figure 6.5** Formic acid purge effects on the QCM mass change.

Based on this condition, saturation behavior as a function of CoDAD dose time was studied. **Figure 6.6a** indicates that Co film growth rate at 180 °C linearly increases with CoDAD dose times, suggesting the CVD growth behavior rather than the ALD growth. As a comparison, a saturation study from a different group using CoDAD is shown; the obtained results are significantly dominated by the CVD growth behavior. The CVD growth behavior can be attributed to three factors: (i) the CoDAD precursor is highly sensitive to the moisture/O<sub>2</sub>, illustrating the precursor is prone to be degraded during the precursor transfer/storage in the glovebox, (ii) the

unstable CoDAD precursor is readily self-decomposed. The decomposition rate can be faster at the heating temperature (100-150 °C) although these temperatures are even lower than its reported decomposition temperature (235 °C), and (iii) different reactor configurations. While the previous study was performed on the commercial reactor (Picosun R-75BE ALD reactor) operated at 6-9 Torr with CoDAD/N<sub>2</sub>/F.A/N<sub>2</sub> = 5/10/0.2/10 s with the precursor booster to increase the delivery of the solid precursor, the current study was carried out on the home-built reactor operated at 1 Torr with CoDAD/N<sub>2</sub>/F.A/N<sub>2</sub> = 10-60/60/0.1/60 s with the bubbler setup.

In order to understand the CVD growth behavior in detail, chamber temperature dependence of film growth rate was investigated in **Figure 6.6b**. Three different processes were compared: (i) sequential dose of Co-DAD/Formic acid, (ii) only Co-DAD dose, and (iii) previous study<sup>25-27</sup>. While the previous study shows ALD window between 160 – 180 °C, the obtained results for case (i) and (ii) indicate no plateau, verifying CVD growth behavior. At lower chamber temperature (140 °C), case (i) shows some ALD growth behavior, but the CVD growth is still dominant.

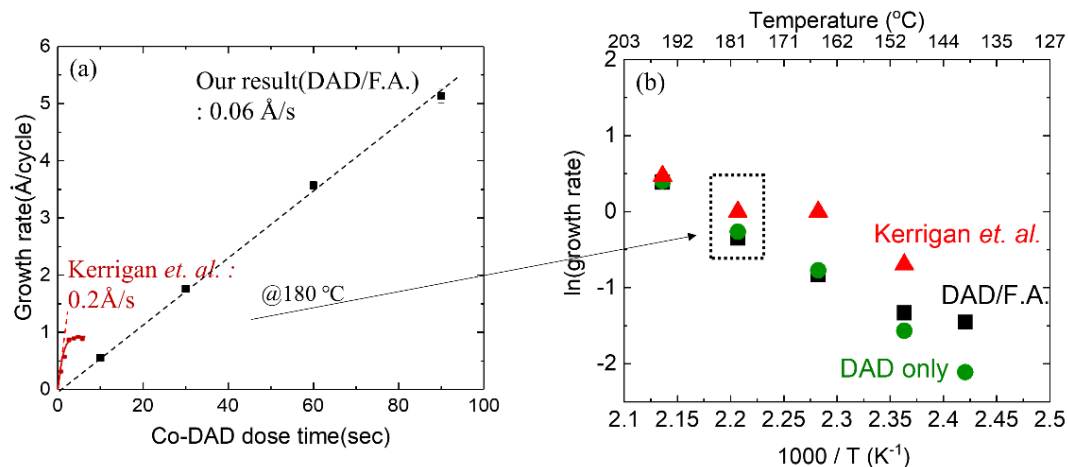


**Figure 6.6** (a) Co film growth rate as a function of Co-DAD dose time at 180 °C. While the previous study exhibits saturation curve with a growth rate of 0.2 Å/s, the obtained results from QCM analysis shows CVD growth behavior with lower growth rate (0.05 Å/s). (b) Co film growth rate as a function of chamber temperature comparing CoDAD/Formic acid, CoDAD only and, previous study (*Kerrigan et al.*)<sup>25-27</sup>. Film growth rate was based on QCM results and Co density.

**Table 6.2** Process condition comparison using CoDAD precursors for Co deposition.

	Source Temp. (°C)	Chamber Temp. (°C)	CoDAD dose/purge	F.A. dose/purge	Working P.	GPC (Å/cycle)
Kerrigan <sup>26-28</sup>	130	170-180	5s/10s	0.2s/10s	6-9 Torr	0.95
Current Recipe	120	180	10, 30, 60, 90s/60s	0.1s/60s	0.5-1.0 Torr	0.55 ~ 5.13

#### 6.4.2 Cobalt ASD and film quality

Despite the CVD growth behavior, Co substrate selectivity was studied on Cu, Au, Pt, Si-H, and TiO<sub>2</sub> substrates. To remove the surface contamination, the metal samples were sonicated in acetone and IPA for 10 min followed by DI water rinsing. The detailed sample information was

described in **section 6.3.1**. After Co deposition, the surface color of Cu and Au substrates clearly changes to gray color while no substantial change is observed on Si-H and TiO<sub>2</sub> substrates in **Table 6.3**, implying Co ASD on metal substrates.

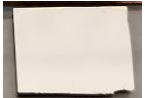
To quantitatively characterize the Co selectivity, high resolution scan of Co 2p peak by XPS was measured after 600 cycles of CoDAD/N<sub>2</sub>/F.A/N<sub>2</sub> = 20/60/0.1/60 s at 180 °C. **Figure 6.7** shows that Co is selectively deposited on Cu and Au relevant to Si-H and TiO<sub>2</sub> surface. This result is corresponding to the previous study showing Co ASD on noble metals compared to Si substrates.<sup>25,26</sup> Co ASD can be explained by the catalytic reaction on metals, decomposing the formic acid and reducing the CoDAD precursor.<sup>29,30</sup> **Table 6.4** shows the elemental composition of all samples in **Figure 6.7**. Strong O 1s and C 1s peaks are observed due to exposure to the air between deposition and XPS analysis. While high Co 2p ratio (23 % on Cu and 20 % on Au) is measured on Cu and Au substrates, low Co signal (3% on TiO<sub>2</sub> 2 % on Si-H) is detected on TiO<sub>2</sub> and Si-H. Instead, high substrate signals (47 % of Si 2p on Si-H and 21 % of Ti 2p on TiO<sub>2</sub>) are measured, consistent with Co 2p results.

**Figure 6.8** shows cross-sectional results of bare Cu and Co on Cu after 600 cycles of CoDAD/N<sub>2</sub>/Formic acid/N<sub>2</sub> = 20/60/0.1/60 s (“CoDAD/F.A”) and 600 cycles of CoDAD/N<sub>2</sub> = 20/60 s (“Only CoDAD”) at 180 °C. Note that the sample denoted as “CoDAD/F.A” is the same sample measured for XPS in **Figure 6.7 and 6.9a**. Compared to bare Cu substrates, ~160 nm of Co films is observed on Cu substrates for both CoDAD/F.A and only CoDAD conditions. This indicates that both conditions exhibit similar growth rate (~2.7 Å/cycle), which is twice higher growth rate than QCM results in **Figure 6.6** (~1.2 Å/cycle, estimated from Co-DAD dose(20 s) and CVD growth rate (0.06 Å/s). This discrepancy can be explained by the extent of the CoDAD degradation. The amount of CoDAD delivery is dependent on the degree of CoDAD self-

decomposition, thereby resulting in inconsistent growth rate. The growth rate of CoDAD/F.A and only CoDAD is the same, showing the similar trend in **Figure 6.6**. It is worthy to note that the surface of bare Cu films exhibits columnar structure (20-50 nm) and this feature is randomly observed on copper surface. This can be associated with the copper oxide, which can be effectively removed by diluted phosphonic acid. With this regard, the surface roughness of bare Cu substrate (RMS = 7.6 nm) is rougher than Co on Cu (RMS = 4.5 and 1.5 nm, for CoDAD/F.A and only CoDAD, respectively).

Since Co films are easily oxidized, it is difficult to evaluate the quality of metal film by merely characterizing the surface where the adventitious carbon and oxygen exist. To study the actual film quality, the Ar sputtering was used for the XPS depth profile. **Figure 6.9a** shows the XPS depth profile of Co 2p on Cu substrates with different etch times. Before the etching, the Co 2p shows broad peak, implying a large oxide composition, whereas after 60 and 120 s etching, sharp and asymmetric Co metal peak appears. This illustrates that the surface contains a lot of carbon and oxygen, and the depth profile is important to characterize the film quality. Given that the growth rates of Co films by CoDAD/F.A and only CoDAD are similar in **Figure 6.6 and 6.8**, Co on Cu by using only CoDAD was also measured by the depth profile. Interestingly, even though the composition ratio on the surface shows no big difference between CoDAD/F.A samples, no clear metal Co peak appears on only CoDAD samples after etching 60 and 120 s. This implies that the reaction from the self-decomposition can't fully remove the carbon ligands, leading to large carbon and oxygen residue. Specifically, 33 at% of oxygen is observed even after 120 s etching (6 % by CoDAD/F.A). This result indicates that the reducing agent would be critical to obtain more pure Co metal.

**Table 6.3** Photographic images of surface color change and sheet resistance before/after Co deposition on various substrates.

Substrate	Cu	Cu	80 nm Au /Si	27 nm Pt/ 10 nmTi/Si	8 nm TiO <sub>2</sub> /Si	Si-H
Pre-cleaning	SC <sup>a</sup> → RO <sup>b</sup>	SC	SC	SC	-	Piranha → HF
Before Dep.						
After Dep.						
Sheet Resistance (mΩ/□) (Before → After)	0.272 → 0.304	0.272 → 0.277	535.7 → 1129	21270 → 3640	∞ → ∞	∞ → ∞

<sup>a</sup>SC stands for solvent clean : 10 min sonication in acetone → 10 min sonication in IPA → DI water rinsing

<sup>b</sup>RO stands for oxide removal : 30 s dipping in 30 wt% H<sub>3</sub>PO<sub>4</sub> in H<sub>2</sub>O → DI water rinsing

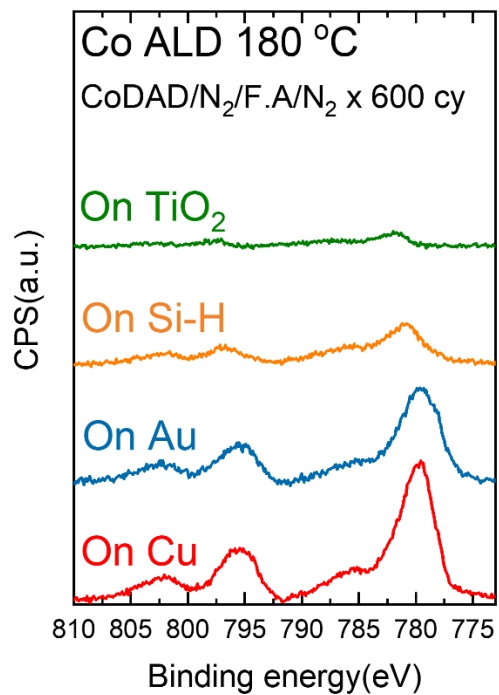


**Figure 6.7** High resolution XPS scans on different substrates (Cu, Au, Si-H, and TiO<sub>2</sub>) after 600 cycles of CoDAD/N<sub>2</sub>/Formic acid/N<sub>2</sub> = 20/60/0.1/60 s at 180 °C.

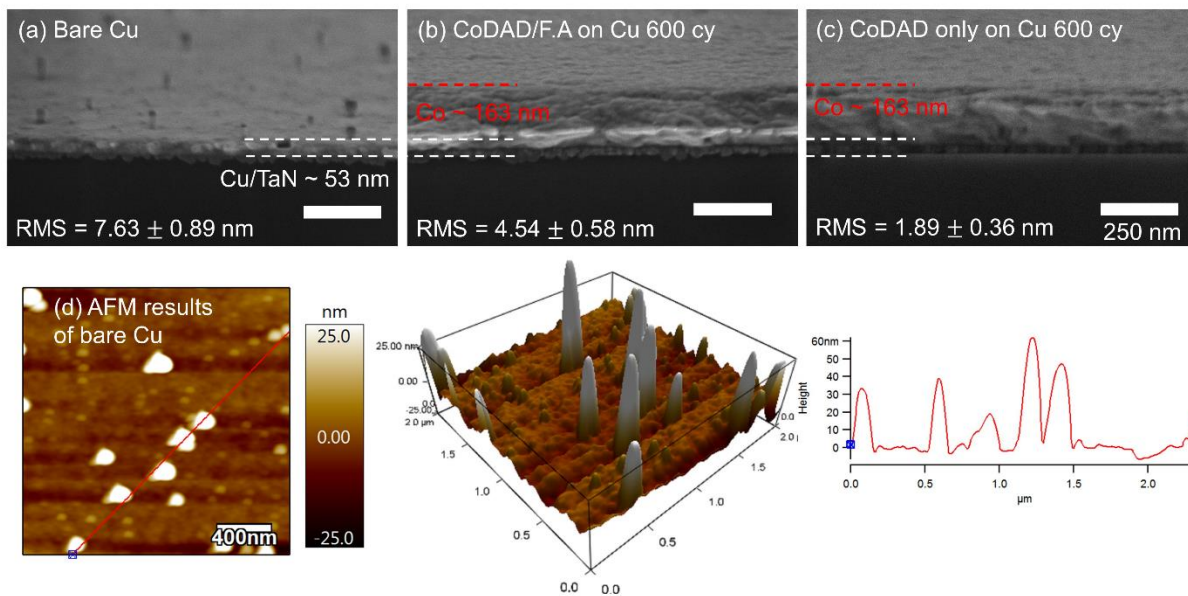


**Figure 6.8** Cross-sectional SEM images of (a) bare Cu, Co on Cu substrates after (b) 600 cycles of CoDAD/N<sub>2</sub>/Formic acid/N<sub>2</sub> = 20/60/0.1/60 s and (c) 600 cycles of CoDAD/N<sub>2</sub> = 20/60 s (Only DAD) at 180 °C. (d) AFM images of bare Cu with 2D, 3D and linescan results showing 20-60 nm columnar features on bare Cu substrates.

**Table 6.4** Elemental composition from XPS analysis in **Figure 6.7**. Values are given in atomic %.

Substrate	Co 2p	C 1s	O 1s	Cu 2p	Au 4f	Si 2p	Ti 2p
On Cu	23.26	22.66	54.08	0	-	-	-
On Au	19.78	30.63	49.15	-	0.44	-	-
On Si-H	3.3	18.15	31.64	-	-	46.93	-
On TiO <sub>2</sub>	2.54	20.85	52.98	-	-	2.77	20.85

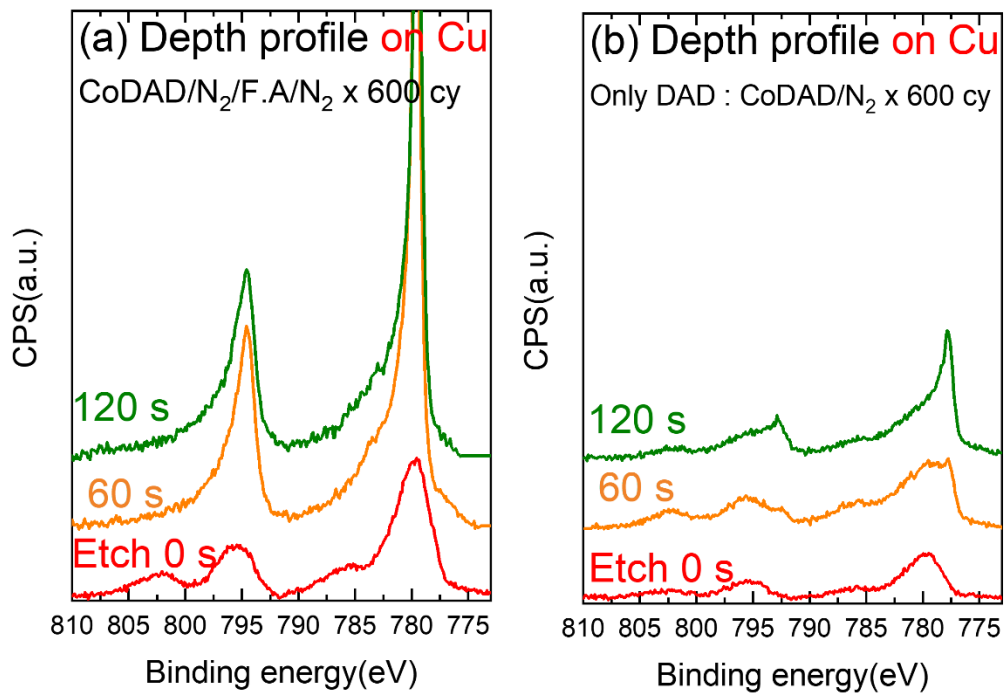


**Figure 6.9** High resolution XPS depth profile scans on different substrates on Cu after (a) 600 cycles of CoDAD/N<sub>2</sub>/Formic acid/N<sub>2</sub> = 20/60/0.1/60 s and (b) 600 cycles of CoDAD/N<sub>2</sub> = 20/60 s (Only DAD) at 180 °C. Note that the result of etch 0 s on panel a is the same result on Cu in **Figure 6.7**. Etch was performed by Ar sputtering.

**Table 6.5** Elemental composition from XPS analysis in **Figure 6.9**. Values are given in atomic %.

Substrate	Etch (s)	Co 2p	C 1s	O 1s	Cu 2p
CoDAD/F.A on Cu	0	23.26	22.66	54.08	0
	60	70.69	20.39	8.92	0
	120	67.84	13.16	6.12	12.87
Only CoDAD on Cu	0	21.98	22.59	53.39	2.03
	60	52.41	0.13	45.57	1.89
	120	60.06	5.85	32.83	1.25

## 6.6 Summary

In summary, this work showed cobalt metal deposition using bis(1,4-di-tert-butyl-1,3-diazadienyl)cobalt (CoDAD) and formic acid (F.A). Various process conditions including precursor temperatures, purge and dose times were studied to understand the fundamental film growth behavior. Results indicated that the purge efficiency can be improved by combining the pump-down step and the higher growth rate was observed for longer purge time of F.A step. The relationship between the chamber temperature and the film growth rate showed that the growth rate of CoDAD/F.A is dependent on the amount of CoDAD dose, indicating the CVD growth. CVD growth behavior is due to the instability and degradation of the precursor or different reactor geometry. To minimize the CVD growth component, lower deposition temperature would be preferred. CVD driven Co-DAD process exhibited substrate selectivity on metal substrate (Cu and Au) vs. Si-H and TiO<sub>2</sub>. Cobalt films can be deposited without reducing agent. However, the XPS depth profile showed that the deposited film without the reducing agent contains a lot of oxygen, illustrating the reducing agent is necessary to obtain more pure Co films. This work gives an important lesson how to achieve more consistent and reproducible ALD processes: a detailed small parameter can be a critical factor, leading to unexpected results. Often, it could be precursor and reactor configuration itself other than the process variation.

## 6.8 References

- (1) Gall, D. Electron Mean Free Path in Elemental Metals Electron Mean Free Path in Elemental Metals. *J. Appl. Phys.* **2016**, *119*, 085101.
- (2) Elko-Hansen, T. D. M.; Ekerdt, J. G. XPS Investigation of the Atomic Layer Deposition Half Reactions of Bis(N-Tert-Butyl-N'-Ethylpropionamidinato) Cobalt(II). *Chem. Mater.* **2014**, *26*, 2642–2646.
- (3) Elko-Hansen, T. D.-M.; Ekerdt, J. G. Selective Atomic Layer Deposition of Cobalt for Back End of Line. *ECS Trans.* **2017**, *80*, 29–37.
- (4) He, M.; Zhang, X.; Nogami, T.; Lin, X.; Kelly, J.; Kim, H.; Spooner, T.; Edelstein, D.; Zhao, L. Mechanism of Co Liner as Enhancement Layer for Cu Interconnect Gap-Fill. *J. Electrochem. Soc.* **2013**, *160*, 3040–3044.
- (5) Yang, C. C.; Flaitz, P.; Wang, P. C.; Chen, F.; Edelstein, D. Characterization of Selectively Deposited Cobalt Capping Layers: Selectivity and Electromigration Resistance. *IEEE Electron Device Lett.* **2010**, *31*, 728–730.
- (6) Yang, C.-C.; Baumann, F.; Wang, P.-C.; Lee, S.; Ma, P.; AuBuchon, J.; Edelstein, D. Characterization of Copper Electromigration Dependence on Selective Chemical Vapor Deposited Cobalt Capping Layer Thickness. *IEEE Electron Device Lett.* **2011**, *32*, 560–562.
- (7) Yang, C. C.; Baumann, F.; Wang, P. C.; Lee, S. Y.; Ma, P.; Aubuchon, J.; Edelstein, D. Dependence of Cu Electromigration Resistance on Selectively Deposited CVD Co Cap Thickness. *Microelectron. Eng.* **2013**, *106*, 214–218.
- (8) Zhu, S.; Meirhaeghe, R. L. Van; Detavernier, C.; Cardon, F.; Ru, P.; Qu, X.; Li, B. Barrier Height Inhomogeneities of Epitaxial CoSi<sub>2</sub> Schottky Contacts on N-Si (100) and (111). *Solid. State. Electron.* **2000**, *44*, 663–671.

- (9) Vo-Van, C.; Kassir-Bodon, Z.; Yang, H.; Coraux, J.; Vogel, J.; Pizzini, S.; Bayle-Guillemaud, P.; Chshiev, M.; Ranno, L.; Guisset, V.; et al. Ultrathin Epitaxial Cobalt Films on Graphene for Spintronic Investigations and Applications. *New J. Phys.* **2010**, *12*, 103040.
- (10) Lutsev, L. V.; Stognij, A. I.; Novitskii, N. N. Giant Magnetoresistance in Semiconductor / Granular Film Heterostructures with Cobalt Nanoparticles. *Phys. Rev. B* **2009**, *80*, 184423.
- (11) Burkov, A. A.; Chigrin, P. G. Effect of Tungsten, Molybdenum, Nickel and Cobalt on the Corrosion and Wear Performance of Fe-Based Metallic Glass Coatings. *Surf. Coatings Technol.* **2018**, *351*, 68–77.
- (12) Gordon, R. G. ALD Precursors and Reaction Mechanisms in *Atomic Layer Deposition for Semiconductors*; Springer, New York, 2014; pp 15-46.
- (13) Miikkulainen, V.; Ritala, M.; Puurunen, R. L. Crystallinity of Inorganic Films Grown by Atomic Layer Deposition : Overview and General Trends. *J. Appl. Phys.* **2013**, *113*, 021301.
- (14) Georgi, C.; Hildebrandt, A.; Waechter, T.; Schulz, S. E.; Gessner, T.; Lang, H. A Cobalt Layer Deposition Study: Dicobalttetrahydrates as Convenient MOCVD Precursor Systems. *J. Mater. Chem. C* **2014**, *2*, 4676–4682.
- (15) Ivanova, A. R.; Nuesca, G.; Chen, X.; Goldberg, C.; Kaloyeros, A. E.; Arkles, B.; Sullivan, J. J. The Effects of Processing Parameters in the Chemical Vapor Deposition of Cobalt from Cobalt Tricarbonyl Nitrosyl. *J. Electrochem. Soc.* **1999**, *146*, 2139–2145.
- (16) Kim, K.; Lee, K.; Han, S.; Jeong, W.; Jeon, H. Characteristics of Cobalt Thin Films Deposited by Remote Plasma ALD Method with Dicobalt Octacarbonyl. *J. Electrochem. Soc.* **2007**, *154*, 177–181.

- (17) Lee, K.; Kim, K.; Park, T.; Jeon, H.; Lee, Y.; Kim, J.; Yeom, S. Characteristics of Ti-Capped Co Films Deposited by a Remote Plasma ALD Method Using Cyclopentadienylcobalt Dicarboxyl. *J. Electrochem. Soc.* **2007**, *154*, 899–903.
- (18) Layer, R. P. A.; Method, D.; Kim, J. Y.; Kim, Y.; Park, S. K.; Lee, J.; Chang, J.; Chang, J. P. Comparison of Co Films Deposited by Remote Plasma Atomic Layer Deposition Method with Cyclopentadienylcobalt Dicarboxyl [CpCo(CO)<sub>2</sub>] and Dicobalt Octacarbonyl [Co<sub>2</sub>(CO)<sub>8</sub>]. *Jpn. J. Appl. Phys.* **2007**, *46*, 173–176.
- (19) Lee, H.; Kim, H. High-Quality Cobalt Thin Films by Plasma-Enhanced Atomic Layer Deposition. *Electrochem. Solid-State Lett.* **2006**, *9*, 323–325.
- (20) Yoon, J.; Lee, H.; Kim, D.; Cheon, T.; Kim, S.; Kim, H. Atomic Layer Deposition of Co Using N<sub>2</sub>/H<sub>2</sub> Plasma as a Reactant. *J. Electrochem. Soc.* **2011**, *158*, 1179–1182.
- (21) Lee, H.-B.-R.; Kim, W.-H.; Lee, J. W.; Kim, J.-M.; Heo, K.; Hwang, I. C.; Park, Y.; Hong, S.; Kim, H. High Quality Area-Selective Atomic Layer Deposition Co Using Ammonia Gas as a Reactant. *J. Electrochem. Soc.* **2010**, *157*, 10–15.
- (22) Kim, J. M.; Lee, H. B. R.; Lansalot, C.; Dussarrat, C.; Gatineau, J.; Kim, H. Plasma-Enhanced Atomic Layer Deposition of Cobalt Using Cyclopentadienyl Isopropyl Acetamidinato-Cobalt as a Precursor. *Jpn. J. Appl. Phys.* **2010**, *49*, 05FA10.
- (23) Kwon, J.; Saly, M.; Halls, M. D.; Kanjolia, R. K.; Chabal, Y. J. Substrate Selectivity of (TBu-Allyl)Co(CO)<sub>3</sub> during Thermal Atomic Layer Deposition of Cobalt. *Chem. Mater.* **2012**, *24*, 1025–1030.
- (24) Kwon, J.; Saly, M.; Kanjolia, R. K.; Chabal, Y. J. Surface Reactions of M<sub>2</sub>-H<sub>2</sub>-(TBu-Acetylene)Dicobalthexacarbonyl with Oxidized and H-Terminated Si(111) Surfaces. *Chem. Mater.* **2011**, *23*, 2068–2074.

- (25) Kerrigan, M. M.; Klesko, J. P.; Rupich, S. M.; Dezelah, C. L.; Kanjolia, R. K.; Chabal, Y. J.; Winter, C. H. Substrate Selectivity in the Low Temperature Atomic Layer Deposition of Cobalt Metal Films from Bis(1,4-Di-Tert-Butyl-1,3-Diazadienyl)Cobalt and Formic Acid. *J. Chem. Phys.* **2017**, *146*, 052813.
- (26) Kerrigan, M. M.; Klesko, J. P.; Winter, C. H. Low Temperature, Selective Atomic Layer Deposition of Cobalt Metal Films Using Bis(1,4-Di-Tert-Butyl-1,3-Diazadienyl)Cobalt and Alkylamine Precursors. *Chem. Mater.* **2017**, *29*, 7458–7466.
- (27) Klesko, J. P.; Kerrigan, M. M.; Winter, C. H. Low Temperature Thermal Atomic Layer Deposition of Cobalt Metal Films. *Chem. Mater.* **2016**, *28*, 700–703.
- (28) Knisley, T. J.; Saly, M. J.; Heeg, M. J.; Roberts, J. L.; Winter, C. H. Volatility and High Thermal Stability in Mid- to Late-First-Row Transition-Metal Diazadienyl Complexes. *Organometallics* **2011**, *30*, 5010–5017.
- (29) Criado, J. M.; Gonzalez, F.; Trillo, J. M. Mechanism of Formic Acid Decomposition on 3d Metal Oxides. *J. Catal.* **1971**, *23*, 11–18.
- (30) Columbia, M. R.; Thiel, P. a. The Interaction of Formic Acid with Transition Metal Surfaces, Studied in Ultrahigh Vacuum. *J. Electroanal. Chem.* **1994**, *369*, 1–14.

## **Chapter 7 Tungsten metal deposition with atomic layer deposition/atomic layer etching to achieve area-selective deposition**

### 7.1 Abstract

Area-selective deposition (ASD) becomes essential for further development of sub-5 nm semiconductor fabrication. For more complex nanoscale patterning, new approaches have been addressed to improve better ASD. Herein, ASD of atomic layer deposition (ALD) and atomic layer etching (ALE) is integrated to achieve ASD of tungsten (W) on hydrogen-terminated silicon (Si-H) vs. hydroxyl silicon (Si-OH) at 275 °C. Using  $\text{WF}_6/\text{SiH}_4$  for ALD and  $\text{O}_2/\text{WF}_6$  for ALE, various ALD/ALE “supercycles” are studied with spectroscopic ellipsometry, X-ray photoelectron spectroscopy, scan electron microscopy, and atomic force microscopy. While unwanted nuclei can be effectively removed on non-growth surface (Si-OH) with the supercycles, W growth is impeded on the growth surface (Si-H) after ALE process. This work highlights that understanding of the etching effect on the subsequent growth is critical to obtain reproducible ASD using ALD/ALE supercycles.

### 7.2 Introduction

Tungsten (W) has been used for the interconnect metallization in the semiconductor fabrication due to its high conductivity ( $\sim 5.28 \mu\Omega\cdot\text{cm}$ )<sup>1</sup>, good electromigration durability (melting point of 3380 °C)<sup>2</sup>, robustness against the contamination, wet cleans, and mechanical stress.<sup>3</sup> Although the resistivity of tungsten is slightly higher than copper and aluminum, these other advantages enable tungsten processes to be applied for middle-of-the-line (MOL) contacts and vias for microelectronic devices.<sup>14</sup> Since tungsten deposition is generally based on the strong reduction reaction between tungsten hexafluoride ( $\text{WF}_6$ ) and a reducing agent such as silane ( $\text{SiH}_4$ )<sup>4-7</sup>,

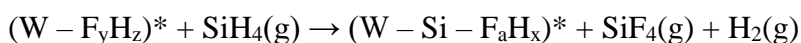
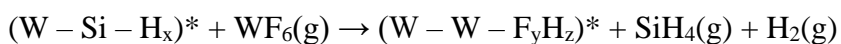
diborane ( $B_2H_6$ )<sup>8</sup>, and hydrogen ( $H_2$ )<sup>9</sup>, titanium nitride (TiN) are required to prevent the fluorine diffusion from  $WF_6$  to silicon (source and drain). TiN is also important to minimize the oxidation of titanium (Ti) seed layer which is essential to enhance the film adhesion on silicide by forming TiSi.<sup>10</sup> In general, tungsten process is processed in two steps: i) conformal and thin W layer with  $WF_6$  and  $SiH_4$  on TiN/Ti barrier layers, and ii) bulk W deposition using  $WF_6$  and  $H_2$ .<sup>15</sup> As the node size of the transistor becomes less than 10 nm, the size effect of W-based metallization (W with barrier layers) significantly increases the resistivity resulting from the electron scattering<sup>11</sup> and larger barrier portion relative to metal fill. The current research trend focuses on developing barrier-less metallization using different metals (cobalt<sup>12</sup>, ruthenium<sup>13</sup>, and molybdenum<sup>14</sup>) to reduce the electrical loss and maintain electromigration reliability at the smaller node system.

For the continued scaling of the semiconductor feature size, new capabilities are required in nanoscale patterning to precisely control film purity, uniformity, dimension, and complex structure.<sup>15,16</sup> The current chip structure is dependent on photolithography where the pattern resolution is limited to the wavelength of the light source (193 nm ArF). Although extreme-ultraviolet lithography (EUV) with 13.5 nm has been employed to address some challenges, inherent alignment problems, namely stochastic effects, and substantial cost seems to be substantial.<sup>17</sup> Bottom-up area-selective deposition (ASD) can bypass the limitation of the physical feature alignment by controlling the surface chemical reaction.<sup>15,16</sup> Inherently self-aligned ASD can offer precise pattern placement even less than 5 nm feature size.

Atomic layer deposition (ALD) is one of the most important techniques for ASD fabrication. Based on self-limiting reactions and chemical specificity, a thin film layer can be deposited on desired-growth surface, whereas the film nucleation is initially impeded on non-growth surface.<sup>5,18</sup> However, extended ALD runs will generate nuclei on non-growth surface,

leading to selectivity loss. To enhance the inherent ASD, additional processes are generally implemented such as surface pretreatment, surface passivation with an organic inhibitor,<sup>19-23</sup> and surface etching.<sup>24-26</sup> Many efforts have been demonstrated to integrate ALD and the etching reaction to remove unwanted nuclei on the non-growth surface. Etching can be processed with wet etch, plasma-based reaction, chemical vapor etching (CVE), and atomic layer etching (ALE). Among various etching methods, ALE offers precise etch control due to its self-limiting reaction. Previously, our group studied TiO<sub>2</sub> ASD by combining ALD (TiCl<sub>4</sub>/H<sub>2</sub>O) and ALE (WF<sub>6</sub>/BCl<sub>3</sub>) at 150–190 °C.<sup>24,25,27</sup> As shown in **Figure 7.1**, inherent TiO<sub>2</sub> ASD on blanket Si-OH vs. Si-H is 1.2 nm, whereas the supercycle of ALD/ALE exhibits much better ASD of 12 nm.<sup>24</sup> TiO<sub>2</sub> ASD can be further improved by carefully controlling the H<sub>2</sub>O dosing times, yielding 32 nm ASD.<sup>25</sup>

Compared to TiO<sub>2</sub> ASD, W shows opposite ASD where the growth surface is Si-H rather than Si-OH. The W ALD is based on fluorosilane elimination chemistry where SiH<sub>4</sub>(g) reduces WF<sub>6</sub>(g) to W<sup>0</sup>(s), producing SiF<sub>4</sub>(g) and H<sub>2</sub>(g).<sup>5,6</sup> The ALD half-reactions are given as



where the asterisk (\*) indicates adsorbed surface species. It is widely known that the reduction of WF<sub>6</sub> on Si-H is thermodynamically favorable, leading to fast nucleation. Therefore, WF<sub>6</sub>/SiH<sub>4</sub> ALD is utilized as a W nucleation process to improve the film coverage on complex features.<sup>4</sup> On the contrary, the reduction reaction on Si-OH is much slower than Si-H. By using the nucleation rate difference between Si-H and Si-OH, previous study obtained ~6 nm W ASD.<sup>5</sup> In addition, W film can be thermally etched by O<sub>2</sub>/WF<sub>6</sub>.<sup>7</sup> **Figure 7.2** shows the ALE of W films at various

temperatures. Using the W density of  $19.3 \text{ g/cm}^3$ , the estimated etching rate is  $-3 \text{ \AA/cycle}$  and  $-6 \text{ \AA/cycle}$  at  $275$  and  $300 \text{ }^\circ\text{C}$ , respectively. In this work, W ASD is studied by combing ALD and ALE to further improve the W selectivity. Varied ALD/ALE conditions are performed to understand the etching effect on a subsequent W ALD process.

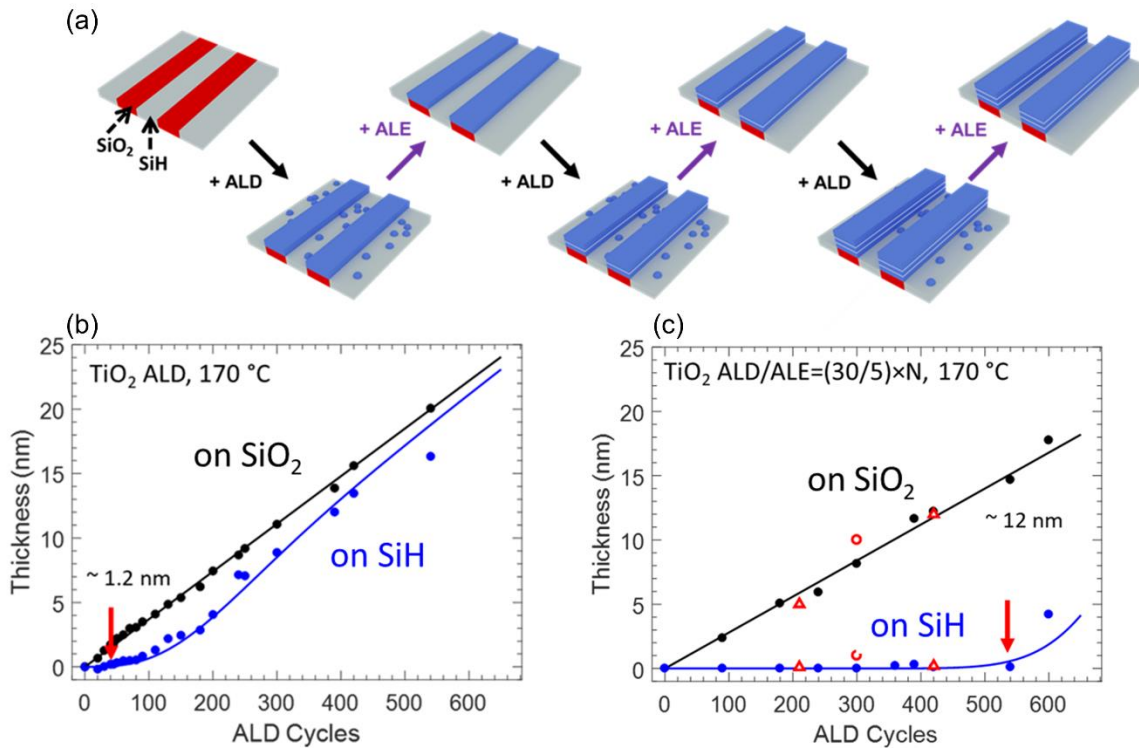


**Figure 7.1** (a) Scheme of the integrated ALD/ALE supercycle (3 cycles) sequence, (b) TiO<sub>2</sub> thickness as a function of ALD cycle at 170 °C on Si-H and Si-OH. (c) TiO<sub>2</sub> thickness as a function of ALD/ALE supercycle at 170 °C on Si-H and Si-OH. Thickness measured by spectroscopy ellipsometry. Figure reproduced from ref.<sup>24</sup>

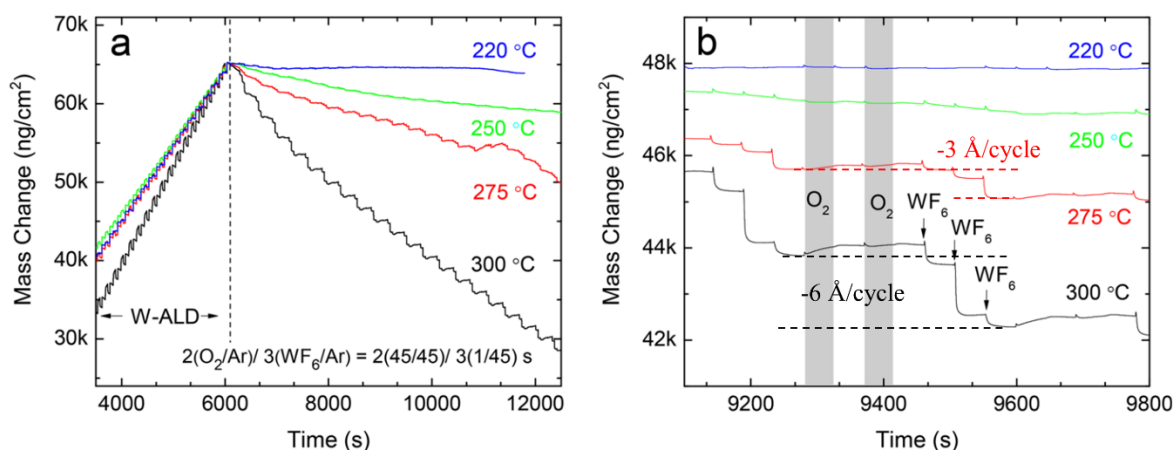


**Figure 7.2** (a) Quartz crystal microbalance of W ALD (WF<sub>6</sub>/SiH<sub>4</sub>) followed by W ALE using O<sub>2</sub> and WF<sub>6</sub> at various temperatures (220~300 °C). (b) An expansion of panel (a) showing mass change vs. process time using  $(2 \times O_2)/(3 \times WF_6)$ . Figure reproduced from ref.<sup>7</sup>

### 7.3 Experimental Section

#### 7.3.1 Substrate Surface Preparation and Deposition Reactants

Silicon (boron-doped Si (100), 6–10 Ω·cm, WRS Materials) and silicon dioxide (SiO<sub>2</sub>, 100 nm of thermally grown SiO<sub>2</sub> on boron-doped Si (100), WRS Materials) were cut into ~1 cm × 1 cm coupons. Before deposition, all silicon, SiO<sub>2</sub>, and patterned wafers were cleaned in a hot piranha bath (1:1 = H<sub>2</sub>SO<sub>4</sub>/H<sub>2</sub>O<sub>2</sub> by volume ratio) for 30 min, rinsed with deionized (DI) water, and dried with N<sub>2</sub>, forming surface silicon hydroxide. To form hydrogen-terminated silicon (Si-H), silicon and patterned wafers were dipped into 5% hydrogen fluoride (HF) aqueous solution for 30 s, rinsed with DI water for 30 s, and dried with N<sub>2</sub>. To minimize surface oxidation and contamination, the HF treatment was conducted immediately before use.

Tungsten hexafluoride (WF<sub>6</sub>, 99.99%, Galaxy Chemical), 2% silane (SiH<sub>4</sub>, 2% diluted with Ar, Airgas), and oxygen (O<sub>2</sub>, 99.999%, Arc3 Gases) were used as received without further

purification. Argon gas (Ar, 99.999%, Airgas) purified with an inert gas filter (Gatekeeper, Entegris) was used as a reactant carrier and purge gas. Upon SiH<sub>4</sub>, WF<sub>6</sub>, and O<sub>2</sub> doses, the pressure increased by ~3.5 Torr, ~0.23 Torr, and ~0.9 Torr, respectively.

### 7.3.2 Reactor Design and Reactor Sequence

Tungsten deposition was performed in a home-built, isothermal, and viscous-flow ALD reactor described previously.<sup>5-7</sup> The reaction chamber was a stainless steel cylinder with ~10 cm inner diameter and ~60 cm length. The sample deposition zone was defined by the substrate holder with ~30 cm long and ~6 cm wide, placed approximately in the middle of the reaction chamber. The reactor was heated resistively using PID controllers, and the temperature was set at 100 – 300 °C. The chamber was pumped by a rotary vane pump (Adixen 2021I, 21 m<sup>3</sup>/h) filled with fluorocarbon oil. The inlet of the rotary pump was filtered through activated charcoal and sodasorb filters (Mass-Vac Inc.). The working pressure with an Ar flow rate of 210 standard cubic centimeters per minute (sccm) was ~1.5 Torr. Ar and reactant flow were controlled by computer-controlled pneumatic diaphragm valves.

Prior to loading substrates into the reactor, the chamber was conditioned with 25 cycles of Al<sub>2</sub>O<sub>3</sub> ALD using trimethylaluminum (TMA, 98%, Strem Chemicals) and DI H<sub>2</sub>O. The Al<sub>2</sub>O<sub>3</sub> ALD sequence followed TMA/Ar/H<sub>2</sub>O/Ar = 0.1/45/0.1/45 s. Without the wall conditioning, inconsistent W deposition was observed due to the increased SiH<sub>4</sub> reaction with the wall.<sup>5</sup>

After reactor wall conditioning, substrates were loaded into the reactor and exposed to Ar flow for 30 min to reach thermal equilibrium with the reactor walls. A cycle of W ALD sequence followed: SiH<sub>4</sub>/Ar/WF<sub>6</sub>/Ar = 45/45/1/60 s. A cycle of W ALE sequence followed: (O<sub>2</sub>/Ar)/5x(WF<sub>6</sub>/Ar) = (45/45)/5x(1/45) s.

### 7.3.3 Sample Characterization

Quartz crystal microbalance (QCM) was measured to understand the reaction behavior during W ALD and ALE. A QCM probe body (Kurt Lesker) with a 6 MHz gold-coated crystal sensor (Inficon) was loaded into the reactor and allowed to stabilize at the reactor temperature. The resonant frequency of the crystal was recorded with a control box (STM-160, Inficon) through a home-designed LabVIEW program and converted to mass change ( $\text{ng}/\text{cm}^2$ ) with the Sauerbrey equation.<sup>28</sup> 40 sccm of Ar backpurge was used to prevent deposition in the electrical contact regions. W thickness was characterized by ex situ spectroscopic ellipsometry (SE,  $\alpha$ -SE ellipsometer, J.A. Woollam) with an incidence angle of  $70^\circ$  and a spectral range of 300 – 900 nm. To build the SE model fit, multiple oscillators were used to fit the measured data. Scanning electron microscopy (SEM, FEI Verios 460L) operated at 2–30 kV with 0.7 nm resolution was used to analyze the surface morphology after W ALD and ALE. X-ray photoelectron spectroscopy (XPS, Kratos Analytical Axis Ultra) with an Al  $K\alpha$  (1486.6 eV) gun was used to analyze the chemical composition of the films. Peak positions were calibrated by referencing either the adventitious C 1s peak to 285.0 eV or O 1s peak to 531.0 eV (if the C 1s peak is invisible).

## 7.5 Results and Discussion

**Figure 7.3** shows W film thickness as a function of ALD cycles using SiH<sub>4</sub>/Ar/WF<sub>6</sub>/Ar = 45/45/1/60 s at 220 and 275 °C. Based on the previous study (Berc *e. al.*)<sup>6</sup>, the ALD temperature window was between 200 and 300 with ~6.0 Å/cycle, whereas the observed growth rates at 220 and 275 °C are substantially different. While the growth rate at 220 °C is similar with the previous study, the growth rate at 275 °C is greatly faster for 15 cycles of W ALD. Given that W ALD shows soft-saturation behavior, the larger precursor doses may have a large impact on the growth rate. Careful SiH<sub>4</sub> and WF<sub>6</sub> doses would be necessary to maintain the ALD window at higher temperatures. Data set at 220 and 275 °C (red and green in **Figure 7.3**) was averaged from at least three different runs to confirm the process reproducibility. Large deviations are often observed, and it is mostly associated with the poor wall conditioning. More careful wall conditions with longer W deposition of 50 cycles and Al<sub>2</sub>O<sub>3</sub> deposition of 200-400 cycles would be helpful to enhance the reproducibility of W ALD process. Since the SE model fit of metal films is challenging due to the light absorption of the metals, it is important to confirm the data's accuracy. **Table 7.1** shows the W thickness measured by SE is consistent with the cross-section TEM results.

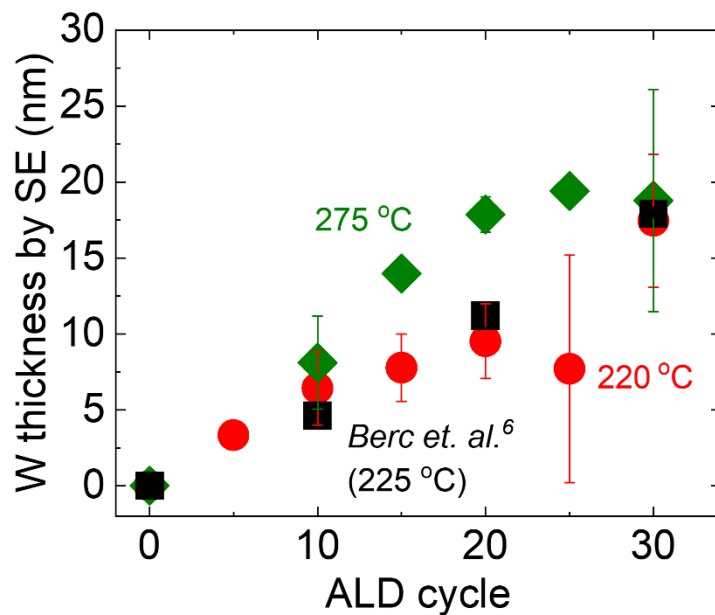


**Figure 7.3** W film thickness on Si-H surfaces as a function of ALD cycle with various temperature. Thickness was measured by spectroscopic ellipsometry. Data at 220 and 275 °C were averaged from at least three different runs. The results are compared with the previously reported result.<sup>6</sup>

**Table 7.1** W thickness on Si-H measured by SE and TEM at 220 °C.

W cycle	W thickness by SE (nm)	W thickness by TEM (nm)
15 cycle	6.7	6.1
20 cycle	9.8	10.0

W ALD was integrated with W ALE process to remove unwanted W nuclei on non-growth surface (Si-H). During the ALE process, W would be etched on both Si-OH and Si-H surfaces, but the inherent selectivity window enables to achieve selective W growth on Si-H while suppressing the nucleation on Si-OH surfaces. To observe the film evolution with ALD/ALE supercycles, SEM were measured with various ALD and ALE conditions. **Figure 7.4** shows the surface morphology of W nuclei on Si-OH. On Si-OH surfaces, W nuclei starts to appear after 15 cycles. Unwanted W nuclei can be effectively removed on Si-OH surfaces by repeating ALD and ALE processes. **Figure 7.4d-f** shows that W nuclei is etched on Si-OH with different supercycle conditions.

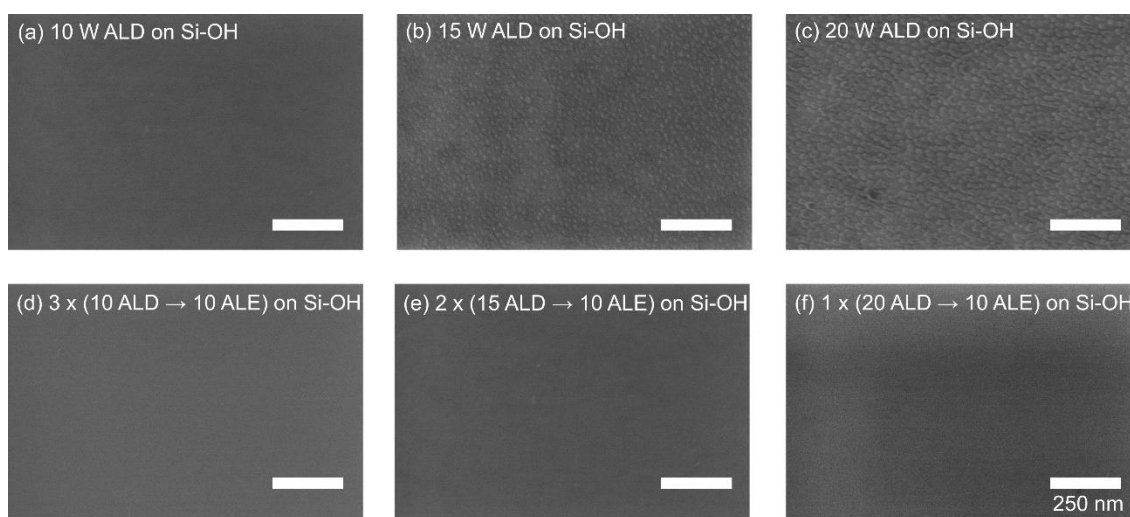


**Figure 7.4** Top-down SEM images of various W ALD/ALE processes on Si-OH at 275 °C. All scales are the same. Unwanted W nuclei is observed after 15 W ALD and the W nuclei can be clearly removed with W ALE processes.

W morphology on Si-H surfaces was also measured by top-down SEM. To evaluate the surface roughness, root mean square (RMS) was measured by AFM shown in **Figure 7.5**.

Compared to W nucleation on Si-OH in **Figure 7.4a-c**, W nuclei is densely distributed on Si-H in **Figure 7.5b, c**, confirming the inherent W ASD. After the first supercycle (10 cycles of W ALD followed by 10 cycles of W ALE), no noticeable morphology change is observed, but after 2 and 3 supercycles, the surfaces dramatically change in **Figure 7.5e-f**, implying that the deposited films would differ from the W metal. Nonetheless, there is no significant change of the surface roughness with different supercycle conditions.

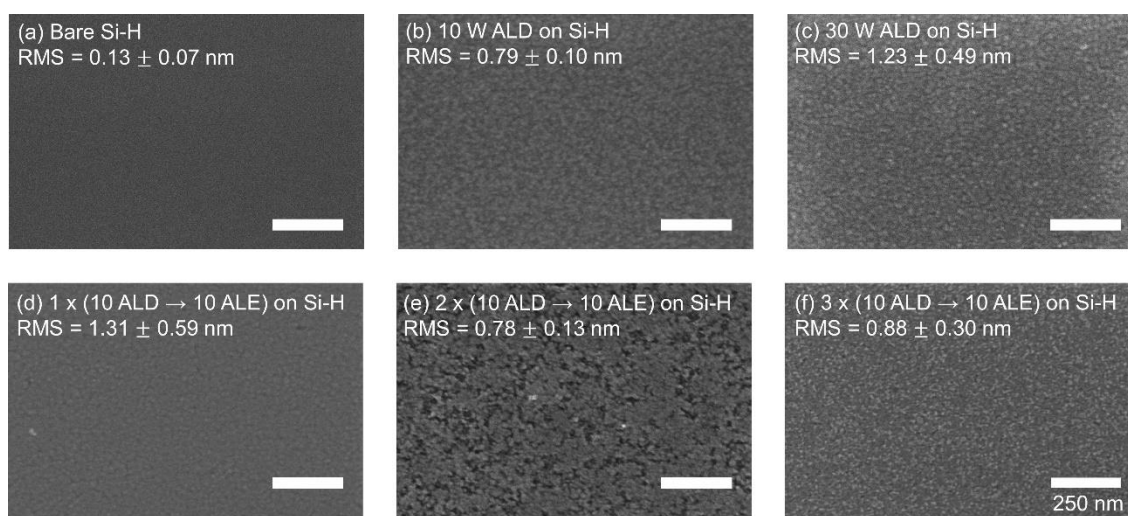


**Figure 7.5** Top-down SEM images of various W ALD/ALE processes on Si-H at 275 °C. All scales are the same. RMS values are the average of three different measurements measured by AFM. With increasing the supercycle, the surface morphology on Si-H gradually changes, whereas no significant change is observed on the surface roughness.

To fully investigate the chemical composition with different supercycles, high resolution XPS was measured in **Figure 7.6**. The observed W 4f peak contains W-O peak due to the native oxidation of the W films. **Table 7.2** summarizes the detailed conditions for the supercycles. Based

on the growth and etching rate, the expected supercycle growth of 10 x ALD / 10 x ALE would be 2~7 nm/supercycle. However, SE data shows that 4.9, 3.4, 3.4, 3.6 nm after 10 W ALD, N = 1 (10W ALD → 10W ALE), N = 2, and N = 3, respectively. This might due to the etching effect on the W film surface, thus changing the light reflection for the SE measurement. High resolution XPS analysis of O 1s and W 4f in **Table 7.3** shows that W atomic composition ratio is almost the same for 10 W ALD, N = 1 and N = 2. However, W ratio dramatically decreases after N = 3, whereas Si 2p intensity significantly increases, indicating that most of W films are removed. Considering O-W peak (530.9 eV)<sup>29-31</sup> and O-Si peak (532.3 eV)<sup>32</sup> on O 1s peak, silicon oxide or hydroxyl silicon surface appears as tungsten oxide is removed after N = 3. This result indicates that the SE fit is inaccurate to estimate W thickness after W ALE processes.

**Table 7.2** W ALD and ALE supercycle conditions.

	W ALD	W ALE	Chamber Temp.
Sequence	SiH <sub>4</sub> /Ar/WF <sub>6</sub> /Ar	O <sub>2</sub> /Ar/5 x (WF <sub>6</sub> /Ar)	275 °C
Time	45/45/1/60 s	45/45/1/45 s	
GPC	5~10 Å/cycle*	~3 Å/cycle <sup>16</sup>	
Combination	1 supercycle : [10 x (ALD) + 10 x (ALE)] Supercycle N : 1, 2, 3		

\* Thickness from 10 cycles of W ALD in **Figure 7.3**

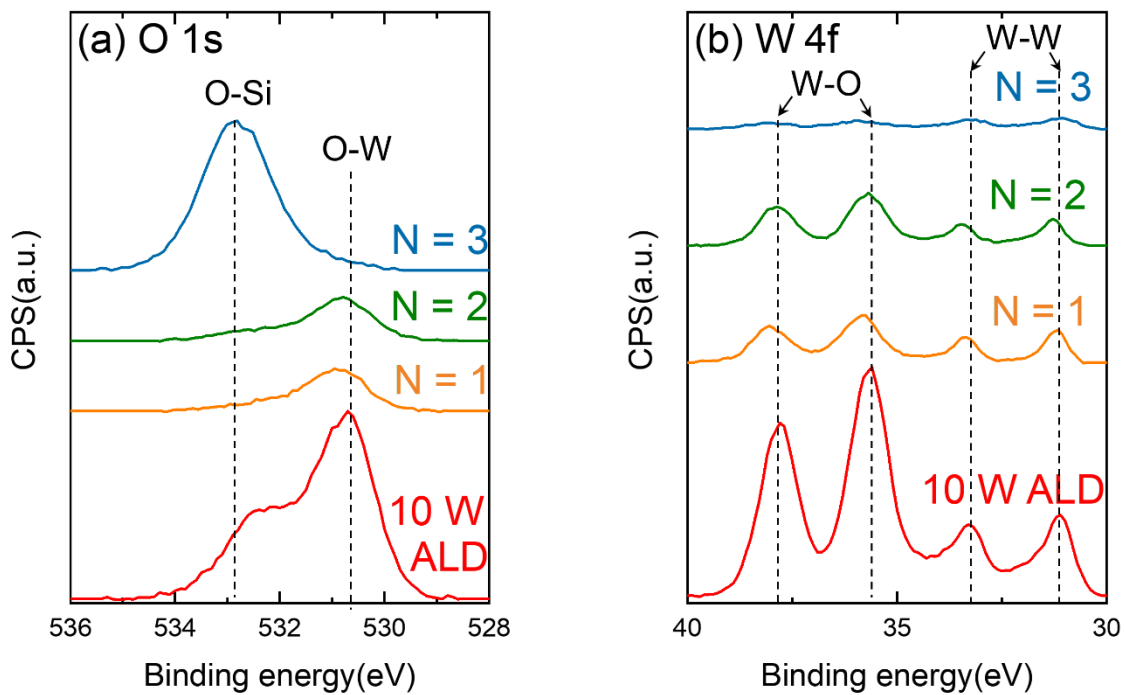


**Figure 7.6** High resolution XPS scans of (a) O 1s and (b) W 4f on Si-H at 275 °C after 10 W ALD, 1 supercycle (N = 1, 10 W ALD → 10 W ALE), N = 2, and N = 3.

**Table 7.3** Elemental composition from XPS analysis. Values are given in atomic %.

	C 1s	O 1s	F 1s	W 4f	Si 2p
10 W ALD	21.06	52.44	1.54	17.74	7.22
N = 1 (10 W -10 ALE)	18.92	54.36	1.25	21.78	3.7
N = 2 2 x (10 W- 10 ALE)	23.08	53.22	0	20.15	3.55
N = 3 3 x (10W -10 ALE)	13.52	49.38	2.42	1.71	32.97

In an ideal scenario, after ALE process, ALD growth behavior should be the same as it is on the pristine surface. However, the current result indicates that ALE process has a significant impact on the subsequent W ALD growth. This might be attributed to the wall effect, resulted from the prolonged  $WF_6$  doses during ALD and ALE processes. Large  $WF_6$  residue on the wall can capture the following  $SiH_4$  doses, retarding the W growth on the substrate. To validate this hypothesis,  $H_2O$  cleaning was employed to remove  $WF_6$ , forming  $WO_3$ . To fully clean off  $WF_6$ , 5 subdoses of ( $H_2O/Ar = 0.1/45$  s) were pre-dosed prior to  $O_2$  doses on the ALE step. **Figure 7.7** shows the mass uptake during 3 supercycles of 15 x ALD/10 x ALE (red) and 4 supercycles of 15 x ALD/10 x ALE with  $H_2O$  predose (blue). After W ALD, mass decreases during the ALE process. For the reference condition (red), the net mass increase of each supercycle is indicated by the green dash line, whereas the black dash line is drawn for the  $H_2O$  treatment process (blue). While inconsistent mass increase is observed for the reference condition, more consistent net mass change is measured with the  $H_2O$  treatment. This illustrates that the wall conditioning is critical to

improve the reproducibility of W supercycles. Other than the wall effect, there would be other factors to affect the W growth behavior after ALE process. More thorough surface analysis would be needed to fully understand the ALE effect on the W surface.

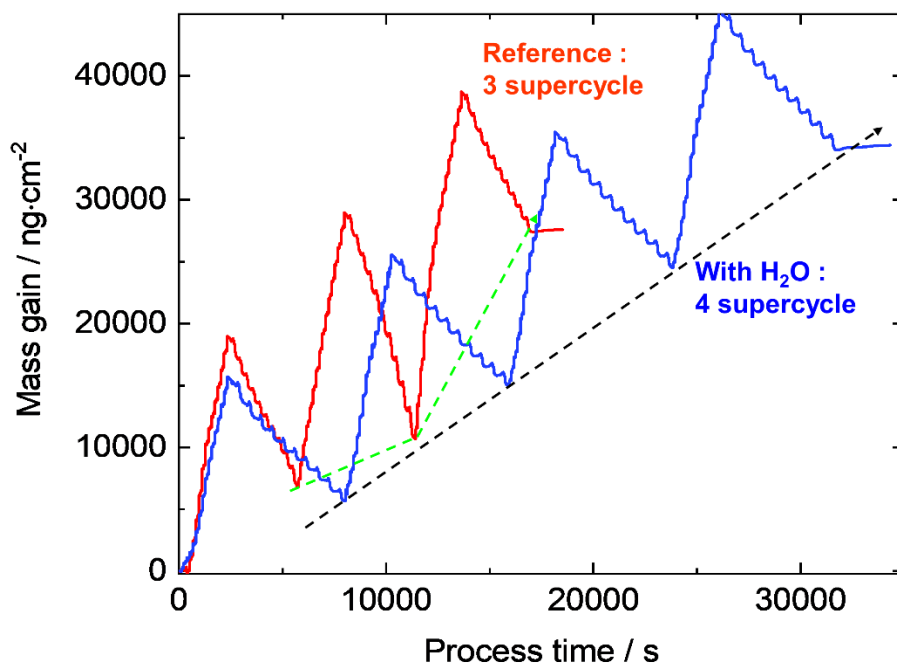


**Figure 7.7** QCM mass change of 3 supercycles of W ALD/ALE (red) and 4 supercycles of W ALD/ALE (blue) where 5 cycles of H<sub>2</sub>O were sequentially dosed before O<sub>2</sub> dose.

## 7.7 Summary

This work described the integration of W ALD ( $\text{WF}_6/\text{SiH}_4$ ) and ALE ( $\text{O}_2/\text{WF}_6$ ) to improve W ASD. During the W ALD process, W growth rate was greatly dependent on the wall condition: poor wall condition led to unexpected growth rate. Results showed that unwanted W nuclei can be removed on non-growth surface (Si-OH), whereas the repeated ALE process has a great impact on the growth surface (Si-H), impeding the W growth. After 3 supercycle of ALD/ALE, W peak by XPS substantially decreased and the surface morphology by SEM changed compared to simple W ALD on Si-H surfaces. The unexpected W growth after ALE process might be due to the wall effect from the prolonged  $\text{WF}_6$  exposure.  $\text{H}_2\text{O}$  treatment was implemented prior to  $\text{O}_2$  doses, indicating more consistent W ALD growth after the ALE. This finding illustrates that it is critical to carefully understand the surface conditions for combining ALD and ALE processes. Although the etching process shows reliable results, the subtle change by the etching chemistry can significantly affect the following ALD process. Understanding the ALE effect on the surface will be a critical step to achieve W ASD by ALD/ALE supercycle.

## 7.9 References

- (1) Czack, G. *Gmelin Handbook of Inorganic Chemistry and Organometallic Chemistry*, 8 Ed, Syst. No. 54, Tungsten. Suppl. Vol. A3; Springer-Verlag: Heidelberg, 1989.
- (2) Lassner, E.; Schubert, W. D. *Tungsten*. Springer US: Boston, MA, 1999.
- (3) Kamineni, V.; Raymond, M.; Siddiqui, S.; Mont, F.; Tsai, S.; Niu, C.; Labonte, A.; Labelle, C.; Fan, S.; Peethala, B.; Adusumilli, P.; Patlolla, R.; Priyadarshini, D.; Mignot, Y.; Carr, A.; Pancharatnam, S.; Shearer, J.; Surisetty, C.; Arnold, J.; Canaperi, D.; Haran, B.; Jagannathan, H.; Chafik, F.; L'Herron, B. *Tungsten and Cobalt Metallization: A Material Study for MOL Local Interconnects*. *IEEE IITC/AMC*, **2016**, 105–107.
- (4) Steinhögl, W.; Steinlesberger, G.; Perrin, M.; Scheinbacher, G.; Schindler, G.; Traving, M.; Engelhardt, M. *Tungsten Interconnects in the Nano-Scale Regime*. *Microelectron. Eng.* **2005**, *82*, 266–272.
- (5) Kalanyan, B.; Lemaire, P. C.; Atanasov, S. E.; Ritz, M. J.; Parsons, G. N. *Using Hydrogen to Expand the Inherent Substrate Selectivity Window during Tungsten Atomic Layer Deposition*. *Chem. Mater.* **2016**, *28*, 117–126.
- (6) Kalanyan, B.; Losego, M. D.; Oldham, C. J.; Parsons, G. N. *Low-Temperature Atomic Layer Deposition of Tungsten Using Tungsten Hexafluoride and Highly-Diluted Silane in Argon*. *Chem. Vap. Depos.* **2013**, *19*, 161–166.
- (7) Xie, W.; Lemaire, P. C.; Parsons, G. N. *Thermally Driven Self-Limiting Atomic Layer Etching of Metallic Tungsten Using  $WF_6$  and  $O_2$* . *ACS Appl. Mater. Interfaces* **2018**, *10*, 9147–9154.

- (8) Kim, C.-H.; Rho, I.-C.; Kim, S.-H.; Han, I.-K.; Kang, H.-S.; Ryu, S.-W.; Kim, H.-J. Pulsed CVD-W Nucleation Layer Using  $WF_6$  and  $B_2H_6$  for Low Resistivity W. *J. Electrochem. Soc.* **2009**, *156*, H685.
- (9) Desatnik, N.; Thompson, B. E. Nucleation on  $SiO_2$  during the Selective Chemical Vapor Deposition of Tungsten by the Hydrogen Reduction of Tungsten Hexafluoride. *J. Electrochem. Soc.* **1994**, *141*, 3532–3539.
- (10) Ramanath, G.; Greene, J. E.; Carlsson, J. R. A.; Allen, L. H.; Hornback, V. C.; Allman, D. J. W Deposition and Titanium Fluoride Formation during  $WF_6$  Reduction by Ti: Reaction Path and Mechanisms. *J. Appl. Phys.* **1999**, *85*, 1961–1969.
- (11) Plombon, J. J.; Andideh, E.; Dubin, V. M.; Maiz, J. Influence of Phonon, Geometry, Impurity, and Grain Size on Copper Line Resistivity. *Appl. Phys. Lett.* **2006**, *89*, 2004–2007.
- (12) Breil, N.; Shemesh, D.; Fernandez, J.; Hung, R.; Bekiaris, N.; Tseng, J.; Naik, M.; Park, J. H.; Bakke, J.; Kumar, A.; Nafisi, K.; Litman, A.; Karnieli, A.; Kuchik, V.; Wachs, A.; Khasgiwale, N.; Chudzik, M. Electron Beam Detection of Cobalt Trench Embedded Voids Enabling Improved Process Control for Middle-Of-Line at the 7nm Node and Beyond. *2017 IEEE International Electron Devices Meeting (IEDM)*, **2017**, 349–352.
- (13) Vega-Gonzalez, V.; Bekaert, J.; Kesters, E.; Le, Q. T.; Lorant, C.; Varela, P. O.; Teugels, L.; Heylen, N.; El-Mekki, Z.; Van Der Veen, M.; Webers, T.; Wilson, C. J.; Vats, H.; Rynders, L.; Cupak, M.; Uk-Lee, J.; Drissi, Y.; Halipre, L.; Charley, A. L.; Verdonck, P.; Witters, T.; Gompel, S. V.; Briggs, B.; Kimura, Y.; Jourdan, N.; Ciofi, I.; Gupta, A.; Contino, A.; Boccardi, G.; Lariviere, S.; Dupas, L.; De-Wachter, B.; Vancoille, E.; Decoster, S.; Lazzarino, F.; Ercken, M.; Debacker, P.; Kim, R.; Trivkovic, D.; Croes, K.; Leray, P.; Dillemans, L.; Chen, Y. F.; Tokei, Z.; Versluijs, J.; Lesniewska, A.; Paolillo, S.; Baert, R.; Puliyalil, H. Three-Layer BEOL Process

Integration with Supervia and Self-Aligned-Block Options for the 3 nm Node. *2019 IEEE International Electron Devices Meeting (IEDM)*, **2019**, 454–457.

(14) Tokei, Z.; Horiguchi, N. Scaling the BEOL – a toolbox filled with new processes, boosters and conductors. <https://www.imec-int.com/en/imec-magazine/imec-magazine-september-2019/scaling-the-beol-a-toolbox-filled-with-new-processes-boosters-and-conductors>.

(15) Parsons, G. N.; Clark, R. D. Area-Selective Deposition: Fundamentals, Applications, and Future Outlook. *Chem. Mater.* **2020**, *32*, 4920–4953.

(16) Clark, R.; Tapily, K.; Yu, K.; Hakamata, T.; Consiglio, S.; Meara, D. O.; Wajda, C.; Smith, J.; Leusink, G. Perspective : New Process Technologies Required for Future Devices and Scaling. *APL Mater.* **2018**, *6*, 058203.

(17) Liu, E.; Lutker-Lee, K.; Lou, Q.; Chen, Y. M.; Raley, A.; Biolsi, P.; Yu, K. H.; Denbeaux, G. Line Edge Roughness Reduction for EUV Self-Aligned Double Patterning by Surface Modification on Spin-on-Carbon and Tone Inversion Technique. *J. Micro/Nanopatterning, Mater. Metrol.* **2021**, *20*, 1–11.

(18) Kim, J. S.; Parsons, G. N. Nanopatterned Area-Selective Vapor Deposition of PEDOT on SiO<sub>2</sub> vs Si-H: Improved Selectivity Using Chemical Vapor Deposition vs Molecular Layer Deposition. *Chem. Mater.* **2021**, *33*, 9221–9230.

(19) Liu, T. L.; Bent, S. F. Area-Selective Atomic Layer Deposition on Chemically Similar Materials: Achieving Selectivity on Oxide/Oxide Patterns. *Chem. Mater.* **2021**, *33*, 513–523.

(20) Merckx, M. J. M.; Sandoval, T. E.; Hausmann, D. M.; Kessels, W. M. M.; Mackus, A. J. M. Mechanism of Precursor Blocking by Acetylacetone Inhibitor Molecules during Area-Selective Atomic Layer Deposition of SiO<sub>2</sub>. *Chem. Mater.* **2020**, *32*, 3335–3345.

- (21) Pattison, T. G.; Hess, A. E.; Arellano, N.; Lanzillo, N.; Nguyen, S.; Bui, H.; Rettner, C.; Truong, H.; Friz, A.; Topuria, T.; Fong, A.; Hughes, B.; Tek, A. T.; DeSilva, A.; Miller, R. D.; Qiao, G. G.; Wojtecki, R. J. Surface Initiated Polymer Thin Films for the Area Selective Deposition and Etching of Metal Oxides. *ACS Nano* **2020**, *14*, 4276–4288.
- (22) Suh, T.; Yang, Y.; Zhao, P.; Lao, K. U.; Ko, H. Y.; Wong, J.; Distasio, R. A.; Engstrom, J. R. Competitive Adsorption as a Route to Area-Selective Deposition. *ACS Appl. Mater. Interfaces* **2020**, *12*, 9989–9999.
- (23) Soethoudt, J.; Hody, H.; Spampinato, V.; Franquet, A.; Briggs, B.; Chan, B. T.; Delabie, A. Defect Mitigation in Area-Selective Atomic Layer Deposition of Ruthenium on Titanium Nitride/Dielectric Nanopatterns. *Adv. Mater. Interfaces* **2019**, *6*, 1900896.
- (24) Song, S. K.; Saare, H.; Parsons, G. N. Integrated Isothermal Atomic Layer Deposition/Atomic Layer Etching Super-Cycles for Area-Selective Deposition of TiO<sub>2</sub>. *Chem. Mater.* **2019**, *31*, 4793–4804.
- (25) Saare, H.; Song, S. K.; Kim, J.-S.; Parsons, G. N. Effect of Reactant Dosing on Selectivity during Area-Selective Deposition of TiO<sub>2</sub> via Integrated Atomic Layer Deposition and Atomic Layer Etching. *J. Appl. Phys.* **2020**, *128*, 105302.
- (26) Vos, M. F. J.; Chopra, S. N.; Verheijen, M. A.; Ekerdt, J. G.; Agarwal, S.; Kessels, W. M. M.; Mackus, A. J. M. Area-Selective Deposition of Ruthenium by Combining Atomic Layer Deposition and Selective Etching. *Chem. Mater.* **2019**, *31*, 3878–3882.
- (27) Lemaire, P. C.; Parsons, G. N. Thermal Selective Vapor Etching of TiO<sub>2</sub>: Chemical Vapor Etching via WF<sub>6</sub> and Self-Limiting Atomic Layer Etching Using WF<sub>6</sub> and BCl<sub>3</sub>. *Chem. Mater.* **2017**, *29*, 6653–6665.

- (28) Sauerbrey, G. The Use of Quarts Oscillators for Weighing Thin Layers and for Microweighing. *Z. Phys.* **1959**, *155*, 206–222.
- (29) Wang, Y.; Wang, X.; Xu, Y.; Chen, T.; Liu, M.; Niu, F.; Wei, S.; Liu, J. Simultaneous Synthesis of  $\text{WO}_{3-x}$  Quantum Dots and Bundle-Like Nanowires Using a One-Pot Template-Free Solvothermal Strategy and Their Versatile Applications. *Small* **2017**, *13*, 1603689.
- (30) Katrib, A.; Hemming, F.; Wehrer, P.; Hilaire, L.; Maire, G. The Multi-Structure of Oxidized-Reduced Tungsten Carbide Surface(S). *Catal. Letters* **1994**, *29*, 397–408.
- (31) Fleisch, T. H.; Mains, G. J. An XPS Study of the UV Reduction and Photochromism of  $\text{MoO}_3$  and  $\text{WO}_3$ . *J. Chem. Phys.* **1982**, *76*, 780–786.
- (32) F., B.; Gallet, J. J.; Kohler, U.; Ellakhmissi, B. B.; Kubsky, S.; Carniato, S.; Rochet, F. Propanoate Grafting on (H,OH)-Si(001)-2 $\times$ 1. *J. Phys. Condens. Matter* **2015**, *27*, 054005.

## **APPENDICES**

## Appendix A. Co-Authored Publications

A.1 Effect of reactant dosing on selectivity during area-selective deposition of TiO<sub>2</sub> *via* integrated atomic layer deposition and atomic layer etching.

Holger Saare, Seung Keun Song, Jung-Sik Kim, and Gregory N. Parsons

*J. Appl. Phys.* **2020**, *128*, 105302

A key hallmark of atomic layer deposition (ALD) is that it proceeds via self-limiting reactions. For a good ALD process, long reactant exposure times beyond that required for saturation on planar substrates can be useful, for example, to achieve conformal growth on high aspect ratio nanoscale trenches, while maintaining consistent deposition across large-area surfaces. Area-selective deposition (ASD) is becoming an enabling process for nanoscale pattern modification on advanced nanoelectronic devices. Herein, we demonstrate that during area-selective ALD, achieved by direct coupling of ALD and thermal atomic layer etching (ALE), excess reactant exposure can have a substantially detrimental influence on the extent of selectivity. As an example system, we study ASD of TiO<sub>2</sub> on hydroxylated SiO<sub>2</sub> (Si–OH) vs hydrogen-terminated (100) Si (Si–H) using TiCl<sub>4</sub>/H<sub>2</sub>O for ALD and WF<sub>6</sub>/BCl<sub>3</sub> for ALE. Using in situ spectroscopic ellipsometry and ex situ x-ray photoelectron spectroscopy, we show that unwanted nucleation can be minimized by limiting the water exposure during the ALD steps. Longer exposures markedly increased the rate of nucleation and growth on the desired non-growth region, thereby degrading selectivity. Specifically, transmission electron microscopy analysis demonstrated that near-saturated H<sub>2</sub>O doses enabled 32.7 nm thick TiO<sub>2</sub> patterns at selectivity threshold  $S > 0.9$  on patterned Si/SiO<sub>2</sub> substrates. The correlation between selectivity and reactant exposure serves to increase

fundamental insights into the effects of sub-saturated self-limiting surface reactions on the quality and effectiveness of ASD processes and methods.

## A.2 Oxidative molecular layer deposition of PEDOT using volatile antimony(V) chloride oxidant

Amanda A. Volk, Jung-Sik Kim, Elizabeth C. Dickey and Gregory N. Parsons

*J. Vac. Sci. Technol. A* **2021**, 39, 032413

Molecular layer deposition and chemical vapor deposition are emerging and promising techniques for the incorporation of high-performance conductive polymers into high surface area devices, such as sintered tantalum anodes for electrolytic capacitors. Until recently, vapor-phase synthesis of poly(3,4-ethylenedioxythiophene) (PEDOT) has relied on solid reactants which require relatively high temperatures and complex dosing schemes for sequential layer-by-layer processes. This work introduces a facile and high-performing layer-by-layer oxidative molecular layer deposition (oMLD) scheme using the volatile liquid oxidant antimony(V) chloride ( $\text{SbCl}_5$ ) to deposit PEDOT thin films. Effects of reactor parameters on PEDOT film characteristics are described, and the necessary foundation for future studies aiming to understand the nucleation and growth of layer-by-layer oMLD PEDOT is detailed.